

Structure-Reactivity Relationships of MoO₃-Based
Catalysts for the Hydrodeoxygenation of Lignin
Pyrolysis Products

Dissertation

zur Erlangung des akademischen Grades
doctor rerum naturalium (Dr. rer. nat.)

der Mathematisch-Naturwissenschaftlichen Fakultät
der Universität Rostock

vorgelegt von
Simon Haida
geboren am 06. Januar 1995 in Wilhelmshaven

Rostock, den 11.10.2024

Die vorliegende Arbeit wurde im Zeitraum von März 2021 bis Oktober 2024 am Leibniz-Institut für Katalyse e.V. an der Universität Rostock im Forschungsbereich „Katalytische in-situ-Studien: Optische Spektroskopie und Thermogravimetrische Methoden“ unter Betreuung von Prof. Dr. Angelika Brückner angefertigt.

Gutachter:

1. Gutachterin

Prof. Dr. Angelika Brückner
Leibniz-Institut für Katalyse e.V.

2. Gutachter

Prof. Dr. Néstor Escalona
Pontificia Universidad Católica de Chile

Datum der Verteidigung: 08.04.2025

Statement of Authorship

I hereby affirm that I have written the present work by myself without outside assistance. No other resources were utilized than stated. All references as well as verbatim extracts were quoted and all sources of information were specifically acknowledged.

Ich versichere hiermit an Eides statt, dass ich die vorliegende Arbeit selbstständig angefertigt und ohne fremde Hilfe verfasst habe. Dazu habe ich keine außer den von mir angegebenen Hilfsmitteln und Quellen verwendet. Die den benutzten Werken inhaltlich und wörtlich entnommenen Stellen habe ich als solche kenntlich gemacht.

Rostock, 11.10.2024

Simon Haida

Danksagung

Mein Dank gebührt zunächst Frau Prof. Dr. Angelika Brückner für die Aufnahme in den großartigen Arbeitskreis, das spannende Promotionsthema und die interessanten Gespräche. Ihre stete Hilfsbereitschaft, Geduld und Förderung haben diese Arbeit und meine persönliche und wissenschaftliche Entwicklung erst ermöglicht.

Dr. Christoph Kubis möchte ich für die gute Betreuung, das Interesse, Vertrauen, für die viele Zeit und die gestalterischen Freiheiten danken. Auch er hat maßgeblich meine Weiterentwicklung mitgetragen.

Sebastian Löbner und Dr. Ali Mohamed Abdel-Mageed möchte ich für die experimentellen Daten, die gute Zusammenarbeit und Austausch in diesem gemeinschaftlichen Projekt danken. Darüber hinaus möchte ich Prof. Dr. Evgenii Kodratenko für die konstruktiven Diskussionen und der Deutschen Forschungsgemeinschaft (DFG) für die Förderung danken.

Der analytischen Abteilung des Leibniz-Instituts möchte ich danken, ohne deren Messungen die Arbeit nicht möglich gewesen wäre. Stellvertretend für die gesamte Abteilung möchte ich insbesondere Dr. Henrik Lund, Dr. Stefan Bartling, Dr. Carsten Kreyenschulte und Anja Simmula danken. Ich möchte mich bei Dr. Hanan Atia für die TPR-Messungen, Dr. Tatiana Otroshchenko für die UV-Vis Experimente bedanken. Auch bei Carl Julius Mussweiler ich mich für seine Unterstützung im Rahmen seines Praktikums bedanken.-

Ebenso möchte ich mich herzlich bei all meinen Kolleginnen und Kollegen Dr. Jana Weiß, Christine Rautenberg die TG-MS und IR-Experimente durchführte, Benedict Leideker, Phong Dam, Dr. Thanh Huyen Vuong die EPR-Versuche für mich durchführte, Dr. Jabor Rabeah, Dr. Elizaveta Fedorova, Lukas Kell, Michael Sebek, Carl Julius Mussweiler, Dr. Abdallah Ibrahim Mohammed, Dr. Nils Rockstroh und Mirjam Schröder für das angenehme Arbeitsklima und den guten Zusammenhalt danken. Dadurch hat die Zeit in der Arbeitsgruppe viel Freude bereitet.

Prof. Dr. Néstor Escalona möchte ich für die Aufnahme, das Ermöglichen der an der Pontificia Universidad Católica de Chile durchgeführten Experimente und übernehmen des Gutachtens danken. Dabei möchte ich insbesondere Dr. César Alexander Pazo Carballo, Josefa Ignacia Pinto Neira, Nubia María Mora Álvarez, Dr. Claudio Cristopher Araya López, Adrien Jean-Jacques Boulard und Dr. Élodie Blanco danken, welche mich bei den experimentellen Arbeiten sehr unterstützt haben.

Zusätzlich bedanke ich mich bei all meinen Freunden für die tollen Erinnerungen, welche eine große Stütze waren und die Zeit in Rostock zu einer unvergesslichen gemacht haben. Ich danke meiner Familie, besonders meinen Eltern und meiner Schwester für die Liebe, das Vertrauen und Unterstützung in allen Lebenslagen.

Copyright Statement

Parts of this dissertation have been published before in the following journal:

S. Haida, S. Löbner, H. Lund, S. Bartling, C. Kreyenschulte, H. Atia, Ali M. Abdel-Mageed, C. Kubis. A. Brückner, *Catal. Sci. Technol.*, 2024, **14**, 2201.

DOI: [10.1039/D3CY01488F](https://doi.org/10.1039/D3CY01488F)

According to the license guidelines of the Royal Society of Chemistry (RSC), authors are not required to request for permission to reuse. It is cited in agreement with the acknowledgement regulations of the RSC.

[Licences copyright and permissions for journal articles \(rsc.org\)](https://www.rsc.org/licenses/copyright-and-permissions-for-journal-articles) (last access: 04.07.2024, 2:35 p.m.)

Licensed media were marked and the permission for reproduction and adaption requested at the corresponding copyright holder.

Zusammenfassung

Zur Produktion von Aromaten innerhalb eines Kohlenstoffkreislaufs ist eine Hydrodeoxygenierung (HDO) von Lignin-Pyrolyseprodukten nötig. Diese wird aktuell in der Flüssigphase unter hohem Druck durchgeführt, könnte aber auch unter den Prozessbedingungen der Pyrolyse mit geeigneten Katalysatoren in der Gasphase erfolgen. Ein Wechsel zu einem Gasphasenprozess wäre besonders aus energetischen Aspekten sinnvoll. In der vorliegenden Arbeit wurde dazu die HDO von Lignin-Modellverbindungen (Anisol, Phenol, Guajakol) mit Hilfe von Molybdänoxid (MoO_3) basierten Katalysatoren untersucht. Diese wurden dazu mit weiteren Metallen (Ni, Co) modifiziert und der Einfluss auf die katalytischen Eigenschaften untersucht, mit dem Ziel die BTX-Aromaten (Benzol, Toluol, Xylol) als Wertprodukt zu erhalten. Ein besonderer Fokus wurde dabei auf die beteiligten aktiven Phasen und deren Bildung unter Reaktionsbedingungen gelegt.

Die Katalysatoren, zumeist nickelmodifiziert, wurden unter Bildung von Nickelmolybdat (NiMoO_4) synthetisiert und anschließend umfassend charakterisiert. Als Referenzkatalysatoren wurden reinphasiges MoO_3 und NiMoO_4 verwendet. Anschließend wurden diese hinsichtlich ihrer katalytischen Eigenschaften sowohl in der Gas- als auch in der Flüssigphasen-HDO untersucht. Dabei zeigte sich, dass durch die Modifikation mit einem Massenanteil von etwa 5 % Nickel der Umsatz unter den gewählten Bedingungen (325 °C , $p_{\text{H}_2} < 1\text{ bar}$) in der Gasphase um bis zu 50 % gesteigert wird, bei ähnlicher Selektivität zu den BTX-Aromaten im Vergleich zum MoO_3 . NiMoO_4 zeigte dabei eine hohe Methanselektivität. Die Modifizierung mit Cobalt hingegen zeigte keine relevante Steigerung der Aktivität. Auch in der Flüssigphase zeigte sich eine verbesserte Aktivität der nickelhaltigen Katalysatoren, allerdings auch eine präferierte Selektivität zu den hydrierten Produkten (Cyclohexan).

Untersuchungen zu den Gründen der verbesserten katalytischen Eigenschaften mittels in-situ XRD zeigten, dass durch Nickel die Bildung der in der Literatur als aktiv beschriebenen Phase, Molybdänoxycarbohydrid ($\text{MoO}_x\text{C}_y\text{H}_z$), deutlich verbessert ist. Dies konnte auf eine verbesserte Reduktion, hervorgerufen durch die Nickelanteile, zurückgeführt werden. Die Regenerationsfähigkeit wurde mit Hilfe von in-situ UV-Vis- und XRD-Untersuchungen untersucht, welche unter oxidativen Bedingungen bei hohen Temperaturen möglich war, was parallel dazu der Verkokung entgegenwirkte.

Die $\text{MoO}_x\text{C}_y\text{H}_z$ Phase beschleunigte jedoch nicht nur die Reaktion, gleichzeitig konnte gezeigt werden, dass der in ihr enthaltene Kohlenstoff zu Methan hydriert wird, was insbesondere in Anwesenheit von einem zunehmenden Nickelgehalt beschleunigt wird. Zusätzlich zeigte sich, dass der Katalysator unter reduktiven Bedingungen nicht nur für die HDO aktiv ist, sondern auch die Bildung von CO und CO_2 katalysiert.

Abstract

Hydrodeoxygenation (HDO) of lignin pyrolysis products is necessary to produce aromatics within a carbon cycle. This is currently carried out in the liquid phase under high pressure but could also take place under the process conditions of pyrolysis with suitable catalysts in the gas phase. Switching to a gas-phase process would be particularly useful from an energy point of view, making it possible to compete with crude oil products.

In the present work, the HDO of lignin model compounds (anisole, phenol, guaiacol) was investigated using molybdenum(VI) oxide (MoO_3)-based catalysts. These were modified with other metals (Ni, Co) and the influence on the catalytic properties was investigated with the aim of obtaining BTX aromatics (benzene, toluene, xylene) as a valuable product. A special focus was placed on the active phases involved and their in-situ accumulation.

The catalysts, mostly nickel-modified, were synthesized to form nickel molybdate (NiMoO_4) and then comprehensively characterized. Pure-phase MoO_3 and NiMoO_4 were used as reference catalysts. These were then analyzed with regard to their catalytic properties in both the gas and liquid phases. It was found that the modification with a mass percentage of around 5 % nickel increased the conversion under the selected conditions (325 °C, $p_{\text{H}_2} < 1$) in the gas phase by up to 50 %, with similar selectivity to the BTX aromatics compared to MoO_3 . NiMoO_4 thus shows a high methane selectivity. Modification with cobalt, on the other hand, did not show any relevant increase in activity. In the liquid phase, the nickel-containing catalysts also showed improved activity, but also a preferential selectivity to the hydrogenated products (cyclohexane).

Investigations into the reasons for the improved catalytic properties using in-situ XRD showed that the formation of the molybdenum oxycarbohydride ($\text{MoO}_x\text{C}_y\text{H}_z$) phase, described in the literature as active, is significantly improved by nickel. This could be attributed to an improved reduction caused by the nickel content. The regeneration capability was investigated by in-situ UV-Vis and XRD analyses, which were conducted under oxidative conditions at elevated temperatures. This approach simultaneously mitigated the effects of coking.

However, the $\text{MoO}_x\text{C}_y\text{H}_z$ phase not only accelerated the reaction, it was also shown that the carbon contained in it is hydrogenated to methane, which is particularly accelerated in the presence of an increasing nickel content. In addition, it was shown that the catalyst is not only active for HDO under reductive conditions, but also catalyzes the formation of CO and CO_2 .

Content

Statement of Authorship.....	I
Danksagung	II
Copyright Statement.....	III
Zusammenfassung.....	IV
Abstract	V
List of Figures	III
List of Tables	VII
List of Abbreviations.....	VIII
1. Introduction and Motivation	1
2. State of the Art and Literature	6
2.1. Lignin Sources and Pyrolysis	6
2.2. Hydrodeoxygenation.....	8
2.2.1. Liquid-Phase Hydrodeoxygenation	10
2.2.2. Gas-Phase Hydrodeoxygenation	12
2.3. Mechanism of HDO at MoO ₃	14
2.4. Active Phases	16
2.5. Doping and Support Influences.....	18
3. Experimental Part and Methods.....	22
3.1. Catalyst Synthesis.....	22
3.2. Catalytic Tests in Gas-Phase	23
3.3. Catalytic Tests in Liquid-Phase	24
3.4. Methods of Characterization.....	24
3.4.1. Powder X-ray Diffraction	24
3.4.2. Electron Paramagnetic Resonance Spectroscopy	27
3.4.3. Vibrational Spectroscopy.....	28
3.4.4. X-ray Photoelectron Spectroscopy	30
3.4.5. Inductively Coupled Plasma Optical Emission Spectroscopy.....	31
3.4.6. Temperature Programmed Reduction	32
3.4.7. Thermogravimetric Measurements.....	32
3.4.8. UV-Vis Spectroscopy	33
3.4.9. Transmission Electron Microscopy.....	34
4. Results and Discussion	36
4.1. Catalytic Results	36
4.1.1. Catalytic Results in Gas-Phase	36
4.1.2. Catalytic Results in Liquid-Phase	41

4.2.	Catalyst Characterization.....	48
4.2.1.	Characterization of Fresh Catalysts	48
4.2.2.	Spent Catalyst Analysis by XRD	51
4.2.3.	Spent Catalyst Analysis by XPS	54
4.2.4.	Oxidation of Spent Catalysts monitored by TG-MS.....	58
4.2.5.	TPR Analysis	60
4.2.6.	DRIFTS Adsorption Test and Operando DRIFTS DME HDO.....	62
4.3.	MoO _x C _y H _z Formation and Regeneration Studies	67
4.4.	In-Situ TEM Study	80
4.5.	In-Situ EPR Investigations of MoO _x C _y H _z	84
4.6.	TPR/TPD of H ₂ /C ₃ H ₆ Treated Samples	89
5.	Structure-Reactivity Relationships	93
6.	Outlook.....	97
7.	References	98
8.	Appendix.....	105

List of Figures

Figure 1: Worlds pulp production for paper production in million tons. Food and Agriculture Organization of the United Nations. ⁸	1
Figure 2: Lignin processing from raw material to valuable products.....	2
Figure 3: Structure of lignin monomers.	3
Figure 4: Overview of different model compounds used in literature.....	7
Figure 5: Reaction network for anisole HDO with Pt/ γ -Al ₂ O ₃ at 300 °C and 140 kPa, adapted with permission from Ref. ⁹³ . Copyright 2011 American Chemical Society.	9
Figure 6: Mo-O bond lengths of a (010) MoO ₃ surface (a) as pristine crystal an (b) with oxygen vacancy, adapted with permission from Ref. ¹⁵³ . Copyright 2011 American Chemical Society.	15
Figure 7: Mechanism of phenol HDO at the MoO ₃ surface, adapted with permission from Ref. ⁹² Copyright 2017 Elsevier.	16
Figure 8: Path of MoO ₃ reduction and MoO _x C _y H _z formation.	17
Figure 9: Phase formation during MoO ₃ reduction, adapted with permission from Ref. ⁴⁴ Copyright 2000 Elsevier.	18
Figure 10: a) Scheme of in-situ XRD set-up b) Stoe HT2 in-situ cell.....	25
Figure 11: Splitting of energy levels in an external magnet field B ₀	27
Figure 12: a) Different interactions of primary electrons and b) a simplified schematic plan of a TEM, adapted with permission from Ref. ¹⁹⁵ . Copyright 2019 Springer Fachmedien Wiesbaden.....	35
Figure 13: Catalytic test over 17 h TOS at 325 °C after pre-reduction at 325 °C for 2 h in 100 % H ₂ , WHSV = 0.31 g _{anisole} ·g ⁻¹ _{cat} ·h ⁻¹ , particle size = 600-800 μm, 200 mg cat. diluted with 2.3 g quartz. Reproduced from Ref. ¹⁹⁷ with permission from the Royal Society of Chemistry.....	36
Figure 14: Conversion over time for the liquid-phase anisole HDO at in a 300 ml batch reactor, at 350 °C, 50 bar H ₂ pressure, 770 rpm agitator speed and 44.4 mmol anisole dissolved in 128 ml <i>n</i> -dodecane with 400 mg catalyst.	41
Figure 15: Conversion and yields for the anisole HDO with MoO ₃ in a 300 ml batch reactor, at 350 °C, 50 bar H ₂ pressure, 770 rpm agitator speed and 44.4 mmol anisole dissolved in 128 ml <i>n</i> -dodecane with 400 mg catalyst.	42
Figure 16: Conversion and yields for the anisole HDO with Ni(5)MoO ₃ in a 300 ml batch reactor, at 350 °C, 50 bar H ₂ pressure, 770 rpm agitator speed and 44.4 mmol anisole dissolved in 128 ml <i>n</i> -dodecane with 400 mg catalyst.	43
Figure 17: Conversion and yields for the anisole HDO with NiMoO ₄ in a 300 ml batch reactor, at 350 °C, 50 bar H ₂ pressure, 770 rpm agitator speed and 44.4 mmol anisole dissolved in 128 ml <i>n</i> -dodecane with 400 mg catalyst.	44
Figure 18: Conversion over time for the liquid-phase guaiacol HDO at in a 300 ml batch reactor, at 350 °C, 50 bar H ₂ pressure, 770 rpm agitator speed and 44.4 mmol anisole dissolved in 128 ml <i>n</i> -dodecane with 400 mg catalyst.	47
Figure 19: Normalized PXRD patterns of the fresh samples calcined at 450 °C for 4 h. Reproduced from Ref. ¹⁹⁷ with permission from Royal Society of Chemistry.	48

Figure 20: Raman spectra of the fresh samples calcined at 450 °C for 4 h measured with $\lambda = 633$ nm and a laser power of 0.085 mW. Reproduced from Ref. ¹⁹⁷ with permission from Royal Society of Chemistry.....	49
Figure 21: SEM overview images in BSE mode of fresh Ni(5)MoO ₃ a) SEM image b) overlaid with the color image of the elemental distributions of Mo (yellow) and Ni (cyan) calculated from the EDX spectra from the area of c). The corresponding EDX spectra is shown in A-30. Reproduced from Ref. ¹⁹⁷ with permission from Royal Society of Chemistry.	50
Figure 22: Normalized XRD patterns of spent catalysts after pre-reduction in 100 % H ₂ for 2 h and gas-phase HDO reaction with anisole for 17 h at 325 °C. Reproduced from Ref. ¹⁹⁷ with permission from the Royal Society of Chemistry.....	52
Figure 23: Normalized XRD patterns of spent catalysts after liquid-phase HDO at 350 °C at 50 bar H ₂ after 4 h reaction with 44.4 mmol anisole dissolved in 128 ml <i>n</i> -dodecane, 400 mg catalyst.	53
Figure 24: Mo3d XP spectra of fresh and used catalysts after TOS = 17 h in the presence of anisole in the gas-phase at 325 °C. The catalysts were pre-reduced in 100 % H ₂ for 2 h before reaction. a) fresh MoO ₃ ; b) spent MoO ₃ ; c) fresh Ni(5)MoO ₃ ; d) spent Ni(5)MoO ₃ ; e) fresh NiMoO ₄ ; f) spent NiMoO ₄ . Reproduced from Ref. ¹⁹⁷ with permission from the Royal Society of Chemistry.	57
Figure 25: Normalized TG-MS profiles of spent catalysts after anisole HDO at 325 °C for 17 h treated in syn. air, 10 °C/min. Reproduced from Ref. ¹⁹⁷ with permission from the Royal Society of Chemistry.	58
Figure 26: TPR of fresh catalysts with 5% H ₂ in Ar and 10 °C/min; m \approx 20 mg. Reproduced from Ref. ¹⁹⁷ with permission from the Royal Society of Chemistry.	61
Figure 27: DRIFT spectra of catalysts after anisole adsorption at 325 °C in 100 % H ₂ (25 ml/min). Reproduced from Ref. ¹⁹⁷ with permission from the Royal Society of Chemistry.	62
Figure 28: DRIFT spectra after a) benzene adsorption in He (25 ml/min) on MoO ₃ is stopped at 325 °C and subsequently b) switch to H ₂ flow (25 ml/min) at 325 °C. Reproduced from Ref. ¹⁹⁷ with permission from the Royal Society of Chemistry.	64
Figure 29: DRIFT spectra after a) benzene adsorption in He (25 ml/min) on NiMoO ₄ is stopped at 325 °C and subsequently b) switch to H ₂ flow (25 ml/min) at 325 °C. Reproduced from Ref. ¹⁹⁷ with permission from the Royal Society of Chemistry.	65
Figure 30: MS signal of DRIFTS/MS experiment with methane evolution (M/Z = 15) after benzene adsorption and switch to a H ₂ atmosphere at 325 °C. Reproduced from Ref. ¹⁹⁷ with permission from the Royal Society of Chemistry.....	66
Figure 31: Simplified scheme for a possible pathway of the methane formation in nickel molybdate catalyst. a) CH ₄ formation by HDO reaction b) CH ₄ formation by MoO _x C _y H _z decomposition. Reproduced from Ref. ¹⁹⁷ with permission from the Royal Society of Chemistry.	67
Figure 32: Normalized in-situ XRD patterns for the MoO ₃ treatment at 350 °C in a H ₂ /CH ₄ mixture (flow: 10 ml/min) at TOS = 300 min for H ₂ :CH ₄ = 9:1 and 1:9, TOS = 305 min for H ₂ :CH ₄ = 1:1. Note, that the broad reflection at $Q \approx 15$ nm ⁻¹ belongs to the SiO ₂ capillary reactor. Ex-situ diffractogram for MoO _x C _y H _z treated in H ₂ :CH ₄ = 9:1 at 325 °C for 1200 min forming a MoO _x C _y H _z phase (\blacktriangle) for comparison with the in-situ data. Heating up was carried out in He for both experiments Reproduced from Ref. ¹⁹⁷ with permission from the Royal Society of Chemistry.	68
Figure 33: Normalized long-time scan ex-situ XRD patterns for NiMoO ₄ after in-situ reduction in pure H ₂ for 120 min and treatment in H ₂ /CH ₄ (1:1) at 325 °C for 1200 min after no further changes in the diffractograms over time were observed. Heating up was	

carried out in He for both experiments. Reproduced from Ref. ¹⁹⁷ with permission from the Royal Society of Chemistry.....	69
Figure 34: Normalized XRD results from the stepwise treatment of Ni(5)MoO ₃ with 100 % H ₂ for 2 h and 100 % CH ₄ for 7 h at 325 °C compared with MoO ₃ . Heating up was carried out in He. Reproduced from Ref. ¹⁹⁷ with permission from the Royal Society of Chemistry.	71
Figure 35: Structural changes of Mo species during in-situ XRD treatment of Ni(5)MoO ₃	71
Figure 36: Results from in-situ XRD investigations on MoO _x C _y H _z formation in MoO ₃ with a) H ₂ :C ₃ H ₆ = 9:1 at 325 °C and b) H ₂ :CH ₄ = 9:1 at 350 °C. Heating up was carried out in He for both experiments. Reproduced from Ref. ¹⁹⁷ with permission from the Royal Society of Chemistry.	72
Figure 37: In-situ XRD measurements of Ni(5)MoO ₃ a) reduction in H ₂ /C ₃ H ₆ (9:1) at 325 °C for 120 min and b) the subsequently oxidation in syn. air for 70 min at 325 °C; c) a second reduction in H ₂ /C ₃ H ₆ (9:1) at 325 °C for 100 min and the d) oxidation in syn. air at 400 °C for 110 min. Heating up was carried out in He for both experiments.	75
Figure 38: In-situ XRD experiments of different samples at 325 °C in a gas mixture of H ₂ /C ₃ H ₆ = 9:1 at TOS = 310 min. a) Ni(5)MoO ₃ ; b) two layers of NiO/MoO ₃ ; c) phys. mix of NiO/MoO ₃ ; d) MoO ₃ . Heating up was carried out in He for both experiments. Reproduced from Ref. ¹⁹⁷ with permission from the Royal Society of Chemistry.	79
Figure 39: In-situ TEM in N ₂ during heat up to a) 200 °C b) 238 °C (red circle shows the starting point of channel formation) c) 325 °C and d) after holding at 325 °C for ca. 4 min.	82
Figure 40: In-situ TEM during treatment in H ₂ /C ₃ H ₆ (9:1) at 325 °C after a) 0 min and b) 1 min after switch c) 6 min and d) 120 min TOS. Red circles show the places of Ni particles.	83
Figure 41: a) Post mortem TEM image after reduction in H ₂ /C ₃ H ₆ (9:1) for 120 min combined with the EDX mapping (spectrum shown in A-89) and b) the magnified area with single element mappings, showing the existence of nickel particles.....	84
Figure 42: In-situ EPR spectra of the fresh samples after calcination (4 h at 450 °C) at 105 K under Ar atmosphere.	85
Figure 43: In-situ EPR spectra of a) MoO ₃ before and after H ₂ reduction measured, b) all reduced samples (in H ₂ atmosphere) measured at 105 K with a modulation amplitude of 1.0G, after H ₂ (100 %) reduction for 120 min at 300 °C.	86
Figure 44: In-situ EPR spectra recorded at 105 K of a) MoO ₃ , b) Ni(1)MoO ₃ , c) Ni(5)MoO ₃ as fresh sample (black lines), after reduction in 100 % H ₂ at 300 °C for 2 h (red lines) and after treatment with a mixture of H ₂ /C ₃ H ₆ (ratio 1:1) for 60 min (blue lines).....	87
Figure 45: In-situ EPR spectra of MoO ₃ and Ni(5)MoO ₃ recorded at 105 K after treatment with a mixture of H ₂ /C ₃ H ₆ for 60 min at 300 °C.	88
Figure 46: In-situ EPR spectra of a) MoO ₃ and b) Ni(5)MoO ₃ recorded at 105 K after reduction with a mixture of H ₂ /C ₃ H ₆ for 120 min at 300 °C (black lines), then flushing in Ar for low temperature EPR measurements and following by heating under Ar and exposing to 100 % H ₂ for 60 min at 300 °C (red lines).	89
Figure 47: TPD-MS of Ni(5)MoO ₃ in Ar with a heating rate of 10 °C/min after 5 h treatment at 325 °C in H ₂ :C ₃ H ₆ (9:1).....	90
Figure 48: TPR-MS of Ni(5)MoO ₃ in H ₂ with a heating rate of 10 °C/min after 5 h treatment at 325 °C in H ₂ :C ₃ H ₆ (9:1).....	91

Figure 49: $\text{MoO}_x\text{C}_y\text{H}_z$ phase formation with MoO_3 -based nickel modified catalysts. Reproduced from Ref.¹⁹⁷ with permission from the Royal Society of Chemistry.94

Figure 50: Extended mechanism of HDO at MoO_3 -based catalysts. Reproduced from Ref.¹⁹⁷ with permission from the Royal Society of Chemistry.....95

List of Tables

Table 1: Overview of catalysts performance in liquid-phase at different conditions.	11
Table 2: Overview of catalysts performance in gas-phase at different conditions.....	13
Table 3: Description and used amount for synthesis of Ni catalysts.	22
Table 4: Description and used amount for synthesis of Co catalysts.	22
Table 5: Anisole conversion and product selectivities (C-mol%) at 325 °C, WHSV = 0.31 g _{anisole} ·g ⁻¹ _{cat} ·h ⁻¹ and TOS = 10 h. Selectivity ratio: S(Arenes)/S(Phenols) = R(A/P). Adapted from Ref. ¹⁹⁷ with permission from the Royal Society of Chemistry. ..	40
Table 6: Initial rates for the catalysts for the different substrates at 350 °C and 50 bar H ₂ pressure.	47
Table 7: Ratio of integral values for reflections at Q = 26.7 nm ⁻¹ (MoO _x C _y H _z) and Q = 25.7 nm ⁻¹ (MoO ₂) of several in-situ XRD experiments.	78
Table 8: EPR parameters of different Mo ⁵⁺ sites in oxidized and reduced samples. Reproduced from Ref. ²¹⁸ with permission from the Royal Society of Chemistry.	85

List of Abbreviations

HDO	Hydrodeoxygenation
BTEX	Benzene, toluene, ethylbenzene and xylenes
DRIFTS	Diffuse reflectance infrared Fourier transform spectroscopy
XPS	X-ray photoelectron spectroscopy
PXRD	Powder X-ray diffraction
O _v	Oxygen vacancy
EPR	Electron paramagnetic resonance spectroscopy
IR	Infra-red
ICP-OES	Inductively coupled plasma optical emission spectroscopy
TEM	Transmission electron microscopy
SEM	Scanning electron microscopy
EDX	Energy dispersive X-ray spectroscopy
ABF	Annular bright field detector
BSE	Back-scattered electron detector
Ref	Reference
S _{arene}	Arene selectivity
TOS	Time on stream
TPR	Temperature programmed reduction
TPO	Temperature programmed oxidation
FID	Flame ionization detector

1. Introduction and Motivation

The increasing threat to the global climate and limited resources are two of the most challenging problems of our modern society, threatening our daily life. To counteract climate change, humanity needs to change the way of consumption.¹ However, it is also clear that these changes are only possible to a limited extent. Certain products are an integral part of our daily lives and may not be easily replaceable. The petrochemical industry, one of the largest sectors of CO₂ emission, is producing products of our daily life and needs to be decarbonized. Just the production of benzene, toluene, ethylbenzene and xylenes (BTEX) was responsible for the emission of 80.1 million tons of CO₂ in 2020.² However, a replacement of this important class of chemicals is not possible, as they are needed for the production of coatings, solvents, resins, plastics and pharmaceuticals.³ This means that sustainable resources must be tapped in order to establish a balanced circular economy on this basis. Some of the requirements for the sustainable sources are high availability, production should not compete with food production and it should be possible to process them efficiently with a low energy input.^{4, 5} Lignin is a raw material that meets these requirements. It is a complex polymer that gives a woody structure and provides the necessary stabilization in plants. Pulp and paper facilities producing world-wide between 50-70 million tons each year and the majority is burned in order to produce electricity and process heat.^{6, 7} Even though digitalization leads to less usage of paper, the amount of lignin produced each year increased during the last 30 years (see Figure 1). Further, the globally increasing online market results in a huge demand of cardboards for shipping, which continues this trend.

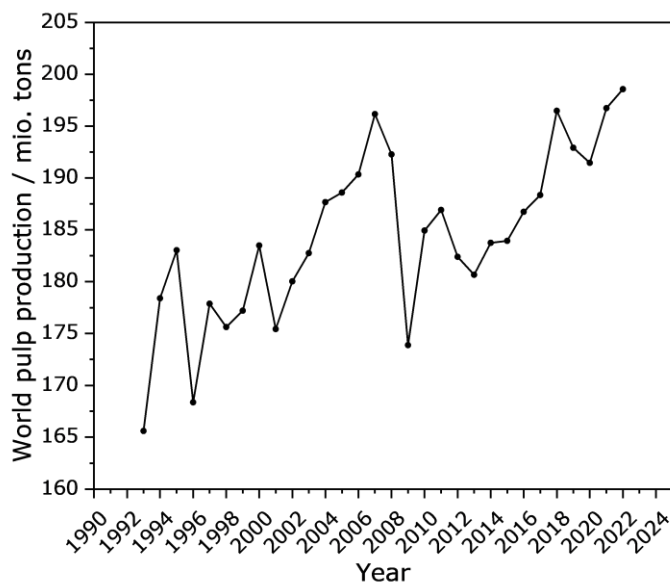


Figure 1: Worlds pulp production for paper production in million tons. Food and Agriculture Organization of the United Nations.⁸

In addition, the production of biofuels is expected to increase, which will lead to an increased byproduct volume of 225 million tons lignin.⁶ As lignin is the only biopolymer consisting of aromatic units, which is available in such large quantities, a commercial utilization makes more sense instead of using it for its thermal value exclusively.

Various options exist for the valorization of the lignin as a macromolecule and in its depolymerized form. Macromolecular lignin is used directly as binders, surfactants and dispersing agents. After depolymerization, the production of bio-char, production of vanillin by oxidation and BTX aromatics by reduction is possible (see Figure 2).^{9, 10} BTX aromatics are normally produced by steam cracking of naphtha, where a fraction of 30-40 % benzene and ≈ 20 % of toluene is obtained. The second important source for BTX aromatics is catalytic reforming, where a small fraction of benzene and a large fraction of toluene and xylenes (≈ 52 %) is produced.³ Besides the fact, that the naphtha production is based on crude oil, these processes demand a lot of energy due to high temperatures (850 °C for steam cracking and 500 °C for catalytic reforming) and the carbon footprint is very high. That makes the substitution by a lignin-based production of these aromatics more interesting.

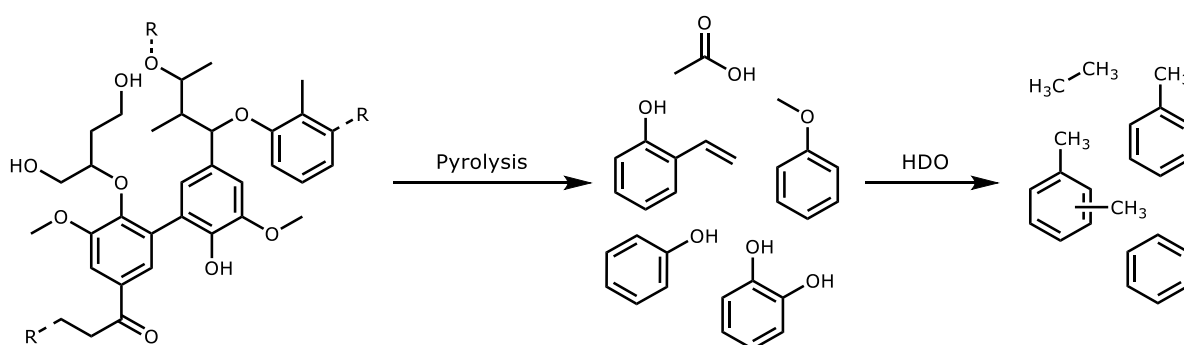


Figure 2: Lignin processing from raw material to valuable products.

Lignin consists of three monomers, the *p*-coumaryl, coniferyl alcohol and sinapyl alcohol (see Figure 3), which are linked via β -O-4 (β -aryl ether), β - β (resinol) and β -5 (phenyl coumaran) linkages.¹¹⁻¹³ However, also many other linkages occur and the fraction of the different monomers varies in dependence on the feedstock (e.g. grass, conifer wood or broadleaf wood). To produce BTX aromatics, the lignin needs to be liquified, which can be done by methods like fast pyrolysis.¹⁴ The fast pyrolysis is done at temperatures of ca. 500 °C and a bio-oil with acidic properties is obtained, which tends to repolymerize. These oils still have a high oxygen content (20-40 %) and therefore need to be processed by hydrodeoxygenation (HDO) to obtain BTX aromatics.^{15, 16}

Normally, the HDO is conducted after condensation in liquid-phase at high H₂ pressures of 50-150 bar and temperatures between 200-350 °C.¹⁷⁻²⁰ Compared to this, the reaction can be also carried out at atmospheric pressure and temperatures between 300-400 °C in the gas-phase.

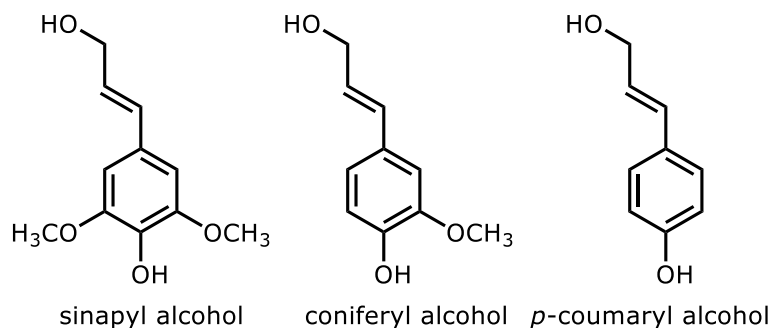


Figure 3: Structure of lignin monomers.

This brings the required reaction conditions closer to those of the pyrolysis, thereby facilitating a more efficient overall process and cost reduction. That would increase the chance to compete with the commercial production of BTX aromatics, which is still more economical.^{15, 17, 21}

Several catalysts have been studied for the HDO reaction in literature, among them precious metals, zeolites, sulfided catalysts and metal oxides.^{7, 22-24} Commercially, the HDO is done within a hydroprocessing treatment using sulfided NiMo/Al₂O₃ and CoMo/Al₂O₃ catalysts. However, sulfided catalysts have the disadvantage of deactivation by the substitution of sulfur with oxygen and contamination of the products with hydrogen sulfide. In recent years, oxidic catalysts gained attention in literature, because these problems do not occur for them. One of them, molybdenum oxide (MoO₃) might be an interesting catalyst for the use in HDO reactions as it seems to combine several advantages. First, it has a high oxophilicity by its intrinsically formed oxygen vacancies (O_v) on which the oxygenates can adsorb easily. Further, in previous studies it was shown that only a low H₂ pressure is required and that even though MoO₃ has not the highest conversion compared to metal catalysts (Ni, Pt...), the arene selectivity is very high and various studies showed selectivities up to 100 % arenes.²⁵⁻²⁹ Additionally, a good regeneration capability by calcination is very important since coking is one of the main deactivation processes during the HDO. This can be done easily with oxidic catalysts, because no sinter effects occur and it was shown that MoO₃ can be regenerated over multiple repetitions.^{25, 29, 30} At the same time, MoO₃ is much cheaper compared to precious metal catalysts, which is an important factor for process commercialization.³¹ A disadvantage for MoO₃ is the second way of deactivation, the reduction to inactive MoO₂. Although this can be countered by an oxidative regeneration, the catalyst must be improved and optimized process conditions must be found to avoid a profound reduction.

The catalytic cycle of HDO is assumed to follow a reversed Mars-van-Krevelen type mechanism, proceeding via oxygen vacancies. The O_v are formed by partial reduction, forming Mo^{5+} sites. Subsequently, the oxygenate substrate is adsorbing and hydrogenolyzed afterwards, followed by product desorption. However, the exact active species is not known but is assumed to be Mo^{5+} . Some reports indicate that a molybdenum oxycarbohydride phase ($MoO_xC_yH_z$) could stabilize Mo^{5+} and prevent it from over-reduction.^{25, 32}

It is known for oxidic catalysts that doping with metals can influence their properties and the O_v formation.^{33, 34} This could enhance catalytic activity since the HDO is proceeding via O_v and improved redox activities might be beneficial. Moreover, the addition of transition metals on the catalyst surface can activate hydrogen and thus influence the catalysts activity. The doping of MoO_3 to form a solid solution is challenging and has not yet been tested in context of the HDO, but preliminary tests indicated its instability under HDO conditions. However, the addition of transition metals has been studied in literature, showing improved catalytic activities by the addition of Pt, Ni or Co.³⁵⁻⁴² It is yet unknown, whether the transition metals operate as active sites directly or if the enhanced attributes are the result of an indirect improvement brought about by increased active phase development. Some reports suggest that the added transition metals act as hydrogen activator and generate free hydrogen atoms, which in turn generate O_v .^{38, 39, 43} Simultaneously, another report showed that Pt can enhance the $MoO_xC_yH_z$ phase formation, supporting the thesis of an indirect improvement of catalytic properties.⁴⁴

Aim of this work

As mentioned above, HDO of lignin pyrolysis products is usually performed after condensation in the liquid-phase under elevated H_2 pressure. A direct transfer to a gas-phase HDO reactor downstream of the pyrolysis reactor may be more attractive. This would eliminate the need for intermediate condensation and thus save costs. The main obstacle to the widespread industrial use of HDO in the gas-phase is probably the fact that only a small number of relevant studies have been carried out to date, most of which have been limited to model substrates.

The aim of this work is therefore a deep investigation of structure-reactivity relationships of molybdenum oxide-based catalysts, which may serve as a basis for further rational development of more efficient catalysts for the gas-phase HDO of lignin pyrolysis products. Moreover, these catalysts will also be tested in the liquid-phase HDO process in collaboration with Néstor Escalona (Pontificia Universidad Católica de Chile) to explore whether they could be a cheaper alternative for the currently used rhenium-based catalysts.

A special focus is set on nickel-modified bulk catalysts, which are obtained by precipitation and, according to the literature, should have improved catalytic properties. Therefore, the following aspect will be addressed:

- Identification of the active phase
- Influence of nickel on the active phase formation
- Impact of different reaction condition (liquid- and gas-phase)
- Regenerability of spent catalysts

This is done by catalytic testing in a fixed-bed system for gas-phase reactions at low H₂ pressures and liquid-phase batch reactions at high H₂ pressures. Additionally, the active phase is revealed by characterization of spent catalysts and systematic in-situ XRD experiments. Furthermore, the effect of adding nickel on the O_v formation is studied with in-situ EPR experiments.

2. State of the Art and Literature

2.1. Lignin Sources and Pyrolysis

Lignin is obtained from biomass and conventionally seized from soft woods. However, it exists a large variety of feedstocks with diverse properties in dependence on the raw materials. In general, biomass consists of cellulose, hemicellulose and lignin but the ratio of these parts can differ, based on the biomass source and part of the plant.^{45,46} For many applications lignin needs to be isolated from the other fractions due to its undesired properties, for which several purification techniques are available.

Lignin can be divided into two different types, sulfur containing and sulfur free lignin.⁴⁷ The second group includes soda lignin, organosolv lignin, steam explosion and hydrolysis lignin. However, only the soda lignin is of commercial interest for the future. Currently, the sulfur containing lignin is exclusively available on the global market as kraft lignin (obtained from kraft pulping, 100 kilo tons per year) and lignosulfonate (from sulfite pulping, 1 million tons per year).^{6, 48,49} Even though kraft lignin has not the highest availability on the market, kraft pulping is the most important chemical pulping process today.⁵⁰⁻⁵²

For lignosulfonate, SO_3 groups are chemically introduced to make the lignin water soluble but this results in a sulfur content of up to 8 %, which is not desirable for downstream processes.^{50, 53-56} Soda lignin has the advantage of being closer to native lignin, since no chemical groups are introduced. Because of this, it can be used for several downstream processes and applications.^{9, 57} Soda pulping is done at moderate temperatures (160 - 170 °C) in a batch reactor and has less contaminations with sugars and ashes compared to other processes.^{9, 53, 58}

After pulping, the dissolved lignin needs to be recovered from the aqueous solution and purified, as it contains numerous impurities pulping chemicals. There are different processes, ranging from chemical methods (precipitation), filtration or centrifugation after which the lignin is obtained as solid product. T. Aro and P. Fatehi provided an overview about the production of lignin from pulping broths and their applications.⁵⁴

There exist various approaches to liquefy lignin, such as solvolysis (organic solvents), hydrolysis, hydrothermal treatment and pyrolysis.^{14, 59-63} They can all be further divided into different techniques and all of them have different products, advantages and disadvantages.^{11, 63-66} However, only pyrolysis will be discussed in detail, as it is likely to be of greater relevance, since a combination of pyrolysis with gas-phase HDO makes particular sense. Additionally, pyrolysis processes are easy to scale, are capable to deal with a wide range of different lignin and the products can be transported economically.^{14, 67-69} The pyrolysis can be divided into three different process technologies, which are:

- Slow pyrolysis^{14, 70, 71}
- Fast pyrolysis^{14, 60, 61, 63, 71, 72}
- Flash pyrolysis^{14, 61, 73}

All these pyrolysis techniques produce a gas-, liquid- and char-fraction. However, besides the used feedstock, the selectivity of the pyrolysis strongly depends on the process conditions. The pyrolysis is carried out in anaerobic environments to avoid oxidation to CO₂. Nevertheless, the gas-fraction always contains H₂, CO, CO₂, CH₄ and H₂O as it is formed from a part of the oxygen contained in the lignin (\approx 40-45 wt.%).^{14,74} Many studies have been conducted on the fast pyrolysis because of its favorable selectivity to liquid products and process conditions. It is carried out at temperatures between 400 – 600 °C and atmospheric pressure with residence times under 5 s and high heating rates (\approx 1000 °C/min). This liquid fraction has a lowered oxygen content of about 35-40 wt.%.¹⁴ However, it is still a complex mixture of different oxygenates such as ethers, ketones, carboxylic acids, aldehydes, alcohols, esters, phenols and aromatic hydrocarbons.^{10, 14, 69, 75} An overview about typical aromatic main compounds can be found in the appendix (A-1). Besides these aromatic compounds, short chained aliphatic compounds like ethane are obtained as well.⁶⁹

Since the pyrolysis oils are extremely complex mixtures, model compounds are in general used to study the HDO. For this purpose, aromatic compounds are selected that show similarities with those of the pyrolysis oils and have different functional groups to understand the specific behavior. Those shown in Figure 4 are established in the literature, with phenol, guaiacol and anisole receiving particular attention. In this work, the focus is placed on anisole, as its physical properties offer advantages in the experimental procedure. For comparison and investigation of the catalyst performance for the HDO with other functional groups, phenol and guaiacol are tested additionally.

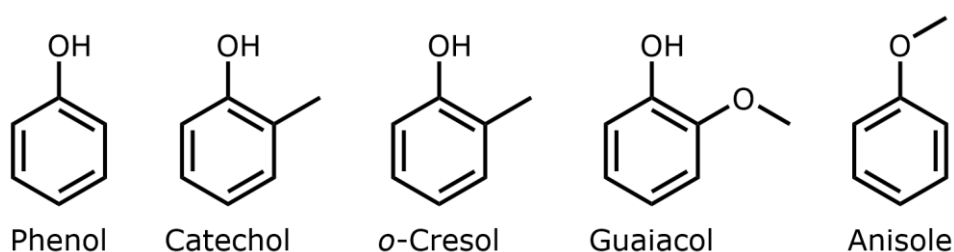


Figure 4: Overview of different model compounds used in literature.

2.2. Hydrodeoxygenation

After pyrolysis, further treatments are necessary to obtain highly valuable products. Bio-oils obtained by fast pyrolysis have several drawbacks, making its direct usage impossible. Among these properties are high viscosity, coking and corrosiveness. Additionally, they tend to repolymerize and condense with time. This process is accelerated by increased temperatures, UV irradiation and oxygen exposure.^{14, 61, 76} To make use of them, their oxygen content must be significantly reduced. In order to utilize them as fuels or for the production of aromatic, high-value products, a valorization by hydrodeoxygenation is required.^{7, 68, 76-78} Depending on the desired products, this upgrading will lead to an improvement of the thermal value and viscosity, facilitating a long-term storage or high value chemicals like BTX aromatics are directly obtained.

The HDO is already done for decades during hydrotreatment of crude oil, where it occurs as a side-reaction. The sulfur and nitrogen content of crude oil needs to be reduced, as fuel which contains these elements can produce NO_x and SO_x during combustion and are poisonous for downstream metal based reforming catalysts.^{24, 78} This is done by hydrodesulfurization and hydrodenitrogenation, and these processes occur with the HDO at the same time. In industry, most of the time CoMo/Al₂O₃ and NiMo/Al₂O₃ catalysts are used in fixed bed reactors.⁷⁸

According to literature, the HDO can be conducted in several ways. It can be divided according to different phases in which the reaction is carried out, namely the gas-phase and the liquid-phase.^{7, 79} But also different reactor types have been tested. Some of these are:

- Fixed-bed reactor^{7, 15, 25, 68, 80}
- Trickle bed reactor^{78, 81-83}
- Slurry reactor⁸⁴⁻⁸⁷
- Liquid-phase batch reactor^{80, 88-91}

Besides this, a pre-mixing of the HDO catalysts and lignin has been tested, to combine pyrolysis and upgrading reaction in one step.⁶⁶

Different HDO catalysts have been studied, which are discussed in more detail in chapter 2.2.1 and 2.2.2. However, not only can deoxygenation be observed but also several side reactions occur. Products are aromatic hydrocarbons, aliphatic hydrocarbons, and aliphatic oxygenates. They are formed by three different reactions. Hydrogenation, deoxygenation and transalkylation. However, the combination of these three reactions can end-up in a complex reaction network, as shown in Figure 5 for the HDO of anisole with a Pt/γ-Al₂O₃ catalyst. Most desired is the direct deoxygenation (DDO), which prevents the aromatic ring from hydrogenation and thus results in a low H₂ consumption. Additionally, the HDO can

proceed via a hydrogenation-deoxygenation pathway, which is producing saturated rings by initial ring hydrogenation. Cyclohexane and cyclohexanol are often formed by following this reaction pathway.^{76, 79, 80, 92} However, in this reaction low hydrogen consumption is desired, because of two reasons. First, high hydrogen consumption increases the costs of the process. Second, it favors the hydrogenation of the aromatic ring and lowers the selectivity to the BTX aromatics, which are more valuable and of interest for the chemical industry. Furthermore, if methoxy groups are present, transalkylation occurs on acidic catalysts.⁹³

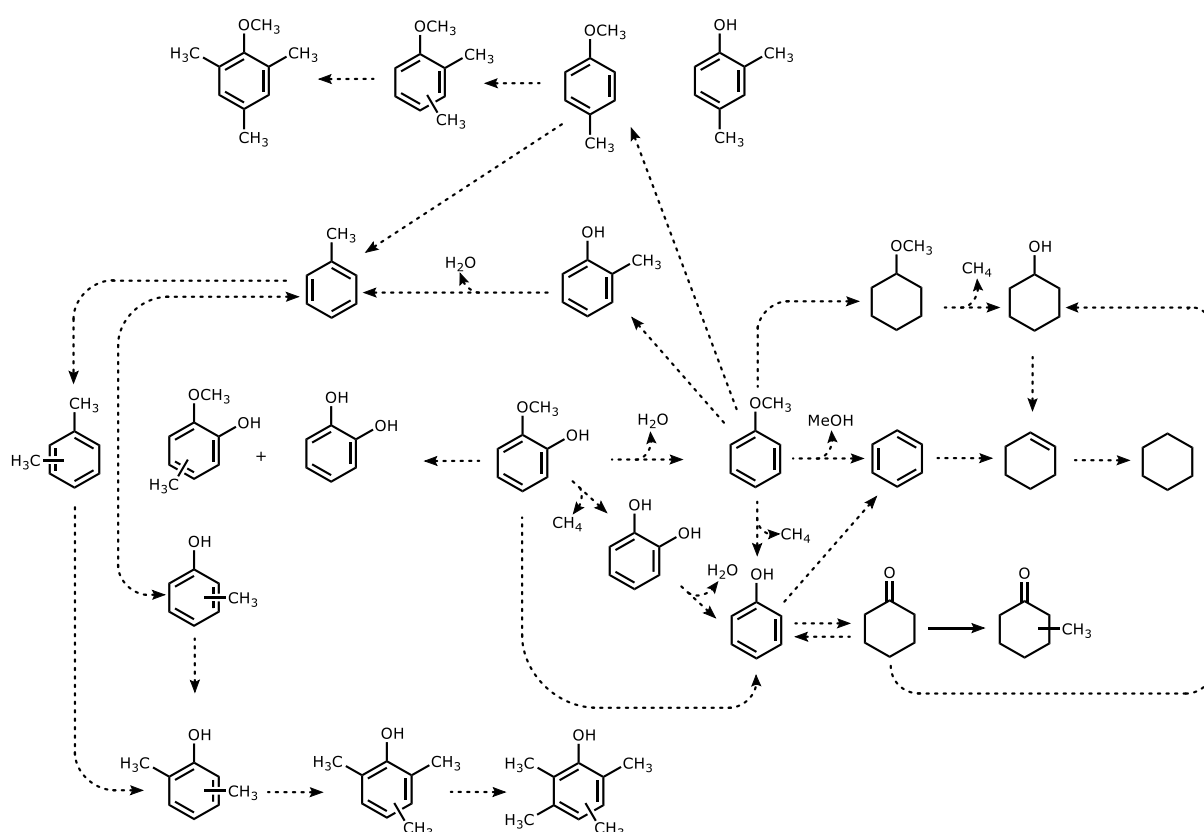


Figure 5: Reaction network for anisole HDO with Pt/ γ -Al₂O₃ at 300 °C and 140 kPa, adapted with permission from Ref.⁹³. Copyright 2011 American Chemical Society.

Thermodynamic considerations have been conducted by Olcese and colleagues. The variation of the Gibbs free energy as a function of temperature at 1 bar pressure demonstrated that the thermodynamic equilibrium for the guaiacol HDO and the preservation of the aromatic ring occurred at a specific temperature.⁹⁴ It was shown that the formation of saturated rings is not favored above 427 °C, because the formation of coke starts to take place. Baddour et al. calculated the equilibrium constant for the hydrogenation of benzene to cyclohexane at different temperatures.⁹⁵ They observed, that primarily at temperatures below 280 °C the hydrogenation is favored and thus the HDO should be done at higher temperatures. Further, high H₂ partial pressures will lead to ring saturation, as shown for the HDO at pressures between 1 bar and 23.5 bar.^{96, 97}

Based on these results, it has been concluded that a high HDO selectivity can be obtained by working at low H₂ partial pressures ($p_{\text{H}_2} \leq 1$ bar) and moderate temperatures (300 – 400 °C) to inhibit the hydrogenation and coke formation at the same time.

2.2.1. Liquid-Phase Hydrodeoxygenation

The liquid-phase HDO is typically done at high hydrogen pressure, which can vary between 5 and 200 bar and at temperatures ranging between 150 – 325 °C.^{7, 23, 76, 91} The reaction is conducted mostly in a batch reactor, whereas different solvents can be used (*n*-dodecane, water, decalin). In literature, many different catalytic systems have been described, e.g. metals, oxides, sulfides, phosphides and carbides. An overview is given in Table 1. They can be used either as bulk materials or supported catalysts. Molybdenum sulfide (MoS₂) catalysts were tested by Wang et al. at 300 °C and 40 bar H₂.^{91, 98, 99} At these conditions they achieved a conversion of 40.4 % cresol and an arene selectivity (S_{arene}) of 74.4 %. Inspired by industrial hydrodesulfurization catalysts for processing of petroleum, Ni-Mo-S and Co-Mo-S catalysts were tested as well.^{98, 100} While for Ni-Mo-S the ring hydrogenation was forced ($S_{\text{arene}} = 25.5$ %), Co-Mo-S showed very good results with a conversion and S_{arene} of 100 % in the HDO of cresol and phenol.¹⁰⁰ The problem for sulfided catalysts is the leaching of sulfur, which makes a co-feed of H₂S necessary.^{14, 78, 101} Unfortunately, a contamination by sulfur is unfavorable. This makes these catalysts inappropriate for industrial application.

Precious metals showed a high hydrogenation capability when employed as catalyst. Their selectivity can be influenced by many different parameters e.g. particle size, oxophilicity, dispersion and electronic state.²² In batch reactions at 275 °C and 10 bar H₂ cyclohexanol was obtained as main product with Ni/SiO₂ catalysts. However, when the particle size decreased, cyclohexane became the main product.⁸⁹ Nevertheless, the ring hydrogenation was not suppressed by the variation of particle sizes.

MoO₃ catalysts showed quite poor activities in liquid-phase HDO, which could be a reason why little work has been spent on them. Whiffen and Smith compared MoO_x, MoP and MoS₂ catalysts for the cresol HDO between 325 °C and 375 °C at H₂ pressures between 41.4 bar and 48.3 bar.⁹¹ They found that MoO₃ has the highest initial rate constants over the whole temperature range, followed by MoP, MoO₂, and MoS₂. At 325 °C and 41.4 bar H₂ they found with 38 % a significant selectivity to hydrogenated products after 280 min reaction. Only MoP had with about 58% a higher selectivity to these products. Interestingly, upon changing to 350 °C and 44 bar, the selectivity to hydrogenated products decreased and the isomerization increased. The isomerization capability of these catalysts was assumed to depend on the acidic properties of molybdenum catalysts. Zhang et al. reported a

hydrogenation of the aromatic ring for the phenol HDO, which decreased with rising temperature. This was assumed to be a thermodynamic effect, as the hydrogenation is an exothermic reaction.¹⁰² Ni-modified MoO₃-based catalysts have not yet been tested but they might show better results than pure phase MoO₃.

Table 1: Overview of catalysts performance in liquid-phase at different conditions.

Catalyst	T (°C)	P (bar)	Solvent	Substrate	X (%)	<i>S</i> _{arene} (%)	Ref.
Mo-S	325	41	Dodecane	Cresol	24	73	91
Mo-S	300	40	Dodecane	Cresol	40.4	74.4	99
Mo-S	300	40	Dodecane	Cresol	67	74.1	98
Ni-Mo-S	300	40	Dodecane	Cresol	87.6	25.5	98
Co-Mo-S	275	40	Dodecane	Cresol	100	92.2	90
Co-Mo-S	300	40	Decalin	Phenol	100	100	100
Co-Mo-S	300	40	Decalin	Cresol	100	100	100
Ni-S	300	40	Dodecane	Cresol	6.8	87.1	103
MoO ₃	300	5	Octane	Phenol	23.1	73.9	102
MoO ₃	340	5	Octane	Phenol	68.5	97.2	102
MoO ₃	325	41	Decalin	Cresol	61	63	91
Ru/C	275	50	Hexadecane	Propylphenol	100	0	104
Ru/C	275	50	Hexadecane	Eugenol	100	0	104
Rh/C	200	50	Water	Phenol	100	0	105
Pd/C	200	50	Water	Phenol	100	0	105
Pt/C	200	50	Water	Phenol	100	0	105
Ru/TiO ₂	300	10	Decane	Anisole	81	79	106
ReO _x /CNF	300	30	Dodecane	Phenol	10	72	107
Re-MoO _x /TiO ₂	300	30	Dodecane	Anisole	10	56	88
Re-MoO _x /TiO ₂	300	50	Dodecane	Phenol	33	85	108
Re-MoO _x /TiO ₂	300	50	Dodecane	Cresol	35	83	108
MoC-SiO ₂	320	60	Hexadecane	Anisole	65	70	109
MoC _x O _y /C	325	43	Decalin	Cresol	25	70	110
Mo ₂ C/TiO ₂	350	25	Decane	Phenol	65	90	111
Mo ₂ N/TiO ₂	350	25	Decane	Phenol	9	91	111
MoP/TiO ₂	350	25	Decane	Phenol	25	82	111
MoP-CA	350	44	Decalin	Cresol	58	60	112
FeMoP	350	21	Decane	Phenol	63	70	97

2.2.2. Gas-Phase Hydrodeoxygenation

The gas-phase HDO is done at low H₂ pressures ($p_{\text{H}_2} \leq 1$ bar), but higher temperatures (280 - 500 °C). Nevertheless, in literature the majority of studies has been done at temperatures around 300 °C.^{26, 113} This is advantageous, since it can save significant amounts of energy because it requires no pressurization and the temperature is within the range required for fast pyrolysis. This makes this reaction both cheaper (scaling effect), safer and therefore ideal for downstream processing.¹¹³ Like for the liquid-phase HDO, various catalyst classes have been tested (see Table 2) for this reaction. Compared to liquid-phase the requirements for the catalysts differ. While for batch reactions the deactivation plays a minor role, it is crucial for continuous gas-phase processes and catalysts should be regenerable and long-term stable.

Frequently tested are noble metal catalysts, with supported Pt, Pd, Ru and Rh. These metals tend to catalyze not only direct deoxygenation, but also hydrogenation and hydrogenolysis, which is disadvantageous for this application. Nimmanwudipong et al. found that for Pt/ γ -Al₂O₃ catalysts, high temperatures will enhance the transalkylation activity by the acidic support and HDO selectivity increased with higher H₂ partial pressures.⁹³ Some groups showed that acidic supports (such as γ -Al₂O₃) are not active for the deoxygenation at all and only catalyze the transalkylation.^{114, 115} This is not surprising, as acidic bifunctional catalysts are used for commercial hydroisomerization.¹¹⁶ When non-acidic supports are used (e.g. SiO₂), only minor amounts of transalkylation products (≤ 1.5 % yield) have been found for Ni/SiO₂ catalysts.^{115, 117} However, the selectivity for the deoxygenation can be improved by variation of the H₂ partial pressure.

Molybdenum-based catalysts showed good activities and selectivities in the gas-phase. Prasomsri et al. showed conversions of 74.2 % and 78.7 % for guaiacol and anisole, respectively.²⁵ For phenol and cresol the conversion was lower with 28.7 % and 48.9 %, respectively. This was explained by different bond energies of the functional groups. While the Ph-OMe bond has an energy of 91.5 kcal·mol⁻¹, Ph-OH has a bond energy of 106.8 kcal·mol⁻¹ and the PhO-Me bond has 52.2 kcal·mol⁻¹. This lowers the potential of C-O bond cleavage for phenolic groups. At the same time, these catalysts are very selective for deoxygenation and the main products are benzene, toluene and other alkylbenzenes. In contrast to metal catalysts and liquid-phase experiments, no hydrogenation products have been observed. The occurrence of transalkylation reactions in presence of methoxy groups can be explained by the acidic properties of partially reduced MoO₃.³² The high selectivity of these catalysts may offers a huge potential, provided that their activity can be further enhanced.

Table 2: Overview of catalysts performance in gas-phase at different conditions.

Catalyst	T (°C)	P (bar)	Substrate	X (%)	S_{arene} (%)	Ref.
Fe	300	1	Cresol	1-10	>90	118
Fe	300	1	Cresol	21	90	119
Ru-Fe	300	1	Cresol	76	98	119
Fe/SiO ₂	400	1	Anisole	>80	>90	15
Fe/SiO ₂	375	1	Anisole	8	85	120
Co/SBA-15	300	1	Anisole	62	70	121
Ni/CeO ₂	290	3	Anisole	96	58	122
Ni/TiO ₂	290	3	Anisole	51	74	122
Ni/Al ₂ O ₃	260	1	Cresol	30	67.8	123
Co/Al ₂ O ₃	260	1	Cresol			123
Pt/Al ₂ O ₃	260	1	Cresol	38	65	123
Pd/ZrO ₂	300	1	Phenol	77	66	124
Pd/TiO ₂	300	1	Phenol	7	66.8	125
Pd/Nb ₂ O ₅	300	1	Phenol	6.6	80.2	126
Pt/Hbeta	400	1	Anisole	100	>90	115
Pt/Hbeta	400	1	Cresol	100	>90	127
MoO ₃	325	1	Cresol	48.9	99.4	25
MoO ₃ /ZrO ₂	320	1	Cresol	78	99	29
MoO ₃ /TiO ₂	320	1	Cresol	47	99	29
MoO ₃ /CeO ₂	320	1	Cresol	8	97	29
MoO ₃ /Al ₂ O ₃	320	1	Cresol	13	76	29
MoO ₃ /SiO ₂	320	1	Cresol	10	90	29
MoO ₃ /TiO ₂	350	25	Phenol	28	89	111
Ni-Mo/SiO ₂	410	1	Phenol	99	99	36
ReO _x Ni/CeO ₂	350	1	Cresol	45.7	83	128
ReO _x Ni/ZrO ₂	350	1	Cresol	63.9	90	128
Mo ₂ C	150	1	Anisole	<14	90-94	129
Mo ₂ C	280	1.1	Phenolic mix.	94	93	130
MoC ₂	350	4.4	Guaiacol	99.8	81	95
MoC ₂	250	1	Anisole	49	87	131

2.3. Mechanism of HDO at MoO₃

The redox properties of molybdenum oxide are beneficial for oxidation catalysis, following a Mars-van-Krevelen mechanism.¹³² This contains the formation of oxygen-vacancies by the substrate oxidation, which are responsible for the high redox activity and are recovered within an oxygen containing atmosphere.¹³³⁻¹³⁵ In 2002 the term “reverse Mars-van-Krevelen mechanism” was used for the first time in context of the HDO of propan-2-ol on reduced ZrO₂.¹³⁶ Since it was demonstrated that MoO₃ is active for the HDO reaction, it was also hypothesized that oxygen-vacancies are involved and the reverse Mars-van-Krevelen mechanism was established in literature.^{30, 32, 79, 137-142}

The O_v are formed by mechanical stress and under high temperatures in non-oxidizing/reductive atmospheres.¹⁴³⁻¹⁴⁶ Several computational studies have been conducted on the O_v formation, mainly for oxidation reactions.¹⁴⁷⁻¹⁵³ However, some studies have been done under reductive conditions for the HDO, mainly with simple model compounds like acetone and furan.^{137, 153, 154}

The reverse Mars-van-Krevelen mechanism includes 5 steps:

- Oxygen-vacancy formation by reduction
- Substrate adsorption via oxygen at O_v
- Hydrogenolysis
- Product desorption
- O_v formation by condensation

Three different oxygen atoms are located at a (010) MoO₃ surface, a symmetrical tricoordinated oxygen (O_s), one asymmetric bicoordinated oxygen (O_{as}) and a single coordinated oxygen (O_t), that is double bonded to the Mo atom.¹⁵² In literature it was found that the direct O_v formation by removing the O_s is energetically unfavored (4.15 eV), while it is much easier for O_t and O_{as} with O_v formation energies of 2.87 eV and 2.95 eV, respectively.¹⁵⁴ This order, which was also found in other reports, is surprising since the O_t double bond is stronger compared to O_{as} and O_s.^{149, 150, 152} As the kinetic barrier for the direct O_v formation is comparatively high, studies showed that this is facilitated in the presence of H₂.^{153, 154} In these studies the formation of O_v is most favorable at the terminal sites, while the energy barrier is too high for an abstraction of the bridging oxygen atom. Nevertheless, when an O_v is formed, the asymmetric oxygen atom will tilt to reconstruct the surface of the MoO₃ crystal (see Figure 6).^{153, 154}

There are three different ways of dissociative H₂ adsorption which can form O_v afterwards. First, the adsorption can lead to the formation of two terminal hydroxyl groups. Another option is the formation of one terminal and one asymmetric hydroxyl, which has a lowered energetic barrier.¹⁵³ The third way is the dissociation at the terminal oxygen and Mo, where a terminal hydroxyl and a direct bond of the hydrogen to the molybdenum would be formed, which is not favored.¹⁵⁴

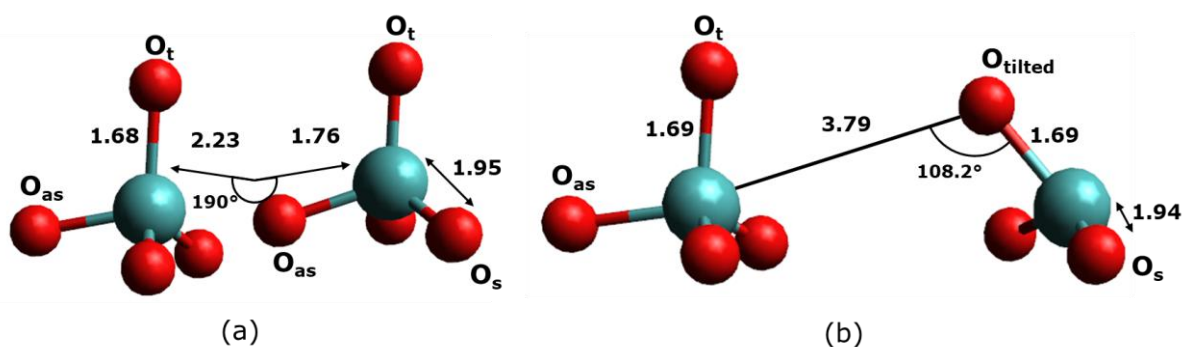


Figure 6: Mo-O bond lengths of a (010) MoO₃ surface (a) as pristine crystal an (b) with oxygen vacancy, adapted with permission from Ref. ¹⁵³. Copyright 2011 American Chemical Society.

Upon vacancy formation, water is formed subsequently on the catalyst surface by two hydroxyl groups. Calculations showed that the combination of two O_tH is energetically favored. As mentioned before, regardless of the combination that formed the defect, it will be always located at the terminal position.¹⁵⁵

It was elucidated for the adsorption of acetaldehyde, that the oxygenates are adsorbing strongly at the O_v in MoO₃.¹⁵⁴ Afterwards, there are different options for C-O bond cleavage. First, one hydrogen could be abstracted from a neighboring -CH₃ or -CH₂R group. That this is possible was calculated e.g. for the HDO of acrolein, acetaldehyde or acetone to propene.^{137, 153, 154} However, this seems to be less likely for molecules like phenol and anisole. A dehydrogenation is not possible on the methoxy group. Additionally, the presence of transalkylated products (e.g. toluene, xylene) and the HDO of phenol to benzene do not indicate such a mechanism at least for these model compounds. Another way, proposed by Gonçalves et al., is the heterolytic dissociation of H₂ to form a O_tH with the second H* bonded directly to the corresponding Mo atom (see Figure 7, right).⁹² As mentioned before, a computational study showed that this is less likely. Therefore, it is likely that acidic hydroxyl groups are formed on the surface. Further, it is known that hydrogen atoms (more precisely a proton and electron) are highly mobile on MoO₃ surfaces and within the bulk. They can be formed elsewhere and diffuse to the adsorbed substrate for hydrogenolysis and HDO reaction.¹⁵⁶ It might be possible that hydrogen is activated at metal particles (e.g. nickel) and transported to O_v afterwards for the HDO reaction.

Subsequently, the HDO of the adsorbed phenol will form benzene which desorbs. The remaining hydroxyl group will be removed by a condensation reaction with the second remaining OH group and form the O_v again (see Figure 7).

It is important to keep in mind that these calculations and models are developed for MoO_3 and clusters, which are idealized models. However, it is also known that several phase changes occur during the reduction and reaction (e.g. formation of $MoO_xC_yH_z$, see chapter 2.4). Further work needs to be done to elucidate the real behavior of these phases and study the presence of O_v in these complex phases.

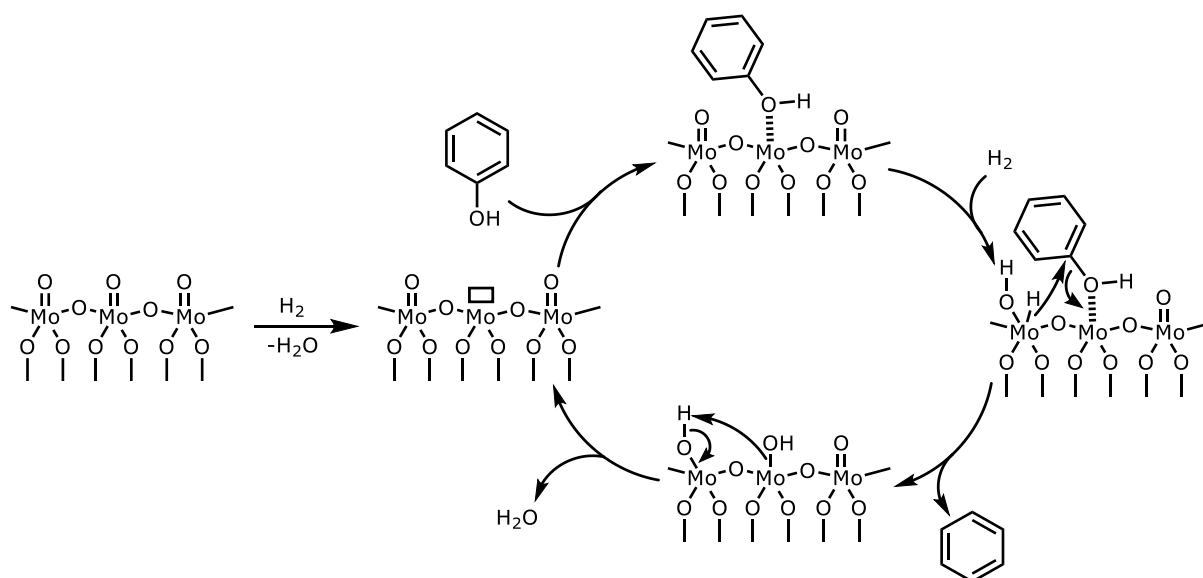


Figure 7: Mechanism of phenol HDO at the MoO_3 surface, adapted with permission from Ref.⁹² Copyright 2017 Elsevier.

2.4. Active Phases

The active phase of a MoO_3 -based HDO catalyst is formed in-situ and differs from the initial MoO_3 . The reverse Mars-van-Krevelen mechanism demands a pre-reduction of the catalyst to form oxygen vacancies (see chapter 2.3). Therefore, MoO_3 is reduced to MoO_2 via different intermediate phases like $Mo_{18}O_{52}$ ¹⁵⁷, $Mo_4O_{10}(OH)_2$ ¹⁵⁸, $Mo_2O_4(OH)_2$ ¹⁵⁸, Mo_4O_{11} ^{159, 160}. Frequently, the partially reduced molybdenum oxide is simplified as MoO_{3-x} .

The interdiffusion of H_2 can also lead to the formation of molybdenum bronzes H_xMoO_3 .^{159, 161} Some of these intermediates are X-ray amorphous, making it challenging to identify these structures especially in a dynamic system which is constantly changing during the reaction. Nevertheless, the active phase cannot be MoO_3 because it is reduced directly under HDO conditions. Other reports suggest that also MoO_2 cannot be mainly responsible for the catalytic activity as it is significantly less active compared to slightly reduced

MoO₃.^{32, 142} Prasomsri et al. showed by in-situ XRD experiments, that a high reaction temperature of 400 °C resulted in a fast deactivation and the formation of MoO₂.^{25, 80}

It is challenging to prevent the catalyst from over-reduction and to keep the formal oxidation state between Mo⁶⁺ – Mo⁴⁺. High temperatures and hydrogen partial pressures are beneficial for the activity but favor a deep reduction. For a prolonged activity a temperature range between 300 < T < 400 °C is advantageous. When MoO₃ is treated within this temperature range with a mixture of H₂ and hydrocarbons, a molybdenum oxycarbonyl phase (MoO_xC_yH_z) is formed.^{25, 32, 41, 44, 161-165} This phase seems to stabilize the Mo⁵⁺, thus extending the catalytic activity.

This phase is formed in-situ after a pre-reduction.²⁵ During the reduction, O_v are formed, which are catalytically active. However, with progressing vacancy enrichment, the crystal lattice (MoO_{3-x}) may rearrange into shear planes (Mo₁₈O₂₄), to eliminate these defects.^{157, 163} This energetically favored process ends subsequently with the formation of MoO₂ when the O_v concentration becomes too high by further reduction (see Figure 8). Once MoO₂ is formed, a MoO_xC_yH_z generation is not possible due to the strong Mo-Mo bond.^{163, 166} When hydrocarbons are present in the atmosphere, an intercalation into the vacancies to prevent the rearrangement to Mo₁₈O₂₄ and MoO₂ is possible.^{32, 163}

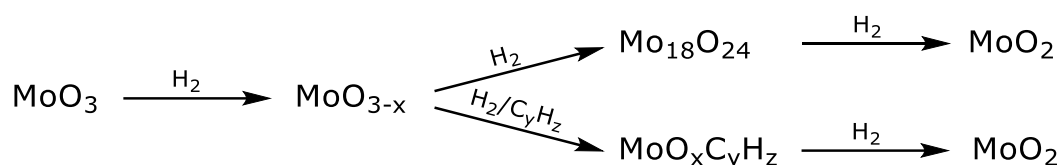


Figure 8: Path of MoO₃ reduction and MoO_xC_yH_z formation.

Besides MoO_xC_yH_z, MoO₂ is always formed in catalytic experiments. However, it is possible to prepare phase pure MoO_xC_yH_z if the molybdenum bronze (H_xMoO₃) and not MoO₃ is used as starting material.^{25, 161} It is assumed that this is possible, because by the bronze provided intercalated hydrogen is needed to form MoO_xC_yH_z, while only atomic hydrogen formed by homolytic scission of H₂ molecules can enter the MoO₃ lattice.^{44, 167} When MoO₃ (**1**) is used as starting material and, therefore, no intercalated hydrogen is available, a reduction to MoO₂ by molecular H₂ is necessary (see Figure 9). The MoO₂ can dissociate the H₂, which can diffuse into MoO_{3-x} (**2**) and form molybdenum oxyhydride (**3**). The MoO_xH_z can be converted into MoO_xC_yH_z (**4**), when exposed to carbon containing feeds.

This explains why the formation of MoO_2 in pure MoO_3 catalysts cannot be avoided completely. Bouchy et al. reported that platinum can enhance the $\text{MoO}_x\text{C}_y\text{H}_z$ formation by an improved H_2 dissociation.⁴⁴ The influence of other metals on the oxycarbohydride formation is not reported so far, although Zhang et al. reported the existence of this phase in a cobalt promoted catalyst.⁴¹ The influence of Ni on the $\text{MoO}_x\text{C}_y\text{H}_z$ formation is studied here.

The advantage of these MoO_3 -based catalysts is the good regeneration capability after oxidation by air. Several reports showed that the catalytic activity was recovered to the initial activity and now differences in the deactivation processes have been observed afterwards.^{25, 30, 36, 41}

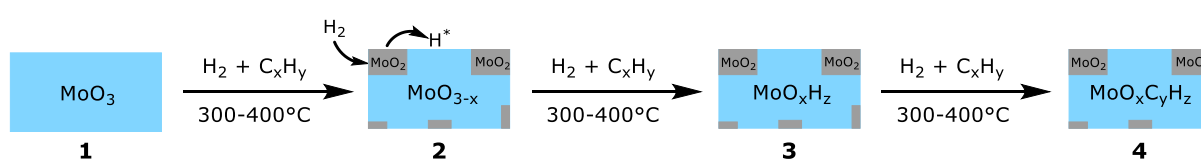


Figure 9: Phase formation during MoO_3 reduction, adapted with permission from Ref.⁴⁴ Copyright 2000 Elsevier.

2.5. Doping and Support Influences

In literature, it is claimed that doping of MoO_3 can be done with low valent dopants (Fe, Zn, Ni) in order to increase the number of O_v .¹⁶⁸⁻¹⁷⁰ To the best of our knowledge, they have not yet been tested in HDO reactions and their stability is unknown under HDO conditions. Nevertheless, there are reports about catalyst systems with various metals added (Ni, Pt, Pd, Co, Cu).^{35-39, 41, 42, 77, 140, 141, 171-174} In the following section, the added metals are designated as secondary metals. When metals are added to Mo-oxides, the formation of the corresponding metal molybdates (MMoO_4) is likely after calcination, due to the high stability of these metal molybdates. It is observed, that the surface impregnation of MoO_3 with metal salts forms MMoO_4 after calcination at $400 - 500^\circ\text{C}$.^{42, 141, 174} For the impregnation of support materials (TiO_2 , SiO_2), the MMoO_4 formation was observed as well, for both co-impregnation and stepwise impregnation of M- and Mo-salts.^{35, 37, 39-41, 171, 173} Besides impregnation and precipitation, also sol-gel, mechanochemical and hydrothermal methods can be used for synthesizing metal molybdates.¹⁷⁵⁻¹⁷⁷ For ratios of $\text{M}/\text{Mo} \neq 1$, the metal molybdate is still formed stoichiometrically, while the exceeding metal is obtained as corresponding oxide and by controlling the calcination conditions, different molybdate phases can be synthesized (different stoichiometries and geometries).^{43, 174}

Under reductive conditions, as present for HDO reactions, the reduction of MMoO_4 is reported at temperatures above 300°C , forming M^0 and a MoO_x species.¹⁷⁸ Depending on

the secondary metal, different phases can occur during this reduction, indicating different active phases or slower activation processes. For example, NiMoO₄ is reduced directly to metallic Ni and MoO_x, while CoMoO₄ is forming intermediate phases (e.g. Co₂Mo₃O₈). These intermediate phases are reduced fast at temperatures above 550 °C.^{160, 167} On the other hand, Zhang et al. showed that after 300 h reaction at 360 °C with a bulk Co/MoO₃ catalyst at 1 bar H₂ pressure in a fixed-bed reactor, no CoMoO₄ or Co₂Mo₃O₈ can be observed. Only MoO₂ and MoO₃ were present, indicating that CoMoO₄ can be fully reduced at temperatures below 550 °C. This could be explained by comparatively long reaction times.⁴¹ However, the role of the secondary metals is not clarified yet. Zhang et al. claimed that the acidic properties of CoMoO₄ are responsible for a formation of MoO_xC_yH_z, which is preventing an over-reduction to inactive MoO₂.⁴¹ They also assumed, that the metal (Ni or Co) can activate H₂ and thus provide activated hydrogen by hydrogen spillover.^{42, 179} This led to an improved reducibility and facilitated the formation of Mo⁵⁺ centers and O_v, which are active in HDO reactions. Further, the activated hydrogen provided via spillover could promote the C-O cleavage of the substrate, which is adsorbed at Mo⁵⁺ species.⁴² Yang et al. observed for NiMoO₄/SiO₂ a doubled O_v concentration compared to NiO/SiO₂ and MoO₃/SiO₂, which was correlated with a higher dispersion and reducibility of Mo species.¹⁷⁴ However, they did not find any molybdenum oxycarbohydride for NiMoO₄/SiO₂, which was found for MoO₃ and CoMoO₄/MoO₃ catalysts.^{25, 41} The influence of supports on the MoO_xC_yH_z formation has not been investigated, though one reason for the absence of this phase might be due to support effects.

The addition of metals is considered to improve catalytic activity but can also lower the selectivity. Especially metals with strong hydrogen activation capabilities (Ni, Pt, Pd), are selective for ring hydrogenation and C-C hydrogenolysis with increasing secondary metal loading.¹⁷⁴ But also the particle size of metals influences the selectivity. Nickel catalysts (Ni/SiO₂) tested for the cresol HDO showed that, besides an increase in activity with decreasing particle size, the selectivity for C-C hydrogenolysis to CH₄ decreased as well. At the same time, direct deoxygenation and hydrogenation became faster.^{89, 117} This could influence the selectivity of metal molybdates as well, when during the reduction a specific particle size of the metal phase is formed.

Not only the added metal has an influence on the catalytic properties, also supports can have significant impacts. Shetty et al. elucidated the effect of different supports on the *m*-cresol HDO for 10 wt.% pure MoO₃ on ZrO₂, TiO₂, CeO₂, γ-Al₂O₃ and SiO₂. The bulk MoO₃ was tested as well for comparison.²⁹ They found that the arene selectivity is 100 % and no ring saturated products have been observed for almost all catalysts. Transmethylation occurred only with MoO₃/γ-Al₂O₃ and very small amounts of dimethyl phenol were formed. While the support influence on selectivity was negligible, this effect was more pronounced for the conversion. The lowest conversion was obtained for MoO₃/CeO₂ (8 %). MoO₃/SiO₂,

MoO₃/γ-Al₂O₃ and pure MoO₃ reached 10 %, 13 % and 13 %, respectively. Compared to this, the conversions for MoO₃/ZrO₂ (78 %) and MoO₃/TiO₂ (47 %) were significantly higher. Interestingly, no MoO_xC_yH_z was found, which is considered as active phase for MoO₃ catalysts (see chapter 2.4).²⁵ XPS analysis of spent catalysts clarified, that catalysts containing MoO₃ supported on ZrO₂ and TiO₂ have significant amounts of Mo⁶⁺ and Mo⁵⁺ at their surface. Compared to this, no Mo⁶⁺ was found for bulk MoO₃ but 30 % of Mo⁰, which was not observed for supported catalysts. This indicates that ZrO₂ and TiO₂ stabilize higher oxidation states and thus showed a decreased deactivation rate over 100 h time on stream (TOS). Interestingly, not only the deactivation behavior differed. The supported catalysts did not show any induction period, while pure phase MoO₃ did for the first 2 h TOS.²⁹ In others reports, this induction period was linked to the MoO_xC_yH_z phase formation.^{25, 32} The absence of this induction period and of any MoO_xC_yH_z reflections in XRD powder patterns of used supported catalysts suggested that the active phase or stabilization effects are different. However, catalyst regeneration after deactivation is possible for both supported and bulk MoO₃.^{25, 30, 165} Nevertheless, the authors still assumed a reverse Mars-van-Krevelen mechanism for supported catalysts. They found a correlation between the catalysts activity and its reducibility by temperature programmed reduction (TPR) and thus a better formation of coordinatively unsaturated Mo sites.²⁹ This correlates too with the XPS results which showed that MoO₃/CeO₂, the catalyst with the lowest activity, had the highest amount of Mo⁶⁺ (75 %) after 7 h reaction. This indicates that CeO₂ stabilized Mo⁶⁺ to an extent, that not enough O_v could be formed to obtain high activity. In contrast to this, TiO₂ and ZrO₂ seem to stabilize Mo⁵⁺. Due to the surface acidity of SiO₂ and γ-Al₂O₃, a relatively fast deactivation by coke deposition was observed, making a higher calcination temperature necessary for regeneration.^{29, 180}

The influence on MoO₃ loading and dispersion was investigated in more detail for MoO₃/ZrO₂.^{27, 28} PXRD and Raman measurements showed that for molybdenum loadings above 15 wt.% crystallites of MoO₃ and Zr(MoO₄)₂ were formed. This resulted in a decrease of reaction rate, normalized on the Mo loading. The optimum was found to be at 15 wt.%, while the specific HDO reaction rate decreased below this loading. In literature it is known that at low MoO₃ loadings isolated MoO_x species are obtained, while with increasing loadings an oligomerization takes place forming condensed MoO_x species.^{181, 182} After monolayer coverage by the condensed MoO_x, further Mo loading will lead to crystalline MoO₃ formation. It was shown that with an increasing degree of oligomerization the reducibility is increased until complete monolayer coverage is reached. Due to hindered O_v formation, this could be one aspect of improved catalytic properties. Because at low loadings the majority of Mo exists as less reducible, isolated MoO_x species, the normalized reaction rates are lowered.²⁸ Additionally, the acidity is increased for higher Mo loadings up to a monolayer coverage.¹³⁵ These Brønsted-sites can catalyze transalkylation reactions,

leading to increased alkylation rates until the support is covered. However, when MoO_3 crystallites are formed, the accessibility of these Brønsted-sites is inhibited and the reaction rates for both, HDO and alkylation are decreasing.²⁸

In literature, there are not many reports about bimetallic (NiMo, CoMo, PtMo) supported catalysts. Ranga et al. studied CoMo catalysts with different Co/Mo ratios supported on TiO_2 , SiO_2 and Al_2O_3 .⁴⁰ They kept the Mo loading at 10 wt.% and varied the ratio between 0 and 1. Interestingly, they found for pure Mo loading a crystalline phase after synthesis on Al_2O_3 as well as on ZrO_2 . However, on TiO_2 no crystalline phase has been found. When Co was added to the sample, a multi-phase catalyst was obtained, forming a MoO_3 , CoMoO_4 and/or Co_3O_4 phase depending on the Co amount. They tested the catalysts in anisole HDO at 340 °C and 5 bar pressure. Compared to pure supported MoO_3 , the best performance was observed for Al_2O_3 . Surprisingly, the addition of Co to $\text{MoO}_3/\text{TiO}_2$ resulted in a less active catalyst under these conditions but the selectivity towards deoxygenated products increased by the Co addition and was the highest for $\text{CoMo}/\text{ZrO}_2 > \text{CoMo}/\text{TiO}_2 > \text{CoMo}/\text{Al}_2\text{O}_3$. Transalkylation was also observed, which was related to the Brønsted-acidity and thus the highest for $\text{CoMo}/\text{Al}_2\text{O}_3$. In contrast to this, when Co together with Mo was supported by zirconia or alumina, the initial activity was higher compared to bare Mo. Nevertheless, the binary catalysts suffered from a faster deactivation, which has been explained by a faster reduction to inactive Mo^{4+} .⁴⁰ The deactivation was not only driven by reduction, also coking played an important role. By temperature programmed oxidation (TPO) it was shown that this has been forced by Al_2O_3 probably due to its high Brønsted-acidity.

Conclusions for this Work

This literature review showed that MoO_3 catalysts show a low performance for the liquid-phase HDO, but metal modified catalysts have not yet been sufficiently tested. They showed promising results for the gas-phase reaction and therefore need to be tested in the liquid-phase as well (see chapter 2.2.1 and 2.2.2). However, the role and influence of modifying metals is not revealed for the gas-phase reaction. Therefore, pure phases of MoO_3 and MMoO_4 as well as MoO_3 with different contents of added MMoO_4 have to be tested. Furthermore, it was shown that the mechanism is assumed to be based on a reverse Mars-van-Krevelen mechanism, but the studies and assumptions are only done for a MoO_3 surface (see chapter 2.3). Hence, the active phase formation must be taken into account as MoO_3 can be transformed into different phases under reaction conditions (see chapter 2.4). Extensive studies on the active phase, its formation, regeneration and stability must be carried out. Since the aim of this work is to investigate the basic phase transformations of the catalyst during the HDO reaction and a catalyst support can have a strong influence on these transformations, the focus is here on bulk catalysts.

3. Experimental Part and Methods

3.1. Catalyst Synthesis

Molybdenum(VI)-oxide has been used as reference catalyst and was purchased from Carl Roth. Further catalysts with different amounts of modifying nickel and cobalt were synthesized.

To synthesize the catalysts, 11.481 g (9.290 mmol) $(\text{NH}_4)_6\text{Mo}_7\text{O}_{24} \cdot 4\text{H}_2\text{O}$ was dissolved in 100 ml of water, then 2.478 g (8.520 mmol) $\text{Ni}(\text{NO}_3)_2 \cdot 4\text{H}_2\text{O}$ was added and completely dissolved at room temperature. The temperature was increased to 85 °C with constant stirring and until most of the water was evaporated. The remaining water was removed in a drying oven at 100 °C until the sample was completely dry. Afterwards, it was calcined at 550 °C for 4 hours. Catalysts with a different nickel content were synthesized using the same procedure and are labelled with the following notation:

Table 3: Description and used amount for synthesis of Ni catalysts.

Description	mass (g)	mass (g)	ICP-results (wt.%)
	$\text{Ni}(\text{NO}_3)_2 \cdot 4\text{H}_2\text{O}$	$(\text{NH}_4)_6\text{Mo}_7\text{O}_{24} \cdot 4\text{H}_2\text{O}$	Nickel
MoO_3	-	-	0
Ni(5)MoO ₃	2.478	11.481	4.91
Ni(3)MoO ₃	0.614	4.906	2.79
Ni(1)MoO ₃	0.496	12.258	1.02
NiMoO ₄	13.303	8.076	26.29

The synthesis of cobalt molybdate catalysts was carried out using the same procedure as for nickel molybdate catalysts described above. The following weights and labeling have been used:

Table 4: Description and used amount for synthesis of Co catalysts.

Description	mass (g)	mass (g)	ICP-results (wt.%)
	$\text{Co}(\text{NO}_3)_2 \cdot 4\text{H}_2\text{O}$	$(\text{NH}_4)_6\text{Mo}_7\text{O}_{24} \cdot 4\text{H}_2\text{O}$	Cobalt
MoO_3	-	-	0
Co(5)MoO ₃	2.496	11.468	5.05
CoMoO ₄	13.297	8.067	26.73

Some of these catalysts were prepared by B. Sc. Carl Julius Mussweiler as part of a methodological internship.

Ni/ α -Al₂O₃ was synthesized by incipient wetness impregnation. Therefore, $\text{Ni}(\text{NO}_3)_2$ (3 wt.% Ni) was impregnated on α -Al₂O₃ spheres ($d_p = 800 - 1000 \mu\text{m}$) and calcined for 4 h at 450 °C with syn. air.

3.2. Catalytic Tests in Gas-Phase

The catalytic test experiments have been conducted in a gas-phase packed-bed flow reactor by M.Sc. Sebastian Löbner at the Likat. The tube reactor had an inner diameter of 11.9 mm which was fixed in a furnace. A thermocouple was used for temperature regulation, placed inside the catalyst bed. The catalyst material was pressed and sieved to achieve particle sizes between 600 – 800 μm . Before the catalyst was placed in the reactor held by quartz-wool, 200 mg of the material was mixed with approximately 2.3 g of SiO_2 for diluting to a fixed volume. The SiO_2 had a particle size of 500 – 800 μm . The anisole was transferred into the reactor by a saturator where the H_2/N_2 -mixture was flushed through. The saturator temperature was kept at 20 $^\circ\text{C}$ which resulted in a total anisole flow of 0.236 ml/min in the gas-phase and a $\text{WHSV} = 0.31 \text{ g}_{\text{anisole}} \cdot \text{g}^{-1}_{\text{cat}} \cdot \text{h}^{-1}$. During reaction 40 ml/min N_2 and 20 ml/min H_2 at ambient pressure were used. Behind the reactor, 6.5 ml/min ethane was added, as an internal standard. All gas flows have been controlled by Bronkhorst mass flow controller units. Prior to the addition of substrate, the catalysts were heated-up in N_2 to 325 $^\circ\text{C}$ and pre-reduced in 100 % H_2 for 2 h at ambient pressure afterwards. After the pre-reduction step the catalysts were flushed with N_2 and bypass measurements were performed for feed analysis. The organic reactants and products were monitored continuously during reaction on stream with an online GC (see technical details below).

The transfer line to the online GC system (Agilent 7890A) was kept at a temperature of 200 $^\circ\text{C}$ and the valve box of the GC was tempered at 210 $^\circ\text{C}$. The sample loop had a volume of 250 μl . The GC column was a Quadrex 624 30 m x 250 μm x 2 μm . Helium was used as a carrier gas. The temperature program started at 40 $^\circ\text{C}$ for 2 min followed by heating up to 160 $^\circ\text{C}$ with 10 $^\circ\text{C}/\text{min}$ and hold time for 5 min. Afterwards the oven was heated to 240 $^\circ\text{C}$ with 20 $^\circ\text{C}/\text{min}$ keeping the target temperature for additional 20 min. A flame ionization detector (FID) was used as a detector.

The calculation of the conversion and selectivity is based on corrected integral values of respective GC peaks using the "Effective Carbon Number Concept". Thus, the integrals of the compounds were normalized by its corresponding response factor ECN (Eq. 1).¹⁸³

$$A_{ECN} = \frac{A}{ECN} \quad (1)$$

The conversion (Eq. 2) was determined by the area of anisole (i) and the average of bypass measurements. The area of the internal standard (IS) is included to account for possible volume changes during the reaction. The selectivities for the products (j) are given as carbon fractions (Eq. 3).

Conversion

$$X = \left(1 - \frac{A_{ECN,i}}{A_{ECN,i,0}} \cdot \frac{A_{ECN,IS,0}}{A_{ECN,IS}} \right) \cdot 100\% \quad (2)$$

Selectivity

$$S_j = \left(\frac{A_{ECN,j} - A_{ECN,j,0}}{A_{ECN,i,0} - A_{ECN,i}} \right) \cdot \frac{C\text{-atoms},j}{C\text{-atoms},i} \cdot 100\% \quad (3)$$

3.3. Catalytic Tests in Liquid-Phase

The catalytic tests in liquid-phase have been done at the Pontificia Universidad Católica de Chile under the supervision of Prof. Néstor Escalona. A Parr 4561 batch reactor with a total volume of 300 ml was used. First, 44.4 mmol of the desired substrate (anisole, phenol, guaiacol) was dissolved in 128 ml *n*-dodecane and 800 μ l of *n*-hexadecane was added as an internal standard. After the addition of 400 mg catalyst, the reactor was closed and flushed by N₂ for 10 min with approx. 50 ml/min. The stirrer was started with 770 rpm and the reactor heated to 350 °C. After reaching the reaction temperature, H₂ was added until a pressure of 50 bar was reached. The starting point of reaction was marked by the H₂ addition. During reaction, filtrated samples for GC analysis were taken (250 μ l, 3 ml in total) and the pressure was kept constant by dosing additional hydrogen. After 4 h reaction, the reactor was cooled down, depressurized and the catalyst was filtered off. The residue was washed with acetone and dried on air. The GC samples were measured with a Shimadzu Nexis GC-2030 equipped with an Agilent DB-WAX 30 m x 250 μ m x 0.5 μ m column.

3.4. Methods of Characterization

3.4.1. Powder X-ray Diffraction

Powder X-ray diffraction (PXRD) is used to determine different crystal phases in the catalyst. The diffraction can be observed due to X-ray interaction with the electrons of lattice atoms. More precisely, the X-rays are scattered at the electron cloud of the atoms, which are distributed periodically in a crystal lattice. If the path-length difference between two adjacent planes is an integer multiple of the wavelength, constructive interference occurs, which is considered as "reflection". For each group of planes only certain angles exist at which the reflection occurs.

The mathematical description for observing these “reflections” is called the Braggs’ Law (Eq. 4), discovered by W.H. Bragg and W.L. Bragg. It gives the relation between the wavelength (λ), interplanar spacing (d) and the diffraction angle (Bragg angle θ).

$$n \cdot \lambda = 2d \cdot \sin(\theta) \quad (4)$$

Typically, crystals have many sets of different planes (hkl), resulting in a set of reflections which is specific for a single compound. The obtained patterns can be compared with patterns of standard materials or diffraction data from literature/databases.

Usually, PXRD data are presented in the form of the intensity as a function the Bragg angle (2θ) for the corresponding wavelength. The wavelength depends on the anode material of the X-ray source (see A-2).

However, wavelength independent scales sometimes are used when special circumstances make it necessary. For this case, the d -spacing can be used, but it reduces the visual resolution at low d -values. Another option is the q -value or q -vector, which offers the best resolution at high diffraction angles compared to other wavelength independent scales. The q -value is calculated by following Eq. 5.¹⁸⁴

$$q\text{-vector} = \frac{4\pi \cdot \sin(\theta)}{\lambda} \quad (5)$$

In this work, different X-ray sources (Cu, Mo) have been used. Because of this, the PXRD data is plotted as a function of the q -vector.

Besides the catalyst characterization after synthesis and reaction, also in-situ experiments have been performed to elucidate the active phase formation under reaction conditions. Here a capillary reactor, consisting of a quartz tube was used (see Figure 10).

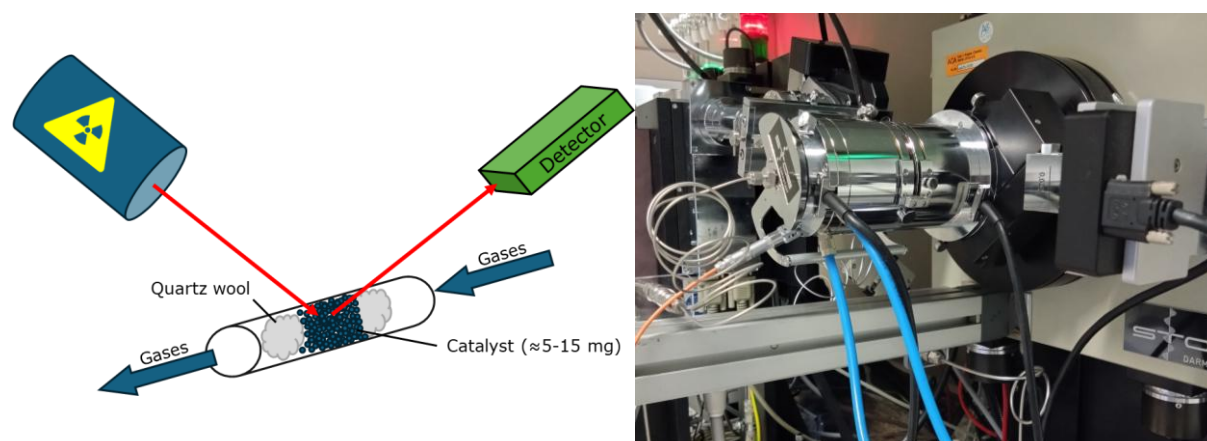


Figure 10: a) Scheme of in-situ XRD set-up b) Stoe HT2 in-situ cell.

Even though in-situ XRD has many benefits for the understanding of heterogeneous catalysis, there are limitations for these set-ups. The quartz capillary is visible in the diffractogram and can cause problems. Further, the high temperature reduces the quality of the diffractograms, reflections are less intense and a broadening occurs. This can cause problems when samples have a low crystallinity or contain only minor amounts of a specific phase, making the identification challenging. Many times, there are no references available for measurements at high temperatures.

Experiment description:

Powder X-Ray diffraction (PXRD) patterns were recorded on a Panalytical X'Pert $\theta/2\theta$ - diffractometer equipped with Xcelerator detector using automatic divergence slits and Cu $K\alpha_1/\alpha_2$ radiation (40 kV, 40 mA; $\lambda = 0.15406$ nm, 0.154443 nm). Cu beta-radiation was excluded using a nickel filter foil. Finely pestled samples were mounted on silicon zero background holders. After data collection, obtained intensities were converted from automatic to fixed divergence slits (0.25°) for further analysis. Additionally, XRD powder patterns were recorded on a Stoe Stadi P transmission diffractometer equipped with a DECTRIS Mythen2 1K detector applying Ge(111) monochromatized Mo $K\alpha_1$ radiation (50 kV, 40 mA, 0.070930 nm). The samples were ground to a fine powder and placed between two acetate foils before the measurement.

In-situ XRD studies were performed on a Stoe Stadi P equipped with a Stoe HT2-in-situ oven and a Mythen 1K detector in Debye-Scherrer geometry using monochromatized Mo $K\alpha_1$ radiation (50 kV, 40 mA, 0.070930 nm). The samples were ground, pressed to pellets at 10 tons, crushed, and sieved to a fraction of $100\text{-}150$ μm . A specimen was filled into a quartz glass capillary (approx. 2 mm outer diameter, 1 mm inner diameter, opened on both sides) until a height of approx. 6 mm was achieved and fixed by quartz glass wool. After mounting the capillary into the oven, the capillary was flushed with He (10 ml/min) and the sample was heated to the desired temperature (350 °C or 325 °C). After equilibration the gas feed was changed to reaction gas mixture (details in corresponding description) with a total flow of 10 ml/min) and the reaction was monitored using static data collection over a 17° angular region (Mo-radiation). Gas dosage was done via a set of Bronkhorst mass flow controller units. The temperature was calibrated according to well-known phase transitions (AgNO_3 , KClO_4 , Ag_2SO_4 , SiO_2 , K_2SO_4 , K_2CrO_4 , WO_3 , BaCO_3). Peak positions and profiles were fitted with Pseudo-Voigt function using the HighScore Plus software package (Panalytical). Phase identification was done by using the PDF-2 database of the International Center of Diffraction Data (ICDD).

3.4.2. Electron Paramagnetic Resonance Spectroscopy

The Electron Paramagnetic Resonance (EPR) Spectroscopy has been used for analysis of paramagnetic species that contain unpaired electrons (e.g. radicals, oxygen-vacancies, metal ions). Although there is a restriction due to this selection rule, the EPR has several advantages, making it an interesting option to study heterogenous catalysts. This method is good for tracking redox processes and radicals, which are frequently involved in catalytic mechanisms. Due to its high sensitivity, the EPR spectroscopy is a good technique for elucidating reaction mechanism and active sites at low concentrations.^{185, 186} For molybdenum, only Mo^{5+} is EPR active, while Mo^{4+} is inactive.

The fundamental principle of EPR spectroscopy is the Zeeman effect. Usually, the energies of the two spin levels of a single electron characterized by the spin quantum numbers $M_s = \pm 1/2$ are degenerated. However, when an unpaired electron is exposed to an external magnetic field, the energy level degeneration is lifted (see Figure 11).¹⁸⁶

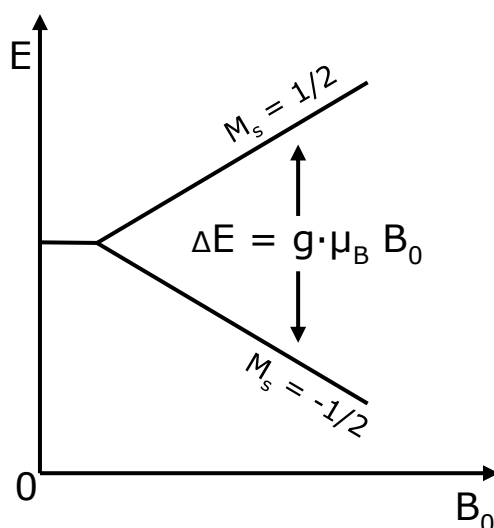


Figure 11: Splitting of energy levels in an external magnet field B_0 .

When the sample within an external magnetic field is exposed to microwave radiation while the field is swept, the resonance condition (Eq. 6) is fulfilled when the microwave energy matches the energy difference between the spin levels once the resonance field value is reached. Then a spin flip occurs.

$$\Delta E = g_e \cdot \mu_B \cdot B_0 = h \cdot \nu \quad (6)$$

An EPR spectrum can be obtained by changing the radiation frequency and keeping the magnetic field constant or vice versa. However, in continuous wave (cw) EPR which was applied in this work, the microwave frequency has been kept constant.¹⁸⁵

Experiment description:

EPR spectra were recorded by an X-band cw-spectrometer ELEXSYS 500-10/12 (Bruker) using a microwave power of 6.3 mW, and a modulation frequency and amplitude of 100 kHz and 5 G, respectively. In-situ EPR experiments were performed in a home-made quartz plug-flow reactor connected to a gas-dosing device with mass flow controllers (Bronkhorst) at the inlet. This reactor was filled with 50 mg of catalyst particles (250-350 μm). For these experiments two procedures were done. In all experiments the total flow rates were 25 ml/min.

3.4.3. Vibrational Spectroscopy

The infrared (IR) spectroscopy is part of the vibrational spectroscopy, based on interaction of light ($12500\text{-}10\text{ cm}^{-1}$) with matter. It can be used for qualitative, as well as for quantitative measurements. Many times, mid IR radiation ($4000\text{-}400\text{ cm}^{-1}$) is used as it allows to identify and quantify a broad range of molecular IR active functional groups. For exciting a molecular vibration, the electric dipole moment of the functional group has to be changed ($d\mu \neq 0$). Modern IR spectrometers use a Fourier transformation (FT), a mathematical function, to calculate an IR spectrum from an interferogram. This construction has many advantages e.g. low measuring time. In heterogenous catalysis, the samples are often solid and in-situ experiments are demanded to obtain information at reaction conditions. Special techniques like diffuse reflectance infrared Fourier transform spectroscopy (DRIFTS) are used to elucidate surface chemistry and adsorbates. Nowadays, it is an important tool for catalysis research to understand reaction mechanisms, promoter effects and effects of dynamic feeds. However, one also has to consider disadvantages like high temperature gradients, catalytically active cell compounds and beam effects.¹⁸⁷ For example, the acid properties can be determined by adsorption of probe molecules like ammonia and pyridine.¹⁸⁸⁻¹⁹⁰

In this work NH_3 -adsorption was used for Lewis- and Brønsted-acid site identification. There are different vibrational bands resulting from the NH_3 protonation by Brønsted-sites to form NH_4^+ and due to the electron donation from NH_3 to the Lewis-site. Additionally, the adsorption of anisole was tested, to understand its interaction with O_v .

Raman spectroscopy is the second vibrational spectroscopy technique used in this work, which is complementary to the IR spectroscopy. It is based on inelastic scattering of photons, which is also called Raman scattering. The selection rule for Raman active interactions is the polarizability of a molecule, that must change. The efficiency of the

Raman effect is comparatively low, which is why there was a limitation of the instrumentation and the application was limited for many years. With the improvement of lasers and spectrometers, it has become a powerful tool for the study of molecular species, oxide phases and surface species. A Raman spectrum consists of three different types of effects. The Rayleigh scattering, which has the wavelength of the excitation light. This is filtered out, because it contains no information and its high intensity. The second one is the Stokes scattering. It occurs when a photon is interacting with a molecule, excites it to a virtual energy state and the molecule subsequently relaxes to an energy state higher than the ground state. Then, the emitted photon has a lower frequency than the excitation source. Anti-Stokes lines have higher energies, as the photons are interacting with molecules in excited states. Thus, they take up energy from the molecule and the scattered photons have higher energies than the incoming ones. The levels of virtual energy states are specific for a species. The number of molecules in the ground- and excited state is given by the Boltzmann distribution (Eq. 7).

$$N_m = N_0 e^{-\frac{mh\nu_0}{kT}} \quad (7)$$

Because of this the intensity of Stokes lines is significantly higher than the anti-Stokes lines. At higher temperatures, the anti-Stokes become more intense. For improving the signal-noise ratio it can be useful to analyze anti-Stokes at high temperatures. Another problem for Raman measurements can be the fluorescence, which might interfere with the Stokes lines. This can be avoided as well by observing the anti-Stokes lines. It is possible to couple the Raman spectrometer with a light microscope, which offers a spatial resolution.¹⁹¹

Experiment description:

In-situ DRIFTS experiments were carried out with a Nicolet 6700 (Thermo Scientific) FTIR spectrometer equipped with an MCT detector and a Praying Mantis (Harrick Scientific) DRIFTS reaction cell. The dome of the reaction cell was mounted with CaF₂ windows. The setup was coupled with an online MS system (Omnistar GSD 320, Pfeiffer Vacuum) with a secondary electron multiplier for gas analysis. The samples were pressed and sieved to obtain a particle size of 250-315 μm. All samples were pre-reduced in pure H₂ (25 ml/min) for 2 h at 325 °C. For adsorption experiments of vaporized liquid substrates, the latter were pumped into an evaporator by a syringe pump (Harvard Apparatus, PHD ULTRA 4400) at a flow rate of 2.75 μl/min with a carrier gas (He) flow rate of 25 ml/min. The DRIFT spectra were registered with an optical resolution of 4 cm⁻¹ with 64 scans per measurement. As a background spectrum, the spectrum of the pre-reduced catalyst at the experiment temperature under helium was used.

Surface acidity of the catalyst materials was analyzed by FTIR spectroscopy of adsorbed ammonia using a Tensor 27 spectrometer (Bruker) equipped with a heatable and evacuable IR reaction cell with CaF₂ windows, which was connected to a gas dosing and evacuation system. For each experiment, 50 mg of catalyst were pressed into a self-supporting wafer with a diameter of 20 mm, which was first evacuated and then pretreated either in synthetic air or hydrogen (50 ml/min) at 325 °C for 120 min. After cooling to room temperature, a background spectrum was recorded and ammonia (5 vol.-% in He) was introduced until saturation of adsorbed ammonia was achieved, followed by evacuation to remove physisorbed ammonia. The desorption of ammonia was followed by heating the sample in vacuum up to 300 °C and recording spectra every $\Delta\theta = 50$ °C. For data analysis, difference spectra were used, obtained by subtraction of a respective background spectrum from the ammonia adsorbate spectrum.

For Raman characterization a Renishaw inVia Raman microscope was used, equipped with a 633 nm laser and a Leica 50x objective. The used laser power was 0.085 mW with an exposure time of 10 s, with one accumulation.

3.4.4. X-ray Photoelectron Spectroscopy

X-ray photoelectron spectroscopy (XPS) or electron spectroscopy for chemical analysis (ESCA) is used to investigate the oxidation state and atomic percentage of elements at the catalyst surface. In this work it has been used for a better understanding of the Mo reduction behavior in the reaction, which is connected to the oxidation states. From the XP spectra one can distinguish between Mo⁶⁺, Mo⁵⁺ and Mo⁴⁺ and these ions can be quantified with this method. This has also been done for Ni/Ni²⁺.

For measuring an XP spectrum, the sample is irradiated with X-ray photons. Many times, Mg K_α (E = 1253.6 eV) or Al K_α (E = 1486.6 eV) X-ray sources are used. These photons can collide elastically with electrons of the sample's atoms and the electrons are emitted (photoelectrons). The X-rays can penetrate the sample quite deep, but because of an increasing chance of interactions between the photoelectrons and the sample atoms with increasing sample thickness, this technique has a limited information depth of 1-10 nm.¹⁹² The kinetic energy (E_{kin}) of photoelectrons is given by Einstein's law and is equal to the X-ray energy subtracted by the binding energy (E_b):

$$E_{kin} = h \cdot \nu - E_b - \phi_s \quad (8)$$

However, the energy is also influenced by the spectrometers work function (ϕ_s).

Experiment description:

XPS (X-ray photoelectron spectroscopy) measurements were carried out using an ESCALAB 220iXL (Thermo Fisher Scientific) with monochromatic Al K α radiation ($E = 1486.6$ eV). The samples were prepared on a stainless-steel base with a conductive, double-sided adhesive carbon tape. The measurements were performed with charge compensation using a channel electron system combining low-energy electrons and Ar $^+$ ions ($p_A = 1 \times 10^{-7}$ mbar). The peak areas were normalized with the transmission function of the spectrometer and the element-specific sensitivity factor of Scofield.

Pseudo-in-situ XPS measurements were performed in a laboratory X-ray photoelectron spectroscopy system at near ambient pressure (NAP-XPS, SPECS Surface Nano Analysis GmbH, Germany). The system is equipped with a differentially pumped Phoibos 150 electronic energy analyzer and a monochromatic Al K α radiation source ($E = 1486.6$ eV) operating at 70 W and 15 kV. The system is connected to a high pressure cell (HPC 20, SPECS Surface Nano Analysis GmbH, Germany), which heats the sample with a halogen lamp (up to 800 °C) and is equipped with four mass flow controllers (MFCs) at the gas inlet and a manual back pressure regulator (Swagelok, USA) at the outlet. For the current experiments at ambient pressure, the samples were heated to 325 °C in N $_2$ with 10 K/min inside the HPC 20 cell. Subsequently, the desired gas mixture (H $_2$, CH $_4$:H $_2$) was added for different times at 325 °C before the sample was cooled down again in N $_2$. Afterwards, the cell was evacuated and the sample transferred to the measurement chamber under vacuum at room temperature. The powder samples were pressed onto a stainless-steel sample plate using a laboratory press with a diameter of 5 mm and a load of approx. 0.5 tons. The temperature was monitored using a thermocouple on the sample plate, which was pressed against the surface of the sample. The electronic binding energies refer to the level of the C 1s nucleus of carbon at 284.8 eV (C-C and C-H bonds). For the analysis, the peaks were deconvoluted with Gauss-Lorentz curves using the Unifit 2023 software.

3.4.5. Inductively Coupled Plasma Optical Emission Spectroscopy

The inductively coupled plasma optical emission spectroscopy (ICP-OES) is used to determine the elemental concentration in the catalyst samples. For this analysis the samples are dissolved by chemical digestion. The solutions are injected into an argon-plasma at temperatures between 6000-8000 K. Within this plasma, the electrons of the atoms are excited by the high energy. Electrons return to the ground state by emitting the energy difference in form of element-specific radiation. The spectral lines occurring in the process are unique for each element. The high energy of the plasma leads to an ionization

of the atom and these ions have several spectral lines as well. The intensity of the emitted light correlates with the element concentration.¹⁹³

Experiment description:

For ICP-OES measurements a Varian 715-ES spectrometer was used. Approximately 10 mg samples were dissolved in 8 ml aqua regia (HCl + HNO₃) and 2 ml HF. The digestion was done microwave assisted with an Anton Paar Multiwave PRO pre-treatment system at 220 °C and 50 bar pressure. Afterwards, the solution was diluted until a total volume of 100 ml was reached and ICP-OES was measured. The data analysis was done by the Varian 715-ES ICP Expert software.

3.4.6. Temperature Programmed Reduction

The temperature programmed reduction (TPR) is used to investigate the reduction behavior of different samples by diluted reductive gases (H₂, CO), when heated up linearly. Therefore, the catalyst is placed in a fixed bed reactor, which is exposed to an H₂ gas flow. The H₂ consumption is measured by a thermal conductivity detector (TCD) related to the temperature. This allows to gain information about the reduction temperatures of metal oxides and understand the influence of dopants and metal-supports interactions on the reducibility. Additionally, because the H₂ consumption can be quantified, the reduction degree can be determined.

Experiment description:

Temperature programmed reduction (TPR) measurements were performed in a micromeritics 3Flex with a quartz tube reactor and a thermal conductivity detector for quantification. Around 50 mg of the samples were loaded in the reactor and pretreated at 400 °C (20 °C/min) under the flow of 5 % O₂/He for 30 min to remove any adsorbed species on the surface of the samples. Afterwards, the sample was cooled to RT under Ar flow. Then, the flow was changed to 50 ml/min H₂/Ar and the sample was ramped to 850 °C at a heating rate of 10 °C/min. The temperature was held at 850 °C for 90 min. The hydrogen consumption peaks were recorded as a function of temperature and quantitative analysis of the TPR data, based on the peak areas, was done after calibration.

3.4.7. Thermogravimetric Measurements

Thermogravimetric (TG) measurements are used to track weight changes in samples during a temperature programmed treatment in different gases (e. g. H₂, syn. Air, He...). Usually, the heating rate is not exceeding 10 °C/min. The TG device can be coupled with a

mass spectrometer to analyze gases which are formed during the treatment or observe the consumption. By this coupling, TPR or temperature programmed oxidation (TPO) can be performed as well. However, the reactor geometry is different since the sample is placed in a cup (e.g. Al_2O_3), while the TPR is using plug flow reactors. Therefore, the results can be influenced by the different reactor types.

Experiment description:

TG measurements were performed on a Sensys TG-DSC (Setaram, Caluire) coupled with a OmniStar quadrupole mass spectrometer (Pfeiffer Vacuum), scanning in the multiple ion detection (MID) mode. The MS ionization source was electron impact (EI) with an ionization energy of 70 eV. The samples were weighted ($m \approx 20$ mg) in open Al_2O_3 crucibles (100 μl) and heated from 25 °C up to 600 °C in syn. air (20 ml/min) with a heating rate of 10 °C/min.

3.4.8. UV-Vis Spectroscopy

UV-vis spectroscopy measures the transition of electrons into a higher excitation state, which is done in the range of UV and visible light (200 – 800 nm). Various electron transitions can occur, namely $n \rightarrow \pi^*$ and $\pi \rightarrow \pi^*$ transitions for organic molecules or d-d and charge transfer transitions for metal oxides and ions. Because electron transitions are investigated, it is also called electron spectroscopy.¹⁹¹ The UV-vis spectroscopy has been used to study conjugated π electron systems, but also inorganic compounds like transition metal oxides can be investigated. Spectra can be measured in diffuse reflectance mode as already described for the DRIFTS spectroscopy (see chapter 3.4.3) or fiber probes with a specific work distance can be introduced into a reactor.¹⁹¹

Experiment description:

In-situ UV-vis measurements were carried out using an Avantes spectrometer (AvaSpec-2048-USB2-RM) equipped with a high-temperature reflection UV-vis probe, an Ava-Light-DH-S-BAL deuterium-halogen light source, and a CCD array detector. The probe consisting of six radiating optical fibers and one reading fiber was threaded through the furnace to face the wall of the quartz tube reactor at the position where the catalyst (~ 250 mg) was located.¹⁹⁴ Before recording UV-vis spectra, the sample was heated up to 325 °C in 20 % O_2 in N_2 (heating rate was 10 $\text{K}\cdot\text{min}^{-1}$) and then purged with N_2 for 15 min. Hereafter, the sample was treated in an 10 % C_3H_6 -90 % H_2 flow for 1 h, purged with N_2 for 15 min, and reoxidized in 20 % O_2 in N_2 for 1 h. UV-vis spectra were recorded every 30 s. Barium sulfate (99.998 %, Aldrich) was used as a white standard.

For visualizing the progress of reduction/reoxidation processes, a relative reflectance (R_{rel}) was defined as the ratio of the reflectance of the sample treated in 10 % C_3H_6 -90 % H_2 or reoxidized in 20 % O_2 - N_2 to that of the fully oxidized one as given in equation (9). From this relative reflectance, we calculated the relative Kubelka-Munk function $F(R_{rel})$ according to equation (10).

$$R_{rel} = \frac{R_{in\ C_3H_6-H_2\ or\ O_2-N_2\ flow}}{R_{oxidized}} \quad (9)$$

$$F(R_{rel}) = \frac{(1 - R_{rel})^2}{2 \cdot R_{rel}} \quad (10)$$

3.4.9. Transmission Electron Microscopy

Transmission electron microscopy (TEM) images have been prepared to get an insight into catalysts morphology and elemental distribution. This is important in heterogenous catalysis to get more insight into e.g. active phase formation, as morphology and elemental distribution can significantly influence the catalytic activity. As can be derived from the name, in TEM electrons are used for imaging, which are transmitted through a specimen. This allows a resolution down to 0.045 nm to be achieved. However, samples must be very thin (less than 100 nm) or used as a suspension to be electron transparent.

For TEM an electron source, mostly a single crystal (LaB_6), is placed at the top. High voltages are used (up to 300 kV) to release electrons into the vacuum and focus on the sample by condenser lenses (see Figure 12 b).¹⁹⁶ After being transmitted through the sample, the electrons are passing objective, lenses and a slit. The objective lenses are focusing the electrons again after interaction with the sample. In TEM the magnification is controlled by the distance between the sample and the magnification lens. At the end the electrons are used to expand the electron beam onto the imaging detector. There are different imaging methods, with specific pros and cons and information content. However, they will be not discussed in detail here.

While TEM is done, the energy dispersive X-ray spectroscopy (EDX) is used for gaining chemical information about the local elemental distribution.¹⁹⁶ When the primary electrons interact with the specimen, different phenomena can occur (see Figure 12 a). One of them is the X-ray emission from an electron in a higher shell that falls down to an electron hole in an inner shell. The latter being formed by interaction with the primary electrons of the beam. This X-ray energy is specific for each element, allowing to perform elemental mappings.

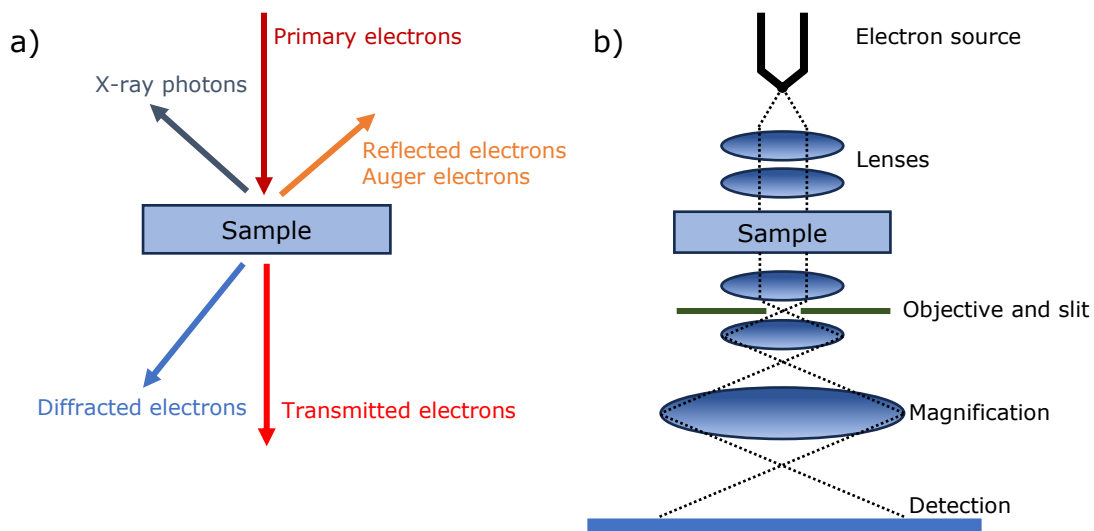


Figure 12: a) Different interactions of primary electrons and b) a simplified schematic plan of a TEM, adapted with permission from Ref.¹⁹⁵. Copyright 2019 Springer Fachmedien Wiesbaden.

Experiment description:

In-situ Scanning Transmission Electron Microscopy was performed on a probe corrected JEOL NEOARM (Japan) operated at 200 kV using High Angle Annular Dark Field (HAADF) detectors for imaging. The in-situ holder is a Protochips Atmosphere 220 MEMS-chip system (see A-3) with the specimen placed onto the heated top chip via dry deposition.

Ex-situ STEM was performed on a probe corrected JEOL JEM-ARM200F operated at 200kV using HAADF and Annular Bright Field (ABF) detectors. Energy Dispersive X-ray Spectroscopy (EDX) mapping was acquired using a JEOL DRY SD60GV detector. For the post-mortem analysis the top chip was removed from the in-situ holder and put into a dedicated inspection holder for MEMS-chips.

Scanning electron microscopy (SEM) data was acquired using a Quattro S (Thermo Fisher) equipped with a Schottky emitter, a 60 mm² SDD detector (Thermo Fisher) for energy dispersive X-ray spectroscopy (EDS), secondary electron (SE) detector (Everhart-Thornley type), and back-scattered electron (BSE) detector (ring semiconductor type). The specimen was deposited dry onto a Si wafer. Acceleration voltage was set to 10 kV for imaging and spectroscopy, with spot size selected for optimum resolution or current respectively. Elemental Maps were calculated from spectral imaging data set using the net counts fitting method provided in the Pathfinder software (Thermo Fisher).

4. Results and Discussion

4.1. Catalytic Results

4.1.1. Catalytic Results in Gas-Phase

The catalytic tests in gas-phase have been done at 325 °C and atmospheric pressure. All samples were reduced in advance at 325 °C in 100 % H₂ for 2 h. Afterwards, a switch to the feed-gas (75 % N₂/25 % H₂/0.4% anisole) marked the starting point at 0 min time on stream (TOS). It can be seen that MoO₃, Ni(1)MoO₃, CoMoO₄ and Co(5)MoO₃ have an induction period within the first 4 - 8 h, which is not visible for nickel containing catalysts with a nickel content exceeding 1 wt.% (see Figure 13). The induction period for MoO₃ and Ni(1)MoO₃ lasted for about 5 h, until conversions of 35 % and 55.9 % were reached after 10 h TOS, respectively. Subsequently, the activity of both catalysts decreased, reaching 31.9 % (MoO₃) and 53.1 % (Ni(1)MoO₃). Interestingly, CoMoO₄ and Co(5)MoO₃ have a longer induction period, but did not start to deactivate directly after reaching maximum conversion. It rather increased over the whole reaction time, even though the increase of conversion became slower with time. The conversion of CoMoO₄ reached 44.5 % after 10 h TOS and increased to 49 % after 17 h TOS.

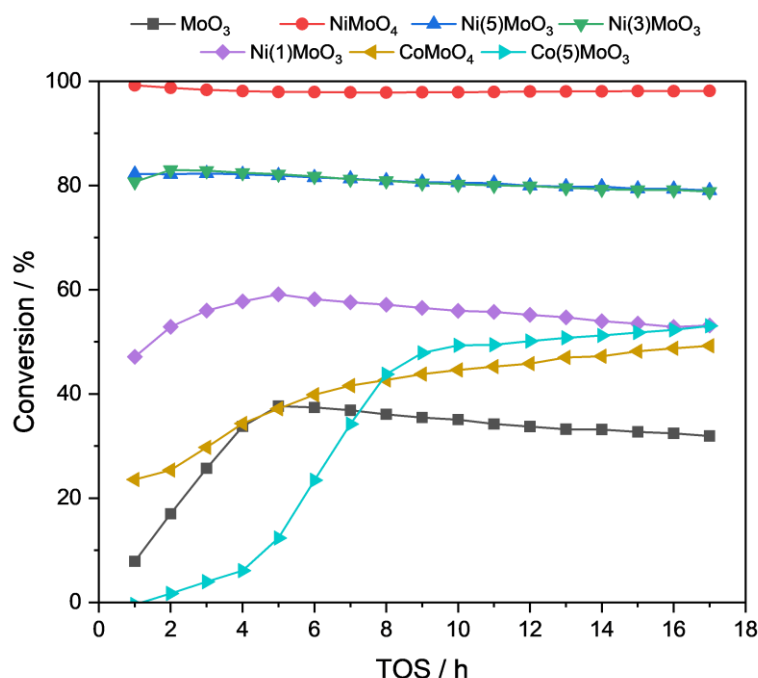


Figure 13: Catalytic test over 17 h TOS at 325 °C after pre-reduction at 325 °C for 2 h in 100 % H₂, WHSV = 0.31 g_{anisole}·g⁻¹_{cat}·h⁻¹, particle size = 600-800 μm, 200 mg cat. diluted with 2.3 g quartz. Reproduced from Ref.¹⁹⁷ with permission from the Royal Society of Chemistry.

At the same time, the induction period of Co(5)MoO_3 lasted for 10 h, reaching 49.3 % conversion afterwards and 53 % after 17 h TOS. Ni(3)MoO_3 , Ni(5)MoO_3 and NiMoO_4 did not show this induction period, but the conversion was much higher compared to other samples. Ni(3)MoO_3 and Ni(5)MoO_3 reached similar conversions of ca. 80 % after 10 h TOS. A slight decrease to 79 % occurred after 17 h TOS. For NiMoO_4 the conversion was about 98 % after 10 h TOS and did not show any significant deactivation over time.

An assumption for the pronounced induction periods could be phase transformations which are of different complexity, depending on the catalyst. For MoO_3 the formation of a $\text{MoO}_x\text{C}_y\text{H}_z$ phase is known and in literature discussed in context with the induction period.^{25, 32} It has been shown that the reduction is a key step for the formation of this phase, which stabilizes the catalytically active Mo^{5+} by preventing it from over-reduction to inactive MoO_2 between 300-400 °C (see chapter 2.4). In other reports it was claimed that more $\text{MoO}_x\text{C}_y\text{H}_z$ is formed, when MoO_3 is pre-reduced or hydrogen activating metals are present and the reduction is the rate determining step.^{25, 44, 163}

This suggests, that the missing induction period for NiMoO_4 , Ni(5)MoO_3 and Ni(3)MoO_3 can be related to the improved reduction properties by forming larger amounts of the precursor (MoO_xH_z) for the $\text{MoO}_x\text{C}_y\text{H}_z$ phase (see chapter 2.4). In addition is the partial carburization to $\text{MoO}_x\text{C}_y\text{H}_z$ significantly faster than the reduction.²⁵ When the nickel content exceeds a certain amount (here 1 wt.%), the reduction is accomplished within the 2 h pre-reduction and the carburization is finished in such a short time, that no induction period can be observed.

In case of cobalt containing catalysts, the occurrence of the induction period could be explained by a different way of reduction. NiMoO_4 is reduced in one step to Ni/MoO_x and there were no intermediate phases visible.¹⁶⁰ From this, the $\text{MoO}_x\text{C}_y\text{H}_z$ phase can be formed directly or the MoO_x part is reduced further, until it will be formed. In contrast to this, several intermediate phases are known for CoMoO_4 (e.g. $\text{Co}_2\text{Mo}_3\text{O}_8$ and CoMoO_3 , see chapter 2.5), which need to be overcome in order to obtain H_2 activating Co^0 and to generate a MoO_x phase at the same time. However, to reduce these phases efficiently, temperatures higher than 325 °C are necessary.

Interestingly, no hydrogenation products were observed for any of these catalysts, suggesting that the reaction might follow a reverse Mars-van-Krevelen mechanism exclusively. The selectivity of phase pure MoO_3 and Ni(1)MoO_3 towards aromatic hydrocarbons is high with a benzene selectivity of 27.7 % and selectivities for toluene and xylenes of 6.1 % and 4.9 %, respectively. Phenolic compounds have been formed as well with a selectivity for cresol of 8.9 % and 18.9 % for phenol (see Table 5). For giving a value of the deoxygenation grade, the ratio of oxygen-free aromatics and phenols ($R(A/P) = S(\text{arenes})/S(\text{phenols})$) have been used as indicator. This value is 1.36 for MoO_3 .

As can be expected for the anisole HDO, methane was produced with a selectivity of 3.4 %. The cobalt catalysts showed an increased selectivity for phenol and cresols compared to MoO₃ with approx. 28 % phenol and 15 % cresols selectivity. Thus, the R(A/P) ratio is reduced to $R \approx 0.78$ for both, CoMoO₄ and Co(5)MoO₃.

Ni(5)MoO₃ and Ni(3)MoO₃ produced an increased content of aromatic products with a benzene selectivity of 32-33 %, 9-10 % for toluene and 1-3 % to the xylenes. Nevertheless, the increased cresol selectivity leads to a R(A/P) ratio of 1.36. For Ni(3)MoO₃ it was slightly enhanced to 1.67. All these catalysts had a selectivity to methane of about 4 %. Compared to this NiMoO₄ obtained the best R(A/P) ratio with 8.85. The benzene selectivity was at 41.8 % with a toluene selectivity of 10.1 %. In parallel, the selectivity of phenol and cresol were only at 4.7 % and 1.5 %, respectively. This could be explained by the high activity of NiMoO₄. The methane selectivity of 20.2 % was very high and is undesired. This cannot be explained exclusively by the HDO of anisole, which produces methane by the deoxygenation of the methoxy group as a byproduct. Additionally, NiMoO₄ had the highest selectivity towards transalkylated products like toluene (10.1 %) and xylenes (4.9 %).

The carbon for the C-transfer and for forming methane cannot be based on the methoxy group alone, as the sum of these products is higher than the amount of anisole and thus the number of methoxy groups. It indicates that a ring decomposition must take place to produce significant amounts of methane. This might also indicate that besides a possible MoO_xC_yH_z phase, which is discussed as the active one, other phases influence the selectivity.^{25, 41}

A direct influence of the nickel on selectivity cannot be excluded. Therefore, a nickel catalyst (3 wt.% Ni on α -Al₂O₃) was tested under the same conditions. After 10 h TOS, a conversion of 16.7 % was obtained, with a methane selectivity of 44.2 % and a benzene selectivity of 25.8 % (see Table 5). This suggests that the selectivity cannot be only dominated by the metallic Ni and might have only minor contributions to it. Furthermore, Ni/Al₂O₃ suffered from very fast deactivation, which was not observed for molybdenum-based catalysts. While the initial activity was comparable to Ni(1)MoO₃, it deactivated down to 11 % conversion after 17 h TOS (see A-11).

Additional tests with benzene as substrate have been done under the same conditions as the anisole HDO for Ni/Al₂O₃, Ni(5)MoO₃ and NiMoO₄ (see A-12, A-13 and A-14). This time, Ni/Al₂O₃ showed a significantly lower conversion of approx. 2.5 %, which decreased to 1 % over 17 h TOS. This can be explained by an increased WHSV with benzene compared to anisole. Therefore, the conversion in gas-phase experiments at 325 °C cannot be compared for different substrates. Products which have been observed were methane with approx. 16 % selectivity and toluene with 5.5 % in average (see A-13). However, for

NiMoO₄, which has a higher Ni content, a conversion of ca. 4 % after 10 h TOS was observed. The main product was methane with a selectivity of 21 % and a toluene selectivity of ca. 9 % (see A-14). Compared to this, Ni(5)MoO₃ had after 10 h TOS 3.3 % conversion, while the selectivities of methane and toluene were at 2.8 % and 1.6 %, respectively (see A-12).

These results show that nickel is active for C-C hydrogenolysis and may enhance the selectivity for methane. This agrees with reports in literature, but demonstrates also that the selectivity cannot be driven by nickel exclusively, since the CH₄ selectivity for NiMoO₄, Ni(5)MoO₃ and Ni(3)MoO₃ is significantly lower.^{198, 199}

This could be explained by the position of nickel on the catalysts. For Ni/Al₂O₃ the nickel was impregnated on the support followed by a calcination. Is the catalyst activated by reduction, the nickel will be exposed on the catalyst surface. This is not the case for NiMoO₄, where the nickel is situated inside the crystal lattice after catalyst synthesis. Is NiMoO₄ reduced, the formed Ni particles are at least partly covered by an MoO_x species as shown later (see chapter 4.4). Hence, the accessibility of the nickel particles by large molecules could be hindered.

Table 5: Anisole conversion and product selectivities (C-mol%) at 325 °C, WHSV = 0.31 g_{anisole}·g⁻¹_{cat}·h⁻¹ and TOS = 10 h. Selectivity ratio: S(Arenes)/S(Phenols) = R(A/P). Adapted from Ref.¹⁹⁷ with permission from the Royal Society of Chemistry.

	X(Anisole)	S(Methane)	S(Benzene)	S(Toluene)	S(Xylenes)	S(Phenol)	S(Cresols)	S(Arenes)/S(Phenols)
MoO₃	35.1	3.4	27.7	6.1	4.9	18.9	8.9	1.36
NiMoO₄	97.9	20.2	41.8	10.1	3.0	4.7	1.5	8.85
Ni(5)MoO₃	80.6	4.2	32.1	8.7	1.0	17.7	13.1	1.36
Ni(3)MoO₃	80.3	3.7	32.7	9.6	3.5	15.4	12.0	1.67
Ni(1)MoO₃	55.9	3.7	31.6	7.8	2.7	18.5	12.0	1.38
CoMoO₄	44.6	3.2	25.3	5.7	1.6	27.9	14.5	0.77
Co(5)MoO₃	49.3	3.6	27.8	5.6	2.0	28.9	16.1	0.79
Ni/Al₂O₃	16.7	44.2	25.8	0.0	0.0	0.0	0.0	-

4.1.2. Catalytic Results in Liquid-Phase

Liquid-Phase Anisole HDO

Catalyst tests were done in liquid-phase at 350 °C and 50 bar H₂ pressure for 4 h, to gain insight into the catalytic properties in both phases. The good catalytic results for the gas-phase reaction of nickel promoted catalysts are promising, even though MoO₃ showed not outstanding results for the liquid-phase reaction in literature (see chapter 2.2.1).

Surprisingly, the catalytic activity of MoO₃ was higher than for CoMoO₄, which is different to the gas-phase experiments (compare Figure 13 and Figure 14). NiMoO₄ was the only catalyst, reaching 100 % conversion after approx. 100 min reaction. At this time 80 %, 61 %, 40 % and 28 % conversion was reached by Ni(5)MoO₃, Ni(1)MoO₃, MoO₃ and CoMoO₄, respectively (see Figure 14). At the final reaction time of 240 min, Ni(5)MoO₃ reached 95 % conversion, while Ni(1)MoO₃ obtained 90 % conversion. With 68 % and 55 % conversion for MoO₃ and CoMoO₄, respectively, their conversion was significantly lower. The trend of increased catalytic activity with increasing nickel content agrees with the results obtained by the gas-phase tests and the order of catalytic activity for the HDO of anisole was almost the same with NiMoO₄ > Ni(5)MoO₃ > Ni(1)MoO₃ > MoO₃ > CoMoO₄.

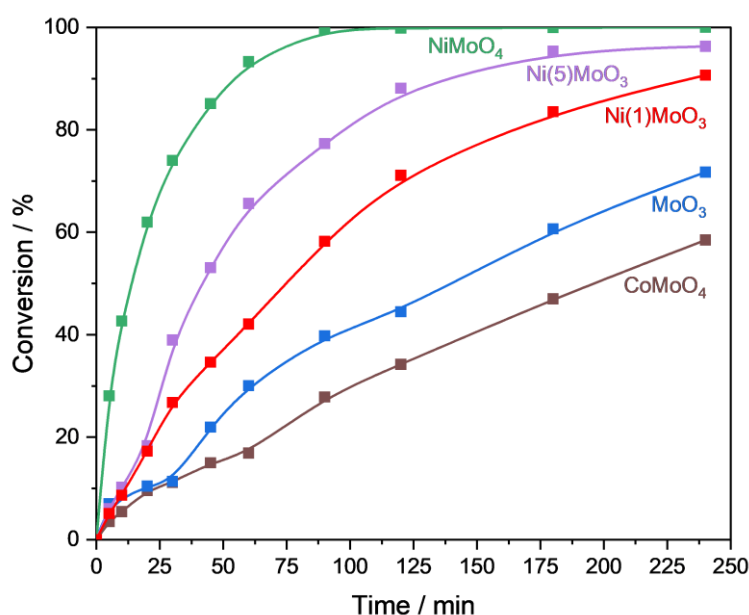


Figure 14: Conversion over time for the liquid-phase anisole HDO at in a 300 ml batch reactor, at 350 °C, 50 bar H₂ pressure, 770 rpm agitator speed and 44.4 mmol anisole dissolved in 128 ml *n*-dodecane with 400 mg catalyst.

To compare the results without the influence of deactivation and product inhibition, the initial rates have been determined. For this, the first three measured points were used and a regression was carried out. The highest rate was obtained for NiMoO₄ with $23.2 \cdot 10^{-5} \text{ mol} \cdot \text{g}^{-1} \cdot \text{s}^{-1}$ for (see Table 6), followed by Ni(5)MoO₃ and Ni(1)MoO₃ with

$6.40 \cdot 10^{-5} \text{ mol} \cdot \text{g}^{-1}_{\text{cat}} \cdot \text{s}^{-1}$ and $5.87 \cdot 10^{-5} \text{ mol} \cdot \text{g}^{-1}_{\text{cat}} \cdot \text{s}^{-1}$, respectively. Even though the final conversions of MoO_3 and CoMoO_4 are different, the initial rates for MoO_3 ($3.51 \cdot 10^{-5} \text{ mol} \cdot \text{g}^{-1}_{\text{cat}} \cdot \text{s}^{-1}$) and CoMoO_4 ($3.38 \cdot 10^{-5} \text{ mol} \cdot \text{g}^{-1}_{\text{cat}} \cdot \text{s}^{-1}$) are very close to each other. This could be explained by a temporary decrease in reaction rate, which forms a plateau for MoO_3 after approx. 20 min (see Figure 14). For Ni(5)MoO_3 an increase of reaction rate can be observed after 20 min as well and it could be explained by an active phase formation (e.g. $\text{MoO}_x\text{C}_y\text{H}_z$). However, since the experiments were not repeated multiple times and reproducibility remains unknown, it is not further discussed.

The product spectrum of the liquid-phase reaction differs from that of the gas-phase reaction. It has to be mentioned that for liquid-phase experiments the yield was analyzed, while the selectivity was used for the gas-phase experiments. This was done because the selectivity depends on the conversion that should be compared for a certain value. However, the measurements for some experiments are inaccurate at low conversion (see A-18 - A-21 and A-24 - A-27). This makes an interpolation for a particular conversion inaccurate. For the HDO of anisole with MoO_3 the main product with 52 % yield was phenol after 240 min reaction (see Figure 15), while benzene was the main product in the gas-phase reaction (Table 5). Interestingly, within the first 30 min the conversion increases, but almost no products were observed. This could indicate that a $\text{MoO}_x\text{C}_y\text{H}_z$ phase is also formed during the liquid phase reaction. After 30 min, the formation of phenol raised quickly along with the conversion until 60 min, before the phenol formation started to slow down. At the same time small amounts of benzene start to form. Nevertheless, the discrepancy between conversion and yield increased with time.

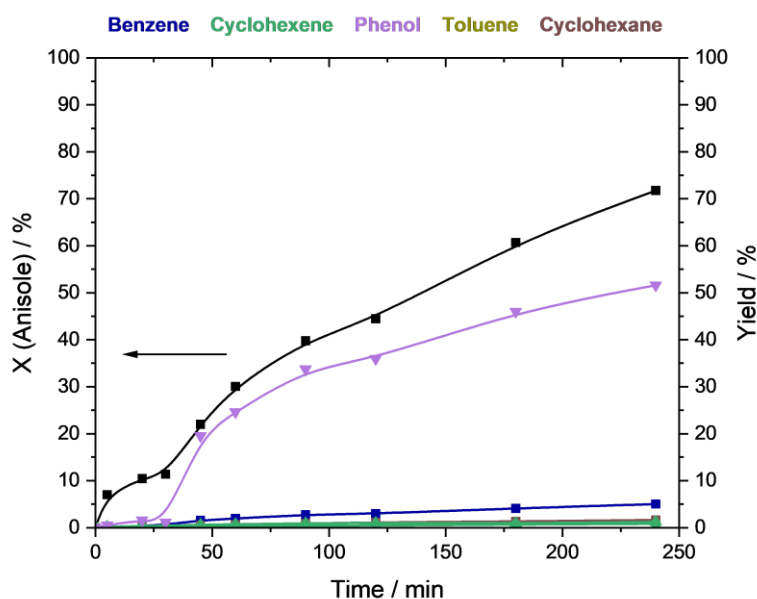


Figure 15: Conversion and yields for the anisole HDO with MoO_3 in a 300 ml batch reactor, at 350 °C, 50 bar H_2 pressure, 770 rpm agitator speed and 44.4 mmol anisole dissolved in 128 ml *n*-dodecane with 400 mg catalyst.

If the sum of all yields does not correspond to the conversion, the carbon balance is not equilibrated and products are probably not analyzed. This difference is observed for MoO_3 (see Figure 15). For Ni(1)MoO_3 it is even more pronounced, besides a changed main product (see A-15). Apart from benzene and phenol, the generation of cyclohexane and minor amounts of cyclohexene ($\leq 3\%$) are observed (see A-15). After 240 min reaction, the main product was phenol with a yield of 28 %, followed by cyclohexane with 22 % yield and benzene with 8 % yield. These changes were even more pronounced for Ni(5)MoO_3 . Immediately after 5 min reaction, cyclohexane was found and became the main product, followed by phenol and benzene (see Figure 16).

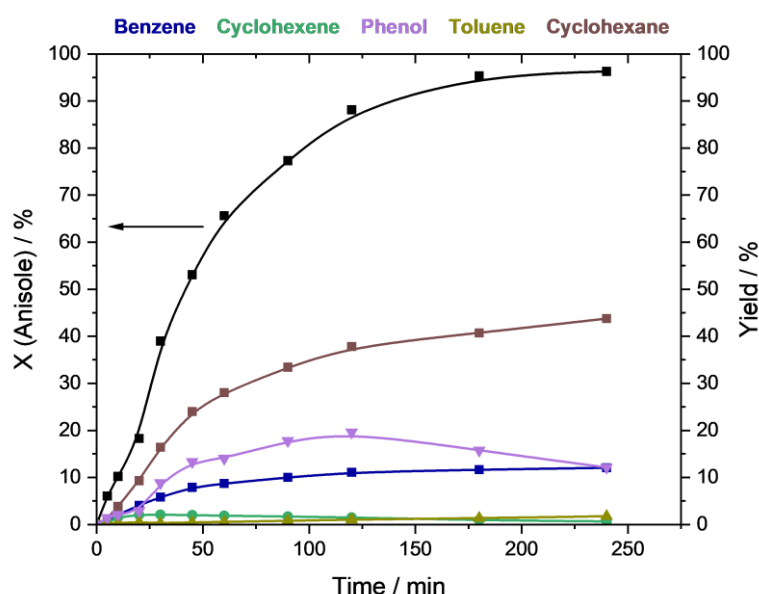


Figure 16: Conversion and yields for the anisole HDO with Ni(5)MoO_3 in a 300 ml batch reactor, at 350 °C, 50 bar H_2 pressure, 770 rpm agitator speed and 44.4 mmol anisole dissolved in 128 ml *n*-dodecane with 400 mg catalyst.

After 120 min the phenol yield reached a maximum at about 20 % and decreased afterwards, while the yield of cyclohexane and benzene increased further. When the reaction was finished after 240 min, ca. 43 % cyclohexane, 12 % benzene and 12 % phenol yield were obtained. With NiMoO_4 as catalyst, the main product was also cyclohexane, with a high formation rate until 45 min (see Figure 17). Afterwards, the yield increased linearly until a value of 66 % was reached after 240 min reaction. Benzene was formed as well and increased during 45 min reaction time up to ca. 26 % yield and decreased afterwards to approx. 14 % after 240 min. Within the first 60 min only negligible amounts of phenol ($\leq 2\%$) have been formed and disappeared with increasing time, while small amounts of toluene started to form but only to a very small extent. As already observed for MoO_3 , Ni(1)MoO_3 and Ni(5)MoO_3 , a certain amount of products are missing and the sum of yields is not matching the conversion.

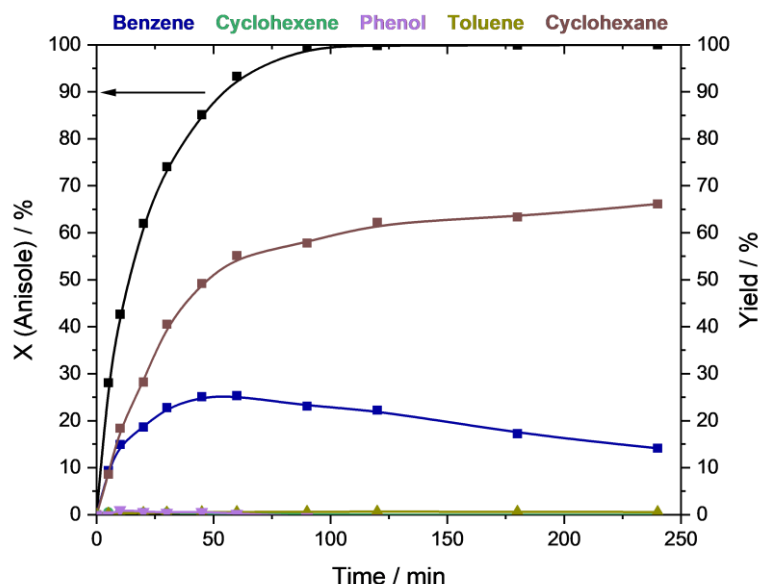


Figure 17: Conversion and yields for the anisole HDO with NiMoO_4 in a 300 ml batch reactor, at 350 °C, 50 bar H_2 pressure, 770 rpm agitator speed and 44.4 mmol anisole dissolved in 128 ml *n*-dodecane with 400 mg catalyst.

The behavior, shown by nickel promoted catalysts, was reflected only partly by CoMoO_4 (see A-16). The main product with a yield of 24 % was phenol. With 8 %, 4 % and 3 % for cyclohexane, benzene, and cyclohexene, respectively, less hydrogenated products have been formed. But products are missing here as well.

Liquid-Phase Phenol HDO

The liquid-phase HDO with phenol showed a similar behavior, but suffered from poor data quality. While NiMoO_4 had a fast conversion with an initial rate of $37.8 \cdot 10^{-5} \text{ mol} \cdot \text{g}^{-1}_{\text{cat}} \cdot \text{s}^{-1}$ and reached 100 % conversion after ca. 20 min, the reaction was significantly slower for Ni(5)MoO_3 (see Table 6 and A-17). An initial rate of $5.87 \cdot 10^{-5} \text{ mol} \cdot \text{g}^{-1}_{\text{cat}} \cdot \text{s}^{-1}$ and after 240 min only 78 % conversion was reached with Ni(5)MoO_3 . For Ni(1)MoO_3 and MoO_3 initial rates of $7.60 \cdot 10^{-5} \text{ mol} \cdot \text{g}^{-1}_{\text{cat}} \cdot \text{s}^{-1}$ and $5.18 \cdot 10^{-5} \text{ mol} \cdot \text{g}^{-1}_{\text{cat}} \cdot \text{s}^{-1}$ were determined, respectively. After 240 min reaction MoO_3 reached 50 % conversion, while Ni(1)MoO_3 reached about 38 %. However, the measurements error is comparatively large at low conversions. During reaction at 350 °C the phenol is dissolved in *n*-dodecane, but when the temperature was lower than 25 °C, parts of the phenol were able to crystallize and falsify the ex-situ GC measurements. Although the GC vials were heated before injection at approx. 50 °C and the crystallization was not visible, fluctuations of conversion by this effect at an early reaction stage cannot be excluded. The fact that the initial rates for the phenol HDO were higher, but lower conversions are obtained, could be explained by the crystallization of the phenol inside the GC vials. This would reduce the dissolved phenol content and thus suggest an increased conversion at an early stage. With increasing conversion, less phenol can crystallize and the error becomes smaller.

Interestingly, for NiMoO₄ the conversion and initial rate are higher in comparison to the anisole test, while they are much lower for all other catalysts (compare Table 6, A-17 and Figure 14). This could indicate that different active phases participate in the reaction. As mentioned before, in literature it is discussed that a MoO_xC_yH_z species is the active for gas-phase reactions (see chapter 2.4). However, the nickel content in NiMoO₄ could be also active for this reaction after it is reduced to Ni⁰. Transition metals (Ru, Pt, Rh) are known to be active in the liquid-phase HDO of phenol at temperatures of 200 – 300 °C (see chapter 2.2.1) and it can be expected that metallic nickel is active for this reaction as well. In addition is the phenolic C-O bond energy higher in comparison to the O-CH₃ group from anisole (see chapter 2.2.2). This might be too high for the reaction on a MoO_x surface and thus reduces the reaction rate for the phenol HDO. Are large amounts of Ni⁰ present, this reaction rate might be unaffected because of the H₂ activating effect of Ni or Ni is a direct active center. Because the HDO of phenol is conducted in a single step, the reaction becomes faster compared to the anisole HDO for NiMoO₄, but slower for the other catalysts.

Even if the conversion of phenol is not determined precisely, it can be assumed that the products are dissolved quantitatively and are reliable. This is also reflected by the product formation, which shows no unexpected fluctuations (see A-18 - A-21). Therefore, a brief discussion of the liquid-phase phenol HDO is done here.

The majority of formed products by MoO₃ is benzene with a yield of 19 % after 240 min (see A-18). Furthermore, only small amounts (≤2 %) of cyclohexane, cyclohexene and toluene are observed. Like in experiments with anisole, the nickel modified catalysts formed significant amounts of cyclohexane. Ni(1)MoO₃ forms benzene with 7 % yield but suffered from low conversion (see A-19). Ni(5)MoO₃ had a cyclohexane yield of 23 % at 80 % conversion after 240 min, while the benzene yield was at 9 %. Additionally, cyclohexene was formed as intermediate, which reached its maximum after 60 min with 5 % yield (see A-20). For NiMoO₄ only cyclohexane and no other products were present after reaction. Interestingly, the benzene yield passed a maximum (15 %) after ca. 20 min and decreased with time until it disappeared after approx. 180 min (see A-21). While the benzene yield decreased, the cyclohexane yield increased to 65 % after 180 min and decreased to 60 % after 240 min. This shows not only that benzene is hydrogenated to cyclohexane after the HDO, but also that cyclohexane must be decomposed, since no other products have been observed.

This supports the assumption that in the liquid-phase the Ni is influencing the activity and selectivity significantly, since for MoO₃ a low conversion was found with a high arene selectivity and only negligible amounts of cyclohexane. Further, these observations indicate that the missing products might be decomposition products. This decomposition, which formed methane, was already observed for NiMoO₄ in gas-phase experiments (see

chapter 4.1.1). This CH₄ would not have been detected for the liquid-phase experiments, since there only liquid samples were analyzed.

To explain the incomplete carbon balance, the phenol HDO has been repeated with MoO₃ and Ni(5)MoO₃. This time, the gas-phase in the autoclave was qualitatively analyzed for methane. This was done by taking samples with a balloon at different times (120 min and 180 min), which are subsequently injected into a mass spectrometer (MS) gas analyzer. Phenol was used for these experiments, because methane can be obtained only by decomposition as no methoxy groups are present. However, it can be assumed this effect occurs also for anisole and guaiacol.

For MoO₃, as well as for Ni(5)MoO₃ CH₄ was found for all samples at three different times (see A-22 and A-23). Unfortunately, a quantification of the methane content to compare catalysts is not possible with this method. Nevertheless, it shows that methane is formed also in the liquid-phase reaction and this might be the missing product.

Liquid-Phase Guaiacol HDO

For the HDO of guaiacol the result surprises, as the order of activity is inverted compared to the other substrates. The initial rate for MoO₃ was the highest with $26.9 \cdot 10^{-5} \text{ mol} \cdot \text{g}^{-1}_{\text{cat}} \cdot \text{s}^{-1}$, followed by Ni(5)MoO₃ and Ni(1)MoO₃ with $16.4 \cdot 10^{-5} \text{ mol} \cdot \text{g}^{-1}_{\text{cat}} \cdot \text{s}^{-1}$ and $15.2 \cdot 10^{-5} \text{ mol} \cdot \text{g}^{-1}_{\text{cat}} \cdot \text{s}^{-1}$, respectively (see Table 6). After ca. 120 min 100 % conversion was reached by Ni(1)MoO₃ and MoO₃, while Ni(5)MoO₃ reached it after 180 min (see Figure 18). MoO₃ reached ca. 90 % conversion after 45 min, but the reaction rate decreased fast afterwards, thus 100 % is reached after 120 min. NiMoO₄ had the lowest initial rate with $9.95 \cdot 10^{-5} \text{ mol} \cdot \text{g}^{-1}_{\text{cat}} \cdot \text{s}^{-1}$ and reached about 75 % conversion after 120 min and 100 % after 240 min. A temporary drop (MoO₃) or change (Ni(1)MoO₃ and Ni(5)MoO₃) of the reaction rate can be observed again (compare Figure 14 and Figure 18). However, because the reproducibility is again unknown, it is not discussed further.

Products which have been observed are high amounts of phenol and minor amounts of other products, primarily anisole (see A-24 - A-26). For MoO₃, Ni(1)MoO₃ and Ni(5)MoO₃ the phenol and anisole yield was at 70-80 % and < 5 %, respectively. For NiMoO₄ the phenol yield was at 60 %, while it was at ca. 8 % for anisole (see A-27). Cyclohexane was obtained in small amounts only for NiMoO₄ (≈ 10 % yield), besides minor amounts of benzene and cyclohexene (< 5 %).

In contrast experiments with anisole and phenol, the reaction rate decreases with increasing nickel content (see Table 6). In addition, a black reaction product was obtained by the experiment with MoO₃ (see A-28). This is unexpected but might be explained by the properties of the catalysts. As shown in chapter 4.2, the MoO₃ catalyst forms after reduction mainly Brønsted-acid sites, whereas NiMoO₄ is characterized by Lewis-acid sites.

The Brønsted sites could be responsible for a polymerization of guaiacol by acid-catalyzed ether formation. This would suggest a conversion of guaiacol by this side reaction and long chained aromatics, bridged by ether bonds, can be formed.²⁰⁰ Since phenol and anisole have only one functional group, polymerization via these functional groups is not possible.

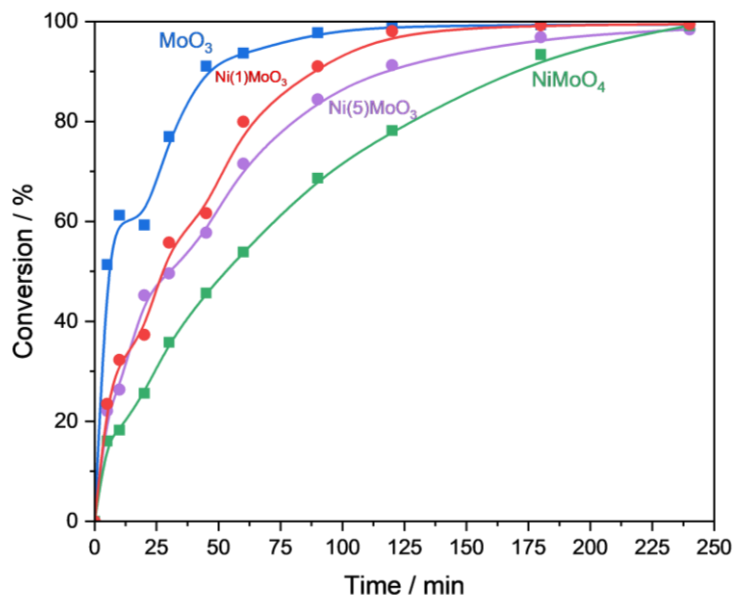


Figure 18: Conversion over time for the liquid-phase guaiacol HDO at in a 300 ml batch reactor, at 350 °C, 50 bar H₂ pressure, 770 rpm agitator speed and 44.4 mmol anisole dissolved in 128 ml *n*-dodecane with 400 mg catalyst.

Instead, they might just form diphenyl ether. Furthermore, polymeric products would not be observed in GC analysis as the boiling point is probably too high. Due to time reasons, CoMoO₄ was not tested with guaiacol.

Table 6: Initial rates for the catalysts for the different substrates at 350 °C and 50 bar H₂ pressure.

Catalyst	Initial rate (anisole) [mol/g _{cat} ·s]	Initial rate (phenol) [mol/g _{cat} ·s]	Initial rate (guaiacol) [mol/g _{cat} ·s]
MoO ₃	3.51·10 ⁻⁵	5.18·10 ⁻⁵	26.9·10 ⁻⁵
NiMoO ₄	23.2·10 ⁻⁵	37.8·10 ⁻⁵	9.95·10 ⁻⁵
Ni(5)MoO ₃	6.40·10 ⁻⁵	5.87·10 ⁻⁵	16.4·10 ⁻⁵
Ni(1)MoO ₃	5.87·10 ⁻⁵	7.60·10 ⁻⁵	15.2·10 ⁻⁵
CoMoO ₄	3.38·10 ⁻⁵	0.69·10 ⁻⁵	-

4.2. Catalyst Characterization

4.2.1. Characterization of Fresh Catalysts

The catalysts have been characterized by XRD, Raman, BET and SEM before. All relevant diffractograms are shown in Figure 19. It can be seen that for MoO_3 , NiMoO_4 and CoMoO_4 the pure phases were synthesized and no secondary phases are present. For nickel added catalysts a two-phase system is obtained, which contains NiMoO_4 and MoO_3 . This can be concluded from the reflections visible at $Q \approx 11 \text{ nm}^{-1}$ and 21 nm^{-1} for Ni(5)MoO_3 , Ni(3)MoO_3 and Ni(1)MoO_3 . The low Ni content in Ni(1)MoO_3 led to NiMoO_4 reflections of low intensity. For an improved visibility, its diffractogram is shown in more detail in A-29. The diffractograms indicate that the nickel forms a secondary NiMoO_4 phase and was not introduced into the MoO_3 lattice as dopant. However, doping in small amounts cannot be excluded.^{33, 168-170} The same is true for the cobalt containing system Co(5)MoO_3 .

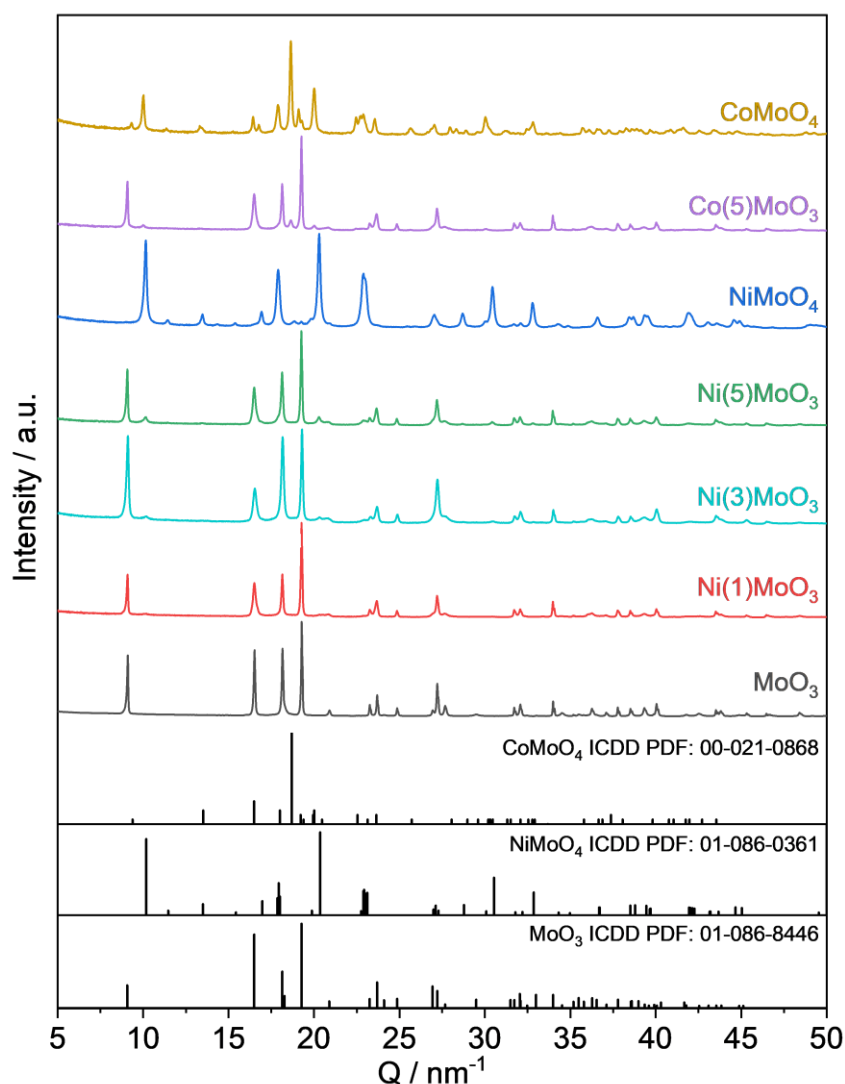


Figure 19: Normalized PXRD patterns of the fresh samples calcined at 450 °C for 4 h. Reproduced from Ref.¹⁹⁷ with permission from Royal Society of Chemistry.

Characterization by Raman Spectroscopy

These results are proved by Raman spectroscopy (see Figure 20). At 818 cm^{-1} and 993 cm^{-1} absorption bands of MoO_3 are visible.²⁰¹ For NiMoO_4 an intense absorption band at 961 cm^{-1} can be observed, which is characteristic for NiMoO_4 . It belongs to the terminal $\text{M}=\text{O}$ group and its symmetric stretching mode.²⁰²

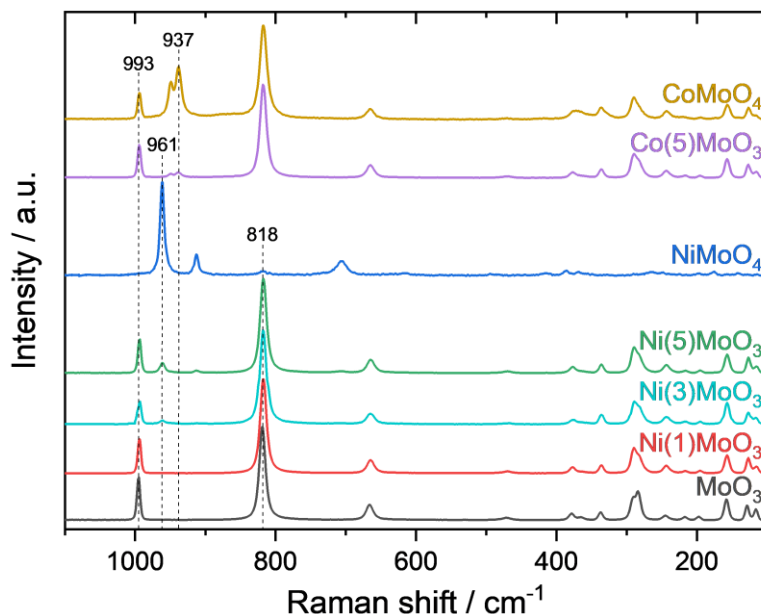


Figure 20: Raman spectra of the fresh samples calcined at $450\text{ }^\circ\text{C}$ for 4 h measured with $\lambda = 633\text{ nm}$ and a laser power of 0.085 mW . Reproduced from Ref.¹⁹⁷ with permission from Royal Society of Chemistry.

As expected, absorption bands of MoO_3 and CoMoO_4 (937 cm^{-1}) are visible for Co(5)MoO_3 . However, the CoMoO_4 sample has an absorption band at 993 cm^{-1} , belonging to the MoO_3 phase. This indicates that two phases are present, even though it was not observed by XRD. The reason might be that Raman spectroscopy has a high sensitivity while the minimum detection limit in the XRD is around 5 wt.%. These results reveal that the phase pure synthesis was not successful for CoMoO_4 .

Even though CoMoO_4 was not obtained completely phase pure, it was used for the prove of principle. As the catalytic behavior of MoO_3 is known in literature and has been tested as well in the apparatus used for this work, an estimation of the resulting error and the real activity can be done. Additionally, the fact that the MoO_3 was not observed in the XRD suggests that its amount is rather low.

Scanning Electron Microscopy

SEM images, combined with EDX have been recorded of the fresh Ni(5)MoO_3 sample as a representative sample, to gain more insight into the morphology of the mixed phase catalysts (see Figure 21). It can be clearly seen that a binary structure is obtained. While

the EDX shows areas where no nickel is present, there are parts with high nickel contents (see Figure 21b). This indicates that MoO_3 is forming large planar planes with sharp edges, which have low surface areas. At the same time, nickel enriched areas of very small particles with a rough surface are present, which are located on the MoO_3 surfaces. These small particles belong to the NiMoO_4 phase, showing that the two phases are existing next to each other and the NiMoO_4 is not embedded.

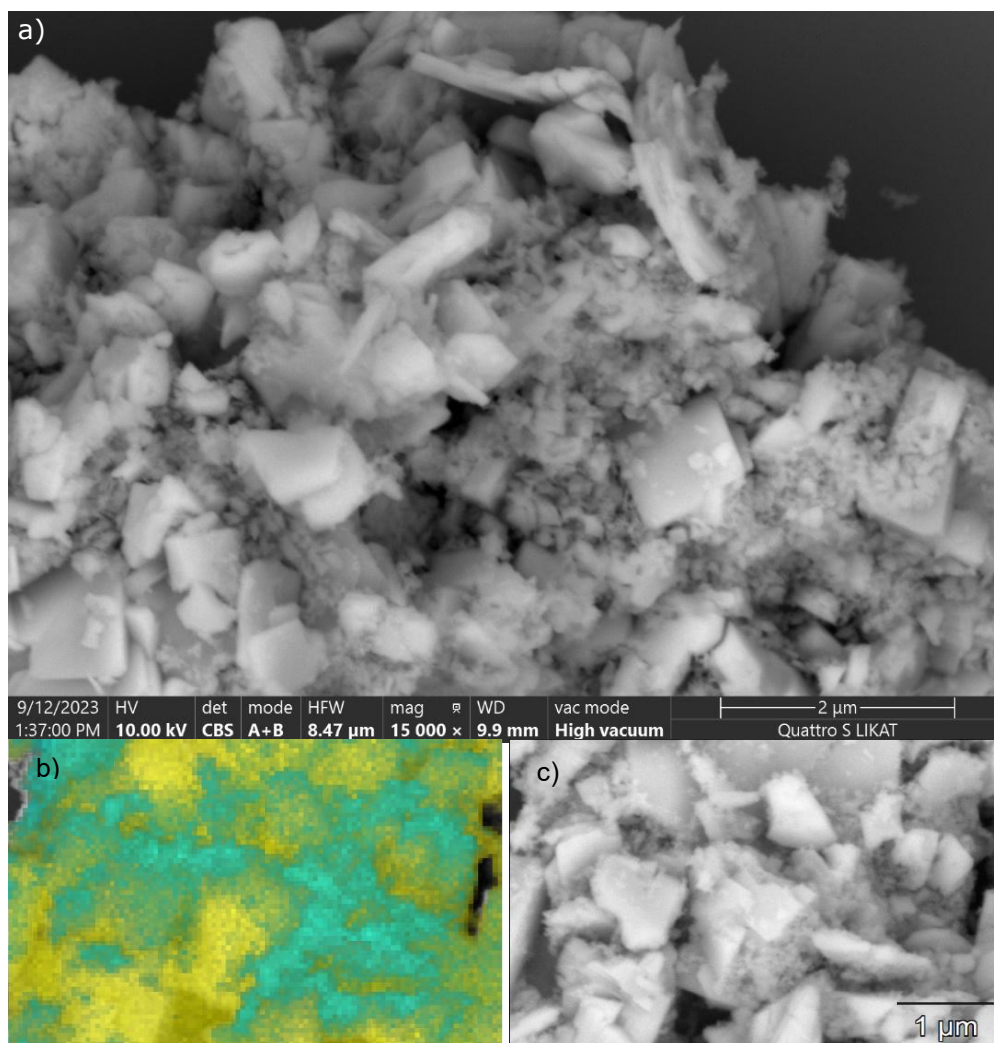


Figure 21: SEM overview images in BSE mode of fresh $\text{Ni}(5)\text{MoO}_3$ a) SEM image b) overlaid with the color image of the elemental distributions of Mo (yellow) and Ni (cyan) calculated from the EDX spectra from the area of c). The corresponding EDX spectra is shown in A-30. Reproduced from Ref.¹⁹⁷ with permission from Royal Society of Chemistry.

This result is also in agreement with N_2 -adsorption experiments. MoO_3 has a surface area of about $3 \text{ m}^2/\text{g}$, which increases for $\text{Ni}(5)\text{MoO}_3$ to $15 \text{ g}^2/\text{g}$. NiMoO_4 has a surface area of $40 \text{ m}^2/\text{g}$. This can be explained by morphology and particle size. Overall, after synthesis a bulk catalyst with low surface area is obtained, which consists of a binary phase system of small structured NiMoO_4 next to MoO_3 that is formed in large particles with planar surfaces.

Acid Site Analysis by NH₃-Adsorption

The acidic properties were investigated by NH₃-adsorption FTIR experiments. For this, the samples were pre-reduced in 100 % H₂ at 325 °C for 2 h as it is done for catalytic tests (see chapter 3.2). Afterwards, the sample was cooled down to room temperature, 5 % NH₃ in He were adsorbed by pulses until saturation and subsequently the samples were heated up to 350 °C in 50 °C steps at which a spectrum was measured.

It can be observed that the acidic sites of MoO₃ and NiMoO₄ are different in nature (see A-32 and A-34). A strong vibrational absorption band at 1425 cm⁻¹ ($\nu(\text{NH}_4^+)$) is visible for MoO₃, which belongs to Brønsted-acid (BA) sites.^{189, 203} NiMoO₄ shows also BA sites with an absorption band at 1425 cm⁻¹ but of much lower intensity. Additionally, vibrational bands of Lewis-acid sites (LA) are observed at 3350 cm⁻¹ and 3270 cm⁻¹ ($\nu(\text{NH}_3)$). They can be observed until a temperature of 300 °C is reached. Compared to this, these LA sites were not detected for MoO₃. LA sites might be a key component of an active catalyst as they are acting as adsorption sites for oxygenates, while BA sites are important for hydrogenolysis. Further it is discussed in literature, that LA sites could have a positive influence on the MoO_xC_yH_z formation and thus for the HDO itself.⁴¹

4.2.2. Spent Catalyst Analysis by XRD

The diffractograms of spent catalysts after gas-phase HDO with anisole at 325 °C are shown in Figure 22. Reflections at 10.1 nm⁻¹, 22.9 nm⁻¹, 31.5 nm⁻¹ and 43.7 nm⁻¹ can be assigned to the MoO_xC_yH_z phase and are visible for all catalysts except NiMoO₄.^{32, 44, 161-163} MoO₂ was present in all samples, except NiMoO₄, with main reflections at 18 nm⁻¹, 25.7 nm⁻¹ and 37 nm⁻¹. The reflections of NiMoO₄ and MoO_xC_yH_z might overlap for the samples Ni(1)MoO₃ to Ni(5)MoO₃ but the low amount of nickel cannot explain these intense reflections and the existence is indicated by the observed reflections for the nickel free sample MoO₃ (see Figure 22). However, MoO_xC_yH_z is characterized by a low crystallinity and in combination with the high detection limit of the PXRD (≥ 5 wt.%) hard to detect.^{32, 161, 163} Hence, the existence of minor MoO_xC_yH_z amounts for NiMoO₄ cannot be fully excluded, even though it is not indicated directly by its reflections.

The formation of MoO₂ and MoO_xC_yH_z can be expected for all catalysts as their occurrence is reported in literature during the HDO with MoO₃.^{25, 32} Also for NiMoO₄ the reduction to MoO₂ and Ni can be expected.^{160, 202} Therefore, it is unclear why NiMoO₄ is fully oxidized after 17 h under reductive reaction conditions. Since XRD is a bulk method, an incomplete reduction of the NiMoO₃ bulk due to the large particle size could explain these results.

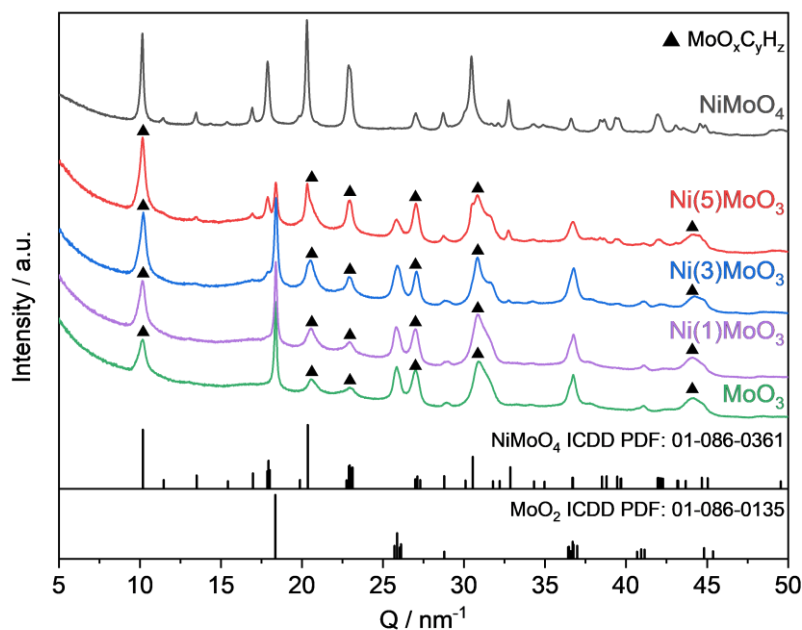


Figure 22: Normalized XRD patterns of spent catalysts after pre-reduction in 100 % H₂ for 2 h and gas-phase HDO reaction with anisole for 17 h at 325 °C. Reproduced from Ref.¹⁹⁷ with permission from the Royal Society of Chemistry.

Further, the exposure to air could be responsible for a reoxidation. The reactor was taken out at higher temperatures (up to 175 °C) to save time. This could initiate a fast reoxidation of nickel species and thus a reformation of NiMoO₄. Another reason is reoxidation by the oxygen containing anisole, which could prevent the catalyst from reduction. While the pre-reduction was done in 100 % H₂, only 30 vol.% H₂ were used during reaction, making the atmosphere less reducing, which could increase the influence of the oxygenate. During the cool down of the reactor, while the catalyst is flushed by N₂, remaining substrate could result in an oxidizing atmosphere.

Spent Catalysts of Liquid-Phase Anisole HDO

Catalysts, which were used in the liquid-phase HDO of anisole are reduced to MoO₂ in the majority shown by intense reflections at 18 nm⁻¹, 25.7 nm⁻¹ and 37 nm⁻¹ (see Figure 23). MoO_xC_yH_z can be observed for all catalysts with reflections at ca. 10.1 nm⁻¹, 20.5 nm⁻¹, 22.9 nm⁻¹, 26.7 nm⁻¹, 31.5 nm⁻¹ and 43.7 nm⁻¹. Only NiMoO₄ seems to be not reduced during reaction or was restored upon reoxidation while exposed to air. This is also indicated by the reflections at 17.9 nm⁻¹ and 20.3 nm⁻¹ of Ni(5)MoO₃, which belong to the NiMoO₄ phase and can be observed for the fresh catalyst as well (see Figure 19). A reoxidation seems to occur in both, liquid- and gas-phase reactions favored by an increased nickel amount as Ni⁰ is highly oxyphilic and tends to reoxidize fast. For NiMoO₄, MoO₂ was not detected but surprisingly some reflections of low intensity point to the presence of the MoO_xC_yH_z phase. The spent catalysts of the liquid-phase HDO using anisole show almost identical results compared to the gas-phase experiments.

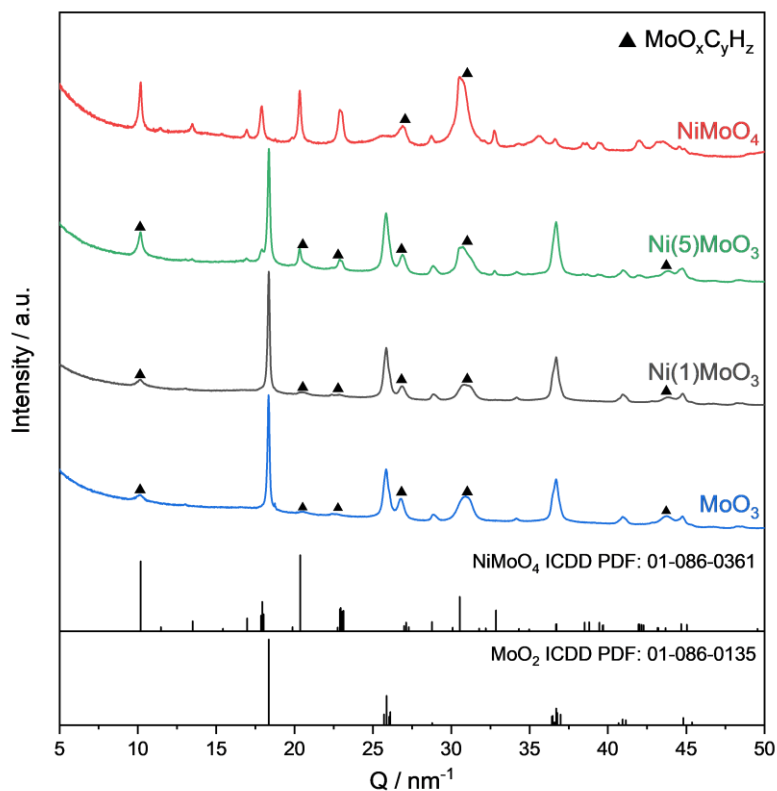


Figure 23: Normalized XRD patterns of spent catalysts after liquid-phase HDO at 350 °C at 50 bar H₂ after 4 h reaction with 44.4 mmol anisole dissolved in 128 ml *n*-dodecane, 400 mg catalyst.

Spent Catalysts of Liquid-Phase Guaiacol HDO

Is guaiacol used as substrate, it can be observed that NiMoO₄ is completely reoxidized after reaction and no reflections of MoO₂ or MoO_xC_yH_z are visible (see A-36). For MoO₃, Ni(1)MoO₃ and Ni(5)MoO₃ the reflections of MoO₂ and MoO_xC_yH_z are visible as for the anisole HDO (compare Figure 23 and A-36). Additionally, a broad reflection at ca. 16.5 nm⁻¹ was detected for these three catalysts. A definite, precise identification by references is not possible for it. Nevertheless, this reflection is typical for coke depositions and organic polymers. Since a black residue was formed during the guaiacol HDO, which could consist of coke or a carbonous polymer generated by acidic sites (see chapter 3.3), it is likely that these depositions are responsible for this reflection.^{204, 205}

Spent Catalysts of Liquid-Phase Phenol HDO

In contrast to guaiacol, no residue was obtained in the HDO of phenol and no reflections of carbonaceous deposits are visible for these samples (see A-37). The patterns do not differ from those of the anisole HDO, resulting in reflections for MoO₂ and MoO_xC_yH_z for MoO₃, Ni(1)MoO₃ and Ni(5)MoO₃. Again, NiMoO₄ is reoxidized but a reflection at ca. 31 nm⁻¹ which might belong to the oxycarbohydride is observable. CoMoO₄ was also tested for the phenol HDO exemplary but was not completely reduced and a Co₂Mo₃O₈ phase has been formed. MoO_xC_yH_z reflections were not observed.

In summary, no major differences were observed in the structure of the spent catalysts after gas- and liquid-phase HDO. The oxycarbohydride was present in all samples except in NiMoO₄. The catalysts have been partly reduced to MoO₂ and a MoO_xC_yH_z phase was formed, except for NiMoO₄. This phase formation could explain the change of reaction rates for the liquid-phase HDO (see chapter 4.1.2), as it is also observed for the gas-phase HDO (see chapter 4.1.1). Small reflections which might belong to MoO_xC_yH_z could indicate an oxycarbohydride is formation for NiMoO₄ in the liquid-phase HDO with anisole and phenol. However, a clear identification was not possible.

4.2.3. Spent Catalyst Analysis by XPS

XPS Analysis of Spent Gas-Phase Anisole HDO Catalysts

XP spectra were measured to analyze the surface oxidation states, since Mo⁵⁺ is discussed to be important for the reaction (see chapter 2.4). Because of limited capacities only MoO₃, Ni(5)MoO₃ and NiMoO₄ were selected as representative samples. For the fitting of the Mo 3d region, a model with three components (Mo⁶⁺, Mo⁵⁺ and Mo⁴⁺) from Murugappan et al. has been used.¹⁶⁴ From the Mo 3d_{1/2} and Mo 3d_{5/2} doublet signal at E ≈ 232.6 eV and 235.9 eV can be concluded that the surfaces of all catalysts expose 100 % Mo⁶⁺ after synthesis (see Figure 24). MoO₃ is the only sample for which approx. 2 % of Mo⁵⁺ are found with a doublet at E ≈ 231.3 eV and 234.4 eV.

The spent catalysts after gas-phase reaction are significantly changed in oxidation states. After 17 h TOS the MoO₃ catalyst contains 57 % Mo⁴⁺ (two doublets, E ≈ 229.9 eV and 233.2 eV, and E ≈ 231.15 eV and 234.5 eV), 10 % Mo⁵⁺ and 33 % Mo⁶⁺ at the surface. Compared to this, on Ni(5)MoO₃ 20 %, 26 % and 54 % of Mo⁴⁺, Mo⁵⁺ and Mo⁶⁺ were formed during reaction, respectively. Surprisingly, the surface of NiMoO₄ was just slightly reduced and 4 % Mo⁴⁺, 11 % Mo⁵⁺ and 85 % Mo⁶⁺ were detected. As already mentioned before (see chapter 2.4), an increased amount of Mo⁵⁺ is of special interest because it is assumed to be part of the catalytically active phase. This partially agrees with the catalytic results, according to which the Mo⁵⁺ fraction for Ni(5)MoO₃ is increased compared to MoO₃ thus represents a catalyst of enhanced activity (see Figure 13). It is also consistent with the literature, where more Mo⁵⁺ was found for Co and Ni modified catalysts.^{41, 42, 174} For NiMoO₄ it surprises that only small amounts of Mo⁶⁺ have been reduced, as NiMoO₄ is reduced easier compared to MoO₃ and is the most active catalyst.²⁰⁶ But this result is in agreement with the PXRD analysis of the spent sample showing NiMoO₄ as major phase (see Figure 22). Additionally, Ni²⁺ was found exclusively for Ni(5)MoO₃ and NiMoO₄ (4 % Ni⁰ for NiMoO₄) showing the fast reoxidation of Ni even though reduced Mo is present (see A-38 and A-39). Thus, reoxidation effects which are not considered here probably can

explain these observations and the Mo^{5+} content for NiMoO_4 could be higher under reaction conditions.

An attempt was made to gain more information about the $\text{MoO}_x\text{C}_y\text{H}_z$ by analyzing the C signal. Unfortunately, it was not possible to gain useful and reliable information since contamination of the surface by other carbonous species could not be excluded after handling the samples on air. For this reason, it is not discussed here.

Supporting Pseudo In-Situ XPS Experiment

However, further experiments are needed to understand these results and pseudo in-situ XPS measurements were carried out for this. Therefore, the samples were treated for 2 h at 325 °C in 100 % H_2 at 1 bar pressure. This resembles the catalysts surface oxidation state at the initial point of reaction at TOS = 0 min. This time, a significantly higher degree of reduction could be observed compared to spent catalysts (see A-40 - A-42), with 94 % Mo^{4+} for NiMoO_4 . For MoO_3 , still 70 % Mo^{4+} and 16 % Mo^{5+} have been found. This was also reflected by the Ni 2p spectra, showing only signals for Ni^0 . Here the degree of reduction increased with the nickel content, suggesting a correlation between its content and an improved reduction behavior (see A-43 and A-44).

XPS Analysis of Spent Liquid-Phase Anisole HDO Catalysts

The spent samples after liquid-phase HDO with anisole were analyzed as well and indicate a similar reduction behavior. For MoO_3 52 % Mo^{4+} , 25 % Mo^{5+} and 22 % Mo^{6+} have been found (see A-45). Compared to the gas-phase reaction at 325 °C, more Mo^{6+} was reduced and Mo^{5+} was formed. For $\text{Ni}(1)\text{MoO}_3$, the amount of Mo^{4+} (43 %) and Mo^{5+} (19 %) decreased, while the amount of Mo^{6+} (38 %) increased (see A-46). For $\text{Ni}(5)\text{MoO}_3$, 45 % Mo^{6+} , 25 % Mo^{5+} and 30 % Mo^{4+} were determined (see A-48). With 64 % Mo^{6+} , 26 % Mo^{5+} and 10 % Mo^{4+} , NiMoO_4 is also more reduced compared to the gas-phase samples at 325 °C (see A-50). For all Ni containing catalysts, the nickel was oxidized to Ni^{2+} presumably because the samples were exposed to air (see A-47, A-49 and A-51). Considering the increased temperature and H_2 pressure it does not surprise that the catalysts are reduced more deeply in comparison to gas-phase experiments (see Figure 24). However, it is not clear to what extent the oxidation state changes after the reaction due to reoxidation in air.

XPS Analysis of Spent Liquid-Phase Guaiacol HDO Catalysts

Catalysts used for the liquid-phase HDO of guaiacol were in a comparable oxidation state as observed for the liquid-phase anisole HDO. For MoO_3 49 %, 26 % and 25 % have been found for Mo^{4+} , Mo^{5+} and Mo^{6+} , respectively (see A-52). Ni(5)MoO_3 was slightly more reduced with 37 % Mo^{4+} , 20 % Mo^{5+} and 43 % Mo^{6+} , while the Ni was fully oxidized (100 % Ni^{2+} , see A-53 and A-54). NiMoO_4 was almost completely oxidized with 14 % Mo^{5+} , 86 % Mo^{6+} and 100 % Ni^{2+} (see A-55 and A-56).

XPS Analysis of Spent Liquid-Phase Phenol HDO Catalysts

For catalysts which were used for the liquid-phase phenol HDO are more deeply reduced compared to the liquid-phase anisole HDO, except MoO_3 which was with 38 % Mo^{4+} , 21 % Mo^{5+} and 41 % Mo^{6+} in a higher oxidation state (compare A-57 and A-45). Surprisingly, the Mo of NiMoO_4 was with 30 % Mo^{4+} , 26 % Mo^{5+} and 44 % Mo^{6+} in a lower oxidation state (compare A-50 and A-60), while 96 % of the nickel are present as Ni^{2+} (see A-61). This is in contrast to the XRD results, showing a NiMoO_4 phase with one small reflection which might indicate a $\text{MoO}_x\text{C}_y\text{H}_z$ phase (see A-37). An explanation for these different results could be the fact that XPS is a surface method, while the bulk is analyzed by XRD. A trend or fundamental oxidation state changes for the liquid-phase HDO with different substrates was not found.

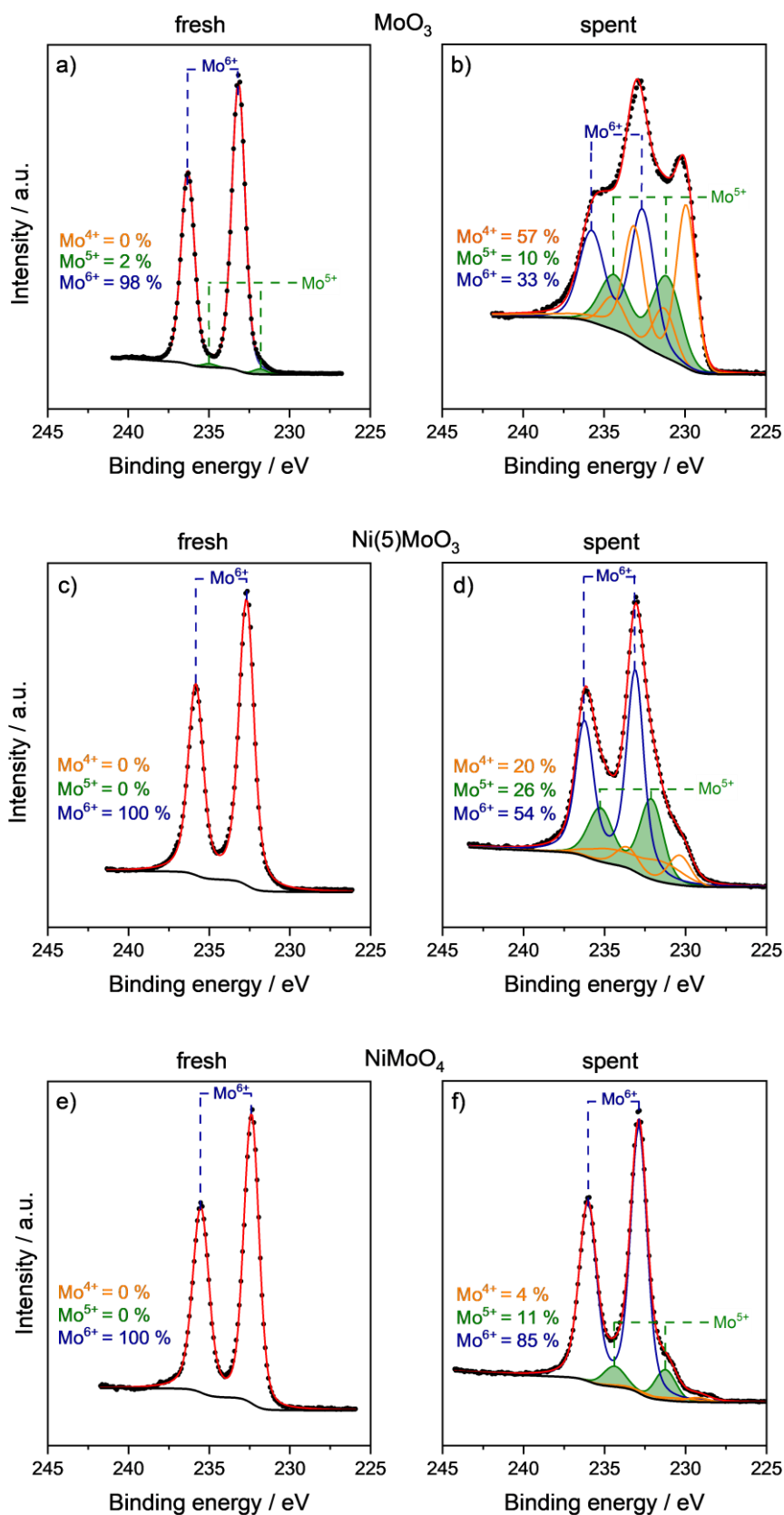


Figure 24: Mo_{3d} XP spectra of fresh and used catalysts after TOS = 17 h in the presence of anisole in the gas-phase at 325 °C. The catalysts were pre-reduced in 100 % H₂ for 2 h before reaction. a) fresh MoO₃; b) spent MoO₃; c) fresh Ni(5)MoO₃; d) spent Ni(5)MoO₃; e) fresh NiMoO₄; f) spent NiMoO₄. Reproduced from Ref.¹⁹⁷ with permission from the Royal Society of Chemistry.

4.2.4. Oxidation of Spent Catalysts monitored by TG-MS

TPO of Spent Gas-Phase Anisole HDO Catalysts

Temperature programmed oxidation (TPO) measurements in synthetic air were conducted with a TG-MS to analyze deposited coke and to prove the existence/absence of the $\text{MoO}_x\text{C}_y\text{H}_z$ phase. The decomposition of coke was tracked by the CO_2 formation ($M/Z = 44$), while the decomposition of $\text{MoO}_x\text{C}_y\text{H}_z$ is indicated by the formation of water ($M/Z = 18$) and CO_2 as the same time.^{161, 162} For MoO_3 used in the gas-phase HDO at 325 °C the CO_2 formation started at a temperature of 350 °C, with a small, sharp peak at ca. 380 °C and the evolution of additional minor amounts of CO_2 until 400 °C (see Figure 25). Also at 380 °C, a rapid evolution of H_2O starts with a maximum at 390 °C which decreased until 430 °C. The H_2O formation could also be observed for $\text{Ni}(1)\text{MoO}_3$, $\text{Ni}(3)\text{MoO}_3$ and $\text{Ni}(5)\text{MoO}_3$, even though it was less pronounced (see A-62 and Figure 25). This confirms the existence of $\text{MoO}_x\text{C}_y\text{H}_z$ and is in agreement with the XRD results (see Figure 22). For NiMoO_4 only the desorption of physisorbed water can be observed at low temperatures (50-280 °C) confirming the absence of the oxycarbohydride phase.

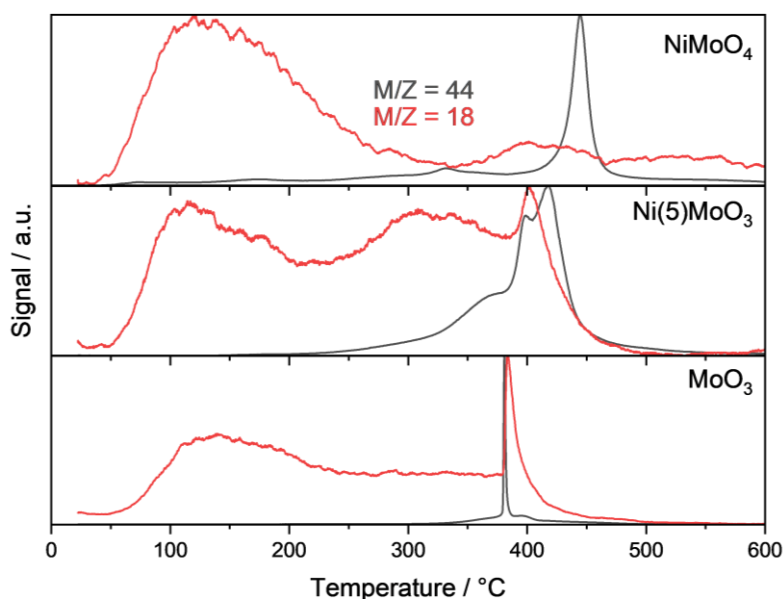


Figure 25: Normalized TG-MS profiles of spent catalysts after anisole HDO at 325 °C for 17 h treated in syn. air, 10 °C/min. Reproduced from Ref.¹⁹⁷ with permission from the Royal Society of Chemistry.

However, in the case of the NiMoO_4 sample a CO_2 peak has been observed at about 435 °C. This temperature is significantly higher compared to $\text{Ni}(5)\text{MoO}_3$ and MoO_3 . It points to the decomposition of graphitic coke while for MoO_3 the CO_2 evolution started at temperatures below 400 °C, suggesting a soft coke decomposition, followed by the decomposition of

MoO_xC_yH_z at 400 °C indicating two different carbon species.²⁵ Since three peaks were observed for Ni(5)MoO₃, one below 400 °C, at 400 °C and above 400 °C, three carbon species, soft coke, MoO_xC_yH_z and graphitic coke are likely present.

TPO of Spent Liquid-Phase Anisole HDO Catalysts

For the liquid-phase HDO it is noteworthy, that not all spent catalysts that exhibit reflections of MoO_xC_yH_z, liberated H₂O in the TG-MS analysis. In case of catalysts tested in the anisole HDO, the formation of H₂O and CO₂ was observed only for MoO₃ at approx. 380 °C. An additional shoulder for CO₂ formation could be identified at 350 °C (see A-63). Ni(5)MoO₃ exhibits two peaks of CO₂ formation at 400 °C and 430 °C with a reduced intensity compared to MoO₃, indicating a shift to higher temperatures since it originated from graphitic coke. The formation of H₂O is not observable after physisorbed H₂O desorbed at low temperatures (T < 200 °C). Interestingly, the formation of CO₂ occurred twice for NiMoO₄, at about 325 °C and 450 °C with a lower intensity compared to MoO₃ and Ni(5)MoO₃.

TPO of Spent Liquid-Phase Phenol HDO Catalysts

MoO₃ and NiMoO₄ used for the phenol HDO show similar results with two separated peaks of CO₂ formation observed at 350 °C and 400 °C for MoO₃ (see A-64). For NiMoO₄ they occurred at 340 °C and 440 °C. Interestingly, four peaks for CO₂ at approximately 380 °C, 410 °C, 430 °C, and 460 °C have been observed for Ni(5)MoO₃. These peaks might originate from different carbon species, since carbides (275 - 355 °C), soft coke and MoO_xC_yH_z (355 - 455 °C) and graphitic coke (455 - 555 °C) can be expected.^{25, 162} A single peak of low intensity for H₂O indicates at 400 °C the MoO_xC_yH_z decomposition for MoO₃ and Ni(5)MoO₃, but was not observed for NiMoO₄. These results are inconsistent with the results of XRD analysis (see A-37), which revealed prominent reflections of MoO_xC_yH_z for Ni(5)MoO₃ and MoO₃. Hence, a more intense H₂O formation would be expected for these samples. One potential explanation is the length of time the sample was stored before conducting the TG-MS analysis, as previous reports have indicated that the sample is not stable, if exposed to air.^{161, 207} Although no immediate decomposition was observed following exposure to air, prolonged storage might result in a degradation of this phase.

TPO of Spent Liquid-Phase Guaiacol HDO Catalysts

Differences between XRD results and TPO were not observed in the case of catalysts employed for the guaiacol HDO. Here, the formation of CO₂ was markedly pronounced and persisted over a considerable temperature range (250 – 500 °C, A-65). Furthermore, the formation of water can be observed across the entire range, with a pronounced peak at ca. 270 °C (250 °C for NiMoO₄). Furthermore, a decline in intensity is evident when moving from MoO₃ to NiMoO₄. These findings are consistent with the results of XRD measurements, which indicate the polymerization of guaiacol, resulting in the formation of undefined carbonaceous deposits (see A-36). The formation of water might be explained here by the oxidation of these polymerization products, which might contain hydrogen as well.

4.2.5. TPR Analysis

TPR analyses have been done for MoO₃, Ni(5)MoO₃ and NiMoO₄ to understand the reduction behavior and set them into context of the spent catalysts analysis. The reduction of MoO₃ started at ca. 630 °C with a large maximum at 777 °C and a shoulder at 705 °C (see Figure 26). This reduction peak belongs to the reduction of MoO₃ to MoO₂. An explanation for the observed shoulder could be the formation of a molybdenum bronze (H_xMoO₃) or the formation of the intermediate Mo₄O₁₁ phase.^{160, 167, 208} However, Matsuda et al. showed that the H_xMoO₃ phase is decomposed as well during the H₂-TPR by the formation of additional water and the amount of consumed H₂ and formed H₂O during the TPR of MoO₃ is equal. This indicates that only the MoO₂ formation is responsible for the H₂O formation and thus the formation of the bronze seems to be improbable for MoO₃.²⁰⁸ After reaching 800 °C a third reduction process started until the experiment was stopped at 850 °C. This corresponds to the reduction of MoO₂ to metallic Mo⁰. For Ni(5)MoO₃ the reduction started significantly earlier at ca. 400 °C. The first maximum was reached at 619 °C with a shoulder of a second peak at 733 °C. Afterwards, at approx. 750 °C the reduction enhanced again and continued until the experiment was stopped. For this sample all reduction processes are shifted to lower temperatures compared to pure MoO₃. Noteworthy are smaller reduction processes between 400 °C and 620 °C, which could be related to a phase separation of NiMoO₄ resulting in particles of metallic nickel embedded in a MoO_x structure as shown by in-situ TEM experiments (see chapter 4.4). It is not clear whether NiMoO₄ is first thermally separated into NiO/MoO₃ and subsequently a fast reduction of the NiO to Ni⁰ takes place or if the reduction directly results in a formation of Ni/MoO_x. In literature it is claimed that intermediate phases might be formed (Ni₂Mo₃O₈, NiMoO₃ or NiMoO_x), but these have not been clearly identified.^{160, 202}

For pure phase NiMoO_4 the reduction starts even earlier at 300 °C with the first maximum at 563 °C, in the same temperature range as the first reduction for Ni(5)MoO_3 occurs. This reduction process may belong to the formation of reduced intermediate phases, or to a phase separation as already discussed for Ni(5)MoO_3 . Between 300 °C and 450 °C a shoulder in the TPR profile is visible indicating a preceding reductive decomposition process until the bulk starts to be reduced. Afterwards, at 650 °C a reduction process takes place which can be assigned to the formation of Mo^0 .¹⁶⁰ A hypothesis for the shift to lower reduction temperatures could be a formation of Ni^0 in the early stage of reduction, which explaining the shoulders in the TPR profiles of NiMoO_4 and Ni(5)MoO_3 and this Ni can activate hydrogen.

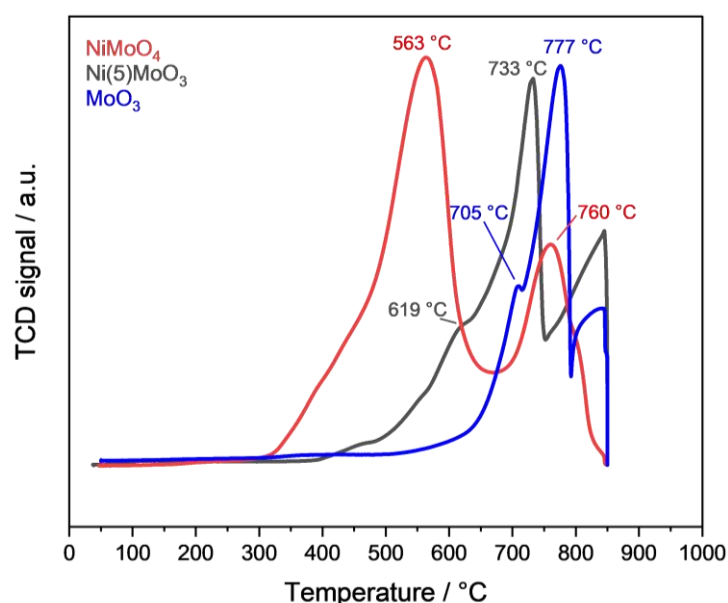


Figure 26: TPR of fresh catalysts with 5% H_2 in Ar and 10 °C/min; $m \approx 20$ mg. Reproduced from Ref.¹⁹⁷ with permission from the Royal Society of Chemistry.

The results of the TPR are in agreement with those of the pseudo in-situ XPS investigation (see chapter 4.2.3), suggesting an enhanced reduction behavior with increasing nickel content. The fact, that this is contrary to the result obtained by XRD of spent catalysts, which suggest that NiMoO_4 is not reduced after reaction (see Figure 22 and Figure 23), leads to the conclusion that a reoxidation must take place. However, it remains unclear whether the exposure to air is responsible for it or the reaction with the substrate, which might reoxidize the catalyst. It must be mentioned that the catalysts were taken out of the reactor at ca. 175 °C and nickel is known for its pyrophoric properties. This could force a fast oxidation, which could even more pronounced with increasing nickel amount. Since only 30 % H_2 is used during the reaction, a less reductive atmosphere than in the pseudo in-situ experiment must also be considered.

4.2.6. DRIFTS Adsorption Test and Operando DRIFTS DME HDO

DRIFTS Anisole Adsorption

The adsorption of anisole was tested by DRIFT spectroscopy to understand a possible influence on the substrate and an activation by adsorption. Therefore, the sample was heated to reaction temperature (325 °C) and afterwards switched to a H₂ atmosphere (100 %) to pre-reduce the sample for 2 h. Subsequently, it was changed to a He flow (25 ml/min) and anisole was injected (2.5 µl/min) by a syringe pump into an evaporator (230 °C) and transported by the He into the DRIFTS cell. After the intensity of the anisole absorption bands did not further increase, the injection was stopped, flushed by He for 10 min to remove gas-phase anisole and switched to H₂ (25 ml/min).

After 5 min TOS no significant changes of the band positions can be observed (see Figure 27). Clearly visible for each sample is the pronounced vibrational band at 1251 cm⁻¹ ν (Ph-O-CH₃) and the ν (C=C) bands at 1495 cm⁻¹ and 1600 cm⁻¹. An additional absorption bands between 3000-2850 cm⁻¹ can be assigned to the ν (CH₃) vibration.²⁰⁹ Moreover, the roto-vibrational band at 3016 cm⁻¹ is visible for all catalysts and shows the formation of methane. This can be expected, as the formation of methane should be favored if a methoxy group is present. This can be explained by the different bonding energies, which is lower for methoxy groups compared to hydroxy groups (see chapter 2.2.2).

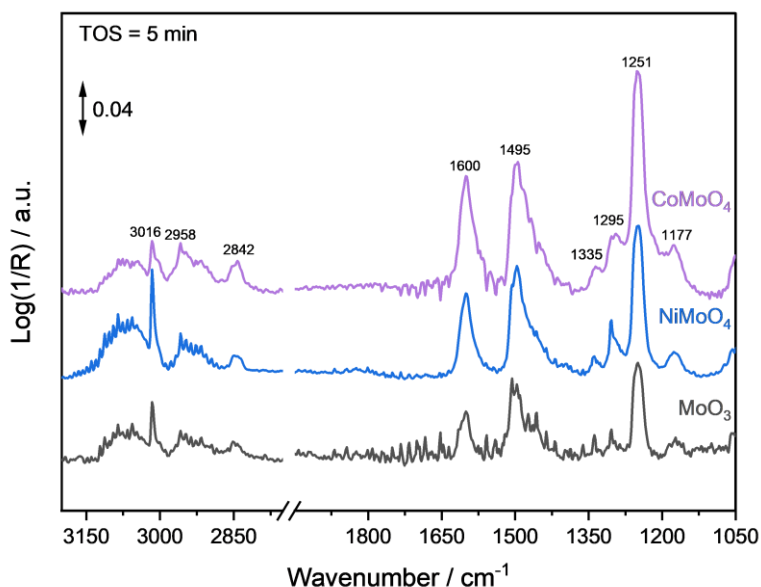


Figure 27: DRIFT spectra of catalysts after anisole adsorption at 325 °C in 100 % H₂ (25 ml/min). Reproduced from Ref.¹⁹⁷ with permission from the Royal Society of Chemistry.

The slow intensity decrease (> 40 min) of the $\nu(\text{Ph-O-CH}_3)$ band at 1251 cm^{-1} indicates a strong adsorption, probably chemisorption, on the surfaces of CoMoO_4 , NiMoO_4 and MoO_3 (see A-66). However, this effect is expected as the adsorption at O_v by e.g. ethers or alcohols is known for metal molybdates and molybdenum oxide.^{30, 92}

Operando DRIFTS of DME HDO

Operando DRIFTS experiments with dimethyl ether (DME) have been conducted to enable more insights into the ongoing processes during reaction with oxygen containing substrates. Surprisingly, unexpected behaviors of both MoO_3 and Ni(5)MoO_3 were observed. The catalysts were reduced for 2 h in advance similar to the catalytic test and afterwards H_2/DME (1:1, 25 ml/min) was introduced into the DRIFTS cell. For the HDO of DME the expected products should be methane and water. In case of an incomplete conversion, the formation of methanol would be possible as well.

After switching to the DME feed, the formation of methane (1305 cm^{-1} and 3016 cm^{-1}) was observed and DME absorption bands at ca. 1200 cm^{-1} and between 2750 cm^{-1} - 3000 cm^{-1} increased simultaneously for the MoO_3 catalyst (see A-67). This was even more pronounced for Ni(5)MoO_3 , which showed very intense absorption bands of gas-phase methane, including its rotational bands (see A-69). However, both catalysts started to form CO_2 and CO at the same time. This was unexpected, since it was not reported for the HDO reaction.

To get further information about this oxidation, the DRIFTS experiment was repeated without a pre-reduction and using a He/DME (1:1) feed (see A-68 and A-70). Again CO_2 , CO and CH_4 have been formed, even though in much lower amounts and more time was necessary until the formation started. Ni(5)MoO_3 formed again more methane compared to MoO_3 . It is not clear whether the CO and CO_2 is formed by the decomposition of the $\text{MoO}_x\text{C}_y\text{H}_z$ phase or a direct oxidation of DME occurs. The formation of these products in context of the HDO is, as far as we know, only reported three times.^{32, 139, 210} Báfero et al. concluded that the CO_2 formation is attributed to the substrate decomposition at temperatures above $400\text{ }^\circ\text{C}$. As the decomposition of DME, including the formation of oxidation products, is also possible, this could explain the results. Since MoO_3 is known as an oxidation catalyst, at these reaction temperatures ($325\text{ }^\circ\text{C}$) the lattice oxygen could be still active for oxidation reactions even in a reductive environment. The oxygen of the used substrates could replace the oxygen of the defective sites and it could explain the formation of water, methane and hydrogen by a complex system of reactions.

Additionally, the formation could be caused by the decomposition of $\text{MoO}_x\text{C}_y\text{H}_z$. It is known that this phase is only stable for temperatures up to $400\text{ }^\circ\text{C}$, but the products of decomposition are not reported (see chapter 2.4). Further experiments are necessary to obtain more insight into the ongoing processes.

DRIFTS Benzene Adsorption

Because the desorption of products is important in heterogeneous catalyzed processes, the adsorption behavior of benzene was tested as well. For this, the benzene was adsorbed by using a syringe pump and evaporator. The benzene was transported via gas-phase (25 ml/min He) to the catalyst surface. Compared to anisole experiments, the benzene is not chemisorbing at the catalyst surface. After the maximum intensity is reached, the benzene dosage on MoO₃ was stopped, flushed with He and the adsorption bands of benzene starting to decrease immediately (see Figure 28). Already 4 min after stopping the addition, only a very small rest of absorption can be observed for the $\nu(\text{CH})$ vibrational band at 3050 cm⁻¹. Subsequently it was switched to a H₂, which did not affect the spectra as expected when no substrate is present at the surface.

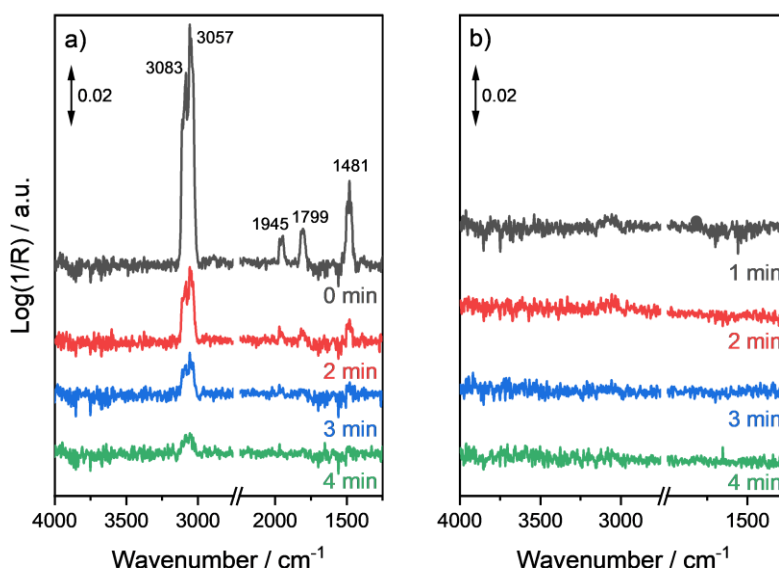


Figure 28: DRIFT spectra after a) benzene adsorption in He (25 ml/min) on MoO₃ is stopped at 325 °C and subsequently b) switch to H₂ flow (25 ml/min) at 325 °C. Reproduced from Ref.¹⁹⁷ with permission from the Royal Society of Chemistry.

The same was done for the NiMoO₄ sample. Here the result regarding the benzene desorption was the same as observed for MoO₃. After 4 min of flushing with He, almost no vibrational bands of benzene are visible and only the $\nu(\text{CH})$ at ≈ 3050 cm⁻¹ is left (see Figure 29a). Interestingly, after switching to H₂ the result was different and after 2 min the evolution of methane can be observed by the roto-vibrational band at 3016 cm⁻¹ (see Figure 29b). The intensity was increasing further and after passing a maximum a slow decrease was observed. For CoMoO₄, this was found as well, but the methane formation started some minutes later and the CH₄ absorption band was less intense (see A-66). Because the DRIFTS cells geometry forbids a quantitative comparison of methane

evolution, these experiments have been repeated and methane ($M/Z = 15$) was tracked by an online MS in parallel to the DRIFTS measurements.

When NiMoO_4 was used, the methane formation started immediately after H_2 is introduced into the chamber (see Figure 30). The relative intensity increases rapidly before it reaches a temporary plateau after ca. 3 min and further increases until the maximum is reached after 12 min. Subsequently, the intensity decreases for about 60 min until the measurement was stopped. CoMoO_4 was showing a comparable behavior with some small differences. The intensity increases much slower for the first 3 min until a larger plateau was reached. However, after 5 min and passing the plateau, it increases very fast, reaching the maximum after ca. 15 min and decreases slowly afterwards. The height of maximum is approximately at the same level as observed for NiMoO_4 and it decreased also for more than 60 min. In contrast to the DRIFTS result MoO_3 formed methane too, even though the maximum relative intensity is reduced by a factor of three. After a moderate increase, the maximum was reached after 20 min and it decreased afterwards. Additionally, a control experiment with a SiO_2 sample was conducted. As can be expected, no methane was formed in this experiment and an unknown methane source can be excluded.

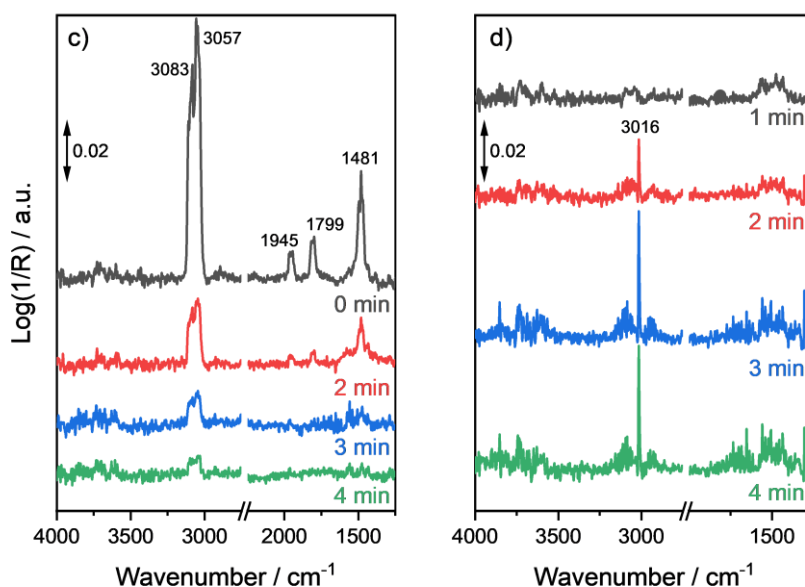


Figure 29: DRIFT spectra after a) benzene adsorption in He (25 ml/min) on NiMoO_4 is stopped at 325 °C and subsequently b) switch to H_2 flow (25 ml/min) at 325 °C. Reproduced from Ref.¹⁹⁷ with permission from the Royal Society of Chemistry.

That methane occurs after benzene adsorption surprises, as it indicates that benzene not just adsorbs, but a chemical process must take place. The decomposition of the aromatic ring was observed previously by a catalytic test with NiMoO_4 in the fixed-bed reactor with benzene instead of anisole but using the same protocol as used for the anisole HDO (see chapter 4.1.1).

It was shown that benzene can be decomposed under HDO conditions and Ni is active for the C-C hydrogenolysis but might not be the dominating active phase which is driving the catalyst selectivity.

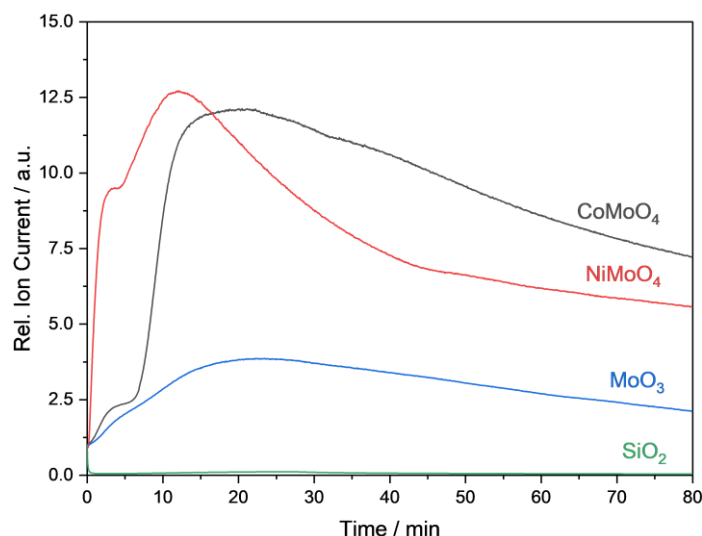


Figure 30: MS signal of DRIFTS/MS experiment with methane evolution ($M/Z = 15$) after benzene adsorption and switch to a H_2 atmosphere at $325\text{ }^\circ\text{C}$. Reproduced from Ref.¹⁹⁷ with permission from the Royal Society of Chemistry.

A hypothesis for this behavior is the formation of a molybdenum oxycarbohydride ($MoO_xC_yH_z$) phase, which might be formed after pre-reduction by benzene. Subsequently, this phase could be hydrogenated by hydrogen, which is activated at Ni^0 , forming MoO_xH_z . This could explain the DRIFTS result as well as the results of the catalytic tests. As discussed before, the occurrence of $MoO_xC_yH_z$ for the MoO_3 catalyzed HDO was already described by Prasomsri et al. (see chapter 2.4).³² As this phase is assumed to be stable at temperatures between $300\text{--}380\text{ }^\circ\text{C}$, it is matching our reaction conditions and making it likely to occur. However, only in one publication a $MoO_xC_yH_z$ phase was observed for a modified (there $CoMoO_4$) MoO_3 -based catalyst and no other reports existing in context of the HDO.⁴¹ Nevertheless, Ledoux and co-workers described the phase already for the isomerization of alkanes, but did not report the formation of CH_4 .^{44, 161, 162}

To understand the effect of methane formation, several things must be considered which occur in this process. It is reported that mixed phases are formed for $NiMoO_4$ and $CoMoO_4$ or a phase separation occurs during reduction (see chapter 4.4 and 4.2.5). By this a MoO_3/MoO_2 phase and metal particles are generated.^{160, 176, 178} Further, the pre-reduced MoO_3 phase can be seen as a molybdenum oxyhydride (MoO_xH_z), which can be further transformed into the $MoO_xC_yH_z$. Afterwards, hydrogen is activated at the nickel centers and is diffusing by hydrogen-spillover to the $MoO_xC_yH_z$ phase.^{42, 156, 163, 179, 211} This activated hydrogen could hydrogenate the carbon atoms and thus form methane (see Figure 31). This might also explain the absence of the $MoO_xC_yH_z$ phase in spent $NiMoO_4$ catalysts after

all experiments, which is contradictory to the Ni(5)MoO₃ sample. The increased nickel content could activate more hydrogen and thus the MoO_xC_yH_z phase is decomposed faster than it is formed, while for Ni(5)MoO₃ not enough activated hydrogen is provided and a MoO_xC_yH_z phase can be accumulated.

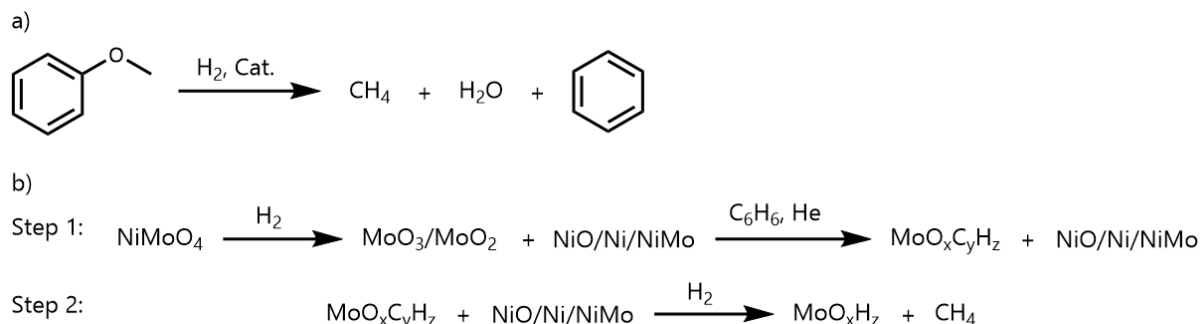


Figure 31: Simplified scheme for a possible pathway of the methane formation in nickel molybdate catalyst. a) CH₄ formation by HDO reaction b) CH₄ formation by MoO_xC_yH_z decomposition. Reproduced from Ref.¹⁹⁷ with permission from the Royal Society of Chemistry.

Additionally, the catalytic test with benzene and the Ni/ α -Al₂O₃ (\approx 3 wt.% Ni) showed that methane can be also formed by C-C hydrogenolysis (see chapter 4.1.1). Because the selectivity to methane was much higher for Ni/ α -Al₂O₃ compared to Ni(3)MoO₃ and NiMoO₄, the Ni does not seem to dominate the selectivities directly. This was not only observed for the reaction with benzene but also for the anisole HDO at 325 °C. This might indicate that another mechanism or phase is responsible for the CH₄ formation for MoO_x containing catalysts and the Ni is not accessible for the substrate, which is also indicated by TEM experiments (see chapter 4.4). The fact that the CH₄ was formed in the second step during the DRIFTS experiments and no surface species was observed indicates that this methane cannot be formed directly by C-C hydrogenolysis. However, it must be assumed that hydrogenolysis and the MoO_xC_yH_z formation occur at the same time.

4.3. MoO_xC_yH_z Formation and Regeneration Studies

MoO_xC_yH_z Formation in MoO₃

For gaining a better knowledge of the effect, which nickel has on the MoO_xC_yH_z phase formation in-situ XRD measurements have been conducted. To understand the behavior of MoO₃, it was started with basic studies on the formation. In literature, MoO_xC_yH_z is obtained by a treatment of MoO₃ in a hydrogen/hydrocarbon mixture at temperatures around 350 °C.^{25, 44, 161, 162} However, heptane/butane has been used as hydrocarbons, which has to be evaporated. This leads to challenges in preventing condensation within the set-up. To address these challenges, methane was selected as the optimal candidate due to its

well-defined chemical properties and its ability to be accurately dosed using MFCs. Additionally, methane is not prone to condensation under the specified conditions, further enhancing its suitability for this application (1 bar, 350 °C). Even though the catalytic tests were conducted at 325 °C, first experiments have been done at 350 °C to make sure that the temperature is sufficient to form the $\text{MoO}_x\text{C}_y\text{H}_z$ with an unreactive molecule like methane.

In order to gain insight into the significance of reduction to form $\text{MoO}_x\text{C}_y\text{H}_z$, the H_2/CH_4 ratio was varied systematically in the order $\text{H}_2/\text{CH}_4 = 9:1, 1:1, 1:9$. Starting with the ratio $\text{H}_2/\text{CH}_4 = 9:1$, after 75 min TOS the first reflections of MoO_2 at 18.3 nm^{-1} and 25.7 nm^{-1} and at the same time the decrease of MoO_3 reflections can be observed (see A-72). Afterwards, reflections of the $\text{MoO}_x\text{C}_y\text{H}_z$ phase at 26.7 nm^{-1} and 31.5 nm^{-1} became visible after approx. 200 min TOS (see Figure 32). They further increased with time until a steady state was reached after about 300 min TOS. Other changes or a reduction of $\text{MoO}_x\text{C}_y\text{H}_z$ to MoO_2 were not observed over a time of 1200 min. Because no reference data for $\text{MoO}_x\text{C}_y\text{H}_z$ exist, molybdenum blue was treated with $\text{H}_2/\text{CH}_4 = 9:1$ at 325 °C for 1200 min. Molybdenum blue is a MoO_3 phase pre-reduced by nascent hydrogen (MoO_xH_z). It has been used in literature to obtain phase pure $\text{MoO}_x\text{C}_y\text{H}_z$ and was synthesized as described by Glemser et al.¹⁵⁸ As shown in Figure 32, the $\text{MoO}_x\text{C}_y\text{H}_z$ was not obtained phase pure and MoO_2 was formed as well. Also, a reflection at 17.9 nm^{-1} is visible, but there is no explanation for this.

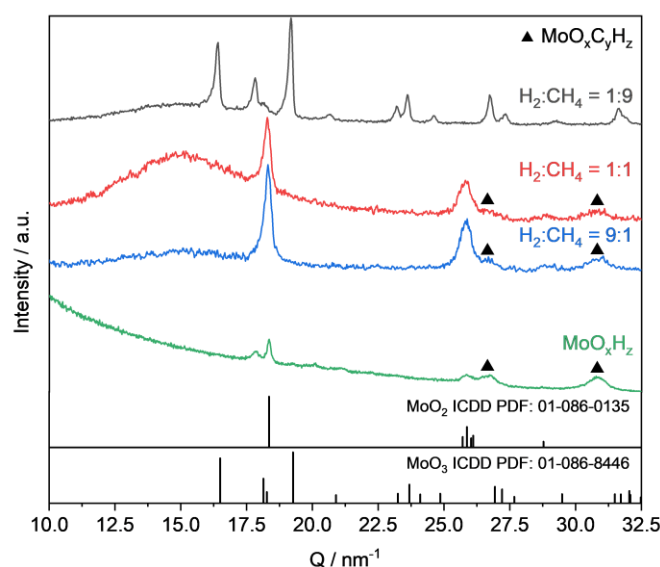


Figure 32: Normalized in-situ XRD patterns for the MoO_3 treatment at 350 °C in a H_2/CH_4 mixture (flow: 10 ml/min) at TOS = 300 min for $\text{H}_2/\text{CH}_4 = 9:1$ and $1:9$, TOS = 305 min for $\text{H}_2/\text{CH}_4 = 1:1$. Note, that the broad reflection at $Q \approx 15 \text{ nm}^{-1}$ belongs to the SiO_2 capillary reactor. Ex-situ diffractogram for MoO_xH_z treated in $\text{H}_2/\text{CH}_4 = 9:1$ at 325 °C for 1200 min forming a $\text{MoO}_x\text{C}_y\text{H}_z$ phase (\blacktriangle) for comparison with the in-situ data. Heating up was carried out in He for both experiments Reproduced from Ref.¹⁹⁷ with permission from the Royal Society of Chemistry.

Nevertheless, the reflections at 26.7 nm^{-1} and 31.5 nm^{-1} have been identified in this sample, providing evidence for the existence of $\text{MoO}_x\text{C}_y\text{H}_z$ for the in-situ treated MoO_3 . These observations are also in agreement with literature. With a feed ratio of $\text{H}_2/\text{CH}_4 = 1:1$, the result was the same. After ca. 75 min TOS, the MoO_2 reflection at 25.7 nm^{-1} appeared and after 125 min the reflections of MoO_3 started to decrease significantly until a steady state was reached after 200 min.

Surprisingly, when the $\text{H}_2/\text{CH}_4 = 1:9$ ratio was used, no reduction and therefore no $\text{MoO}_x\text{C}_y\text{H}_z$ phase was observed up to 1200 min (see Figure 32 and A-74). From this it can be concluded that a certain amount of hydrogen is necessary to reduce MoO_3 , to form Mo^{5+} and subsequently the molybdenum oxycarbohydride.

$\text{MoO}_x\text{C}_y\text{H}_z$ Formation in NiMoO_4

Because NiMoO_4 showed a high catalytic activity and the assumption that $\text{MoO}_x\text{C}_y\text{H}_z$ is responsible for the high methane selectivity, the reduction and treatment in H_2/CH_4 was investigated by in-situ XRD. However, because of the high methane selectivity in the reaction (see chapter 4.1.1) it is questionable whereas the $\text{MoO}_x\text{C}_y\text{H}_z$ phase can be observed. Possible is a fast decomposition when the formation is not carried out stepwise. With respect to the enhanced reducibility of NiMoO_4 compared to MoO_3 , the reaction temperature was lowered to $325 \text{ }^\circ\text{C}$. Initially, the reduction behavior is elucidated for NiMoO_4 as always and a pre-reduction is performed. After 120 min of NiMoO_4 reduction, only reflections at 26.8 nm^{-1} , 30.3 nm^{-1} , 35.1 nm^{-1} and 42.5 nm^{-1} belonging to Ni and NiO are visible (see Figure 33).

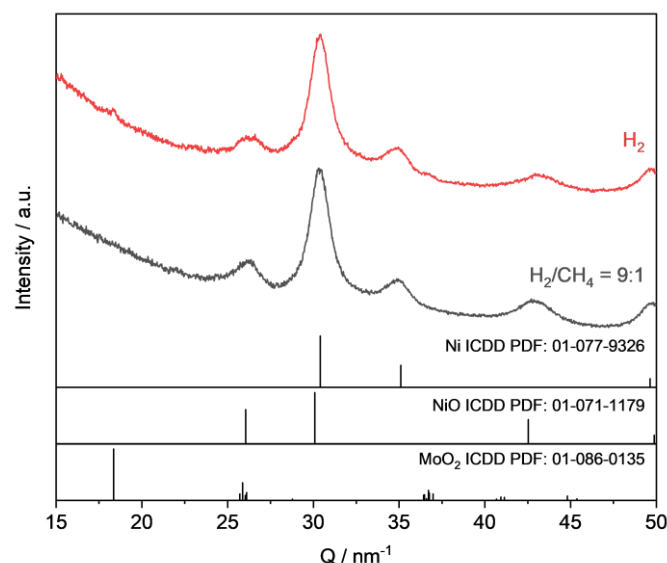


Figure 33: Normalized long-time scan ex-situ XRD patterns for NiMoO_4 after in-situ reduction in pure H_2 for 120 min and treatment in H_2/CH_4 (1:1) at $325 \text{ }^\circ\text{C}$ for 1200 min after no further changes in the diffractograms over time were observed. Heating up was carried out in He for both experiments. Reproduced from Ref.¹⁹⁷ with permission from the Royal Society of Chemistry.

However, it is surprising that only a very small reflection at 18.4 nm^{-1} of MoO_2 has been detected. Since molybdenum is present stoichiometrically its reflections should be much more pronounced. Pseudo in-situ XPS measurements indicate that most of the nickel at the surface is present as Ni^0 (see A-43).

When NiMoO_4 was treated with the H_2/CH_4 (9:1) mixture, the XRD result was nearly identical compared to reduction in 100 % H_2 . But this time, no Mo species can be observed. The reflection of MoO_2 is not visible anymore and only Ni/NiO are detected. A reason for the absence of reflections of Mo containing species reflections could be a small crystallite size and a low crystallinity resulting in weak or no reflections as observed before (see Figure 32). Therefore, it is not clear if the $\text{MoO}_x\text{C}_y\text{H}_z$ phase was formed.

Next, the in-situ XRD experiment has been done with the $\text{Ni}(5)\text{MoO}_3$ catalyst. In contrast to the dominance of Ni in the diffractogram after the NiMoO_4 treatment, the lower content of only 5 wt.% Ni in $\text{Ni}(5)\text{MoO}_3$ should avoid this effect. Additionally, the high catalytic activity combined with a favored selectivity for the anisole HDO makes this catalyst much more interesting. This time the treatment was done stepwise. First the sample was pre-reduced in 100 % H_2 for 2 h at $325 \text{ }^\circ\text{C}$ and afterwards exposed to methane for several hours.

The reflections of MoO_3 decreased directly, after the treatment started and reached a first steady state after 120 min TOS (see A-77). After switching to methane, the $\text{MoO}_x\text{C}_y\text{H}_z$ phase was built up immediately. After 420 min TOS the gas has been switched back to hydrogen, to observe the decomposition of the $\text{MoO}_x\text{C}_y\text{H}_z$ phase. However, the reflection at 31.5 nm^{-1} became more intense, while the remaining MoO_3 reflections decreased further until they vanished completely. To obtain a diffractogram over the enlarged angle area with improved intensity, a long-time scan was made after the reaction has been completed (see Figure 34).

The reflections at $Q = 27 \text{ nm}^{-1}$, 31.5 nm^{-1} and 44.2 nm^{-1} are in agreement with those of the $\text{MoO}_x\text{C}_y\text{H}_z$ phase found during the reference measurement with molybdenum blue and in literature (see Figure 32).^{25, 161} Even though the reflections of nickel species are contributing to the diffractogram and are overlapping with those of the $\text{MoO}_x\text{C}_y\text{H}_z$ phase at $Q \approx 31.5 \text{ nm}^{-1}$ the major contribution of this reflection should originate from the oxycarbohydride as the Ni content is only at 5 wt.%. Additionally, the reflections of MoO_2 can be observed at 25.7 nm^{-1} and 37 nm^{-1} . Compared to MoO_3 the amount of $\text{MoO}_x\text{C}_y\text{H}_z$ seems to be higher in relation to MoO_2 . This matches the catalytic results and supports the hypothesis that the $\text{MoO}_x\text{C}_y\text{H}_z$ phase and its quantity could be the reason for an improved catalytic activity.

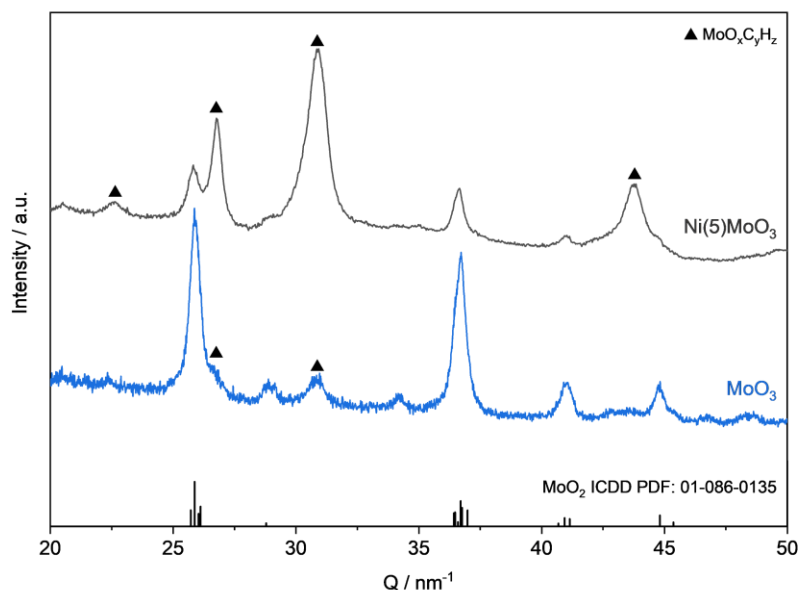


Figure 34: Normalized XRD results from the stepwise treatment of Ni(5)MoO₃ with 100 % H₂ for 2 h and 100 % CH₄ for 7 h at 325 °C compared with MoO₃. Heating up was carried out in He. Reproduced from Ref.¹⁹⁷ with permission from the Royal Society of Chemistry.

However, the addition of H₂ after CH₄ addition could not directly confirm the DRIFTS results (see chapter 4.2.6). The addition of H₂ should hydrogenate the MoO_xC_yH_z phase to MoO_xH_z while forming CH₄. That the corresponding reflections were not decreasing, but became more intense is in contrast with this. Bouchy et al. found that the molybdenum oxyhydride (MoO_xH_z) is isostructural with the MoO_xC_yH_z phase (see Figure 35).¹⁶² This would lead to a superposition of reflections and a further decrease of MoO₃ reflections upon by reduction to the oxyhydride would explain the increase of the reflection at 31.5 nm⁻¹. The structural model assumed by Bouchy et al. was an FCC structure, which, however, could not be derived from in-situ XRD experiments due to the poor data quality and therefore cannot be compared.

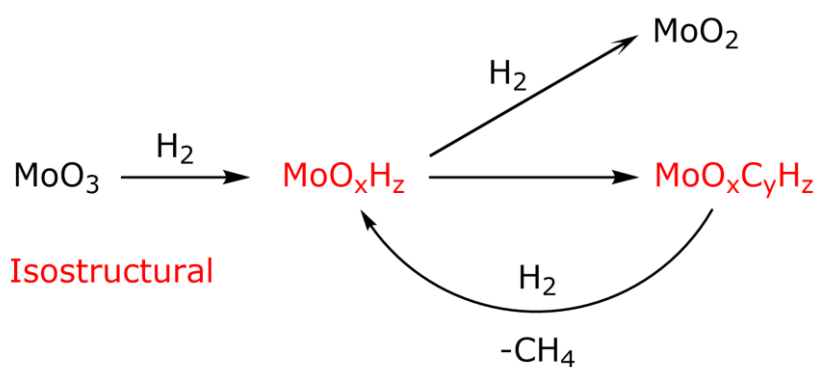


Figure 35: Structural changes of Mo species during in-situ XRD treatment of Ni(5)MoO₃.

Substrate Influence on $\text{MoO}_x\text{C}_y\text{H}_z$ Formation

Since the $\text{MoO}_x\text{C}_y\text{H}_z$ formation with methane was successful, propene was tested as a more reactive hydrocarbon. The test was done with MoO_3 as reference material at lower temperature ($325\text{ }^\circ\text{C}$) and with the same hydrogen/hydrocarbon ratio ($\text{H}_2/\text{C}_3\text{H}_6 = 9:1$). This experiment showed that reactive hydrocarbons can improve the oxycarbohydride formation not only in regards to the quantity, which is indicated by a larger integral ratio of $\text{MoO}_x\text{C}_y\text{H}_z/\text{MoO}_2$. The $\text{MoO}_x\text{C}_y\text{H}_z$ phase is also formed in a shorter period of time. The data is presented in Figure 36 for comparison. Note that the time scale is different in the figure and only important diffractograms are shown to obtain a better overview.

In in-situ XRD experiments, performed at $325\text{ }^\circ\text{C}$ using C_3H_6 , the reflections at $Q = 31.5\text{ nm}^{-1}$ and $Q = 26.7\text{ nm}^{-1}$ have been assigned to $\text{MoO}_x\text{C}_y\text{H}_z$ (see Figure 36a). They were observed after 100 min TOS and a steady state has been reached after 170 min TOS, in which intense reflections of the $\text{MoO}_x\text{C}_y\text{H}_z$ phase could be observed next to the reflections of MoO_2 , while MoO_3 was reduced completely. For the experiment with MoO_3 in H_2/CH_4 at $350\text{ }^\circ\text{C}$ (see Figure 36b) the formation of the $\text{MoO}_x\text{C}_y\text{H}_z$ phase began noticeably after 190 min TOS and a stationary state was reached after 230 min TOS. This change took significantly more time compared to propene experiments. Additionally, much more MoO_2 was formed compared to the $\text{MoO}_x\text{C}_y\text{H}_z$ phase. However, these results cannot only be explained by the more reactive substrate, but several aspects must be considered. At first, the slightly increased temperature ($350\text{ }^\circ\text{C}$) for the reaction with methane could increase the reduction rate to such an extent, that a reduction to MoO_2 was forced. Once the inactive MoO_2 is formed, it cannot be transformed into $\text{MoO}_x\text{C}_y\text{H}_z$.

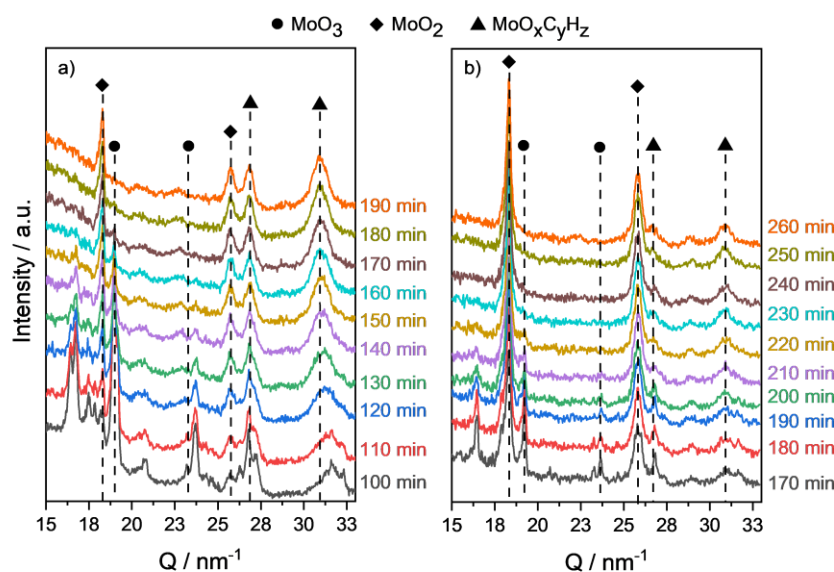


Figure 36: Results from in-situ XRD investigations on $\text{MoO}_x\text{C}_y\text{H}_z$ formation in MoO_3 with a) $\text{H}_2:\text{C}_3\text{H}_6 = 9:1$ at $325\text{ }^\circ\text{C}$ and b) $\text{H}_2:\text{CH}_4 = 9:1$ at $350\text{ }^\circ\text{C}$. Heating up was carried out in He for both experiments. Reproduced from Ref.¹⁹⁷ with permission from the Royal Society of Chemistry.

This is since $\text{MoO}_x\text{C}_y\text{H}_z$ is formed from MoO_{3-x} (see chapter 2.4) and MoO_2 is already at a deeper reduction state. Furthermore, the low reactivity of methane could be a reason. When the carburization of the pre-reduced state (MoO_{3-x}) is hindered, the reduction becomes relatively faster and more MoO_2 is obtained. As already shown for the $\text{Ni}(5)\text{MoO}_3$ catalyst, an improved reduction could promote the oxycarbohydride formation. Since propene has a reducing effect on MoO_3 , the third reason could be an enhanced reduction by the feed.¹³² This suggests that an activation procedure with a reactive hydrocarbon and hydrogen could be advantageous to accumulate an oxycarbohydride phase and subsequently obtain catalysts with improved activity and stability.

Regeneration Studies

Since coking is one of the main deactivation processes for the gas-phase HDO, the catalyst regeneration by calcination is an important aspect. As discussed before (see chapter 2.2.2), the regeneration of MoO_3 is known to be facile and the catalytic activity can be recovered.^{25, 29, 30} Therefore, the regeneration behavior of nickel modified molybdenum oxide catalysts was tested. In case of nickel molybdate, the phase separation into Ni/MoO_x resulting in Ni^0 particle formation at the surface and an oxidation to nickel molybdate seems less likely. However, according to a report the nickel molybdate formation is possible under oxidative conditions.²⁰²

The regeneration capability was tested by in-situ XRD with $\text{Ni}(5)\text{MoO}_3$ by a sequential reduction/oxidation. The reduction was conducted with a $\text{H}_2/\text{C}_3\text{H}_6 = 9:1$ mixture at 325 °C and after the $\text{MoO}_x\text{C}_y\text{H}_z$ phase formation was accomplished, the sample was oxidized at 325 °C in syn. air. Afterwards, it was switched again to the initial hydrogen/hydrocarbon mixture under the same conditions, in order to form the $\text{MoO}_x\text{C}_y\text{H}_z$ phase again. Subsequently, the sample was oxidized in syn. air at 400 °C. The exact time of each step varied because an automatization was not possible with this set-up. Therefore, the experiment was continued with the next step after reaching a steady state. The initial diffractogram is dominated by MoO_3 reflections ($Q = 16.5 \text{ nm}^{-1}$, 18.1 nm^{-1} , 19.3 nm^{-1}) and reflections of low intensity from NiMoO_4 at $Q = 20.3 \text{ nm}^{-1}$ (see Figure 37a). The reductive treatment in $\text{H}_2/\text{C}_3\text{H}_6$ lead to the decrease of MoO_3 and NiMoO_4 reflections, while the formation of MoO_2 reflections became slightly visible after 30 min TOS. In parallel the formation of the $\text{MoO}_x\text{C}_y\text{H}_z$ phase started and its reflections at $Q = 26.7 \text{ nm}^{-1}$ and 30.5 nm^{-1} are dominating the diffractogram after 140 min TOS. Additionally, reflections of MoO_2 at $Q = 18.3 \text{ nm}^{-1}$ and 25.7 nm^{-1} are visible, while MoO_3 and NiMoO_4 reflections completely vanished.

The oxidation at 325 °C was carried out until no further changes were observed after 70 min TOS. Is the gas switched to syn. air, the decrease of the $\text{MoO}_x\text{C}_y\text{H}_z$ phase can be observed immediately after 10 min (see Figure 37b). Surprisingly, the reflections of MoO_2

became more intense at the same time, which was not expected for an oxidation step. This could be explained by a rearrangement after the oxidation of the carbon species of $\text{MoO}_x\text{C}_y\text{H}_z$. In literature $\text{MoO}_x\text{C}_y\text{H}_z$ is discussed to prevent Mo from reduction to Mo^{4+} by a blockage of the rearrangement due to the intercalated carbon.¹⁶³ Are parts of the carbon oxidized to CO/CO_2 , it might leave the lattice and induce this rearrangement. The reflection intensity of the MoO_2 phase is changing only within the first 10 min and seems to remain constant during the next 60 min. Nevertheless, the intensity of MoO_3 reflections is increasing until 50 min TOS. The results demonstrate that MoO_2 is unable to undergo complete oxidation at 325 °C. However, it can be further accumulated by the decomposition of $\text{MoO}_x\text{C}_y\text{H}_z$, which appears to form MoO_3 and MoO_2 simultaneously.

Following the reduction of the sample at the same temperature, a gradual reduction of MoO_3 was observed, indicated by a decrease in MoO_3 reflections until 50 min TOS. (see Figure 37c). After 60 min TOS the MoO_3 reflections almost vanished, MoO_2 reflections became more intense and $\text{MoO}_x\text{C}_y\text{H}_z$ was formed again indicated by a reflection at 30.5 nm^{-1} . In parallel the intensity of MoO_2 increased further, until approx. 70 min TOS.

Compared to the first reduction sequence, the amount of MoO_2 was higher than the $\text{MoO}_x\text{C}_y\text{H}_z$ phase, which can be explained by the fact that MoO_2 was not oxidized before and cannot be converted into the oxycarbohydride phase (see chapter 2.4). In the last oxidation step, at 400 °C, the oxidation was very fast and after 10 min the diffractogram was dominated by MoO_3 (see Figure 37d). This time, reflections of MoO_2 decreased significantly. After 30 min TOS reflections of MoO_2 and $\text{MoO}_x\text{C}_y\text{H}_z$ are not detected anymore and only MoO_3 is observed. Interestingly, after the first reduction step, NiMoO_4 cannot be observed and a regeneration to the initial state of Ni(5)MoO_3 is at temperatures up to 400 °C not observed. This agrees with the results of the in-situ TEM experiments, showing that exposure to air after reduction did not oxidize the nickel (see chapter 4.4).

Another experiment was conducted where Ni(1)MoO_3 was reduced in $\text{H}_2/\text{C}_3\text{H}_6$ (9:1) at 325 °C and oxidized in O_2/He (1:9) at 325 °C. After reduction and reaching a steady state, $\text{MoO}_x\text{C}_y\text{H}_z$ and MoO_2 were formed. MoO_3 was not observed and $\text{MoO}_x\text{C}_y\text{H}_z$ became again the dominant phase (see A-80). Afterwards, the sample was oxidized and when the steady state was reached, small reflections of MoO_2 were observed again at $Q = 18.3 \text{ nm}^{-1}$ and 25.7 nm^{-1} . This agrees with the results obtained with Ni(5)MoO_3 . Interestingly, NiMoO_4 was observed at $Q = 20.3 \text{ nm}^{-1}$ this time. During the second time of reduction, the same amounts of $\text{MoO}_x\text{C}_y\text{H}_z$ and MoO_2 were formed and no indication for a significant MoO_2 accumulation was given. However, compared to the experiment with Ni(5)MoO_3 , only small amounts of MoO_2 were observed after oxidation and poor data quality made it challenging to decide whether MoO_2 is accumulated or not. Nevertheless, it can be assumed that MoO_2 is accumulated in high amounts after multiple regeneration steps at 325 °C.

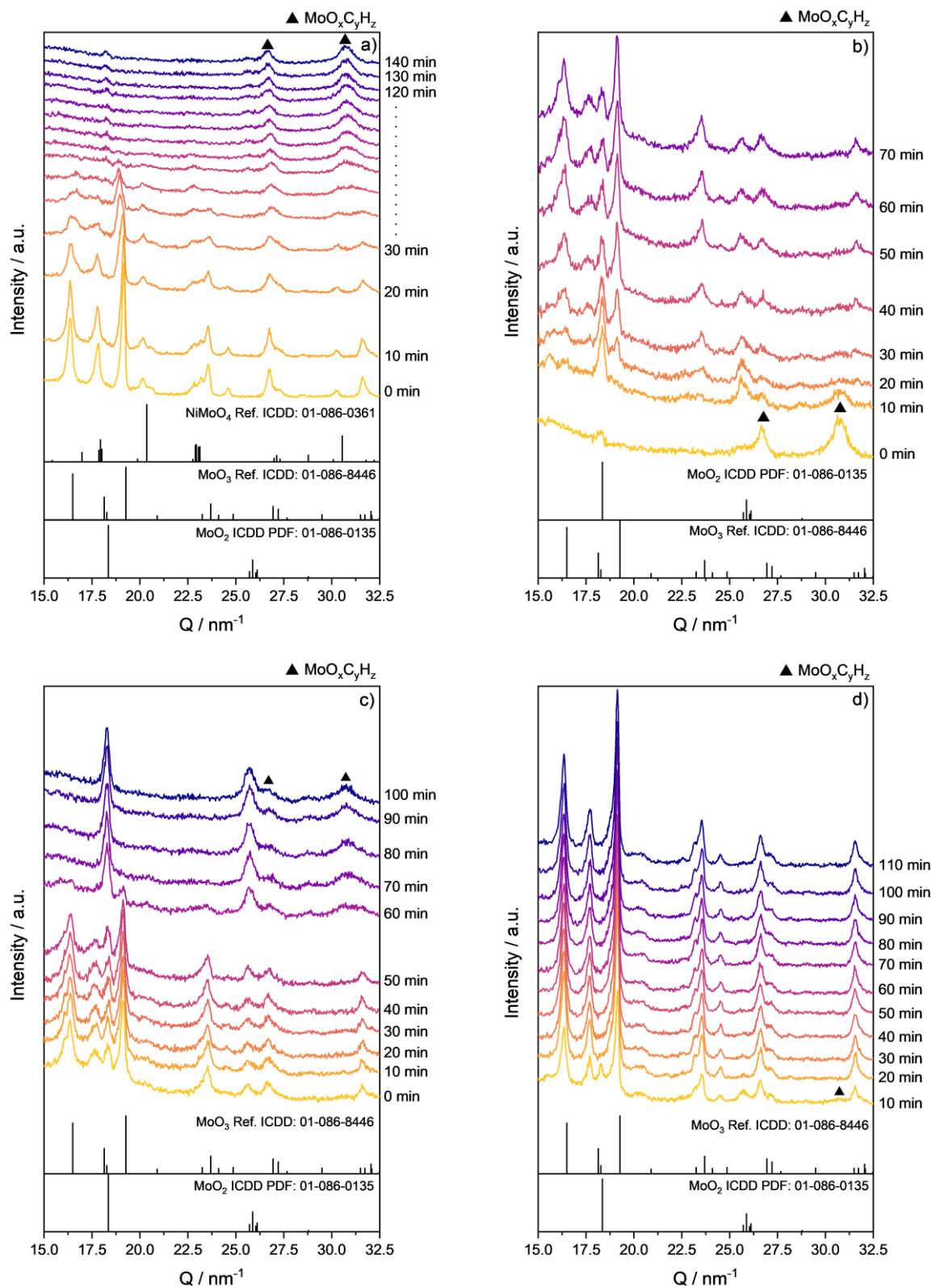


Figure 37: In-situ XRD measurements of Ni(5)MoO₃ a) reduction in H₂/C₃H₆ (9:1) at 325 °C for 120 min and b) the subsequently oxidation in syn. air for 70 min at 325 °C; c) a second reduction in H₂/C₃H₆ (9:1) at 325 °C for 100 min and the d) oxidation in syn. air at 400 °C for 110 min. Heating up was carried out in He for both experiments.

In addition to these experiments the reoxidation behavior was studied by UV-Vis experiments. Compared to the in-situ XRD setup, the UV-Vis setup allows to treat the sample with a water containing feed. This is of particular interest since H₂O is a coupled product of the HDO and thus might reoxidize the catalyst again. During reduction, MoO₃ turns blue to dark blue while O_v are formed. MoO₂ is black, which results in a strong, undefined adsorption in the UV-Vis spectrum.^{146, 212} This is indicating the proceeding reduction. The reduction of MoO₃ and Ni(5)MoO₃ was conducted in a fixed-bed reactor with a H₂/C₃H₆ (9:1) mixture at 325 °C for 1 h. Afterwards an oxidation was done with 30 % H₂O in N₂ at 325 °C to test the influence of water for 1 h on the oxidation under applied reaction conditions. Due to technical limitations, the amount of water could not be reduced further to imitate the amount of water occurring during the HDO. Nevertheless, this experiment can indicate if MoO_x is reoxidized by water at all. The H₂O treatment was followed by oxidation with synthetic air, as well at 325 °C for 1 h.

It can be observed that the reduction of MoO₃ in H₂/C₃H₆ (9:1) is very fast within the first 20 minutes (see A-81). After 10 min reaction approx. 50 % of the total reduction degree is reached. At the end of the 60 min reduction time, the reduction degree is increasing only slightly. This is in accordance with the in-situ XRD experiments, showing that the reduction is accomplished after a short period of time. Surprisingly, after the feed was switched to the water containing feed, the oxidation could not be observed to a significant extent. Subsequently, the oxidation performed at 325 °C in syn. air oxidized the sample rather fast and after 15 min TOS the absorption decreased more than 50 %.

A similar behavior was observed for the reduction with 100 % H₂ and oxidation with H₂O for Ni(5)MoO₃. While the sample reduced rather fast, the oxidation was not successful (see A-82). Surprisingly, the oxidation with syn. air was also not possible at 325 °C for Ni(5)MoO₃. To exclude that an insufficient temperature is responsible for this, the experiments have been repeated for MoO₃, Ni(1)MoO₃ and Ni(5)MoO₃ with a reduction in H₂/C₃H₆ (9:1) at 325 °C and an oxidation in syn. air at 400 °C. As can be expected, MoO₃ was reduced and oxidized fast (see A-83). Ni(1)MoO₃ was reduced fast as well as Ni(5)MoO₃, but they are also not oxidized at an increased temperature (see A-84 and A-85).

The reason for the incomplete oxidation of nickel containing catalysts in the UV-Vis experiments is unknown. However, the absorption contributions of reduced NiMoO₄ and MoO₂ are not clear and a quantitative oxidation of the Ni component to form NiMoO₄ might be necessary to recover the initial absorption properties. Another reason could be an increased amount of MoO₂ due to an enhanced reduction behavior by Ni (see chapter 4.2.3 and 4.2.5). The significantly larger particle size (250 – 315 μm) and sample size (m ≈ 250 mg) compared to the in-situ XRD experiments (100 – 150 μm; m ≈ 5-10 mg) could have led to an insufficient oxidation afterwards within 1 h. A prolonged calcination

time might be beneficial. Nevertheless, these experiments showed that the initial catalyst cannot be recovered by oxidation at 325 °C but at 400 °C. An MoO₂ accumulation is possible due to incomplete oxidation and over several steps as shown for Ni(5)MoO₃ but a regeneration might be possible, if the conditions are chosen correctly.

Promoting Effect of Ni on MoO_xC_yH_z Formation

The beneficial role of the nickel on the oxycarbohydride phase formation was studied by in-situ XRD experiments. MoO₃ and Ni(5)MoO₃ have been used as reference material and are compared to a physical mixture of NiO/MoO₃ and layers of NiO and MoO₃. An improved MoO_xC_yH_z phase formation by nickel containing catalysts might indicate that the improved reduction properties are beneficial for this. It must be mentioned that for pure phase NiMoO₄ no MoO_xC_yH_z was found, probably caused by a fast hydrogenation under CH₄ formation. Thus, lower Ni contents seem to be beneficial enough for the molybdenum oxyhydride (MoO_xH_z) formation. It is formed by activated hydrogen, which subsequently forms large amounts of MoO_xC_yH_z. However, the lowered Ni amount is not enough for a fast hydrogenation of MoO_xC_yH_z. When nickel particles are formed, they should be located randomly distributed, but only at the NiMoO₄ parts (see Figure 21 and Figure 40). This means, that for the binary phase catalysts (Ni(5)MoO₃) the majority will not be covered by nickel particles. But also, MoO₃ could obtain activated hydrogen from the Ni centers, which is provided by the spillover effect. Experiments with bifunctional catalysts (Pt/H-erionite) for hydroisomerization have shown, that the spillover can act over longer distances, when the catalysts are separated but in contact.²¹¹ The spillover effect is also known to be present at MoO₃ surfaces, where the H atoms are adsorbed as single protons and electrons, which are highly mobile because of H bonding at the surface and within the bulk.¹⁵⁶ This could enhance the MoO_xH_z formation not only for NiMoO₄ but also for the MoO₃ particles.

At first, the experiment with two layers was conducted. The upper layer comprised NiO, with a height of approx. 1 cm, and the subsequent layer consisted of MoO₃, also with a height of 1 cm. Both layers were positioned within a quartz capillary. Because the X-ray beam was placed in the MoO₃ layer, no nickel species are visible in this diffractogram. The reduction of NiO was tested in an external experiment to prove a complete reduction (see A-79). For the second experiment, a physical mixture was used to investigate differences by the dispersion and to offer "short" ways for the hydrogen spillover. The amount of nickel for the physical mixture was 5 wt.% as used for Ni(5)MoO₃. In case of the layered system, the amount of nickel was increased for experimental reasons. As feed a mixture of H₂/C₃H₆ = 9:1 was used at a temperature of 325 °C for 5 h.

To compare the results and the amount of $\text{MoO}_x\text{C}_y\text{H}_z$ which is formed, the integral ratios for the reflections of the $\text{MoO}_x\text{C}_y\text{H}_z$ phase at 26.7 nm^{-1} and for MoO_2 at 25.7 nm^{-1} were calculated at a fixed TOS ($\approx 310 \text{ min}$). Therefore, the background was subtracted and a pseudo-Voigt model was used. This indicates how much MoO_3 has been reduced to inactive MoO_2 . For all samples, the formation of the oxycarbohydride phase began directly with start of the reduction (see A-78 - A-87) showing reflections at 26.7 nm^{-1} and 30.6 nm^{-1} of $\text{MoO}_x\text{C}_y\text{H}_z$. But the reduction to MoO_2 can be observed as well with reflections at 25.7 nm^{-1} and 36.5 nm^{-1} (see Figure 38).

As discussed before, the change from methane to propene as hydrocarbon will lead to a significant increase of formed $\text{MoO}_x\text{C}_y\text{H}_z$ phase. For MoO_3 treated in a H_2/CH_4 mixture, a ratio ($R = A(\text{MoO}_x\text{C}_y\text{H}_z)/A(\text{MoO}_2)$) of $R = 0.1$ was determined, while for the same sample treated in $\text{H}_2/\text{C}_3\text{H}_6$, a ratio of 1.5 was observed (see Table 7). If Ni(5)MoO_3 is used, the amount of formed $\text{MoO}_x\text{C}_y\text{H}_z$ is even bigger with $R = 2.8$ for an activation treatment in H_2/CH_4 . However, when $\text{H}_2/\text{C}_3\text{H}_6$ is used with Ni(5)MoO_3 the ratio is with $R = 4.4$ much more increased, indicating the importance of nickel for a good phase formation.

Interestingly, for the layered sample in $\text{H}_2/\text{C}_3\text{H}_6$ the ratio ($R = 1.5$) was the same as for the unpromoted MoO_3 . This indicated that a H spillover is not working here over a longer distance. For the test with the physical mixture, the ratio remained nearly unchanged at $R = 1.7$. Note, that a reflection at $Q = 35.4 \text{ nm}^{-1}$ of the metallic nickel is visible. This shows that long distances are not the reason for the absence of an improved $\text{MoO}_x\text{C}_y\text{H}_z$ phase formation and probably other effects than the H spillover are the reason for the improved $\text{MoO}_x\text{C}_y\text{H}_z$ phase formation.

Table 7: Ratio of integral values for reflections at $Q = 26.7 \text{ nm}^{-1}$ ($\text{MoO}_x\text{C}_y\text{H}_z$) and $Q = 25.7 \text{ nm}^{-1}$ (MoO_2) of several in-situ XRD experiments.

Catalyst	Gas mixture	Ratio $A(\text{MoO}_x\text{C}_y\text{H}_z)/A(\text{MoO}_2)$
MoO_3	H_2/CH_4 (9:1)	0.1
MoO_3	$\text{H}_2/\text{C}_3\text{H}_6$ (9:1)	1.5
MoO_3+NiO	$\text{H}_2/\text{C}_3\text{H}_6$ (9:1)	1.5
MoO_3+NiO (phys. Mix)	$\text{H}_2/\text{C}_3\text{H}_6$ (9:1)	1.7
Ni(5)MoO_3	$\text{H}_2/\text{C}_3\text{H}_6$ (9:1)	4.4
Ni(5)MoO_3	H_2/CH_4 (9:1)	2.8

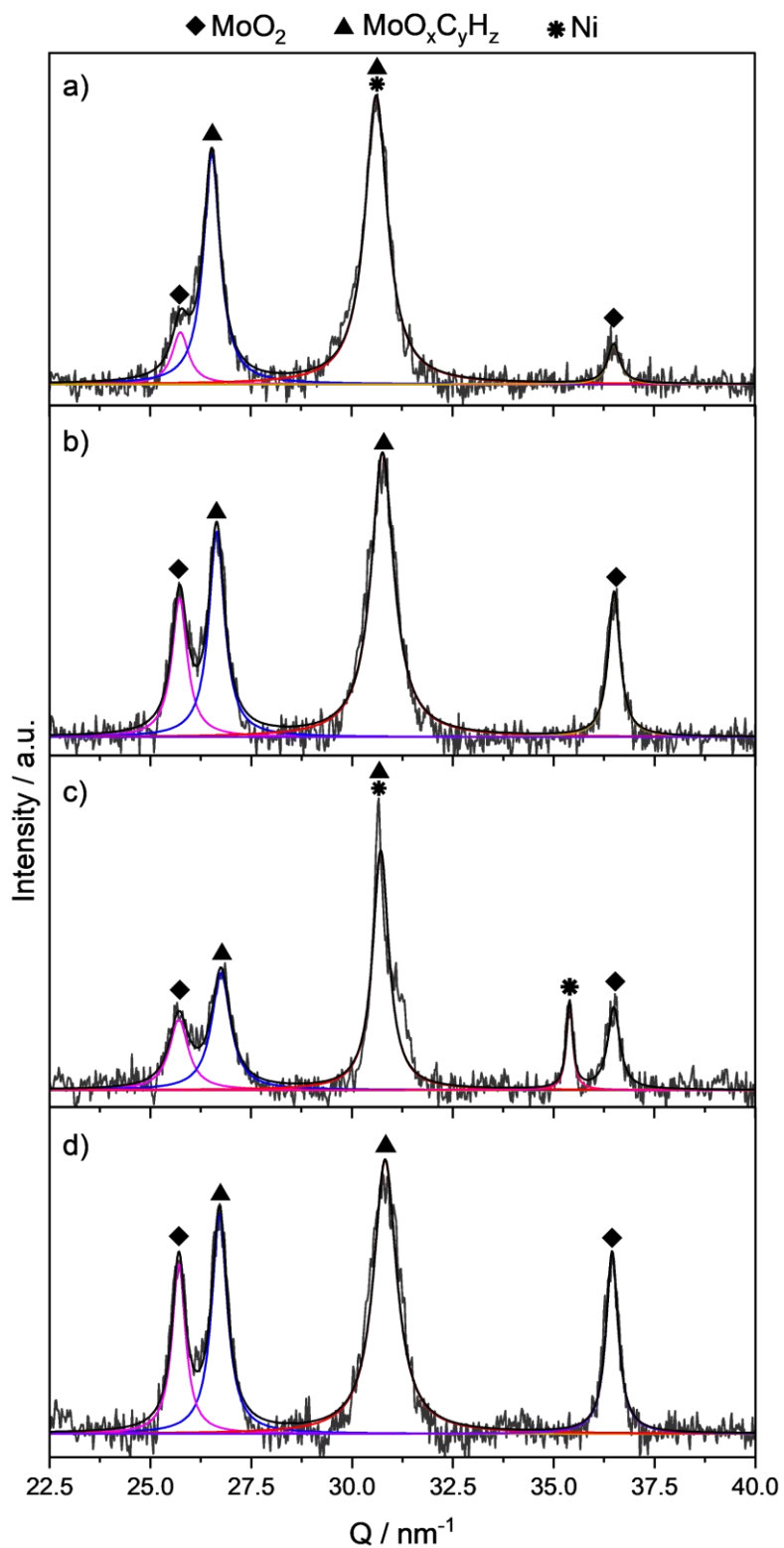


Figure 38: In-situ XRD experiments of different samples at 325 °C in a gas mixture of $\text{H}_2/\text{C}_3\text{H}_6 = 9:1$ at TOS = 310 min. a) Ni(5)MoO₃; b) two layers of NiO/MoO₃; c) phys. mix of NiO/MoO₃; d) MoO₃. Heating up was carried out in He for both experiments. Reproduced from Ref.¹⁹⁷ with permission from the Royal Society of Chemistry.

Interestingly, the reflection of metallic Ni was only observed for the physical mixture and not for the binary Ni(5)MoO₃ system. This is surprising, as the amount of nickel is with 5 wt.% the same in both experiments. An explanation could be the particle size, which could be expected to be much bigger for the layered system and phys. mixture. The NiO particles are pressed and sieved to a particle size of 100-150 μm and are mixed with the MoO₃ particles of the same size. However, when the NiMoO₄ is reduced and Ni⁰ is formed at the surface, the particle size is expected to be much lower.¹⁷⁸ It is possible that these particles are too small to be detected by XRD. At the same time, a high dispersion of these small particles could be an explanation for the improved MoO_xC_yH_z phase formation. They can provide a higher surface area and thus activate more hydrogen and good dispersion result in a better coverage of the MoO_x species. Additionally, during the reduction an intermediate micro- and mesoporous MoO_{3-x} structure could be formed, which could be beneficial for the formation of mixed phases and the tendency to form MoO_xC_yH_z.¹⁶³

These experiments demonstrate that improved reduction properties and H spillover cannot be the only reason for an enhanced MoO_xC_yH_z formation. It is rather a synergy of different effects like H₂ activation, metal dispersion, structural properties and substrate properties and they are cumulative.

4.4. In-Situ TEM Study

To learn more about the pathway of the oxycarbohydride formation in H₂/C₃H₆, in-situ TEM measurements have been performed. As already described, Ni(5)MoO₃ consists of a binary phase system, where NiMoO₄ and MoO₃ exist in parallel (see chapter 4.2.1). The improved MoO_xC_yH_z formation cannot be explained exclusively by a quantitative transformation of the NiMoO₄ part since only 5 wt.% are nickel. This leads to the question, if nickel has a “long distance” effect by hydrogen spillover or how the MoO_xC_yH_z phase is formed in such an extent (see Table 7). In literature, it is claimed that the MoO_xC_yH_z phase is characterized by a relatively poor crystallinity and an interlayer spacing of 0.24 nm and an angle of 70°. ^{41, 161, 165} This could allow to observe the phase formation (MoO_xC_yH_z) and differences between catalysts with and without nickel. Moreover, it has been suggested that this phase may be formed by intercalation of carbon into shear-planes (see chapter 2.4). Seeing this could provide a better understanding of the formation mechanism. Further, the nickel itself is of particular interest since it can be an active site in the HDO reaction and its state under reaction conditions is unclear. Some reports indicate that metallic nickel particles are formed during the reduction, acting as H₂ activation sites.^{42, 178} However, XRD measurements of the present spent catalysts did not show any reflections of metallic Ni.

For the in-situ TEM experiment, Ni(5)MoO₃ was transferred into an "in-situ chip" and after fitting into the STEM it was kept in a N₂ flow of 0.1 ml/min at 1.007 bar. The sample was heated with 10 °C/min up to 325 °C, while the first changes were observed after the temperature exceeded more than 200 °C. As Ni(5)MoO₃ is a binary mixture, two particles with distinct morphology are shown in the image, one smaller particle at the right side (NiMoO₄) which is located directly at a large MoO₃ crystallite on the left (see Figure 39a). At about 240 °C the MoO₃ became slightly porous at two different independent parts (Figure 39b, red circle). This effect became more pronounced with increasing temperature. It continued until at 325 °C the crystallite became traversed by many small channels of ca. 2 nm diameter. During heating in N₂ flow, this behavior is surprising, as such a destruction would rather have been expected for the reduction process. Indeed, it has been observed in MoO₃ samples which were pretreated in an external reactor in H₂/CH₄ flow at 325 °C for several hours. After this treatment, MoO₃ showed the same porous morphology as observed in the in-situ TEM experiment during heat up in N₂ (compare Figure 39 and A-88).

The reason for this channel formation in Figure 39 is unclear, but it seems likely that small MoO₂ particles are formed by the reduction, although no H₂ was present during the heat up.^{213, 214} A beam damage effect that could reduce MoO₃ to MoO₂²¹⁵ can be excluded as regions which had not been illuminated during heat up showed similar structural modifications. MoO₃ is known to be reduced by thermal treatment and in vacuum, forming O_v at the surface, but this occurs usually not below 350 °C.^{132, 216, 217} Possibly, such reduction is facilitated already at lower temperature in a very small flat sample as used in the in-situ TEM experiment.

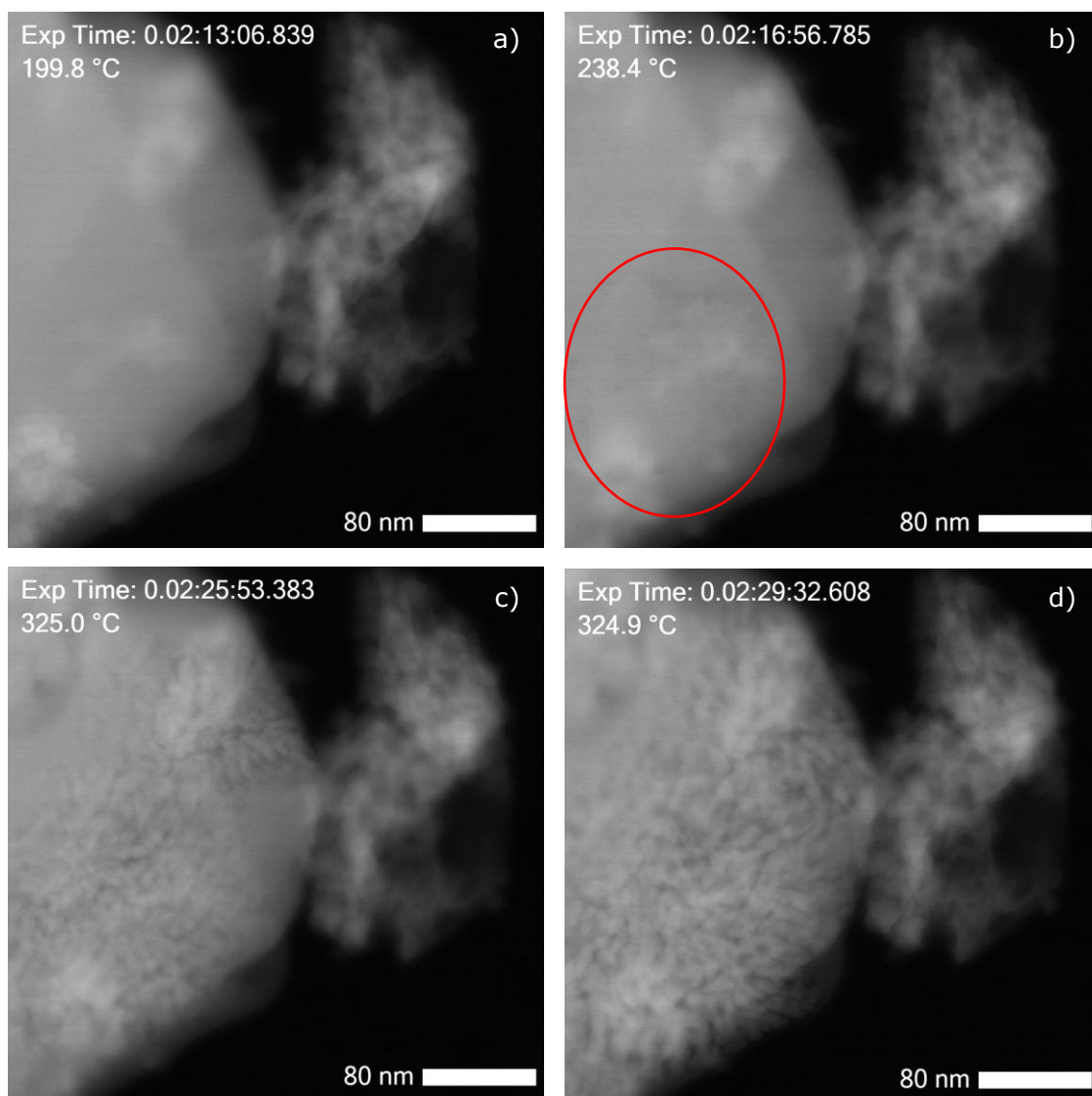


Figure 39: In-situ TEM in N₂ during heat up to a) 200 °C b) 238 °C (red circle shows the starting point of channel formation) c) 325 °C and d) after holding at 325 °C for ca. 4 min.

After heating up the feed was switched to H₂/C₃H₆ (9:1) at 325 °C for 140 min. This should cause a reduction and the formation of a MoO_xC_yH_z phase. However, no changes are visible for the MoO₃ crystallite after this treatment (see Figure 40). This supports the thesis that MoO₃ was already reduced in advance. In contrast to this, the NiMoO₄ phase was further reduced which can be concluded from the bright dots distributed over the whole particle (red circles on the right side of Figure 40). This reduction process is fast and major changes were achieved within the first minute. After 6 min TOS, up to 140 min, no further changes were observable. It can be assumed that these particles contain a nickel enriched phase, presumably Ni⁰.

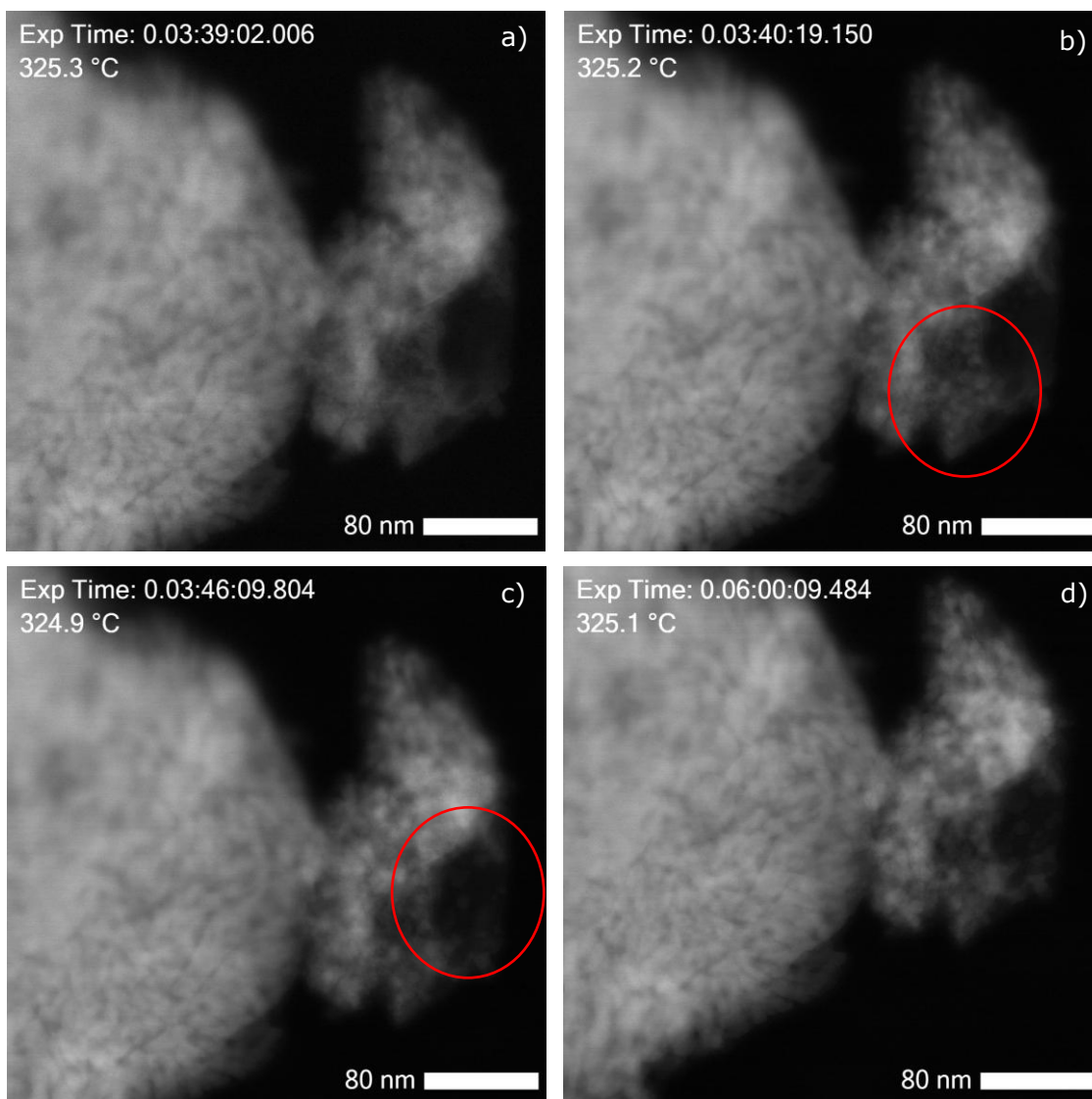


Figure 40: In-situ TEM during treatment in $\text{H}_2/\text{C}_3\text{H}_6$ (9:1) at 325 °C after a) 0 min and b) 1 min after switch c) 6 min and d) 120 min TOS. Red circles show the places of Ni particles.

This is suggested by a post mortem EDX mapping of the same sample, which remained on the chip but was transferred to an inspection holder, to clarify the elemental distribution ex-situ. There it turned out that Ni is concentrated within the dots (see Figure 41). At the same time the general structure remains intact. This means that during reduction the NiMoO_4 phase is separated into a Ni^0 and a MoO_x phase and the Ni nanoparticles are embedded into this structure and formed on top by agglomeration. These data show that the accessibility of nickel by molecules in the dimension of anisole may be hindered, as it is at least partly covered by an MoO_x structure. Nevertheless, due to the porosity, H_2 could have access and its activation on the Ni^0 surface might be possible. The close contact between the Ni and MoO_x surfaces indicates that a migration of H atoms by spillover is possible. Evidence for the presence of the $\text{MoO}_x\text{C}_y\text{H}_z$ phase or for its improved formation were not observed, although the phase was observed already in literature.^{41, 165} Surprisingly, a reoxidation as seen for air exposed spent catalysts by XRD and XPS (see chapter 4.2.2 and 4.2.3) was not observed.

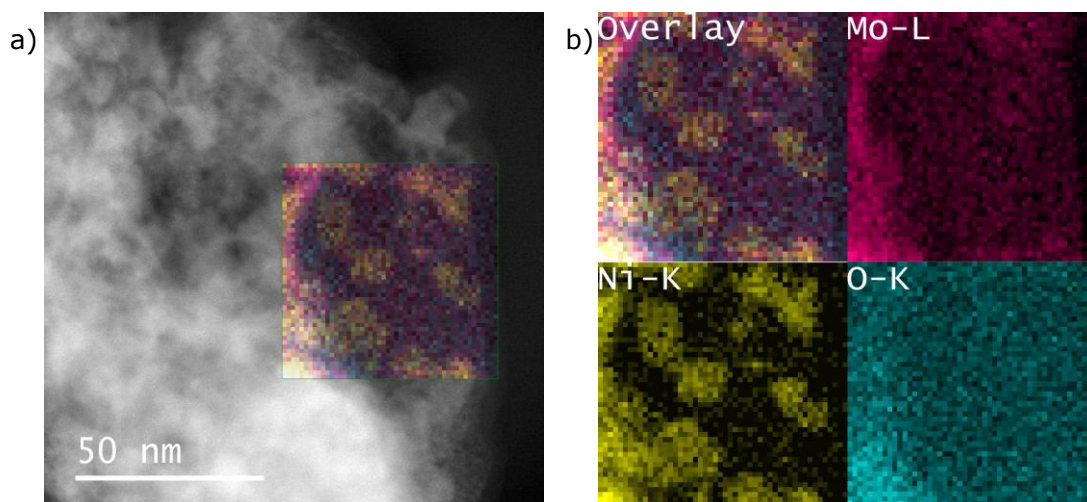


Figure 41: a) Post mortem TEM image after reduction in H_2/C_3H_6 (9:1) for 120 min combined with the EDX mapping (spectrum shown in A-89) and b) the magnified area with single element mappings, showing the existence of nickel particles.

4.5. In-Situ EPR Investigations of $MoO_xC_yH_z$

The possibility to detect Mo^{5+} by EPR spectroscopy (see chapter 3.4.2) enables this technique to elucidate both the $MoO_xC_yH_z$ and Mo^{5+} formation. Therefore, in-situ EPR experiments were conducted to reveal the influence of Ni on the reduction. The fresh samples were measured at 105 K under argon atmosphere, resulting in a broad signal of Mo^{5+} with components between $g = 1.957-1.942$, which might arise from overlapping signals of Mo^{5+} species in different local environment (see Figure 42). In literature one can find assignments of signals in this range to Mo^{5+} species in specific coordination (see Table 8).²¹⁸ However, due to the low signal-to-noise ratio in Figure 42, we do not want to follow such a detailed assignment. Additionally, the signal G at $g = 2.003$, close to the g -value of free electrons, might arise from defects such as F-centers or O^- species.²¹⁸ An intense, narrow signal at $g = 1.975$ can be observed for MoO_3 but not for $Ni(1)MoO_3$ and $Ni(5)MoO_3$. Łabanowska assigned this to Mo^{5+} ions without molybdenyl oxygen ($M=O$), surrounded by oxygen ions situated at the corners of an elongated square pyramid with rhombic distortion.²¹⁹ The higher intensity of Mo^{5+} signals for MoO_3 indicates that Ni can stabilize Mo^{6+} in $Ni(1)MoO_3$ and $Ni(5)MoO_3$. This is in accordance with XPS results, which showed a small Mo^{5+} concentration (3 %) for MoO_3 and 100 % Mo^{6+} for Ni containing catalysts (see chapter 4.2.3).

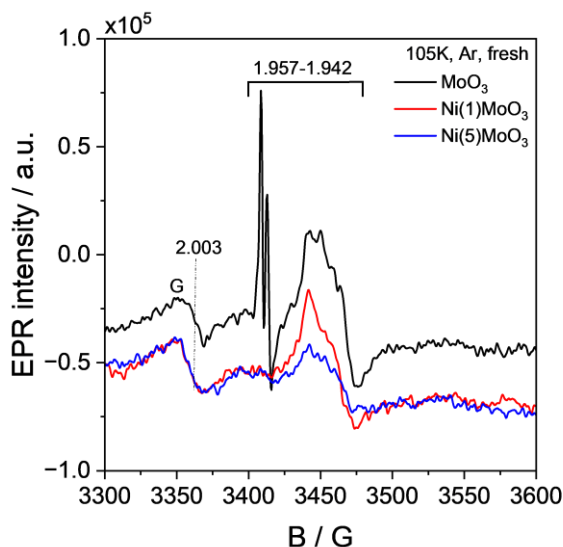


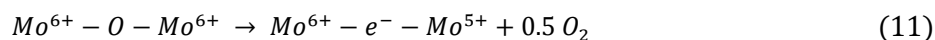
Figure 42: In-situ EPR spectra of the fresh samples after calcination (4 h at 450 °C) at 105 K under Ar atmosphere.

Table 8: EPR parameters of different Mo⁵⁺ sites in oxidized and reduced samples. Reproduced from Ref.²¹⁸ with permission from the Royal Society of Chemistry.

Signal	Oxidized	Reduced	Assignment
A	$g_{\perp} = 1.942$ $g_{\parallel} = 1.866$	$g_{\perp} = 1.942$ $g_{\parallel} = 1.88$	Hexacoordinated Mo ⁵⁺ in axially distorted MoO ₆ octahedra
A'	$g_1 = 1.951$ $g_2 = 1.946$ $g_3 = 1.87$	$g_{\perp} = 1.947$ $g_{\parallel} = 1.88$	Hexacoordinated Mo ⁵⁺ in rhombically distorted MoO ₆ , typical for MoO ₃ lattice
F	$g_1 = 1.957$ $g_2 = 1.944$ $g_3 = 1.866$	$g_{\perp} = 1.950$ $g_{\parallel} = 1.89$	Mo ⁵⁺ with one weakened Mo-O bond or one removed oxygen, or Mo ⁵⁺ with an oxygen vacancy in the x-y plane of MoO ₆ octahedron
E	$g_{\perp} = 1.938$ $g_{\parallel} = 1.89$	$g_{\perp} = 1.937$ $g_{\parallel} = 1.89$	Hexacoordinate Mo ⁵⁺ in shear defects
C	$g_1 = 1.975$ $g_2 = 1.973$ $g_3 = 1.89$	$g_{\perp} = 1.979$ $g_{\parallel} = 1.89$	Mo ⁵⁺ ions without a molybdenyl oxygen
G	$g_1 = 2.059$ $g_2 = 2.004$ $g_3 = 1.974$		(Mo-O) ⁵⁺ - hole center
B		$g_{\perp} = 1.936$ $g_{\parallel} = 1.89$	Mo ⁵⁺ in octahedra along the shear planes

The samples were reduced in-situ for 2 h in 100 % H₂, which reflects the initial state of the reaction. In comparison to other experiments, the reduction temperature was reduced to 300 °C due to technical limitations. To obtain a better signal-to-noise ratio, the spectra was recorded after cooling to -168 °C (see Figure 43a). After reduction the signals at $g = 2.003$ of F-centers (O_v with a trapped single electron) as well as the broad signal around

1.957 - 1.942 of Mo^{5+} species increased strongly. This is due to a reduction according to Eq. 11. Similar changes were observed for $\text{Ni}(1)\text{MoO}_3$ and $\text{Ni}(5)\text{MoO}_3$, yet the signal intensity decreases with rising Ni content (see Figure 43b).



Since Mo^{4+} is an EPR inactive non-Kramers ion, the Mo^{5+} concentration does not correlate linearly with the reduction degree. This means that the highest signal intensity for O_v and Mo^{5+} in MoO_3 might prove the lower reduction. The nickel containing samples showed lower intensities for both the O_v and Mo^{5+} species, which correlates with the nickel concentration. The smallest intensity, which was found for $\text{Ni}(5)\text{MoO}_3$ after reduction in H_2 suggests the strongest reduction of Mo^{5+} to the EPR inactive Mo^{4+} . This agrees with the results obtained from pseudo in-situ XPS measurements (see A-40 - A-44), in-situ XRD (see chapter 4.3) and H_2 -TPR (see chapter 4.2.5), showing a significantly increased formation of Mo^{4+} and a MoO_2 formation for nickel containing catalysts. This can be explained by the formation of metallic nickel particles (see chapter 4.4), which are located at the surface, activating H_2 and providing it by H spillover to remove terminal oxygen in MoO_3 and subsequently reducing the Mo^{5+} .¹⁷⁶

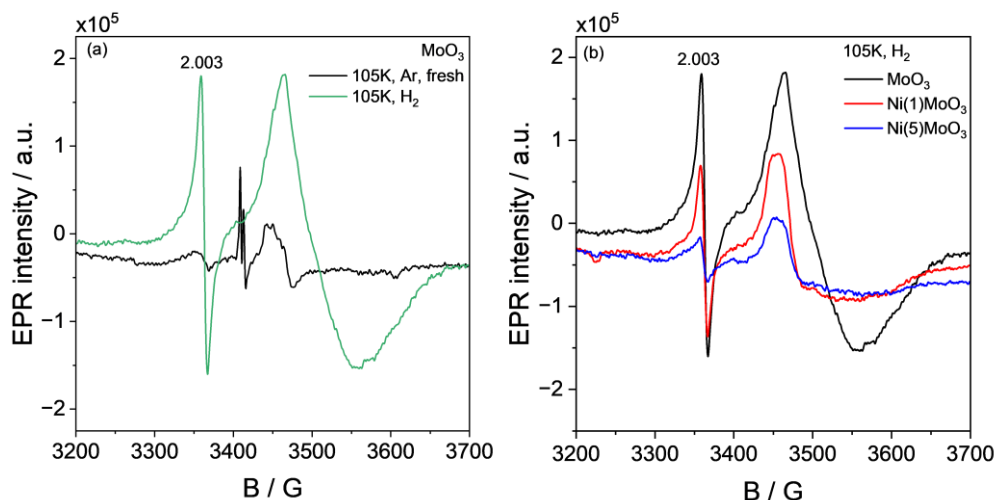


Figure 43: In-situ EPR spectra of a) MoO_3 before and after H_2 reduction measured, b) all reduced samples (in H_2 atmosphere) measured at 105 K with a modulation amplitude of 1.0G, after H_2 (100 %) reduction for 120 min at 300 °C.

In a second step, the pre-reduced samples were exposed to a $\text{H}_2/\text{C}_3\text{H}_6$ (1:1) mixture at 300 °C to investigate the influence on the $\text{MoO}_x\text{C}_y\text{H}_z$ formation. Spectra recorded at -168 °C after this treatment showed a strongly increased intensity of the O_v signal and Mo^{5+} species in different environments compared to spectra obtained after pre-reduction (see Figure 44). The EPR spectra of carbon-centered radicals is specified by an isolated signal with g-values close to the free electron in dependence on the location of the radical

inside the organic matrix. Carbon-centered radicals with neighboring oxygen atoms exhibit EPR spectra with slightly higher g-values in the range of 2.003 – 2.004, compared to completely carbon-centered radicals.^{220, 221}

Additionally, an interaction between carbon radicals and reduced paramagnetic Mo species might result in a decrease of the spin lattice relaxation time, which could increase the line width. For that reason, the signal at $g = 2.003$ with a line width of $\Delta B = 5.3$ G for Ni(5)MoO₃ could be assigned to carbon radicals with closely located paramagnetic Mo species, while the signal of MoO₃ with a line width of $\Delta B = 3.7$ G originates from carbon-centered radicals (see Figure 45).¹⁵¹ This interaction of paramagnetic Mo and carbon radicals may indicate the formation of a MoO_xC_yH_z phase and thus, an improved oxycarbide formation for nickel containing catalysts.

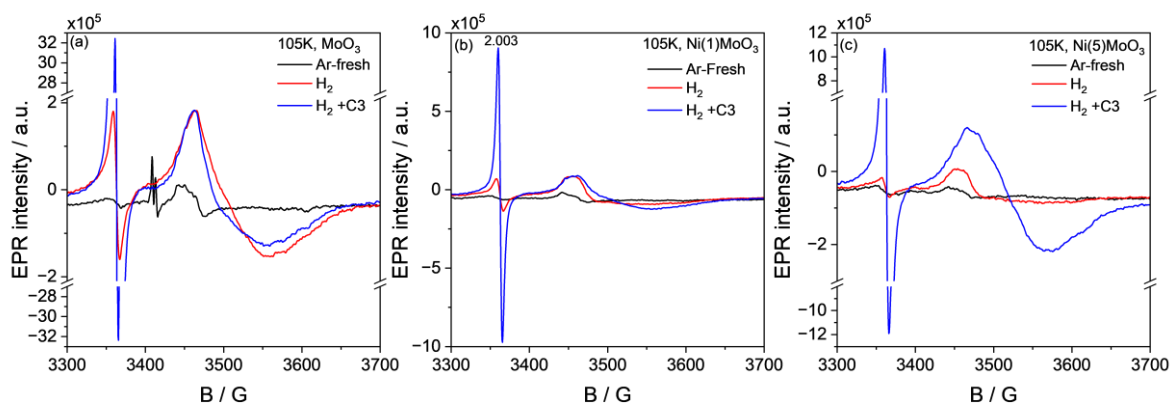


Figure 44: In-situ EPR spectra recorded at 105 K of a) MoO₃, b) Ni(1)MoO₃, c) Ni(5)MoO₃ as fresh sample (black lines), after reduction in 100 % H₂ at 300 °C for 2 h (red lines) and after treatment with a mixture of H₂/C₃H₆ (ratio 1:1) for 60 min (blue lines).

During reduction by H₂, Ni²⁺ is reduced to Ni⁰, which could donate an electron to an O_v. The electron is further transferred from the O_v to organic substrates (C₃H₆). This suggests that O_v can serve as intermediate for electron transfer reactions and thus enhances the electron transfer from Ni⁰ to other species. Similar results have been found by Wang et al. for Ni/ZrO₂ catalysts for the dry reforming of methane.²²² But not only H₂ can be responsible for the O_v formation. Propene can adsorb on the Ni⁰ sites and react with neighboring oxygen to form oxygenated carbon compounds. Simultaneously, the surface oxygen is consumed and O_v are formed. Moreover, in comparison to MoO₃, the EPR signal of Ni(5)MoO₃ exhibits a shift in the g_{\perp} to a smaller value (1.936), whereas no alteration in the g_{\parallel} of both samples after treatment in the mixture of H₂/C₃H₆ indicating the formation of new Mo⁵⁺ sites.

This was observed as well by M. Narayana et al. for the adsorption of probe molecules (H_2O , CH_3OH , NH_3 , CH_3CN) at in H_2 pre-reduced Mo/SiO_2 . They assigned the Mo^{5+} sites to some with adsorbates in the first coordination sphere.²²³ Consequently, the carbon might coordinate to the Mo^{5+} , resulting in the signal shift and indicating the formation of a molybdenum oxycarbide (MoO_xC_y) phase.

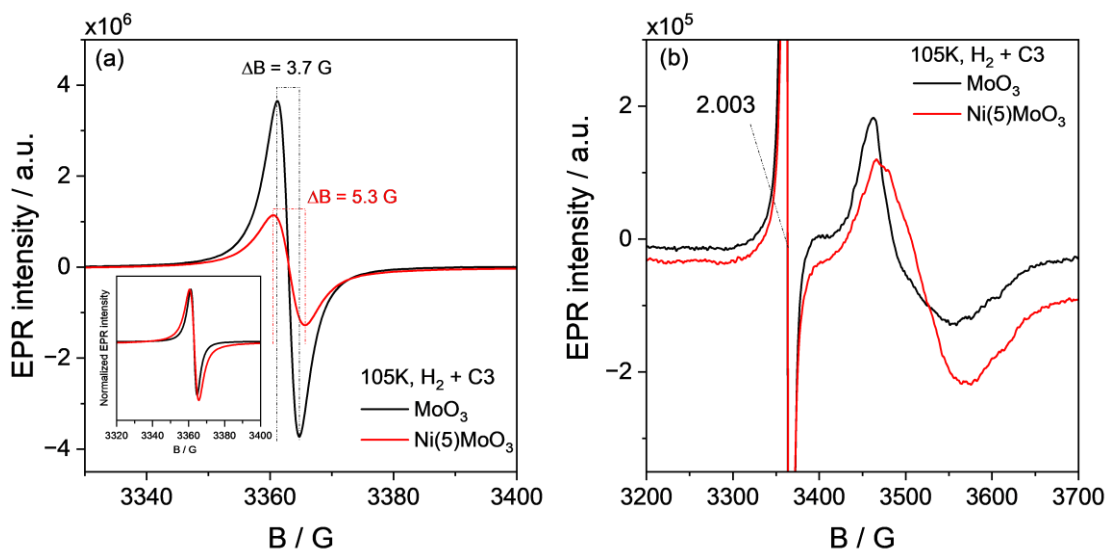


Figure 45: In-situ EPR spectra of MoO_3 and $\text{Ni}(5)\text{MoO}_3$ recorded at 105 K after treatment with a mixture of $\text{H}_2/\text{C}_3\text{H}_6$ for 60 min at 300 °C.

In a third experiment, the fresh MoO_3 and $\text{Ni}(5)\text{MoO}_3$ were reduced directly in a $\text{H}_2/\text{C}_3\text{H}_6$ (1:1) mixture at 300 °C for 2 h. Afterwards measured spectra at -168 °C were comparable to pre-reduced and subsequently in $\text{H}_2/\text{C}_3\text{H}_6$ treated samples with a strong signal at $g = 2.003$ and an broad signal of various Mo^{5+} species in different environments (see A-90a).

For MoO_3 the intensity of $g = 2.003$ is again significantly higher with a smaller line width, indicating that again more carbon radicals with interaction to paramagnetic Mo^{5+} species in the lattice are formed in $\text{Ni}(5)\text{MoO}_3$. Moreover, the shift of g_{\perp} to smaller values of Mo^{5+} sites of $\text{Ni}(5)\text{MoO}_3$ supports an increased $\text{MoO}_x\text{C}_y\text{H}_z$ formation as well (see A-90b). After the samples were subsequently treated in 100 % H_2 , the intensity of the dominant signal at $g = 2.003$ decreases, while the signal of different Mo^{5+} species remained unchanged (see Figure 46). This may indicate that parts of $\text{MoO}_x\text{C}_y\text{H}_z$ are hydrogenated. This agrees with previously obtained results from in-situ DRIFTS results, where methane is formed by a subsequent H_2 treatment (see chapter 4.2.6). Furthermore, it is in accordance with the literature suggesting that $\text{MoO}_x\text{C}_y\text{H}_z$ stabilize Mo^{5+} , preventing it from reduction to inactive Mo^{4+} .²⁵ These EPR results indicate that the carbon radicals might be reduced more easily and Mo^{5+} is reduced afterwards.

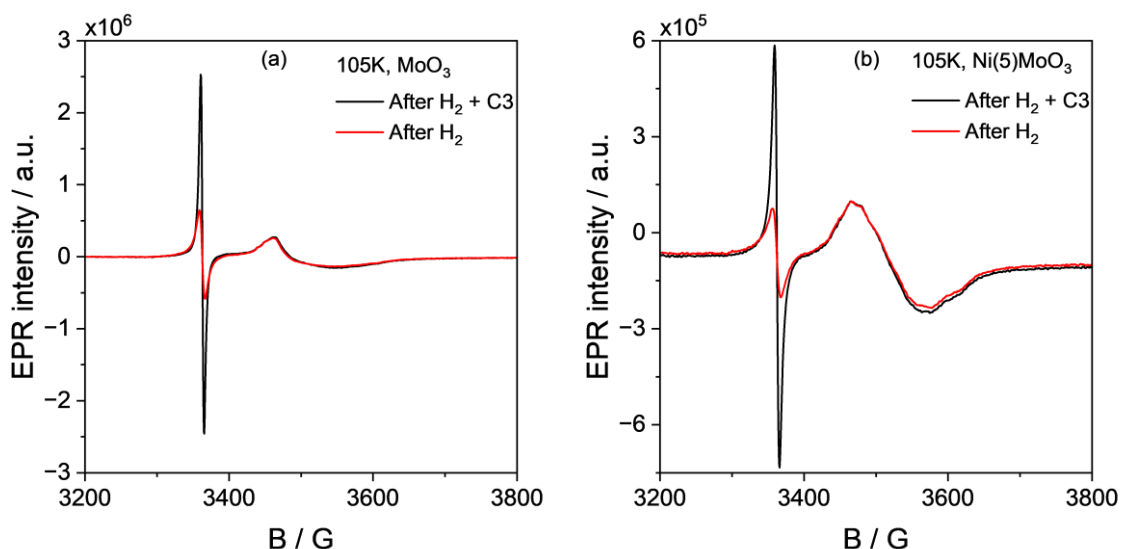


Figure 46: In-situ EPR spectra of a) MoO_3 and b) $\text{Ni}(5)\text{MoO}_3$ recorded at 105K after reduction with a mixture of $\text{H}_2/\text{C}_3\text{H}_6$ for 120 min at 300 °C (black lines), then flushing in Ar for low temperature EPR measurements and following by heating under Ar and exposing to 100 % H_2 for 60 min at 300 °C (red lines).

4.6. TPR/TPD of $\text{H}_2/\text{C}_3\text{H}_6$ Treated Samples

As discussed before for the operando DRIFTS investigations of the DME HDO, it is not clear if the $\text{MoO}_x\text{C}_y\text{H}_z$ phase can be decomposed and forms CO and CO_2 at reaction temperature (see chapter 4.2.6). Therefore, TPD/TPR experiments have been carried out to investigate the potential role of $\text{MoO}_x\text{C}_y\text{H}_z$ for this gas formation during the HDO. To avoid a carbon and oxygen source by the feed gas, $\text{Ni}(5)\text{MoO}_3$ and MoO_3 were treated in a separate activation reactor with $\text{H}_2/\text{C}_3\text{H}_6$ (9:1) for ca. 5 h at 325 °C to form $\text{MoO}_x\text{C}_y\text{H}_z$ (see chapter 4.3). Subsequently, TPR experiments in 5 % H_2 and TPD experiments in Ar were conducted for both samples with a heating rate of 10 °C/min.

The TPD experiment of $\text{Ni}(5)\text{MoO}_3$ showed that first a desorption of water occurs, which seems to have two different reasons as the first maximum is at ca. 150 °C and a second one approx. at 320 °C (see Figure 47). It is likely that the first desorption is related to the physisorbed water after the sample is exposed to air. The second one could be related to water that desorbs at higher temperatures due to chemisorption effects and stronger interactions with the surface like the O_v . The propene, which is adsorbed after the treatment desorbs at 150 °C and no further propene can be observed. At 300 °C the evolution of H_2 started and increased until its maximum was reached at 450 °C. A second maximum is visible at ca. 730 °C, but stopped at 850 °C. At 340 °C the formation of CO and CO_2 started in parallel and reached the first maximum at 520 °C. At ca. 600 °C the formation of CO and CO_2 started again to increase and reached a maximum at 700 °C. Additional sharp peaks are visible at 700 °C, 750 °C and a large, intense peak at 870 °C is observable. For MoO_3 , the same compounds have been found, except propene, whose

desorption was observed (see A-91). Here the evolution of H₂ started at 300 °C as well with a maximum at 400 °C. In comparison to Ni(5)MoO₃ an additional maximum of the water formation at 450 °C occurred, but in accordance to it the CO and CO₂ formation started at ca. 400 °C and a maximum existed at 720 °C and at 820 °C.

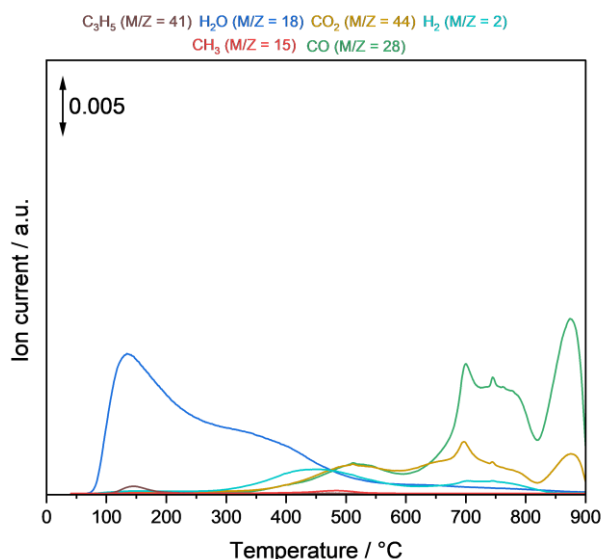


Figure 47: TPD-MS of Ni(5)MoO₃ in Ar with a heating rate of 10 °C/min after 5 h treatment at 325 °C in H₂:C₃H₆ (9:1).

For the TPR experiment with hydrogen, the result does not differ significantly. Ni(5)MoO₃ started to desorb a very small amount of propene at \approx 140 °C, while water started to desorb at ca. 90 °C with two maximums at 130 °C and 190 °C, followed by a shoulder at 330 °C (see Figure 48). It decreased slightly until 500 °C is reached and the water formation started to increase again. It can be assumed that this is related to the MoO_x reduction by H₂. However, since several phases (MoO_xH_z, MoO_xC_yH_z, MoO_{3-x}) are present and the water peaks are not clearly separated, it is difficult to distinguish between H₂O, which desorbs at low temperatures and water formed by reduction.

CO and CO₂ started to form at ca. 350 °C with a first maximum ca. 530 °C. As observed for the TPD experiments, several peaks at higher temperatures (720 °C, 780 °C and 880 °C) for the CO₂ and CO evolution were observed again. Only very small amounts of methane were formed between 380 °C and ca. 500 °C. This was also observed when MoO₃ is tested by H₂-TPR (see A-92). However, between MoO₃ and Ni(5)MoO₃ were differences visible, which were not observed in the TPD experiments (compare A-92 and Figure 48). After the first desorption of water at ca. 150 °C, this signal started to decrease until it increased again until a large maximum at 580 °C was reached. The formation of CO and CO₂ was only hardly observable in the range between 400 °C and 500 °C for MoO₃ but started significantly at 650 °C (see A-92). It had two maximums, one at 830 °C and one shoulder at lower temperatures (780 °C).

These obtained results can be explained by two effects, which might occur at the same time. First, during the initial treatment in H_2/C_3H_6 a coke layer could be deposited on the catalyst surface. This coke could be degraded at higher temperatures, which is done by an oxidation making use of the lattice oxygen (see Eq. 12).²²⁴ Because only a limited amount of lattice oxygen can be provided, the oxidation slows down with increasing temperature. Theoretically, the MoO_2 reduction by carbon forming metallic Mo^0 or MoC_2 would be possible as well and could explain the CO/CO_2 formation at temperatures above 700 °C. The second reason could be a decomposition of the formed $MoO_xC_yH_z$ phase (see Eq. 13).²⁵ The formation of hydrogen might originate from nascent hydrogen which is intercalated into the lattice structure of the molybdenum oxycarbide or molybdenum oxide (see Eq. 14 and Eq. 15).^{44, 162, 163} During the H_2 -TPR it is not possible to distinguish between formed H_2 or a decreasing reduction process.

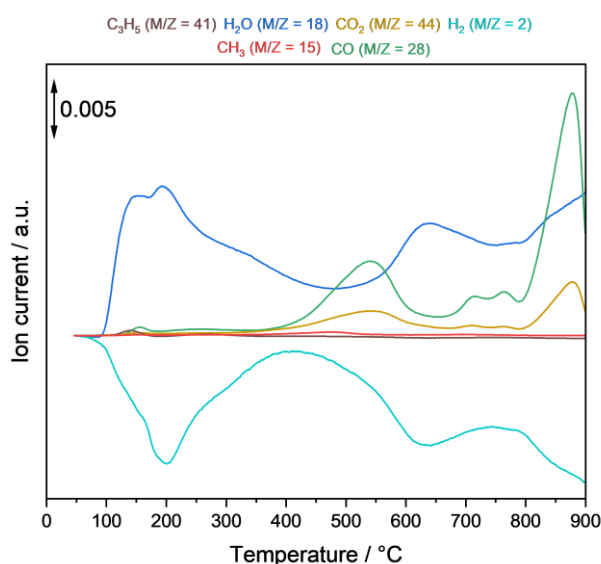
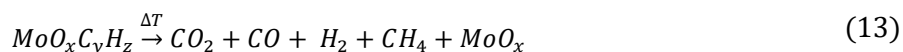
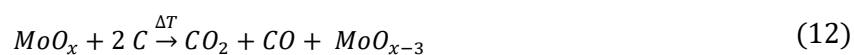


Figure 48: TPR-MS of Ni(5)MoO₃ in H₂ with a heating rate of 10 °C/min after 5 h treatment at 325 °C in H₂:C₃H₆ (9:1).

The CO is most likely generated by the $MoO_xC_yH_z$ degradation as the intrinsic oxygen could also oxidize the carbon. This could cause CO_2 formation as well. The fact that CO is a MS fragment of CO_2 makes it difficult to differentiate between processes which form these gases. Nevertheless, the TPD of Ni(5)MoO₃ shows that they are formed simultaneously at least in the range between 350 °C and 600 °C, since the signal intensity is equal and only minor amounts of CO_2 are fragmented to CO (see Figure 47). This matches the temperature range at which the $MoO_xC_yH_z$ phase is decomposed according to literature.²⁵ Additionally, the absence of these peaks for MoO_3 , which is known for forming less $MoO_xC_yH_z$, supports this and is an explanation for the DRIFTS results (see chapter 4.2.6).

Therefore, it can be assumed that CO and CO₂ are formed by a thermal treatment in either inert atmosphere, oxidative or under reductive conditions. Presumably the decomposition of MoO_xC_yH_z is responsible for the formation at temperatures around 400 °C and at high temperatures (≥ 700 °C) it is the degradation of carbonous deposits. It indicates that the catalyst is working as an oxidation catalyst as well under working conditions.



5. Structure-Reactivity Relationships

The structure-reactivity relationships can be derived from the results obtained in this work, which demonstrate that the $\text{MoO}_x\text{C}_y\text{H}_z$ phase is a crucial factor in the activity and stability of nickel-modified MoO_3 -based catalysts in HDO reactions. Initially, it was demonstrated that the introduction of nickel to MoO_3 catalysts did not result in a doped form of MoO_3 in which lattice Mo atoms are substituted. Instead, a NiMoO_4 phase was formed, composed of small crystallites situated alongside larger MoO_3 crystallites. This was evidenced by XRD and REM measurements. The addition of small amounts Ni (≤ 5 wt.%) significantly enhanced the catalytic activity, while exhibiting minimal impact on selectivity. It was observed that an increase in Ni content beyond a certain threshold resulted in an enhancement of activity, accompanied by a notable rise in methane selectivity. This phenomenon can be attributed to the decomposition of aromatic rings. The $\text{MoO}_x\text{C}_y\text{H}_z$ phase was identified in all catalysts, whether in a liquid- or gas-phase reaction, by ex-situ XRD, except for pure NiMoO_4 . This suggests that $\text{MoO}_x\text{C}_y\text{H}_z$ is also present in the active phase of nickel-added catalysts, as it has been previously identified in the literature for pure phase MoO_3 .

In liquid-phase experiments, MoO_3 exhibited low activity with regard to anisole and phenol. The addition of Ni resulted in an increase in activity, although the selectivity shifted towards hydrogenated products (cyclohexane). In the case of guaiacol, it was unexpected that MoO_3 exhibited the highest level of activity, but the formation of a black reaction product was observed. This phenomenon can be attributed to the Brønsted acidity of the catalyst, which facilitated the polymerization of guaiacol, a process that is not feasible for other substrates. These results demonstrate that MoO_3 -based catalysts appear to be unsuitable for liquid-phase HDO with guaiacol.

Catalytic tests conducted with $\text{Ni}/\alpha\text{-Al}_2\text{O}_3$ (3 wt.% Ni) demonstrated that metallic Ni is primarily active in the C-C hydrogenolysis. However, the activity and selectivity towards methane was found to be increased in comparison to $\text{Ni}(5)\text{MoO}_3$ and NiMoO_4 , indicating that Ni is not a dominating active phase for nickel modified MoO_3 -based catalysts. Furthermore, the deactivation of $\text{Ni}/\alpha\text{-Al}_2\text{O}_3$ was observed to occur rapidly, while almost no deactivation was observed for nickel modified MoO_3 -based catalysts within 17 h TOS.

A systematic XRD study on the $\text{MoO}_x\text{C}_y\text{H}_z$ phase demonstrated that the addition of nickel and reactive substrates are beneficial for its formation. Tests were conducted in a H_2/CH_4 and $\text{H}_2/\text{C}_3\text{H}_6$ mixture, which demonstrated that the use of a propene mixture resulted in a significantly more pronounced formation of the $\text{MoO}_x\text{C}_y\text{H}_z$ phase. The reason for this phenomenon is not yet fully clear. It may be explained by an improved reduction promoted by propene and thus an improved carbon insertion. Nevertheless, the enhanced reduction

of MoO_3 is beneficial for the $\text{MoO}_x\text{C}_y\text{H}_z$ formation, which explains the greater formation of it in Ni-added catalysts.

For example, if Ni(5)MoO_3 (**1**) is reduced, it results in the reduction of the NiMoO_4 part, for which a phase separation occurs forming Ni particles embedded in a MoO_x matrix (**2**) (see Figure 49). This was observed by TPR, pseudo in-situ XPS and in-situ TEM experiments. The metallic nickel can activate hydrogen, which can migrate via H-spillover on and inside the MoO_x lattice and forms MoO_xH_z (**3**). $\text{MoO}_x\text{C}_y\text{H}_z$ (**4**) is formed in a carbon containing atmosphere by inserting carbon and prevents the formation of MoO_2 . It has been demonstrated in literature that pre-reduced MoO_3 forms the oxycarbohydride rapidly (see chapter 2.4). In order to form $\text{MoO}_x\text{C}_y\text{H}_z$ without metallic Ni, the MoO_3 must be reduced to MoO_2 , which is also able to activate hydrogen but does not catalyze the HDO reaction. Because the MoO_2 cannot be transformed into $\text{MoO}_x\text{C}_y\text{H}_z$ this will result in a less active catalyst with a higher amount of MoO_2 . However, the presence of Ni does not prevent MoO_2 formation, but rather reduces its formed content. Therefore, it can be concluded that a maximization of $\text{MoO}_x\text{C}_y\text{H}_z$ is directly related to a highly active catalyst.

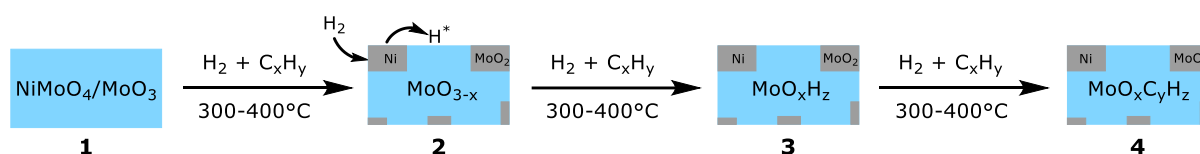


Figure 49: $\text{MoO}_x\text{C}_y\text{H}_z$ phase formation with MoO_3 -based nickel modified catalysts. Reproduced from Ref.¹⁹⁷ with permission from the Royal Society of Chemistry.

In-situ DRIFTS experiments on pre-reduced NiMoO_4 , Ni(5)MoO_3 and MoO_3 revealed that methane is produced following the adsorption of benzene and the introduction of hydrogen into the cell. As benzene desorbed completely before switching to the H_2 feed, a direct C-C hydrogenolysis is not feasible and the only plausible explanation for the observed methane evolution is the hydrogenation of the $\text{MoO}_x\text{C}_y\text{H}_z$ phase. Simultaneous mass spectroscopic monitoring demonstrated that methane is formed by NiMoO_4 and MoO_3 catalysts, with a significantly enhanced CH_4 production observed for nickel molybdate. This observation explains not only the high methane selectivity but also indicates the formation of the oxycarbohydride for NiMoO_4 , despite the absence of its identification in spent catalysts or in-situ XRD experiments. It can thus be postulated that following reduction and subsequent formation of $\text{MoO}_x\text{C}_y\text{H}_z$, the concentration of nickel is so high that $\text{MoO}_x\text{C}_y\text{H}_z$ is hydrogenated at a faster rate than it is formed.

Based on these results, an extended mechanism for the HDO with MoO_3 -based catalysts can be postulated. Starting from MoO_3 (**1**), it includes the formation of an active phase by the creation of a molybdenum bronze (**2**) (MoO_xH_z) by reduction and the subsequent formation of the oxycarbohydride (**3**) $\text{MoO}_x\text{C}_y\text{H}_z$ (see Figure 50). This phase can be

hydrogenated back to the bronze (**2**), which results in an equilibrium between both phases and the formation of methane. Afterwards, the HDO is conducted at O_v of $MoO_xC_yH_z$ as postulated in literature for MoO_3 . The substrate (here anisole) is adsorbing at the O_v (**4**) and hydrogen forms an acidic hydroxyl and a hydride (**5**) by hydrogenating the $M=O$ group. After hydrogenolysis of the methoxy group and methane formation, phenol is formed on the catalyst surface and the $M=O$ group is restored (**6**). Subsequently, a hydroxyl group and hydride are formed again by hydrogen addition, which deoxygenated the phenol (**7**) and forms benzene. Finally, the second hydroxyl group is removed by a condensation reaction (**8**) restoring the O_v and ending up in the initial state (**3**). There deoxygenation can start again, or the $MoO_xC_yH_z$ can be hydrogenated. It needs to be mentioned, that the exact structure of $MoO_xC_yH_z$ is not known and this catalytic cycle is a model. Additionally, MoO_xH_z could have O_v as well and catalyze the HDO.

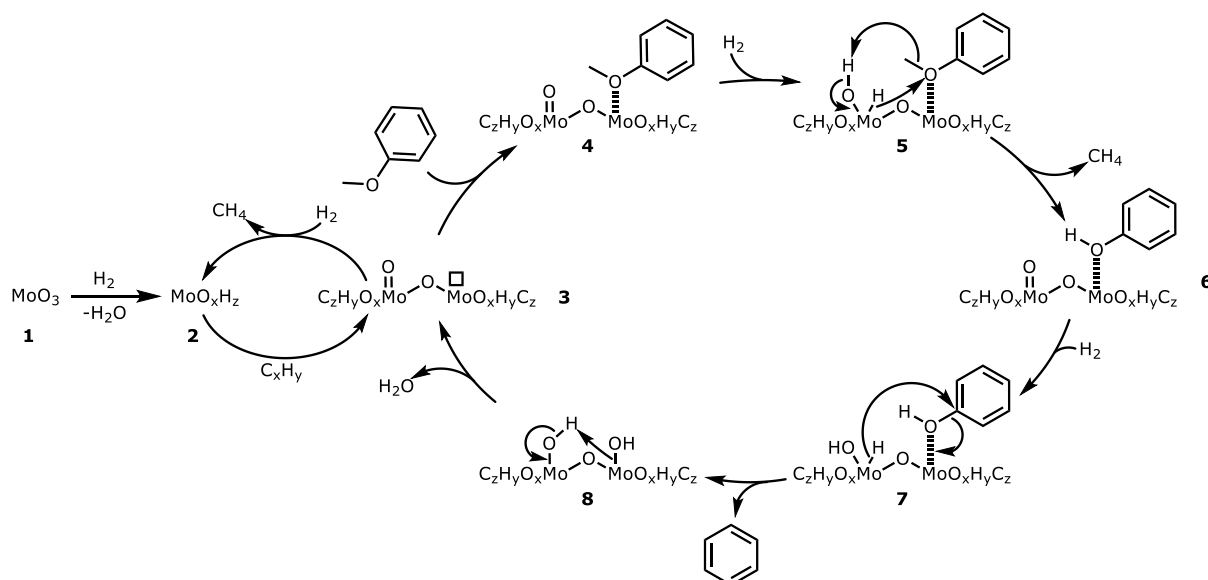


Figure 50: Extended mechanism of HDO at MoO_3 -based catalysts. Reproduced from Ref.¹⁹⁷ with permission from the Royal Society of Chemistry.

For catalysts with a high concentration of Ni (e.g. $NiMoO_4$), more H_2 might be activated and this shifts the equilibrium towards MoO_xH_z . However, this does not imply that $MoO_xC_yH_z$ is not formed, rather it is hydrogenated immediately, thereby increasing the methane selectivity. Furthermore, $MoO_xC_yH_z$ is discussed to protect Mo^{5+} from reduction to inactive Mo^{4+} . It is conceivable that this protection is achieved by a more reactive carbon atom within the oxycarbohydride structure, which is hydrogenated at a faster rate than the lattice oxygen, consuming available H_2 . These findings were corroborated by in-situ EPR experiments, which revealed that the O_v concentration increases when samples are treated in a H_2/C_3H_6 mixture at 300 °C. Additionally, the formation of a carbonous species and distinct Mo^{5+} species was observed, indicating that this oxidation state is crucial for O_v formation and consequently for the HDO reaction.

Operando DRIFTS and TPD/TPR experiments of activated samples in H_2/C_3H_6 at 325 °C suggest that MoO_3 -based catalysts are still active for oxidation reactions under reductive conditions. In both cases, CO and CO_2 have been found at temperatures above 300 °C. A hypothesis is that $MoO_xC_yH_z$ is decomposing itself by oxidizing the carbon with lattice oxygen. Nevertheless, it can be assumed that carbon species e.g. coke deposits and reaction educts are oxidized as well and MoO_3 -based catalysts do not lose their oxidation capabilities at reductive conditions. However, a gas-phase analysis under operando conditions has not been done yet to prove this hypothesis.

6. Outlook

Although progress has been made in the understanding of the structure-reactivity relationships of MoO₃-based HDO catalysts, further investigation is required in certain areas. First, the impact of different reaction parameters, which were evaluated here solely at 325 °C and atmospheric pressure, must be examined to identify the optimal operational conditions. The influence of an increased pressure on the gas-phase HDO has not yet been studied.

For more insights into the structure-reactivity relationships, catalytic test with a MoO_xC_yH_z enriched MoO₃ without the addition of nickel might be useful. This would help to understand the single contributions to the catalyst performance of Ni and MoO_xC_yH_z. It could be done by selecting the right precursor and pretreatment. Molybdenum blue is discussed in literature to form a pure phase MoO_xC_yH_z.

Moreover, additional research is required to elucidate the gas-phase product composition and the activity of MoO₃-based catalysts for oxidation reactions in a reductive atmosphere. Consequently, in addition to the online GC, an MS must be coupled, and further modifications to the test configuration are required. An additional product stream must be incorporated, whereby the condensate products with high boiling points are directed through a cold trap to protect the online gas analyzer. Nevertheless, this data is crucial, as experimental findings suggest the existence of CO and CO₂ compounds.

Finally, studies on catalyst improvements can be made. The influence of different support materials has not been studied so far but would have the chance to increase the activity by e.g. increased surface areas. Furthermore, the influence of alternative modifying metals instead of nickel might enhance the catalyst performance. For this, metals like Cu, Re, Pt or Fe can be used to study their influence on active phase formation and catalysts activity.

But not only the addition of these metals to form metal molybdates could provide promising results. Doping by replacing the lattice position of Mo could be interesting, as dopants with low valence (Ce, V, Zn, Cu) could have an influence on the O_v properties and concentration. This could have an impact on the adsorption of organic substrates and intermediates. New synthesis methods need to be found to obtain these doped catalysts, as the metal molybdates are very stable and would be preferentially formed. This would subsequently require the search for suitable reaction conditions to avoid the destruction of the doped materials under HDO conditions.

7. References

1. R. Shwom and J. A. Lorenzen, *WIREs Clim. Change*, **2012**, 3, 379-395.
2. A. Isella and D. Manca, *Energies*, **2022**, 15, 7560-7573.
3. M. Baerns, A. Behr, A. Brehm, J. Gmehling, K.-O. Hinrichsen, H. Hofmann, U. Onken, R. Palkovits and A. Renken, *Technische Chemie*, Wiley-VCH, Weinheim, **2013**.
4. R. A. Sheldon, *Green Chem.*, **2014**, 16, 950-963.
5. R. Ahorsu, F. Medina and M. Constantí, *Energies*, **2018**, 11, 3366-3385.
6. D. S. Bajwa, G. Pourhashem, A. H. Ullah and S. G. Bajwa, *Ind. Crops Prod.*, **2019**, 139, 111526-111537.
7. J. H. Zhang, J. M. Sun and Y. Wang, *Green Chem.*, **2020**, 22, 1072-1098.
8. <https://www.fao.org/forestry/statistics/80571/en/>, (accessed 20.03.2024).
9. L. A. Zevallos Torres, A. Lorenci Woiciechowski, V. O. de Andrade Tanobe, S. G. Karp, L. C. Guimarães Lorenci, C. Faulds and C. R. Soccol, *J. Cleaner Prod.*, **2020**, 263, 121499-121517.
10. P. J. De Wild, W. J. J. Huijgen and R. J. A. Gosselink, *Biofuels, Bioprod. Biorefin.*, **2014**, 8, 645-657.
11. J. Y. Kim, H. W. Lee, S. M. Lee, J. Jae and Y. K. Park, *Bioresour. Technol.*, **2019**, 279, 373-384.
12. C. Li, X. Zhao, A. Wang, G. W. Huber and T. Zhang, *Chem. Rev.*, **2015**, 115, 11559-11624.
13. F. Yue, F. Lu, R. Sun and J. Ralph, *Chemistry*, **2012**, 18, 16402-16410.
14. G. W. Huber, S. Iborra and A. Corma, *Chem. Rev.*, **2006**, 106, 4044-4098.
15. R. Olcese, M. M. Bettahar, B. Malaman, J. Ghanbaja, L. Tibavizco, D. Petitjean and A. Dufour, *Appl. Catal., B*, **2013**, 129, 528-538.
16. H. Y. Zhao, D. Li, P. Bui and S. T. Oyama, *Appl. Catal., A*, **2011**, 391, 305-310.
17. J. Feroso, P. Pizarro, J. M. Coronado and D. P. Serrano, *WIREs Energy Environ.*, **2017**, 6.
18. P. M. Mortensen, J. D. Grunwaldt, P. A. Jensen, K. G. Knudsen and A. D. Jensen, *Appl. Catal., A*, **2011**, 407, 1-19.
19. A. M. Robinson, J. E. Hensley and J. W. Medlin, *ACS Catal.*, **2016**, 6, 5026-5043.
20. J. C. Serrano-Ruiz and J. A. Dumesic, *Energy Environ. Sci.*, **2011**, 4, 83-99.
21. R. N. Olcese, G. Lardier, M. Bettahar, J. Ghanbaja, S. Fontana, V. Carre, F. Aubriet, D. Petitjean and A. Dufour, *ChemSusChem*, **2013**, 6, 1490-1499.
22. X. C. Wang, M. Arai, Q. F. Wu, C. Zhang and F. Y. Zhao, *Green Chem.*, **2020**, 22, 8140-8168.
23. S. Kim, E. E. Kwon, Y. T. Kim, S. Jung, H. J. Kim, G. W. Huber and J. Lee, *Green Chem.*, **2019**, 21, 3715-3743.
24. R. J. Angelici, *Polyhedron*, **1997**, 16, 3073-3088.
25. T. Prasomsri, M. Shetty, K. Murugappan and Y. Roman-Leshkov, *Energy Environ. Sci.*, **2014**, 7, 2660-2669.
26. M. Shetty, E. M. Anderson, W. H. Green and Y. Roman-Leshkov, *J. Catal.*, **2019**, 376, 248-257.
27. C. Ranga, R. Lodeng, V. I. Alexiadis, T. Rajkhowa, H. Bjorkan, S. Chytil, I. H. Svenum, J. Walmsley, C. Detavernier, H. Poelman, P. Van der Voort and J. W. Thybaut, *Chem. Eng. J.*, **2018**, 335, 120-132.
28. M. Shetty, K. Murugappan, W. H. Green and Y. Roman-Leshkov, *ACS Sustainable Chem. Eng.*, **2017**, 5, 5293-5301.
29. M. Shetty, K. Murugappan, T. Prasomsri, W. H. Green and Y. Roman-Leshkov, *J. Catal.*, **2015**, 331, 86-97.
30. T. Prasomsri, T. Nimmanwudipong and Y. Román-Leshkov, *Energy Environ. Sci.*, **2013**, 6, 1732-1738.
31. L.-P. Xiao, S. Wang, H. Li, Z. Li, Z.-J. Shi, L. Xiao, R.-C. Sun, Y. Fang and G. Song, *ACS Catal.*, **2017**, 7, 7535-7542.
32. G. B. Báfero, G. B. Strapasson, D. S. Leite and D. Zanchet, *ChemCatChem*, **2023**, 15, 13.
33. E. W. McFarland and H. Metiu, *Chem. Rev.*, **2013**, 113, 4391-4427.

34. H. Metiu, S. Chretien, Z. P. Hu, B. Li and X. Y. Sun, *J. Phys. Chem. C*, **2012**, 116, 10439-10450.
35. A. Aqsha, L. Katta and N. Mahinpey, *Catal. Lett.*, **2015**, 145, 1351-1363.
36. T. He, X. Liu, Y. Ge, D. Han, J. Li, Z. Wang and J. Wu, *Catal. Commun.*, **2017**, 102, 127-130.
37. T. Hu, S. M. Gericke, X. Tong, D. Nykypanchuk, T. Kristensen, C. Hulteberg, D. Stacchiola, S. Blomberg and A. R. Head, *J. Phys. Chem. C*, **2023**, 127, 19440-19450.
38. V. Itthibenchapong, P. Chakthranont, C. Sattayanon, T. Butburee, K. Faungnawakij and S. Namuangruk, *Appl. Surf. Sci.*, **2021**, 547.
39. K. Kon, T. Toyao, W. Onodera, S. M. A. H. Siddiki and K. i. Shimizu, *ChemCatChem*, **2017**, 9, 2822-2827.
40. C. Ranga, V. I. Alexiadis, J. Lauwaert, R. Lodeng and J. W. Thybaut, *Appl. Catal., A*, **2019**, 571, 61-70.
41. J. Zhang, C. Li, W. X. Guan, X. Z. Chen, X. Chen, C. Tsang and C. H. Liang, *Ind. Eng. Chem. Res.*, **2020**, 59, 4313-4321.
42. J. Zhang, C. Li, W. X. Guan, X. Z. Chen, X. Chen, C. W. Tsang and C. H. Liang, *J. Catal.*, **2020**, 383, 311-321.
43. D. Raikwar, M. Munagala, S. Majumdar and D. Shee, *Catal. Today*, **2019**, 325, 117-130.
44. C. Bouchy, C. Pham-huu and M. J. Ledoux, *J. Mol. Catal. A: Chem.*, **2000**, 162, 317-334.
45. H. Yu, W. Xiao, L. Han and G. Huang, *Bioresour. Technol.*, **2019**, 282, 69-74.
46. J. D. Medina, A. Woiciechowski, A. Zandona Filho, M. D. Nosedá, B. S. Kaur and C. R. Soccol, *Bioresour. Technol.*, **2015**, 194, 172-178.
47. N.-E. E. Mansouri and J. Salvadó, *Ind. Crops Prod.*, **2006**, 24, 8-16.
48. R. J. A. Gosselink, E. de Jong, B. Guran and A. Abacherli, *Ind. Crops Prod.*, 2004, 20, 121-129.
49. L. Dessbesell, M. Paleologou, M. Leitch, R. Pulkki and C. Xu, *Renewable Sustainable Energy Rev.*, **2020**, 123, 109768-109779.
50. M. Ghorbani, J. Konnerth, H. W. G. van Herwijnen, G. Zinovyev, E. Budjav, A. Requejo Silva and F. Liebner, *J. Appl. Polym. Sci.*, **2017**, 135, 45893-45904.
51. F. S. Chakar and A. J. Ragauskas, *Ind. Crops Prod.*, **2004**, 20, 131-141.
52. D. Mboowa, *Biomass Convers. Biorefin.*, **2021**, 14, 1-12.
53. S. Goncalves, J. Ferra, N. Paiva, J. Martins, L. H. Carvalho and F. D. Magalhaes, *Polymers*, **2021**, 13, 4196-4225.
54. T. Aro and P. Fatehi, *ChemSusChem*, **2017**, 10, 1861-1877.
55. T. Li and S. Takkellapati, *Biofuels, Bioprod. Biorefin.*, **2018**, 12, 756-787.
56. G. Gellerstedt, *Ind. Crops Prod.*, **2015**, 77, 845-854.
57. C. J. Biermann, *Handbook of Pulping and Papermaking*, Academic Press Inc, San Diego, 2 edn., **1996**.
58. M. S. Jahan, M. M. Rahman and Y. Ni, *Biofuels, Bioprod. Biorefin.*, **2020**, 15, 100-118.
59. E. Terrell, L. D. Dellon, A. Dufour, E. Bartolomei, L. J. Broadbelt and M. Garcia-Perez, *Ind. Eng. Chem. Res.*, **2019**, 59, 526-555.
60. C. Xu, R. A. Arancon, J. Labidi and R. Luque, *Chem. Soc. Rev.*, **2014**, 43, 7485-7500.
61. C. Liu, H. Wang, A. M. Karim, J. Sun and Y. Wang, *Chem. Soc. Rev.*, **2014**, 43, 7594-7623.
62. J. Zakzeski, P. C. Bruijninx, A. L. Jongerius and B. M. Weckhuysen, *Chem. Rev.*, **2010**, 110, 3552-3599.
63. R. G. Ramirez Brenes, E. M. Alhadeff, N. Bojorge, L. E. M. Trales and G. A. D. Pazos, *Biofuels, Bioprod. Biorefin.*, **2022**, 17, 664-681.
64. E. I. Kozliak, A. Kubátová, A. A. Artemyeva, E. Nagel, C. Zhang, R. B. Rajappagowda and A. L. Smirnova, *ACS Sustainable Chem. Eng.*, **2016**, 4, 5106-5122.
65. H. M. Wang, J. Male and Y. Wang, *ACS Catal.*, **2013**, 3, 1047-1070.
66. Y. Huang, Y. L. Hu, F. H. Ye and Y. M. Fang, *Energy Fuels*, **2017**, 31, 8356-8362.
67. J. G. Brammer, M. Lauer and A. V. Bridgwater, *Energy Policy*, **2006**, 34, 2871-2880.

68. S. Gillet, M. Aguedo, L. Petitjean, A. R. C. Morais, A. M. D. Lopes, R. M. Lukasik and P. T. Anastas, *Green Chem.*, **2017**, 19, 4200-4233.
69. A. Kumar, Anushree, J. Kumar and T. Bhaskar, *J. Energy Inst.*, **2020**, 93, 235-271.
70. H. Tan, C. T. Lee, P. Y. Ong, K. Y. Wong, C. P. C. Bong, C. Li and Y. Gao, *IOP Conf. Ser.: Mater. Sci. Eng.*, **2021**, 1051, 012075-012083.
71. L. Cao, I. K. M. Yu, Y. Liu, X. Ruan, D. C. W. Tsang, A. J. Hunt, Y. S. Ok, H. Song and S. Zhang, *Bioresour. Technol.*, **2018**, 269, 465-475.
72. L. Fan, Y. Zhang, S. Liu, N. Zhou, P. Chen, Y. Cheng, M. Addy, Q. Lu, M. M. Omar, Y. Liu, Y. Wang, L. Dai, E. Anderson, P. Peng, H. Lei and R. Ruan, *Bioresour. Technol.*, **2017**, 241, 1118-1126.
73. J. O. Ighalo, F. U. Iwuchukwu, O. E. Eyankware, K. O. Iwuozor, K. Olotu, O. C. Bright and C. A. Igwegbe, *Clean Technol. Environ. Policy*, **2022**, 24, 2349-2363.
74. J. N. Putro, F. E. Soetaredjo, S.-Y. Lin, Y.-H. Ju and S. Ismadji, *RSC Adv.*, **2016**, 6, 46834-46852.
75. G. Chang, Y. Huang, J. Xie, H. Yang, H. Liu, X. Yin and C. Wu, *Energy Convers. Manage.*, **2016**, 124, 587-597.
76. L. Qu, X. Jiang, Z. Zhang, X.-g. Zhang, G.-y. Song, H.-l. Wang, Y.-p. Yuan and Y.-l. Chang, *Green Chem.*, **2021**, 23, 9348-9376.
77. J. Poissonnier, C. Ranga, R. Lødeng and J. W. Thybaut, *Fuel*, **2022**, 308, 121940-121949.
78. E. Furimsky, *Appl. Catal., A*, **2000**, 199, 147-190.
79. M. W. Nolte and B. H. Shanks, *Energy Technology*, **2017**, 5, 7-18.
80. W. Jin, L. Pastor-Perez, D. K. Shen, A. Sepulveda-Escribano, S. Gu and T. R. Reina, *ChemCatChem*, **2019**, 11, 924-960.
81. M. J. Gilkey, C. Brady, D. G. Vlachos and B. Xu, *Ind. Eng. Chem. Res.*, **2018**, 57, 5591-5598.
82. Y. Muharam and J. A. Soedarsono, *International Journal of Technology*, **2020**, 11, 1292-1299.
83. D. U. Dkala, M. D. Saban, A. M. Orlovic, V. W. Meyn, D. K. Severin, I. G. H. Rahimian and M. V. Marjanovic, *Ind. Eng. Chem. Res.*, **1991**, 30, 2059-2065.
84. M. Grilc and B. Likozar, *Chem. Eng. J.*, **2017**, 330, 383-397.
85. R. S. Kukard and K. J. Smith, *Energy Fuels*, **2015**, 29, 5274-5281.
86. B. K. Sharma and K. Kohli, *ISTC Reports*, **2020**.
87. M. Grilc, B. Likozar and J. Levec, *Biomass Bioenergy*, **2014**, 63, 300-312.
88. I. T. Ghampson, G. Pecchi, J. L. G. Fierro, A. Videla and N. Escalona, *Appl. Catal., B*, **2017**, 208, 60-74.
89. P. M. Mortensen, J.-D. Grunwaldt, P. A. Jensen and A. D. Jensen, *Catal. Today*, **2016**, 259, 277-284.
90. W. Wang, K. Zhang, L. Li, K. Wu, P. Liu and Y. Yang, *Ind. Eng. Chem. Res.*, **2014**, 53, 19001-19009.
91. V. M. L. Whiffen and K. J. Smith, *Energy Fuels*, **2010**, 24, 4728-4737.
92. V. O. O. Gonçalves, C. Ciotonea, S. Arrii-Clacens, N. Guignard, C. Roudaut, J. Rousseau, J.-M. Clacens, S. Royer and F. Richard, *Appl. Catal., B*, **2017**, 214, 57-66.
93. T. Nimmanwudipong, R. C. Runnebaum, D. E. Block and B. C. Gates, *Energy Fuels*, **2011**, 25, 3417-3427.
94. R. N. Olcese, M. Bettahar, D. Petitjean, B. Malaman, F. Giovanella and A. Dufour, *Appl. Catal., B*, **2012**, 115-116, 63-73.
95. F. G. Baddour, V. A. Witte, C. P. Nash, M. B. Griffin, D. A. Ruddy and J. A. Schaidle, *ACS Sustainable Chem. Eng.*, **2017**, 5, 11433-11439.
96. S. L. Yohe, H. J. Choudhari, D. D. Mehta, P. J. Dietrich, M. D. Detwiler, C. M. Akatay, E. A. Stach, J. T. Miller, W. N. Delgass, R. Agrawal and F. H. Ribeiro, *J. Catal.*, **2016**, 344, 535-552.
97. D. J. Rensel, S. Rouvimov, M. E. Gin and J. C. Hicks, *J. Catal.*, **2013**, 305, 256-263.
98. W. Wang, L. Li, K. Wu, K. Zhang, J. Jie and Y. Yang, *Appl. Catal., A*, **2015**, 495, 8-16.
99. W. Wang, K. Zhang, Z. Qiao, L. Li, P. Liu and Y. Yang, *Ind. Eng. Chem. Res.*, **2014**, 53, 10301-10309.

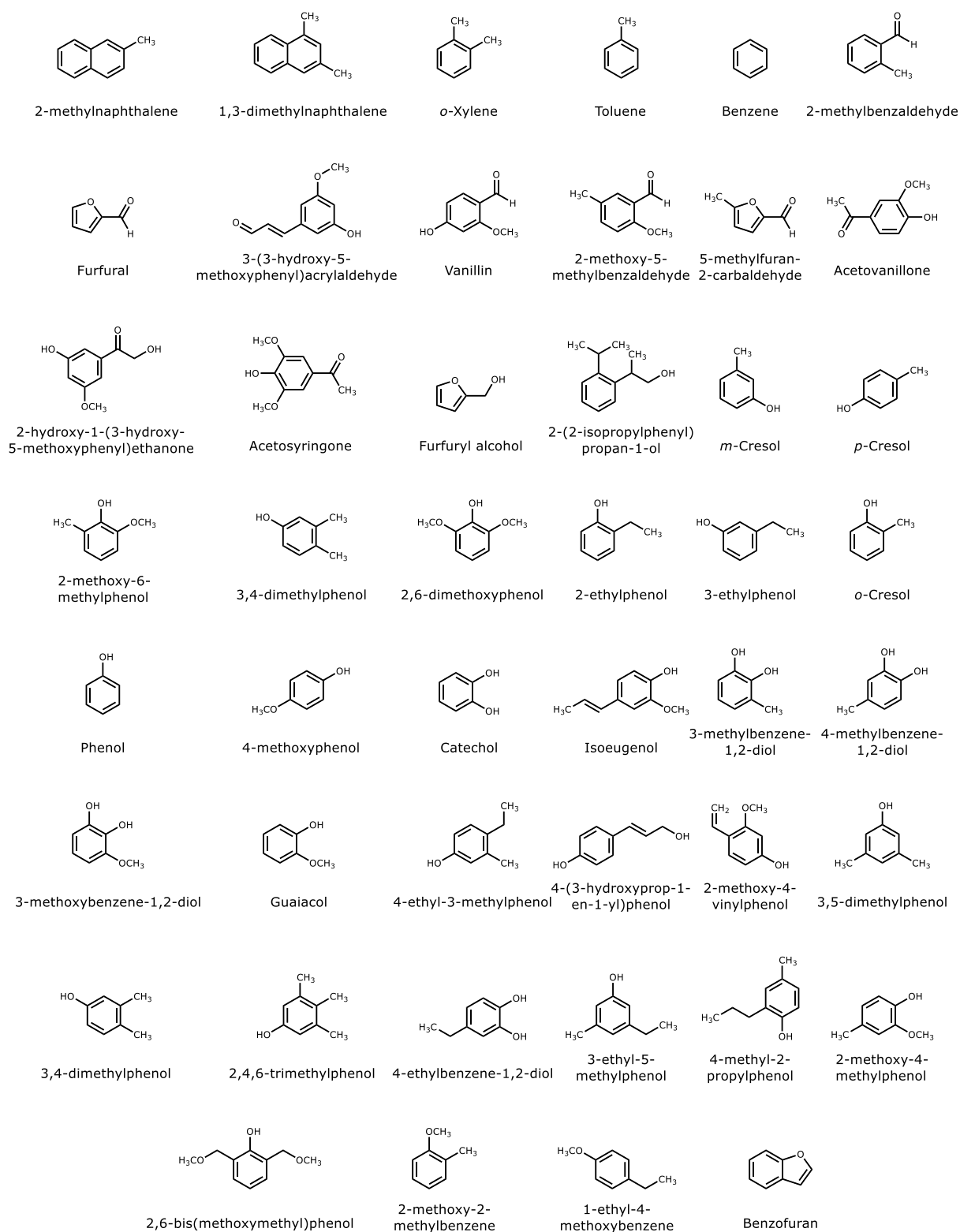
100. W. Song, S. Zhou, S. Hu, W. Lai, Y. Lian, J. Wang, W. Yang, M. Wang, P. Wang and X. Jiang, *ACS Catal.*, **2018**, 9, 259-268.
101. O. İ. Şenol, T. R. Viljava and A. O. I. Krause, *Appl. Catal., A*, **2007**, 326, 236-244.
102. X. H. Zhang, J. J. Tang, Q. Zhang, Q. Y. Liu, Y. P. Li, L. G. Chen, C. G. Wang and L. L. Ma, *Catal. Today*, **2019**, 319, 41-47.
103. W. Wang, K. Wu, L. Li, S. Tan, G. Zhu, W. Li, Z. He and Y. Yang, *Catal. Commun.*, **2016**, 74, 60-64.
104. A. Bjelić, M. Grilc and B. Likozar, *Chem. Eng. J.*, **2018**, 333, 240-259.
105. C. Zhao, J. He, A. A. Lemonidou, X. Li and J. A. Lercher, *J. Catal.*, **2011**, 280, 8-16.
106. T. N. Phan and C. H. Ko, *Catal. Today*, **2018**, 303, 219-226.
107. I. T. Ghampson, C. Sepúlveda, R. García, J. L. G. Fierro and N. Escalona, *Catal. Sci. Technol.*, **2016**, 6, 4356-4369.
108. I. T. Ghampson, R. Canales and N. Escalona, *Appl. Catal., A*, **2018**, 549, 225-236.
109. A. A. Smirnov, Z. Geng, S. A. Khromova, S. G. Zavarukhin, O. A. Bulavchenko, A. A. Saraev, V. V. Kaichev, D. Y. Ermakov and V. A. Yakovlev, *J. Catal.*, **2017**, 354, 61-77.
110. H. Wang, S. Liu and K. J. Smith, *Energy Fuels*, **2016**, 30, 6039-6049.
111. S. Boulloussa-Eiras, R. Lødeng, H. Bergem, M. Stöcker, L. Hannevold and E. A. Blekkan, *Catal. Today*, **2014**, 223, 44-53.
112. V. M. L. Whiffen, K. J. Smith and S. K. Straus, *Appl. Catal., A*, **2012**, 536, 112882-112895.
113. H. Pourzolfaghar, F. Abnisa, W. M. A. Wan Daud and M. K. Aroua, *J. Anal. Appl. Pyrolysis*, **2018**, 133, 117-127.
114. R. C. Runnebaum, T. Nimmanwudipong, D. E. Block and B. C. Gates, *Catal. Sci. Technol.*, **2012**, 2, 113-118.
115. X. Zhu, L. L. Lobban, R. G. Mallinson and D. E. Resasco, *J. Catal.*, **2011**, 281, 21-29.
116. W. Wang, C.-J. Liu and W. Wu, *Catal. Sci. Technol.*, **2019**, 9, 4162-4187.
117. F. Yang, D. Liu, Y. Zhao, H. Wang, J. Han, Q. Ge and X. Zhu, *ACS Catal.*, **2018**, 8, 1672-1682.
118. Y. Hong and Y. Wang, *Catal. Commun.*, **2017**, 100, 43-47.
119. Y. Hong, H. Zhang, J. Sun, K. M. Ayman, A. J. R. Hensley, M. Gu, M. H. Engelhard, J.-S. McEwen and Y. Wang, *ACS Catal.*, **2014**, 4, 3335-3345.
120. Q. Tan, G. Wang, A. Long, A. Dinse, C. Buda, J. Shabaker and D. E. Resasco, *J. Catal.*, **2017**, 347, 102-115.
121. Y. Yang, G. Lv, L. Deng, B. Lu, J. Li, J. Zhang, J. Shi and S. Du, *Microporous Mesoporous Mater.*, **2017**, 250, 47-54.
122. T. M. Sankaranarayanan, A. Berenguer, C. Ochoa-Hernández, I. Moreno, P. Jana, J. M. Coronado, D. P. Serrano and P. Pizarro, *Catal. Today*, **2015**, 243, 163-172.
123. P. T. M. Do, A. J. Foster, J. Chen and R. F. Lobo, *Green Chem.*, **2012**, 14, 1388.
124. P. M. de Souza, R. C. Rabelo-Neto, L. E. P. Borges, G. Jacobs, B. H. Davis, T. Sooknoi, D. E. Resasco and F. B. Noronha, *ACS Catal.*, **2015**, 5, 1318-1329.
125. P. M. de Souza, R. C. Rabelo-Neto, L. E. P. Borges, G. Jacobs, B. H. Davis, D. E. Resasco and F. B. Noronha, *ACS Catal.*, **2017**, 7, 2058-2073.
126. A. M. Barrios, C. A. Teles, P. M. de Souza, R. C. Rabelo-Neto, G. Jacobs, B. H. Davis, L. E. P. Borges and F. B. Noronha, *Catal. Today*, **2018**, 302, 115-124.
127. X. Zhu, L. Nie, L. L. Lobban, R. G. Mallinson and D. E. Resasco, *Energy Fuels*, **2014**, 28, 4104-4111.
128. P. Sirous-Rezaei, J. Jae, K. Cho, C. H. Ko, S.-C. Jung and Y.-K. Park, *Chem. Eng. J.*, **2019**, 377, 120121-120127.
129. W.-S. Lee, Z. Wang, R. J. Wu and A. Bhan, *J. Catal.*, **2014**, 319, 44-53.
130. C.-J. Chen, W.-S. Lee and A. Bhan, *Appl. Catal., A*, **2016**, 510, 42-48.
131. T. Iida, M. Shetty, K. Murugappan, Z. Wang, K. Ohara, T. Wakihara and Y. Román-Leshkov, *ACS Catal.*, **2017**, 7, 8147-8151.
132. T. Ressler, J. Wienold, R. E. Jentoft and F. Girgsdies, *Eur. J. Inorg. Chem.*, **2003**, 301-312.
133. M. A. Banares, J. L. G. Fierro and J. B. Moffat, *J. Catal.*, **1993**, 142, 406-417.
134. J. S. Chung, R. Miranda and C. O. Bennett, *J. Catal.*, **1988**, 114, 398-410.

135. I. E. Wachs, *Catal. Today*, **1996**, 27, 437-455.
136. D. Eder and R. Kramer, *Phys. Chem. Chem. Phys.*, **2002**, 4, 795-801.
137. D. R. Moberg, T. J. Thibodeau, F. G. Amar and B. G. Frederick, *J. Phys. Chem. C*, **2010**, 114, 13782-13795.
138. M. Rellán-Piñeiro and N. López, *ACS Sustainable Chem. Eng.*, **2018**, 6, 16169-16178.
139. M. W. Nolte, A. Saraeian and B. H. Shanks, *Green Chem.*, **2017**, 19, 3654-3664.
140. L. A. Gomez, R. Bababrik, M. R. Komarneni, J. Marlowe, T. Salavati-fard, A. D. D'Amico, B. Wang, P. Christopher and S. P. Crossley, *ACS Catal.*, **2022**, 12, 6313-6324.
141. D. G. B. Dionizio, L. Forrer, G. Berhault, P. M. de Souza and C. A. Henriques, *Mol. Catal.*, **2023**, 536, 112882-112895.
142. A. J. Kohler, C. H. Walter and B. H. Shanks, *ACS Catal.*, **2023**, 13, 14813-14827.
143. P. L. Gai-Boyes, *Catal. Rev.*, **1992**, 34, 1-54.
144. P. A. Spevack and N. S. McIntyre, *J. Phys. Chem.*, **1992**, 96, 9029-9035.
145. G. Mestl, N. F. D. Verbruggen, E. Bosch and H. Knözinger, *Langmuir*, **1996**, 12, 2961-2968.
146. M. Dieterle, G. Weinberg and G. Mestl, *Phys. Chem. Chem. Phys.*, **2002**, 4, 812-821.
147. R. Tokarz-Sobieraj, K. Hermann, M. Witko, A. Blume, G. Mestl and R. Schlögl, *Surf. Sci.*, **2001**, 489, 107-125.
148. M. Witko and R. Tokarz-Sobieraj, *Catal. Today*, **2004**, 91-92, 171-176.
149. R. Coquet and D. J. Willock, *Phys. Chem. Chem. Phys.*, **2005**, 7, 3819-3828.
150. Y.-H. Lei and Z.-X. Chen, *J. Phys. Chem. C*, **2012**, 116, 25757-25764.
151. V. Agarwal and H. Metiu, *J. Phys. Chem. C*, **2016**, 120, 19252-19264.
152. K. Inzani, T. Grande, F. Vullum-Bruer and S. M. Selbach, *J. Phys. Chem. C*, **2016**, 120, 8959-8968.
153. M. Shetty, B. Buesser, Y. Román-Leshkov and W. H. Green, *J. Phys. Chem. C*, **2017**, 121, 17848-17855.
154. D. Mei, A. M. Karim and Y. Wang, *J. Phys. Chem. C*, **2011**, 115, 8155-8164.
155. Y.-H. Lei and Z.-X. Chen, *Appl. Surf. Sci.*, **2016**, 361, 107-113.
156. R. Prins, *Chem. Rev.*, **2012**, 112, 2714-2738.
157. T. Ressler, J. Wienold, R. E. Jentoft and T. Neisius, *J. Catal.*, **2002**, 210, 67-83.
158. O. Glemser and G. Lutz, *Z. anorg. allg. Chemie*, **1951**, 264.
159. T. Leisegang, A. A. Levin, J. Walter and D. C. Meyer, *Cryst. Res. Technol.*, **2004**, 40, 95-105.
160. J. A. Rodriguez, H. Y. Kim, J. C. Hanson and J. L. Brito, *Catal. Lett.*, **2002**, 82, 103-109.
161. C. Bouchy, C. Pham-Huu, B. Heinrich, C. Chaumont and M. J. Ledoux, *J. Catal.*, **2000**, 190, 92-103.
162. C. Bouchy, C. Pham-Huu, B. Heinrich, E. G. Derouane, S. B. Derouane-Abd Hamid and M. J. Ledoux, *Appl. Catal., A*, **2001**, 215, 175-184.
163. P. Delporte, F. Meunier, C. Phamhuu, P. Vennegues, M. J. Ledoux and J. Guille, *Catal. Today*, **1995**, 23, 251-267.
164. K. Murugappan, E. M. Anderson, D. Teschner, T. E. Jones, K. Skorupska and Y. Roman-Leshkov, *Nature Catal.*, **2018**, 1, 960-967.
165. K. Cui, L. Yang, Z. S. Ma, F. Yan, K. Wu, Y. S. Sang, H. Chen and Y. D. Li, *Applied Catalysis B-Environmental*, **2017**, 219, 592-602.
166. P. A. Spevack and N. S. McIntyre, *J. Phys. Chem.*, **2002**, 97, 11031-11036.
167. M. Burgstaller, H. Lund, M. O'Sullivan and H. Huppertz, *Int. J. Refract. Met. Hard Mater.*, **2023**, 111, 106054.
168. A. L. Al-Otaibi, T. Ghrib, M. Alqahtani, M. A. Alharbi, R. Hamdi and I. Massoudi, *Chem. Phys.*, **2019**, 525, 110410.
169. J. L. Shen, S. J. Guo, C. Chen, L. Sun, S. P. Wen, Y. Chen and S. P. Ruan, *Sensors and Actuators B-Chemical*, **2017**, 252, 757-763.
170. H. Xian, H. Guo, J. Xia, Q. Chen, Y. Luo, R. Song, T. Li and E. Traversa, *ACS Appl Mater Interfaces*, **2021**, 13, 7142-7151.

171. M. Selvaraj, K. Shanthi, R. Maheswari and A. Ramanathan, *Energy Fuels*, **2014**, 28, 2598-2607.
172. R. G. Kukushkin, O. A. Bulavchenko, V. V. Kaichev and V. A. Yakovlev, *Appl. Catal., B*, **2015**, 163, 531-538.
173. X. Cao, F. Long, Q. Zhai, P. Liu, J. Xu and J. Jiang, *Renewable Energy*, **2020**, 162, 2113-2125.
174. F. F. Yang, N. J. Libretto, M. R. Komarneni, W. Zhou, J. T. Miller, X. L. Zhu and D. E. Resasco, *ACS Catal.*, **2019**, 9, 7791-7800.
175. A. A. Smirnov, S. A. Khromova, D. Y. Ermakov, O. A. Bulavchenko, A. A. Saraev, P. V. Aleksandrov, V. V. Kaichev and V. A. Yakovlev, *Appl. Catal., A*, **2016**, 514, 224-234.
176. C. Wang, L. Guo, K. Wu, X. Li, Y. Huang, Z. Shen, H. Yang, Y. Yang, W. Wang and C. Li, *Journal of Energy Chemistry*, **2023**, 84, 122-130.
177. M. Chen, J. L. Wu, Y. M. Liu, Y. Cao, L. Guo, H. Y. He and K. N. Fan, *J. Solid State Chem.*, **2011**, 184, 3357-3363.
178. R. B. Patil, S. D. House, A. Mantri, J. C. Yang and J. R. McKone, *ACS Catal.*, **2020**, 10, 10390-10398.
179. J. J. F. R. Erre, *Stud. Surf. Sci. Catal.*, **1983**, 17, 285-293.
180. A. Marafi, A. Stainslaus, A. Hauser and K. Matsushita, *Pet. Sci. Technol.*, **2007**, 23, 385-408.
181. S. Xie, K. Chen, A. T. Bell and E. Iglesia, *J. Phys. Chem. B*, **2000**, 104, 10059-10068.
182. K. Chary, K. R. Reddy, G. Kishan, J. W. Niemantsverdriet and G. Mestl, *J. Catal.*, **2004**, 226, 283-291.
183. J. T. Scanlon and D. E. Willis, *J. Chromatogr. Sci.*, **1985**, 23, 333-340.
184. V. K. Pecharsky and P. Y. Zavalij, *Fundamentals of Powder Diffraction and Structural Characterization of Materials*, Springer Science + Business Media, New York, 2 edn., **2009**.
185. A. Brückner, *Chem. Soc. Rev.*, **2010**, 39, 4673-4684.
186. D. T. Petasis, *EPR Spectroscopy*, de Gruyter, Berlin, 1 edn., **2022**.
187. F. C. Meunier, *Chem. Soc. Rev.*, **2010**, 39, 4602-4614.
188. B. Bonelli, M. Cozzolino, R. Tesser, M. Di Serio, M. Piumetti, E. Garrone and E. Santacesaria, *J. Catal.*, **2007**, 246, 293-300.
189. G. Busca, *Phys. Chem. Chem. Phys.*, **1999**, 1, 723-736.
190. M. C. Kung and H. H. Kung, *Catal. Rev.*, **2006**, 27, 425-460.
191. I. E. Wachs and M. A. Bañares, *Springer Handbook of Advanced Catalyst Characterization*, Springer Nature Switzerland, Cham, **2023**.
192. F. A. Stevie and C. L. Donley, *J. Vac. Sci. Technol. A*, **2020**, 38, 063204.
193. J. Nölte, *ICP Emissionsspektrometrie für Praktiker*, WILEY-VCH, Weinheim, **2002**.
194. O. Ovsitser, M. Cherian, A. Brückner and E. V. Kondratenko, *J. Catal.*, **2009**, 265, 8-18.
195. G. H. Michler, *Kompakte Einführung in die Elektronenmikroskopie*, Springer Fachmedien Wiesbaden, Wiesbaden, **2019**.
196. R. F. Egerton, *Physical Principles of Electron Microscopy*, Springer Nature, Cham, 2 edn., **2016**.
197. S. Haida, S. Löbner, H. Lund, S. Bartling, C. Kreyenschulte, H. Atia, A. M. Abdel-Mageed, C. Kubis and A. Brückner, *Catal. Sci. Technol.*, **2024**, 14, 2201-2217.
198. G. Leclercq, *J. Catal.*, **1986**, 99, 1-11.
199. K. Kochloefl and V. Bažant, *J. Catal.*, **1968**, 10, 140-148.
200. M. Jayakannan and S. Ramakrishnan, *Macromol. Chem. Phys.*, **2000**, 201, 759-767.
201. J. E. Herrera and D. E. Resasco, *J. Phys. Chem. B*, **2003**, 107, 3738-3746.
202. H. M. Abdel-Dayem, *Ind. Eng. Chem. Res.*, **2007**, 46, 2466-2472.
203. D. Nicosia, I. Czekaj and O. Kröcher, *Appl. Catal., B*, **2008**, 77, 228-236.
204. M. Patel and A. Kumar, *Renewable Sustainable Energy Rev.*, **2016**, 58, 1293-1307.
205. S. Gutierrez-Rubio, I. Moreno, D. P. Serrano and J. M. Coronado, *ACS Omega*, **2019**, 4, 21516-21528.
206. J. L. Brito, J. Laine and K. C. Pratt, *J. Mater. Sci.*, **1989**, 24, 425-431.

207. P. Del Gallo, F. Meunier, C. Pham-Huu, C. Crouzet and M. J. Ledoux, *Ind. Eng. Chem. Res.*, **1997**, 36, 4166-4175.
208. T. Matsuda, S. Uozumi and N. Takahashi, *Phys. Chem. Chem. Phys.*, **2004**, 6, 665-672.
209. W. J. Balfour, *Spectrochim. Acta, Part A*, **1983**, 39, 795-800.
210. G. Zhou, P. A. Jensen, D. M. Le, N. O. Knudsen and A. D. Jensen, *ACS Sustainable Chem. Eng.*, **2016**, 4, 5432-5440.
211. F. Roessner and U. Roland, *J. Mol. Catal. A: Chem.*, **1996**, 112, 401-412.
212. M. Dieterle and G. Mestl, *Phys. Chem. Chem. Phys.*, **2002**, 4, 822-826.
213. X. Chen, R. M. de Boer, A. Kosari, H. van Gog and M. A. van Huis, *J Phys Chem C Nanomater Interfaces*, **2023**, 127, 21387-21398.
214. J. Dang, G.-H. Zhang and K.-C. Chou, *High Temp. Mater. Processes (London)*, **2014**, 33, 305-312.
215. D. Wang, D. S. Su and R. Schlögl, *Z. Anorg. Allg. Chem.*, **2004**, 630, 1007-1014.
216. I. de Castro Silva, A. C. Reinaldo, F. A. Sigoli and I. O. Mazali, *RSC Adv*, **2020**, 10, 18512-18518.
217. A. Borgschulte, O. Sambalova, R. Delmelle, S. Jenatsch, R. Hany and F. Nuesch, *Sci Rep*, **2017**, 7, 40761.
218. K. Dyrek and M. Łabanowska, *J. Chem. Soc., Faraday Trans.*, **1991**, 87, 1003-1009.
219. M. Łabanowska, *Phys. Chem. Chem. Phys.*, **1999**, 1, 5385-5392.
220. M. M. Ross, M. R. Chedekel, T. H. Risby, S. S. Lestz and R. E. Yasbin, *Environment International*, **1982**, 7, 325-329.
221. U. Green, Z. Aizenshtat, S. Ruthstein and H. Cohen, *Phys. Chem. Chem. Phys.*, **2012**, 14, 13046-13052.
222. Y. Wang, L. Li, G. Li, Q. Zhao, X. s. Wu, Y. Wang, Y. Sun and C. Hu, *ACS Catal.*, **2023**, 13, 6486-6496.
223. M. Narayana, R. Zhan and L. Kevan, *J. Phys. Chem.*, **1985**, **89**, 636-641.
224. F. J. Maldonado-Hódar, L. M. Palma Madeira and M. Farinha Portela, *J. Catal.*, **1996**, 164, 399-410.

8. Appendix

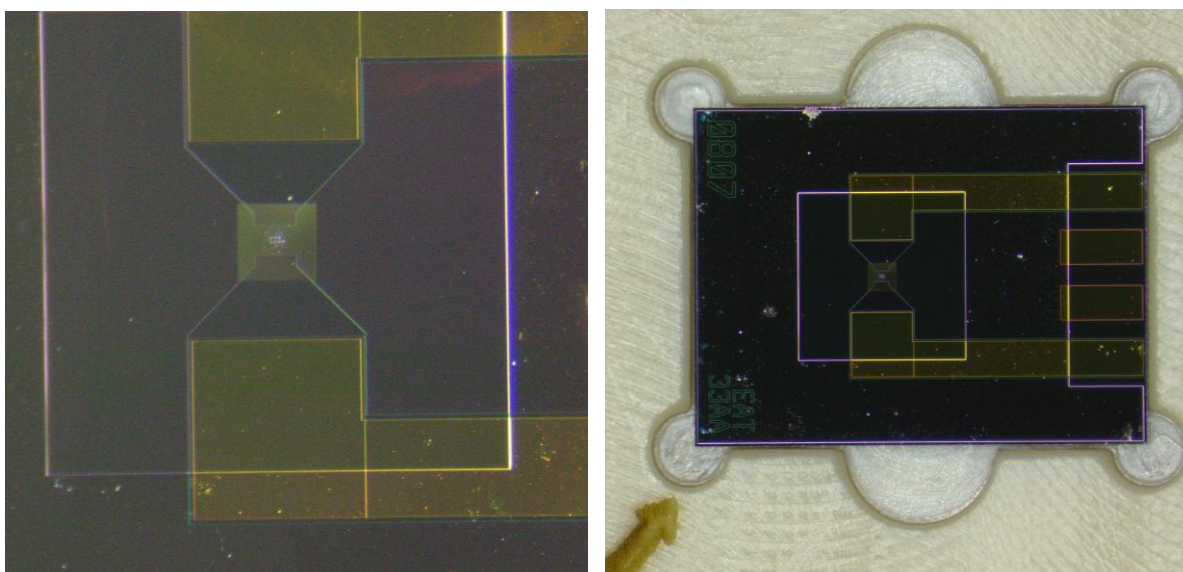


A-1: Overview about different typical compounds occurring in lignin pyrolysis oils, adapted with permission from Ref.⁶⁹. Copyright 2020 Elsevier.

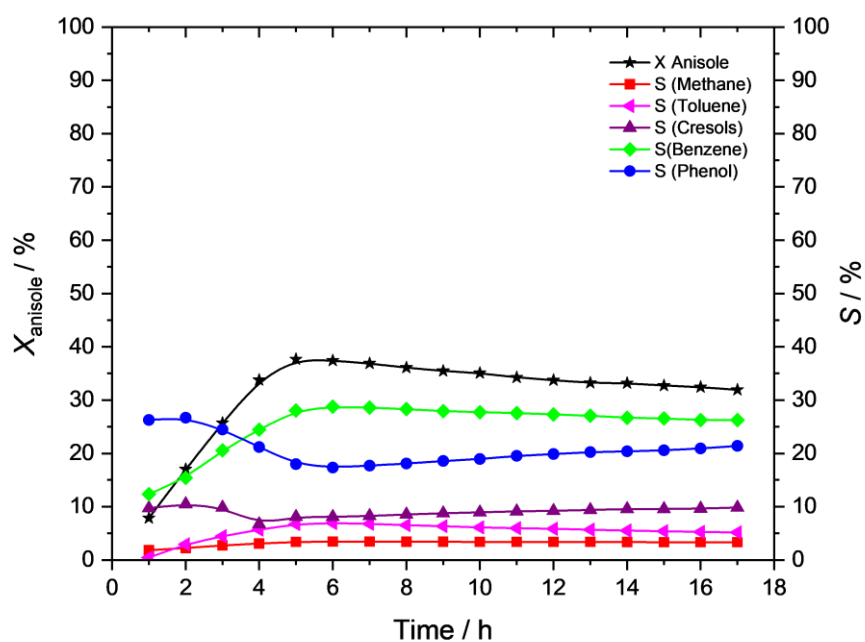
A-2: Characteristic wavelengths of common anode materials, adapted with permission from Ref.¹⁸⁴. Copyright 2009 Springer Science+Business Media.

Anode material	Wavelength (nm)			
	$K\alpha^a$	$K\alpha_1$	$K\alpha_2$	$K\beta$
Cr	0.229105	0.228975	0.2293652	0.208491
Cu	0.154187	0.15405929	0.154441	0.139225
Co	0.179030	0.178900	0.179289	0.162082
Mo	0.071075	0.07093171	0.071361	0.063230

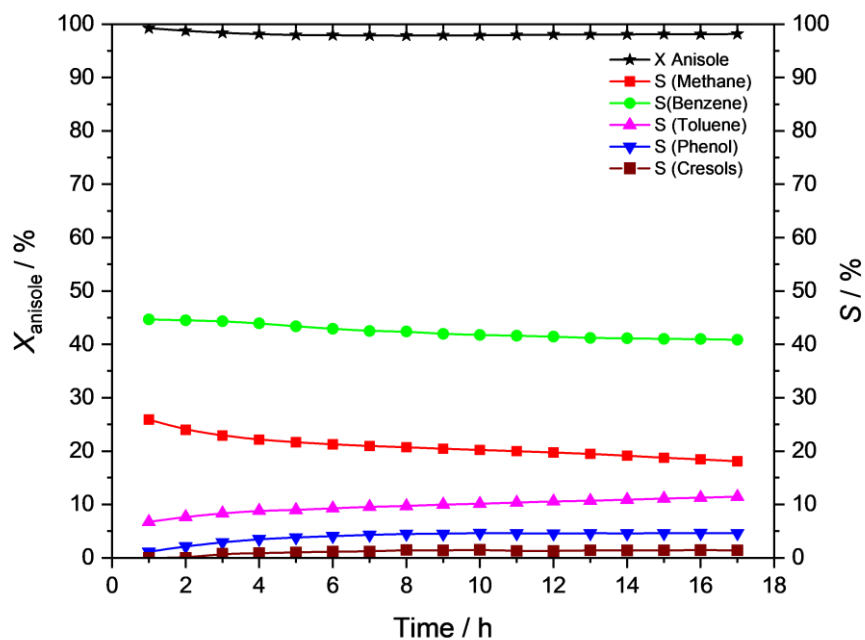
^a Weighted average value, calculated as $\lambda_{\text{average}} = (2\lambda_{K\alpha_1} + 2\lambda_{K\alpha_2})/3$



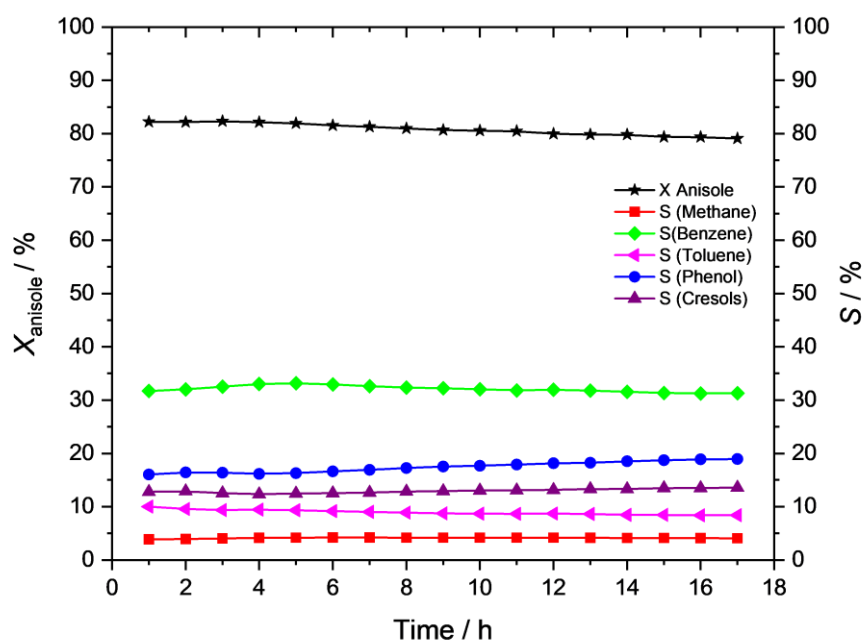
A-3: Chip for in-situ TEM experiments under a light microscope.



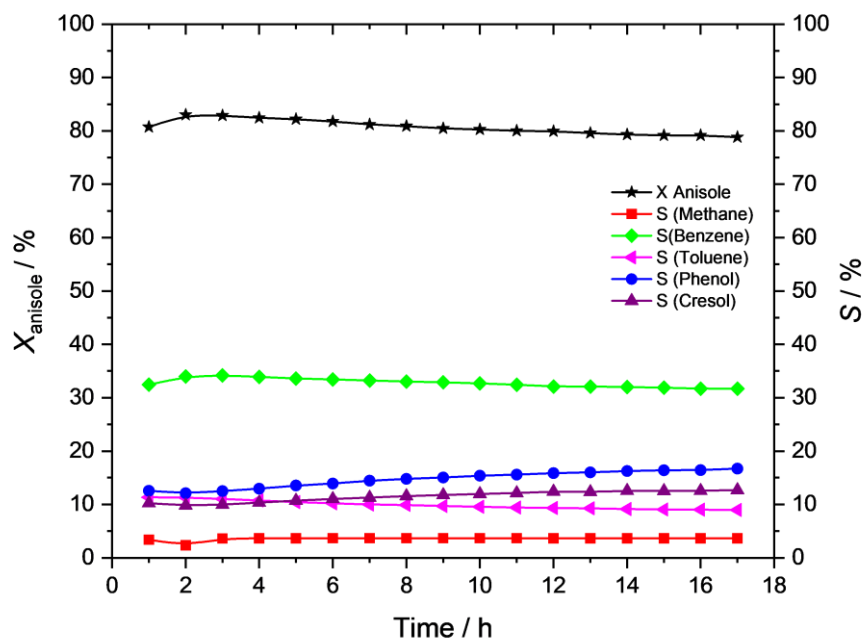
A-4: Averaged conversion and selectivities of the relevant compounds for MoO₃ at T = 325 °C, pre-reduced in 100 % H₂ for 2 h at 325 °C, WHSV = 0.31 g_{anisole}·g⁻¹cat·h⁻¹, particle size = 600-800 μm, 200 mg cat. diluted with 2.3 g quartz.



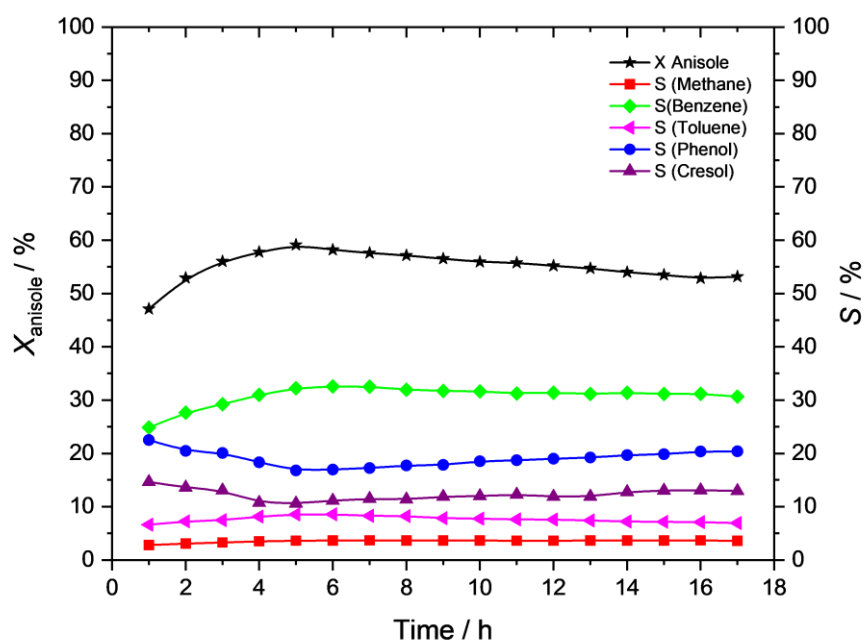
A-5: Averaged conversion and selectivities of the relevant compounds for NiMoO₄ at T = 325 °C, pre-reduced in 100 % H₂ for 2 h at 325 °C, WHSV = 0.31 g_{anisole}·g⁻¹cat·h⁻¹, particle size = 600-800 μm, 200 mg cat. diluted with 2.3 g quartz.



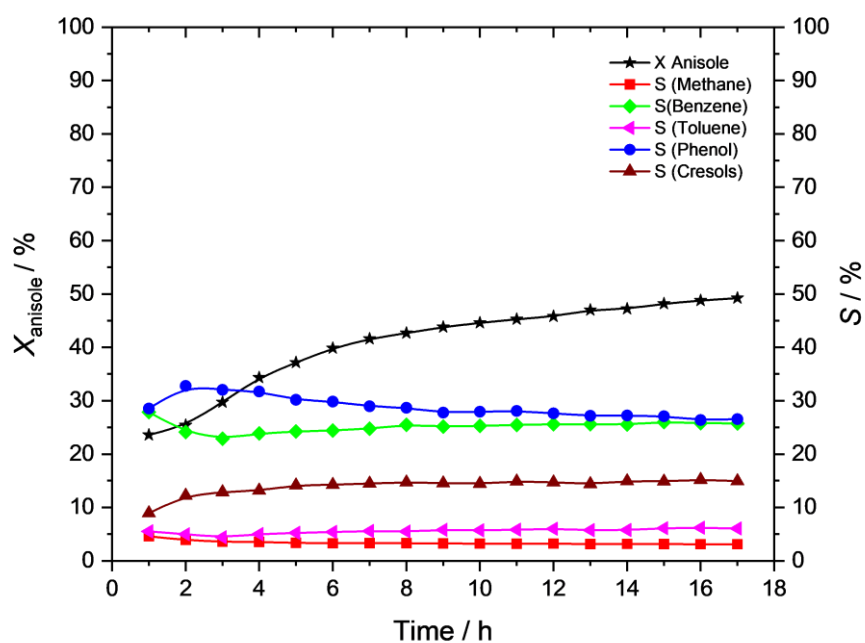
A-6: Averaged conversion and selectivities of the relevant compounds for Ni(5)MoO₃ at T = 325 °C, pre-reduced in 100 % H₂ for 2 h at 325 °C, WHSV = 0.31 g_{anisole} g⁻¹cat·h⁻¹, particle size = 600-800 μm, 200 mg cat. diluted with 2.3 g quartz.



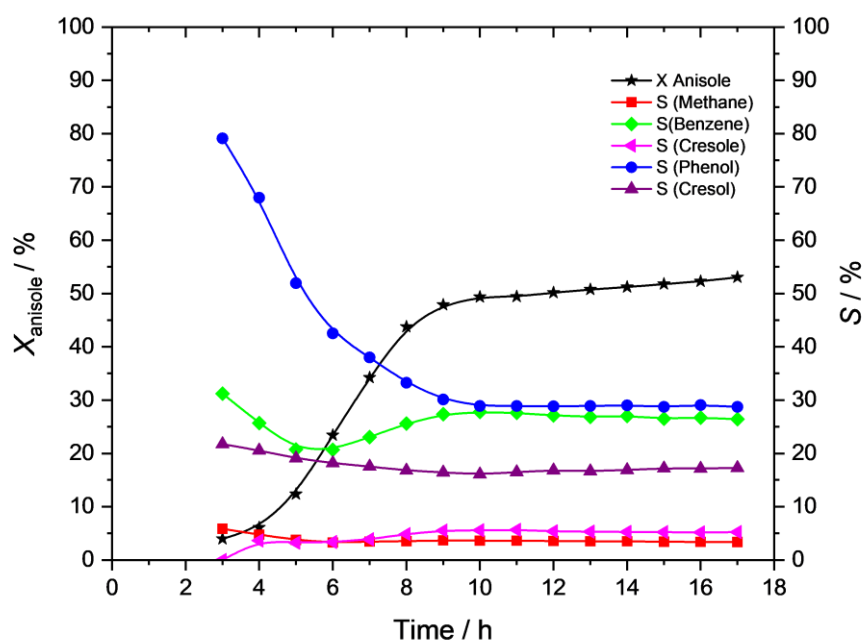
A-7: Averaged conversion and selectivities of the relevant compounds for Ni(3)MoO₃ at T = 325 °C, pre-reduced in 100 % H₂ for 2 h at 325 °C, WHSV = 0.31 g_{anisole}·g⁻¹cat·h⁻¹, particle size = 600-800 μm, 200 mg cat. diluted with 2.3 g quartz.



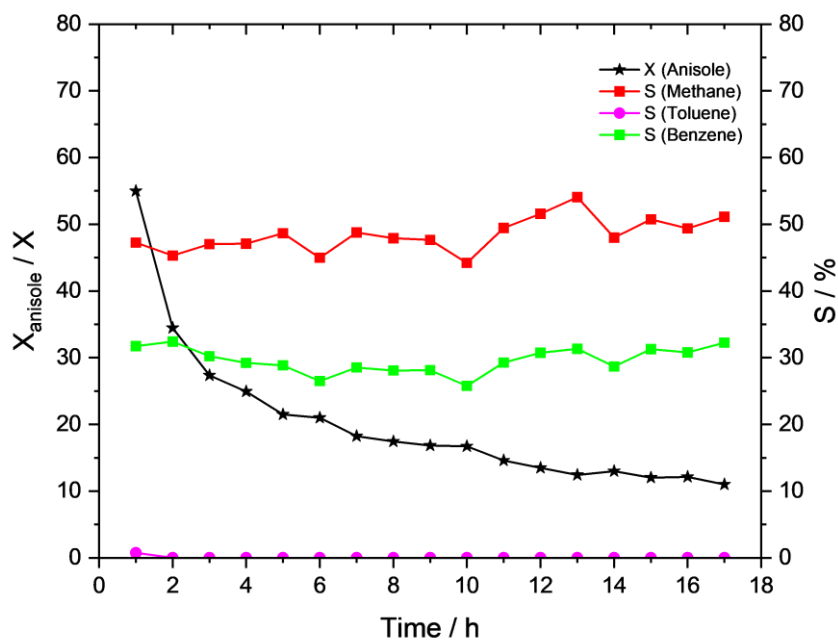
A-8: Averaged conversion and selectivities of the relevant compounds for Ni(1)MoO₃ at T = 325 °C, pre-reduced in 100 % H₂ for 2 h at 325 °C, WHSV = 0.31 g_{anisole}·g⁻¹cat·h⁻¹, particle size = 600-800 μm, 200 mg cat. diluted with 2.3 g quartz.



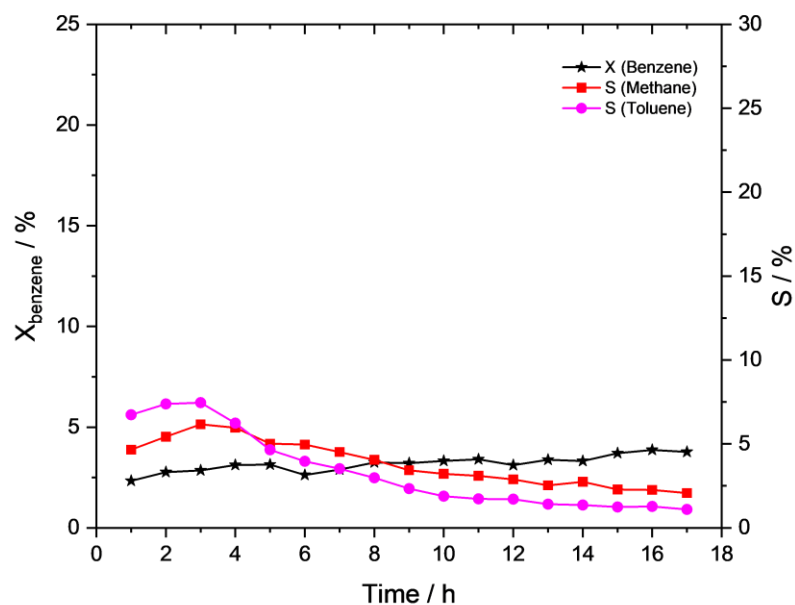
A-9: Conversion and selectivities of the relevant compounds for CoMoO₄ at T = 325 °C, pre-reduced in 100 % H₂ for 2 h at 325 °C, WHSV = 0.31 g_{anisole}·g⁻¹cat·h⁻¹, particle size = 600-800 μm, 200 mg cat. diluted with 2.3 g quartz.



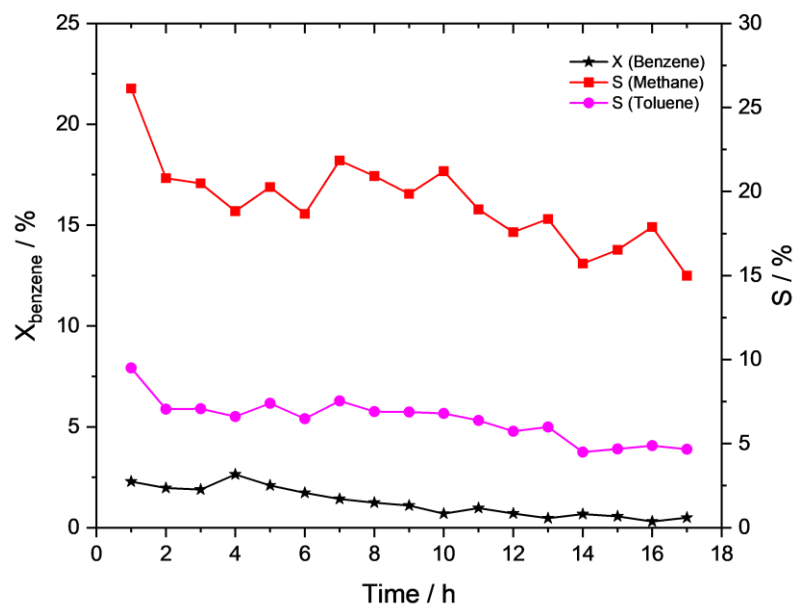
A-10: Conversion and selectivities of the relevant compounds for $\text{Co}(5)\text{MoO}_3$ at $T = 325\text{ }^\circ\text{C}$, pre-reduced in 100 % H_2 for 2 h at $325\text{ }^\circ\text{C}$, $\text{WHSV} = 0.31\text{ g}_{\text{anisole}}\cdot\text{g}^{-1}\text{cat}\cdot\text{h}^{-1}$, particle size = 600-800 μm , 200 mg cat. diluted with 2.3 g quartz.



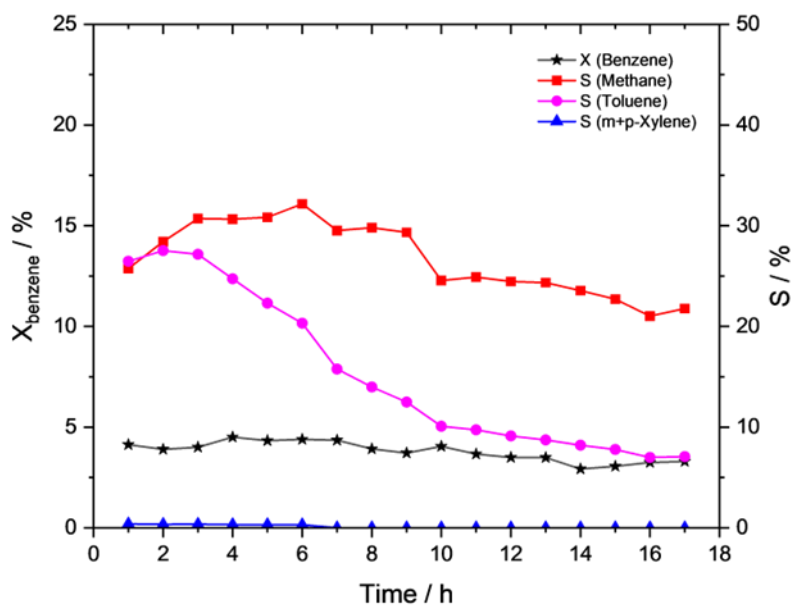
A-11: Conversion of anisole and selectivities of the relevant products for $\text{Ni}/\alpha\text{-Al}_2\text{O}_3$ (Ni content: 3 wt.%) as catalyst at $T = 325\text{ }^\circ\text{C}$, pre-reduced in 100 % H_2 for 2 h at $325\text{ }^\circ\text{C}$, $\text{WHSV} = 0.31\text{ g}_{\text{anisole}}\cdot\text{g}^{-1}\text{cat}\cdot\text{h}^{-1}$, particle size = 600-800 μm , 200 mg cat. diluted with 2.3 g quartz.



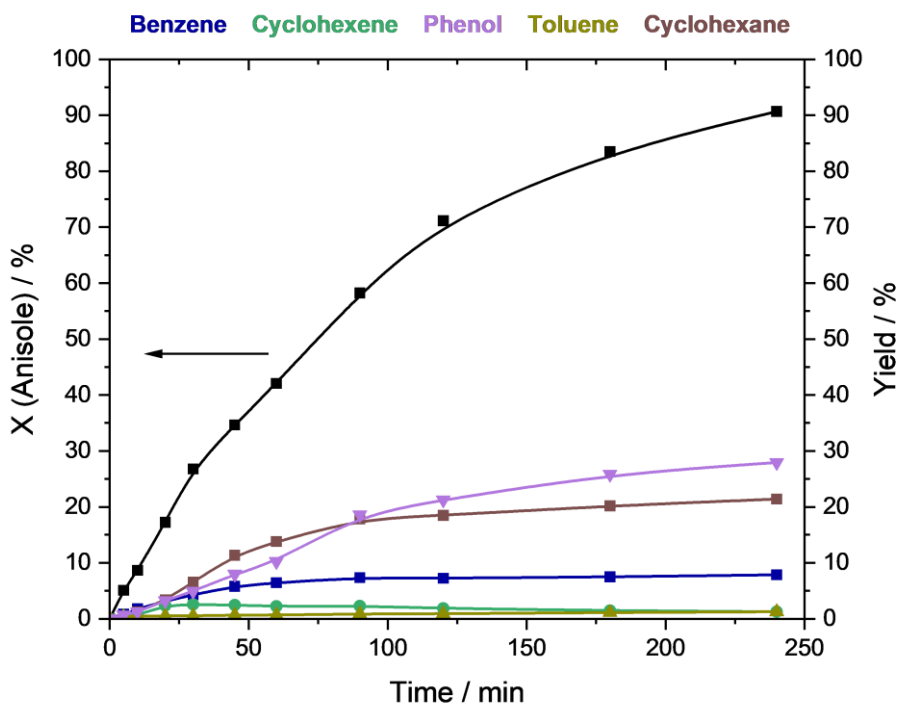
A-12: Conversion of benzene and product selectivities for Ni(5)MoO₃ as catalyst at T = 325 °C, pre-reduced in 100 % H₂ for 2 h at 325 °C, WHSV = 6.30 g_{benzene}·g⁻¹cat·h⁻¹, particle size = 600-800 μm, 200 mg cat. diluted with 2.3 g quartz.



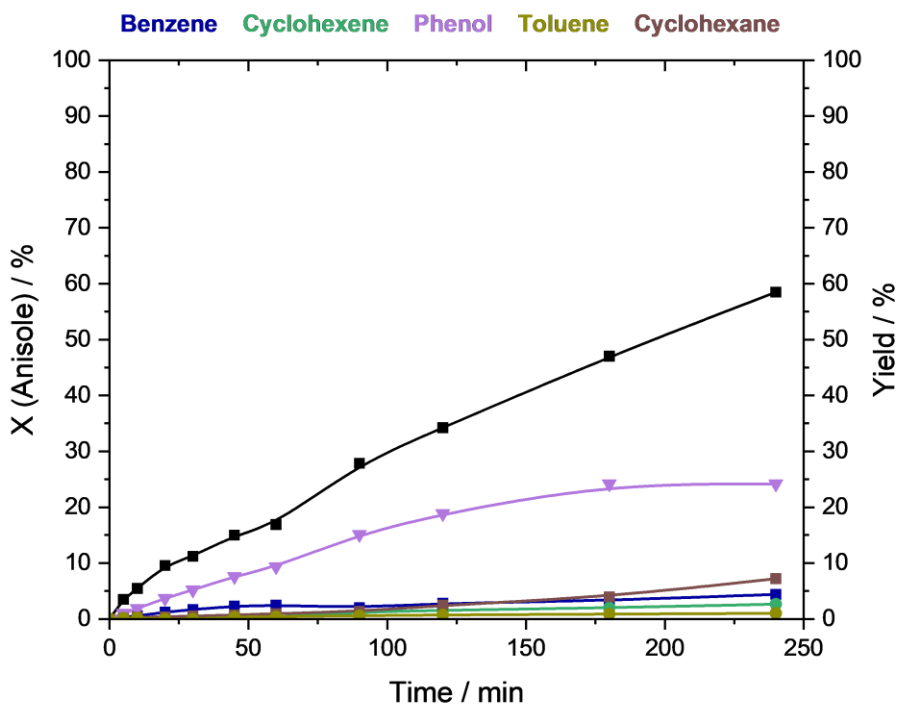
A-13: Conversion of benzene and product selectivities for Ni/α-Al₂O₃ (Ni content: 3 wt.%) as catalyst at T = 325 °C, pre-reduced in 100 % H₂ for 2 h at 325 °C, WHSV = 6.30 g_{benzene}·g⁻¹cat·h⁻¹, particle size = 600-800 μm, 200 mg cat. diluted with 2.3 g quartz.



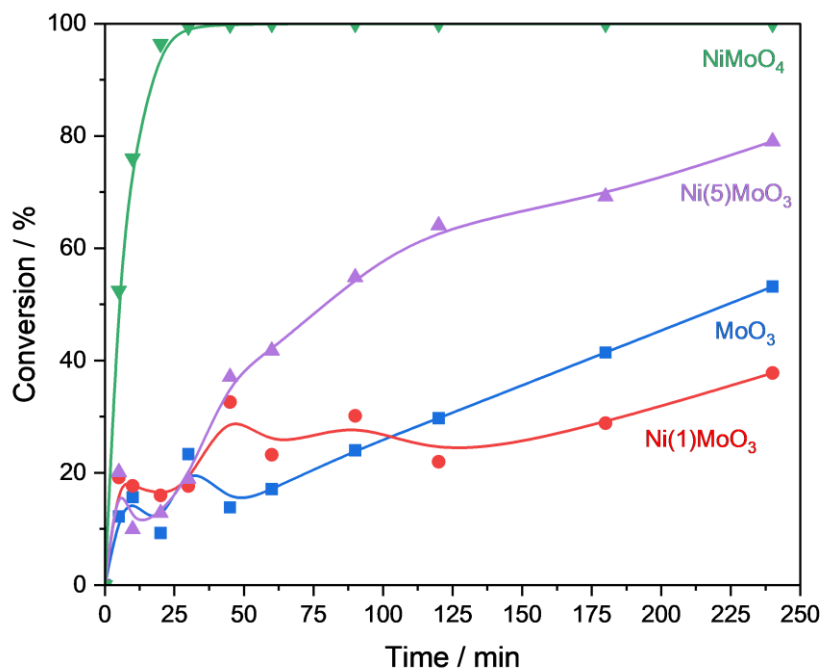
A-14: Conversion of benzene and product selectivities for NiMoO₄ as catalyst at T = 325 °C, pre-reduced in 100 % H₂ for 2 h at 325 °C, WHSV = 6.30 gbenzene·g⁻¹cat·h⁻¹, particle size = 600-800 μm, 200 mg cat. diluted with 2.3 g quartz.



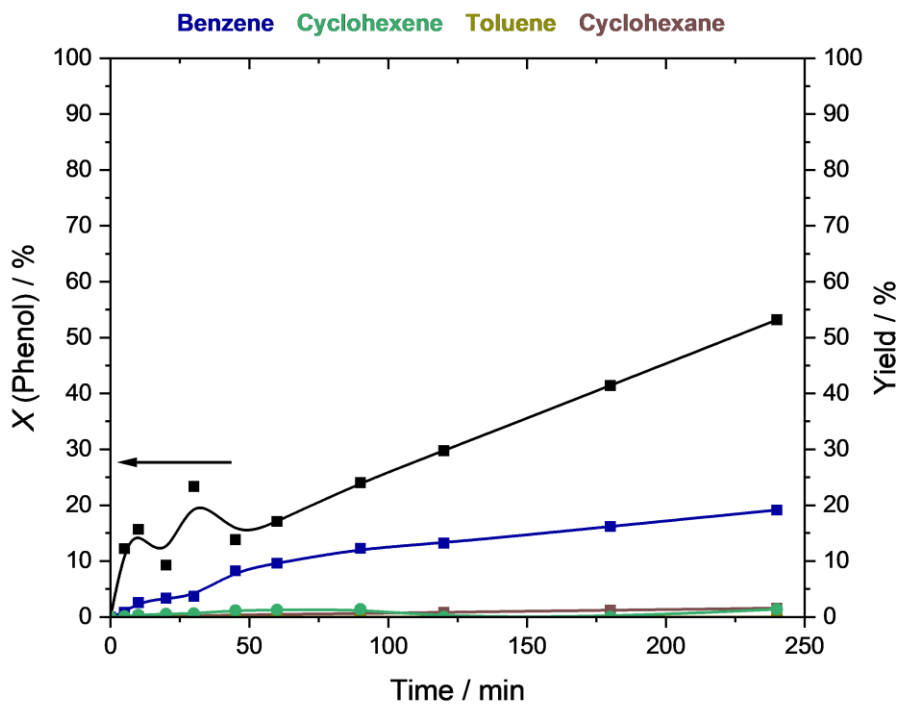
A-15: Conversion and yields for the anisole HDO with Ni(1)MoO₃ in a 300 ml batch reactor, at 350 °C, 50 bar H₂ pressure, 770 rpm agitator speed and 44.4 mmol anisole dissolved in 128 ml *n*-dodecane with 400 mg catalyst..



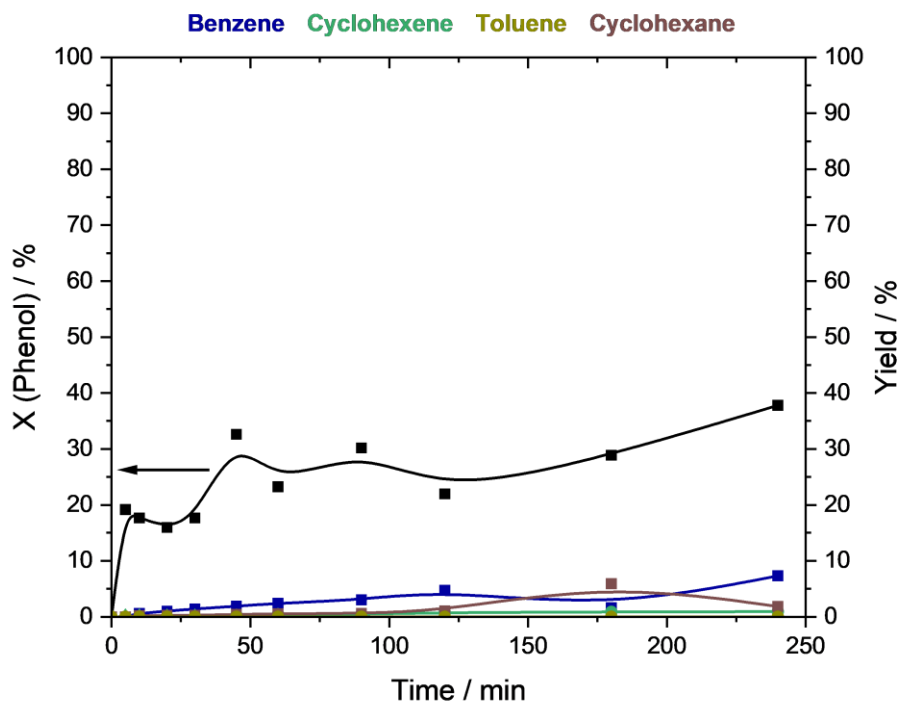
A-16: Conversion and yields for the anisole HDO with CoMoO_4 in a 300 ml batch reactor, at 350 °C, 50 bar H_2 pressure, 770 rpm agitator speed and 44.4 mmol anisole dissolved in 128 ml *n*-dodecane with 400 mg catalyst.



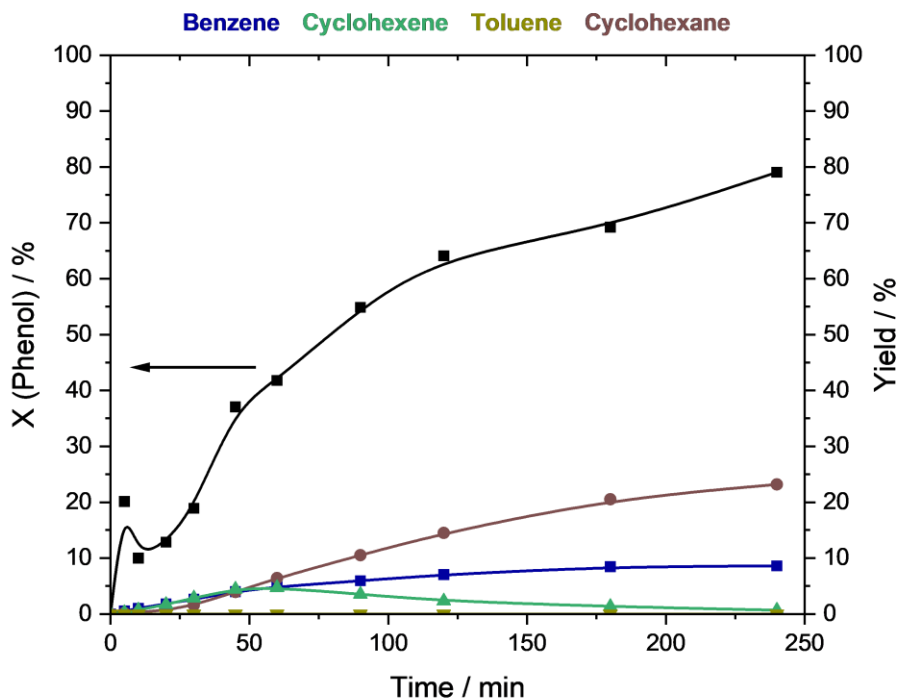
A-17: Conversion over time for the liquid-phase phenol HDO at in a 300 ml batch reactor, at 350 °C, 50 bar H_2 pressure, 770 rpm agitator speed and 44.4 mmol anisole dissolved in 128 ml *n*-dodecane with 400 mg catalyst.



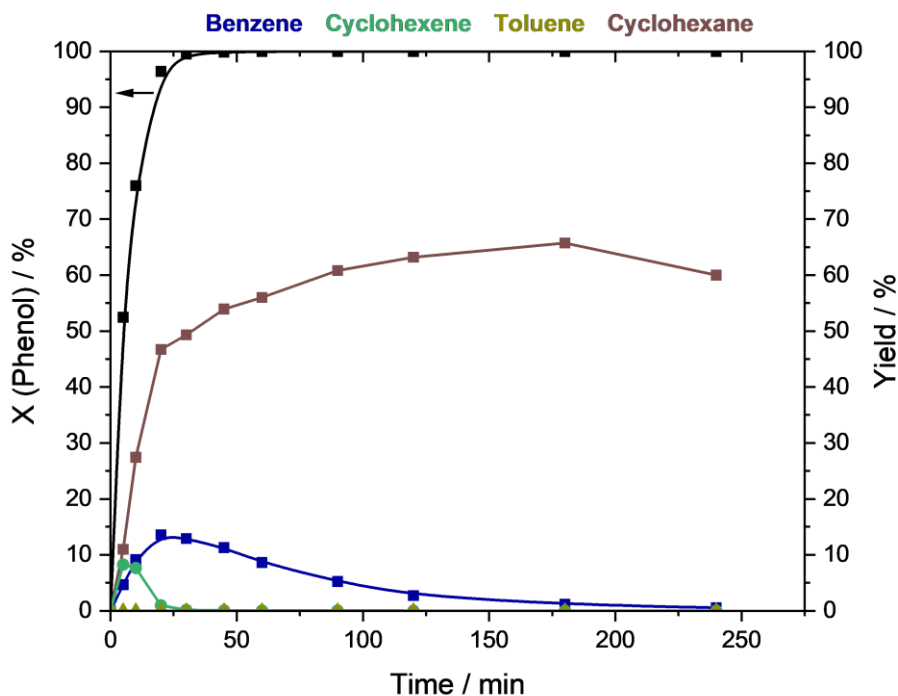
A-18: Conversion and yields for the phenol HDO with MoO_3 in a 300 ml batch reactor, at 350 °C, 50 bar H_2 pressure, 770 rpm agitator speed and 44.4 mmol anisole dissolved in 128 ml *n*-dodecane with 400 mg catalyst.



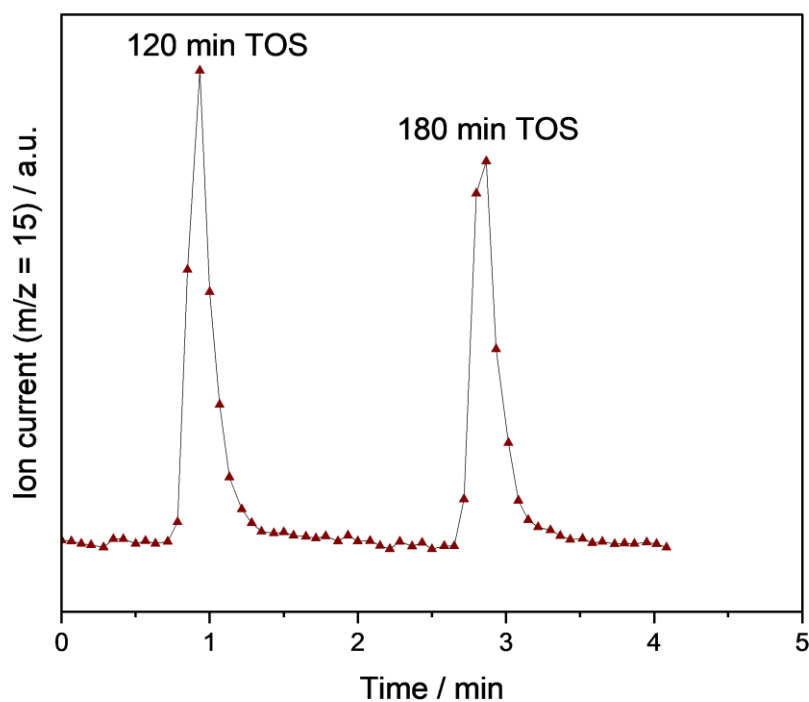
A-19: Conversion and yields for the phenol HDO with Ni(1)MoO_3 in a 300 ml batch reactor, at 350 °C, 50 bar H_2 pressure, 770 rpm agitator speed and 44.4 mmol anisole dissolved in 128 ml *n*-dodecane with 400 mg catalyst.



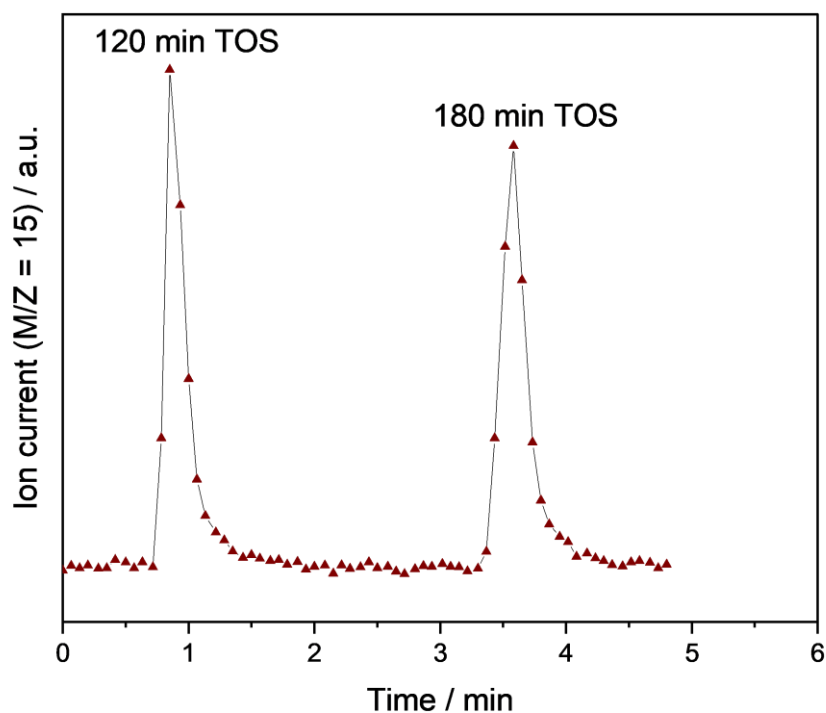
A-20: Conversion and yields for the phenol HDO with Ni(5)MoO₃ in a 300 ml batch reactor, at 350 °C, 50 bar H₂ pressure, 770 rpm agitator speed and 44.4 mmol anisole dissolved in 128 ml *n*-dodecane with 400 mg catalyst.



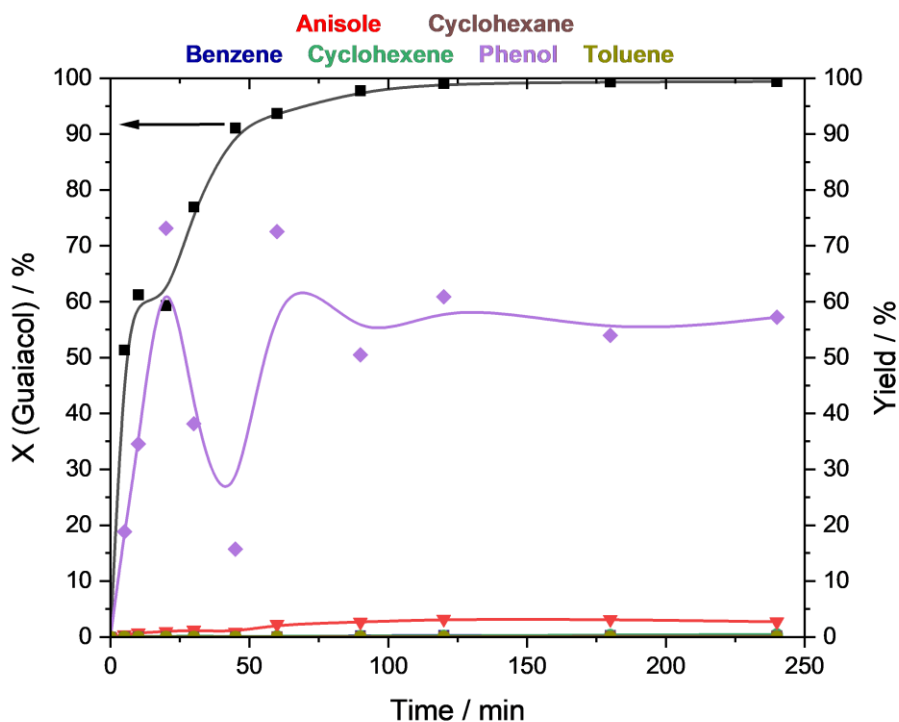
A-21: Conversion and yields for the phenol HDO with NiMoO₄ in a 300 ml batch reactor, at 350 °C, 50 bar H₂ pressure, 770 rpm agitator speed and 44.4 mmol anisole dissolved in 128 ml *n*-dodecane with 400 mg catalyst.



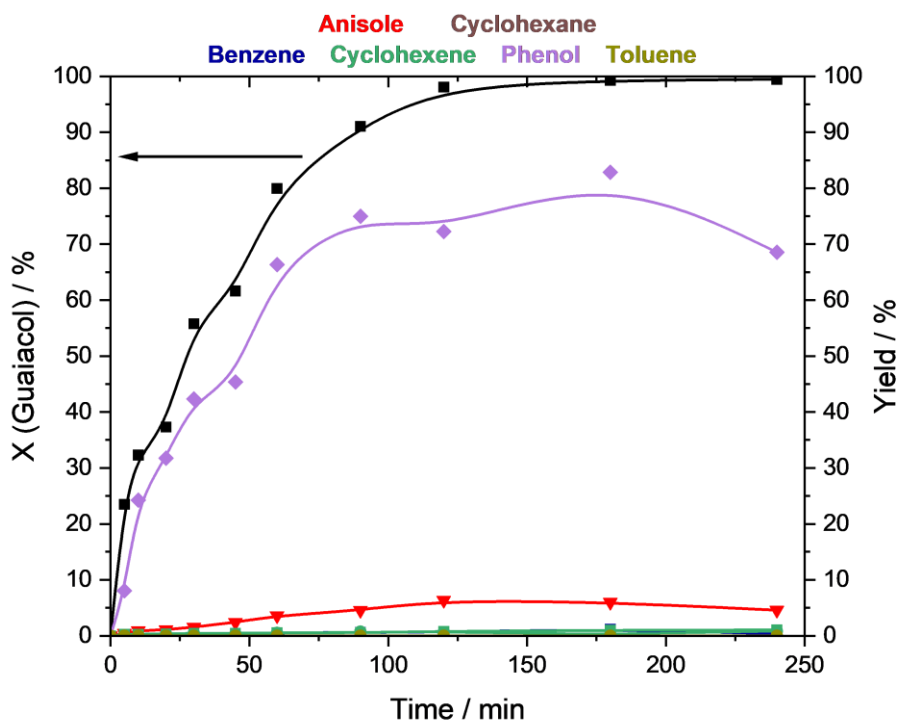
A-22: M/Z = 15 trace of gas samples taken from the liquid-phase HDO of phenol with Ni(5)MoO₃ at 350 °C and 50 bar H₂ pressure after 120 min and 180 min TOS. Note that the x-axis is representing the time which the MS was running for injections and not the reaction time.



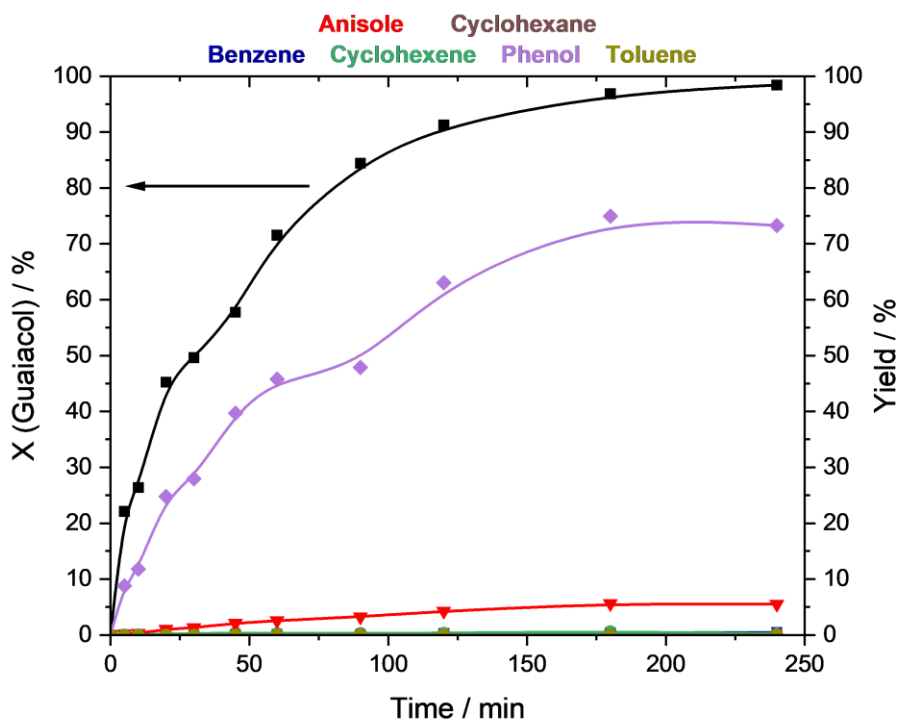
A-23: M/Z = 15 trace of gas samples taken from the liquid-phase HDO of phenol with MoO₃ at 350 °C and 50 bar H₂ pressure after 120 min and 180 min TOS. Note that the x-axis is representing the time which the MS was running for injections and not the reaction time.



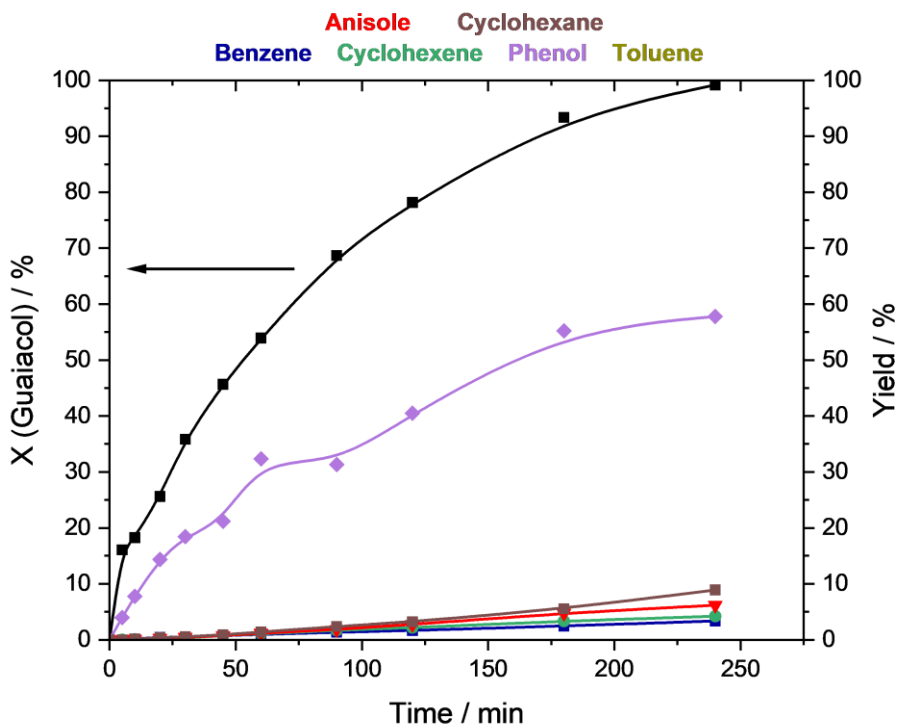
A-24: Conversion and yields for the guaiacol HDO with MoO₃ in a 300 ml batch reactor, at 350 °C, 50 bar H₂ pressure, 770 rpm agitator speed and 44.4 mmol anisole dissolved in 128 ml *n*-dodecane with 400 mg catalyst.



A-25: Conversion and yields for the guaiacol HDO with Ni(1)MoO₃ in a 300 ml batch reactor, at 350 °C, 50 bar H₂ pressure, 770 rpm agitator speed and 44.4 mmol anisole dissolved in 128 ml *n*-dodecane with 400 mg catalyst.



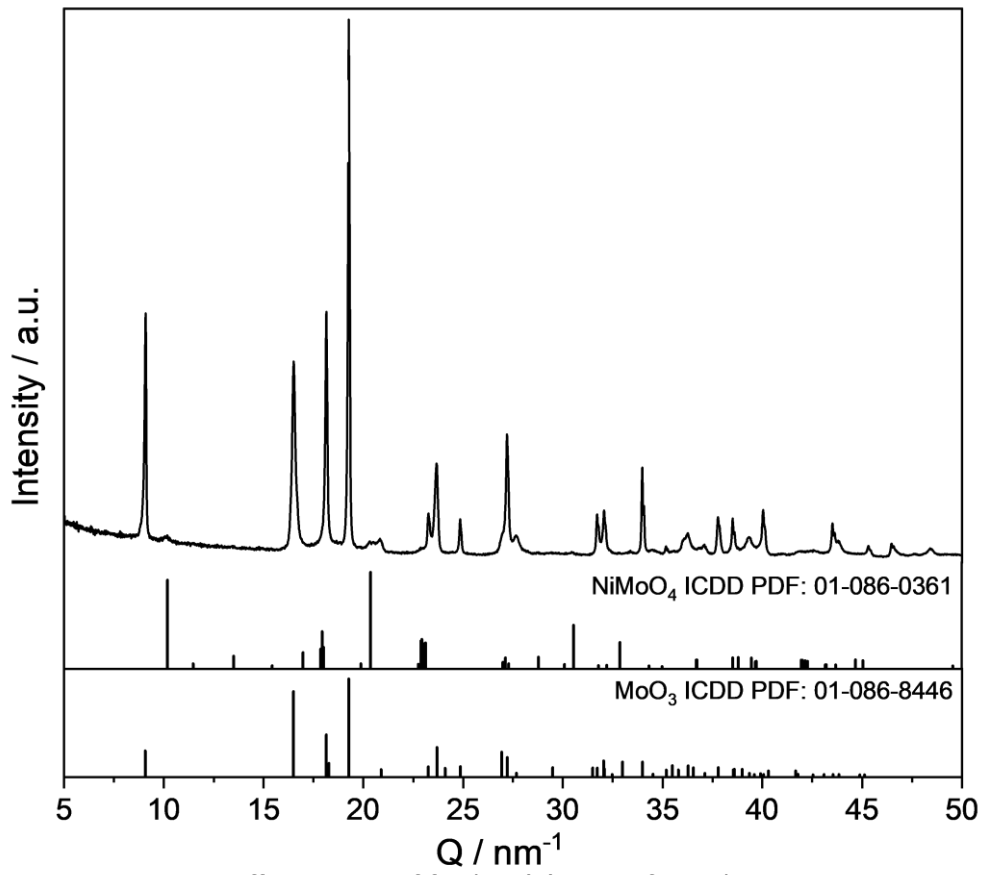
A-26: Conversion and yields for the guaiacol HDO with Ni(5)MoO₃ in a 300 ml batch reactor, at 350 °C, 50 bar H₂ pressure, 770 rpm agitator speed and 44.4 mmol anisole dissolved in 128 ml *n*-dodecane with 400 mg catalyst.



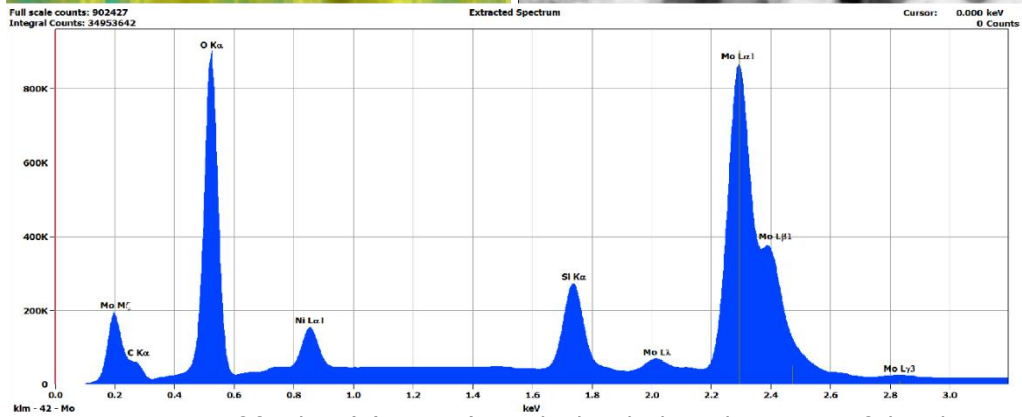
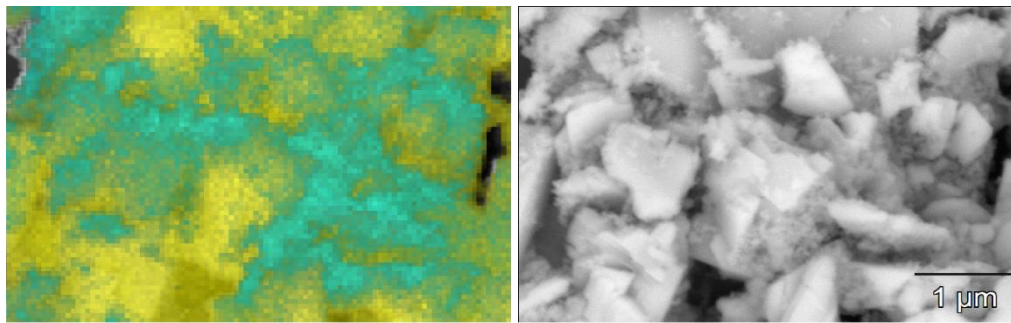
A-27: Conversion and yields for the guaiacol HDO with NiMoO₄ in a 300 ml batch reactor, at 350 °C, 50 bar H₂ pressure, 770 rpm agitator speed and 44.4 mmol anisole dissolved in 128 ml *n*-dodecane with 400 mg catalyst.



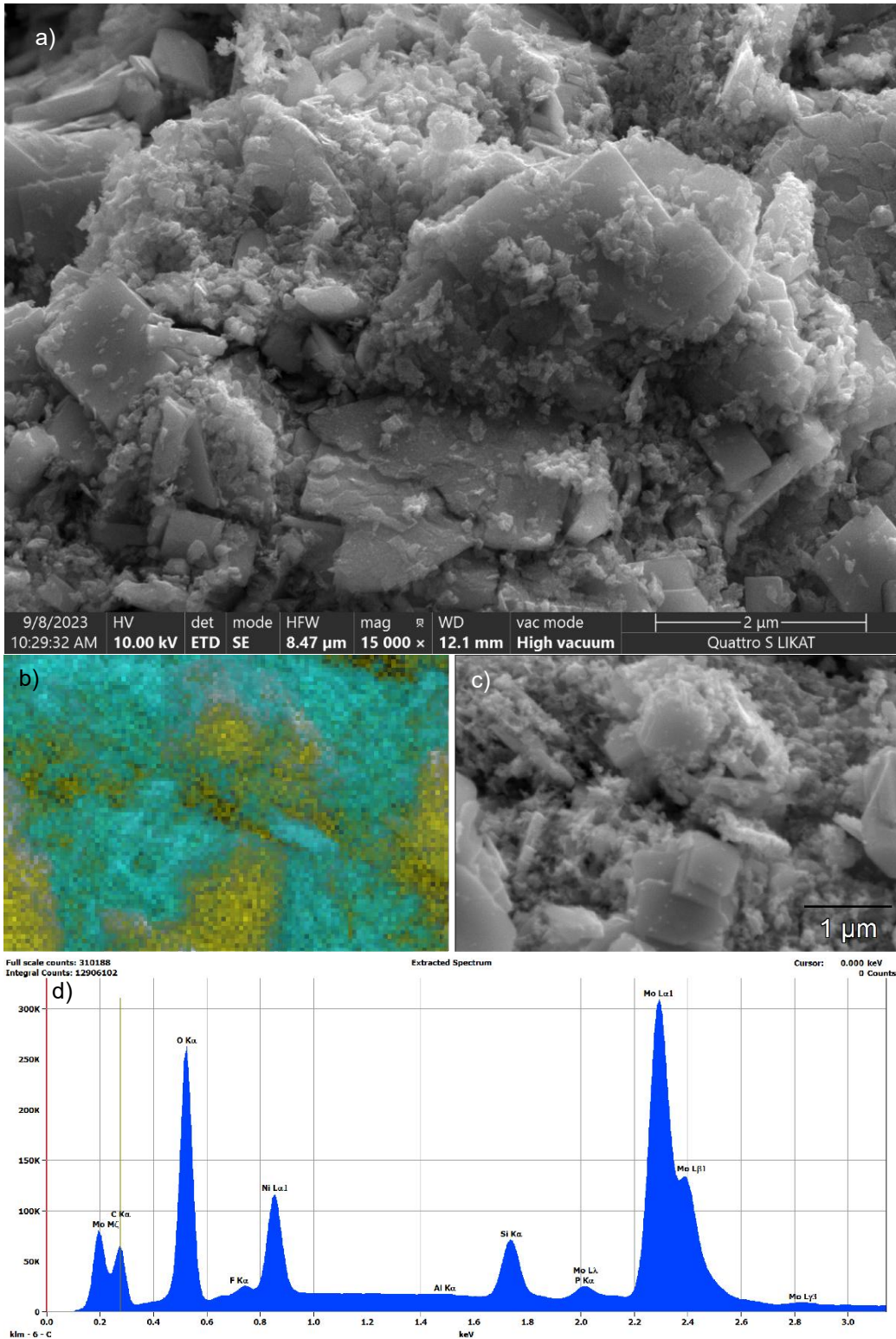
A-28: Reaction product after HDO with guaiacol at 350 °C and 50 bar H₂ pressure.



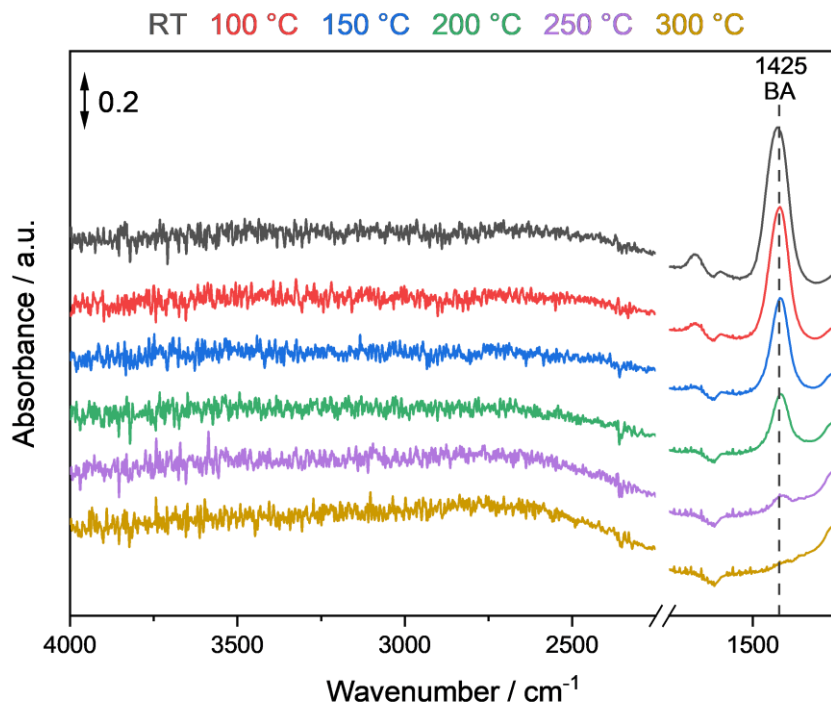
A-29: Diffractogram of fresh Ni(1)MoO₃ after calcination.



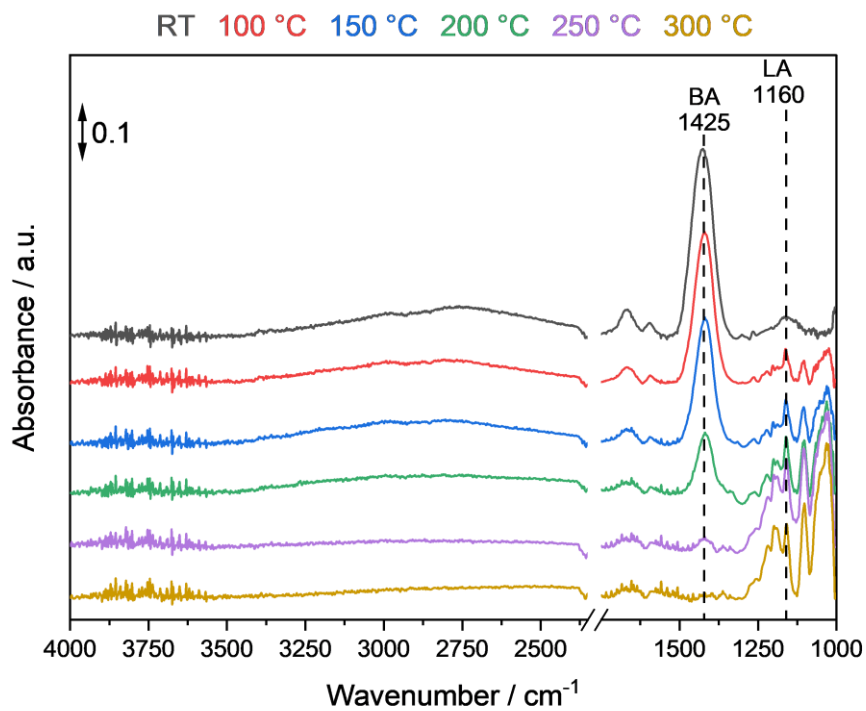
A-30: EDX-spectra of fresh Ni(5)MoO₃ a) overlaid with the color image of the elemental distributions of Mo (yellow) and Ni (cyan) calculated from the c) EDX spectra and the b) SEM image.



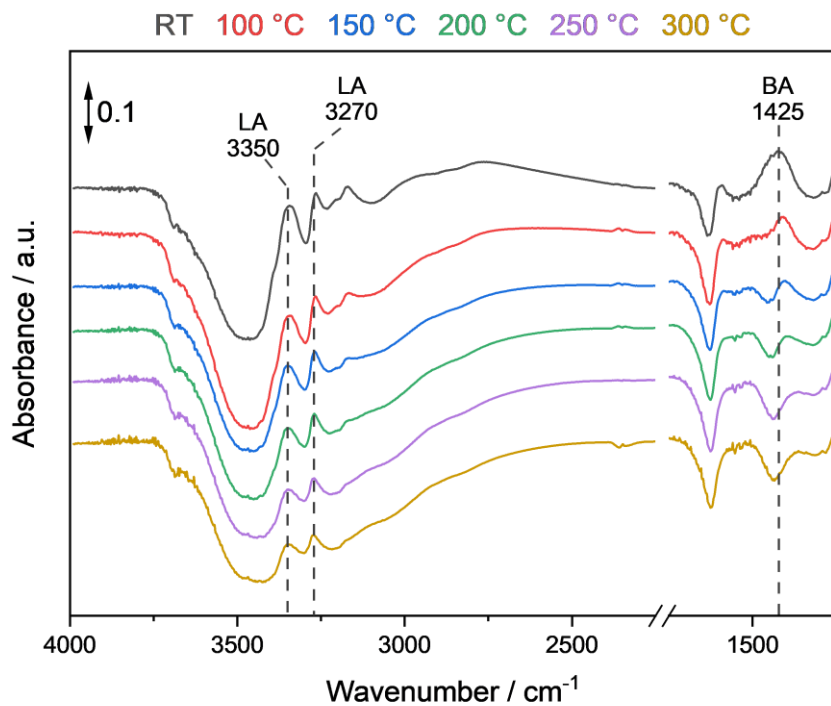
A-31: SEM overview images in SE mode of spent Ni(5)MoO₃ a) SEM image b) overlaid with the color image of the elemental distributions of Mo (yellow) and Ni (cyan) calculated from the EDX spectra from the area of c) and d) the EDX spectra of spent Ni(5)MoO₃.



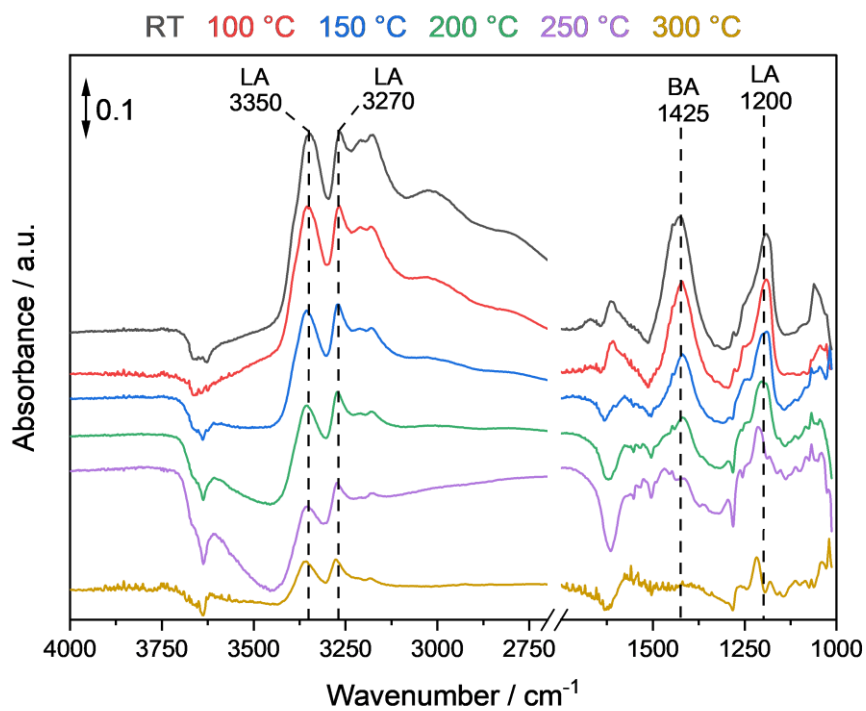
A-32: NH_3 -adsorption transmission FTIR experiments of MoO_3 after reduction at 325 °C for 2 h in 100 % H_2 .



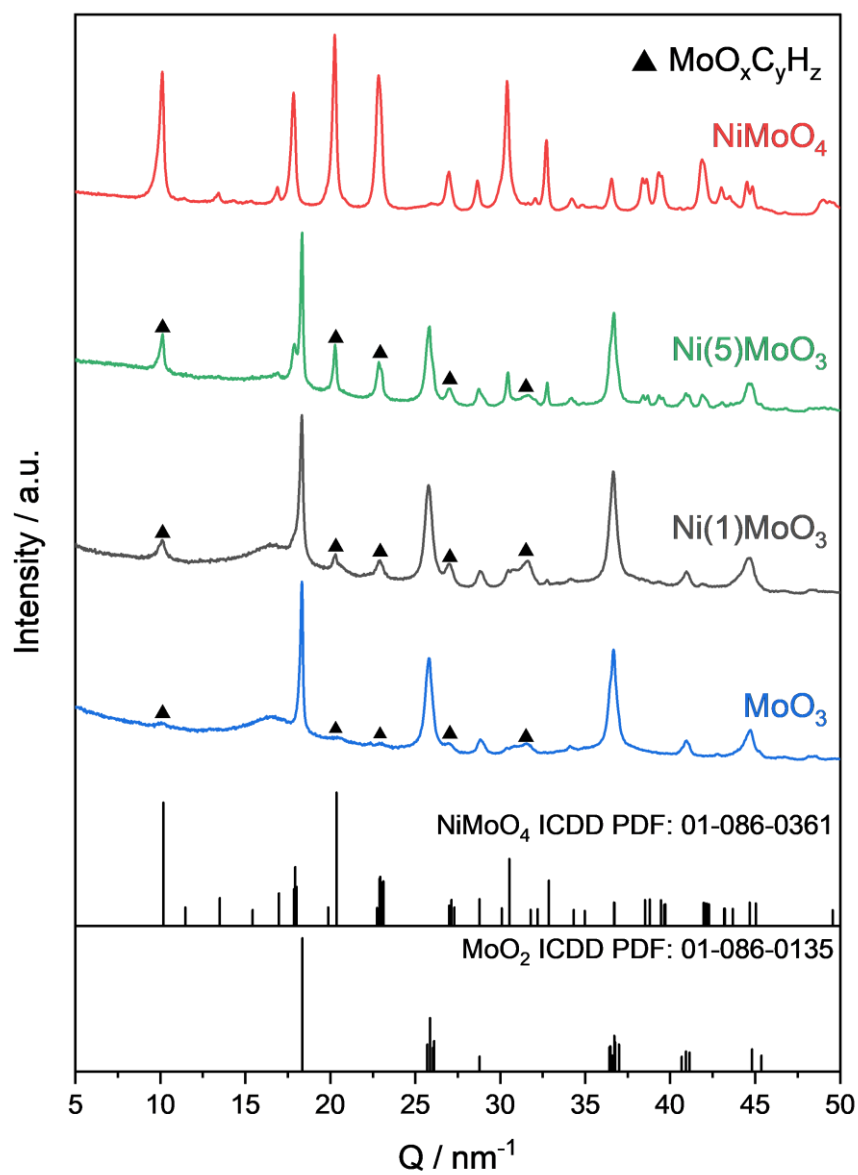
A-33: NH_3 -adsorption transmission FTIR experiments of MoO_3 after calcination at 325 °C for 2 h in 100 % syn. air.



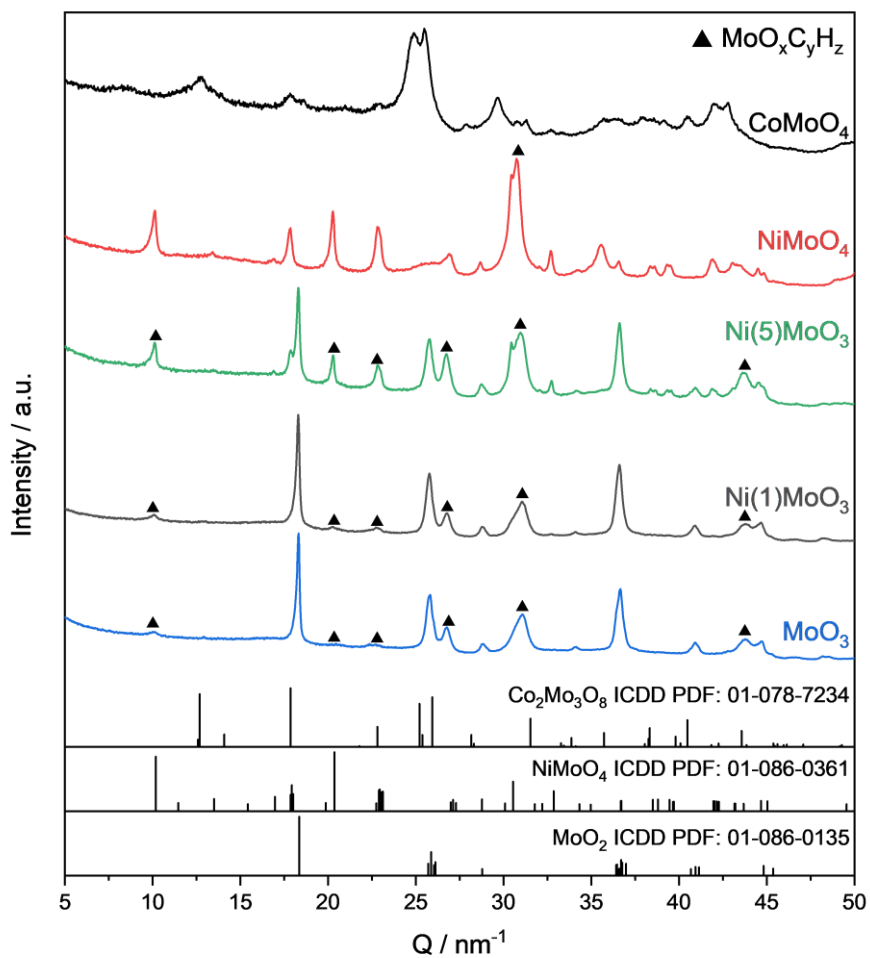
A-34: NH_3 -adsorption transmission FTIR experiments of NiMoO_4 after reduction at 325 °C for 2 h in 100 % H_2 .



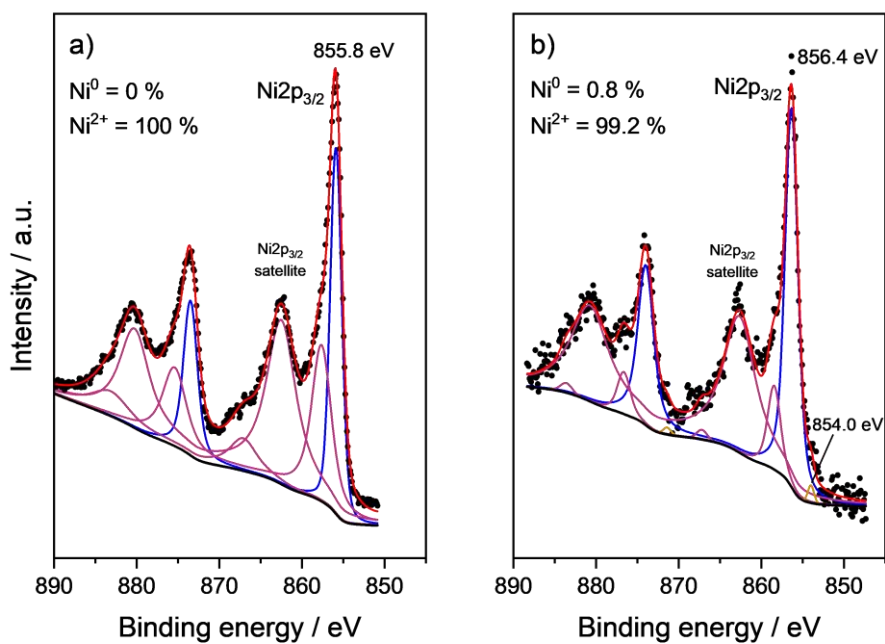
A-35: NH_3 -adsorption transmission FTIR experiments of NiMoO_4 after calcination at 325 °C for 2 h in 100 % syn. air.



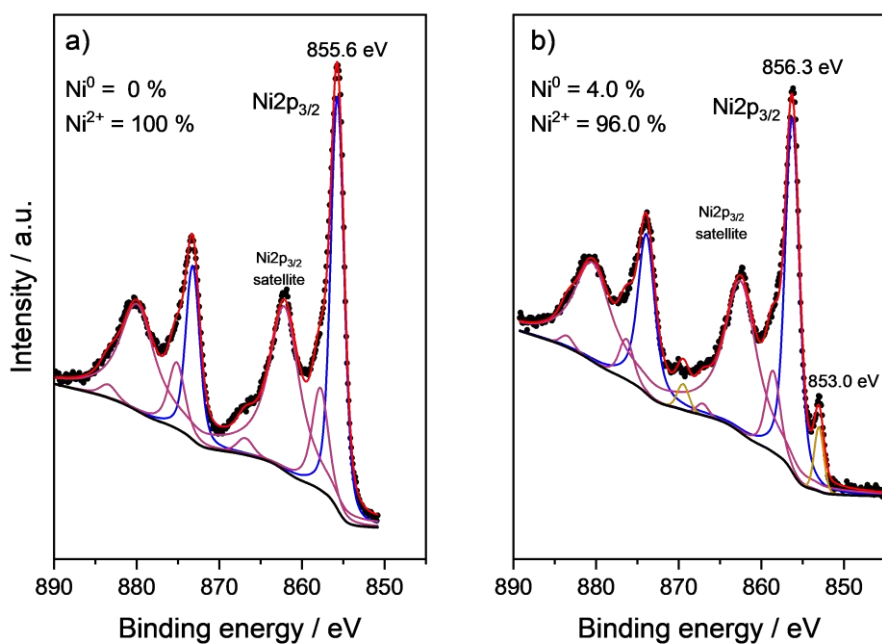
A-36: Normalized XRD patterns of spent catalysts after liquid-phase HDO at 350 °C at 50 bar H_2 after 4 h reaction with 44.4 mmol guaiacol dissolved in 128 ml *n*-dodecane, 400 mg catalyst.



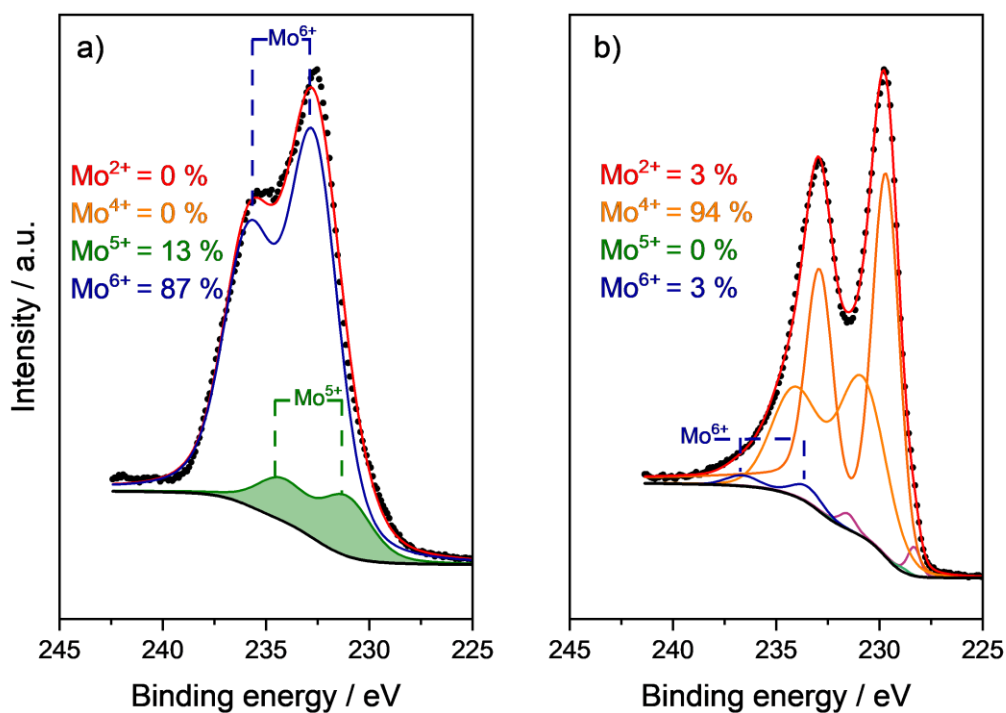
A-37: Normalized XRD patterns of spent catalysts after liquid-phase HDO at 350 °C at 50 bar H_2 after 4 h reaction with 44.4 mmol phenol dissolved in 128 ml *n*-dodecane, 400 mg catalyst.



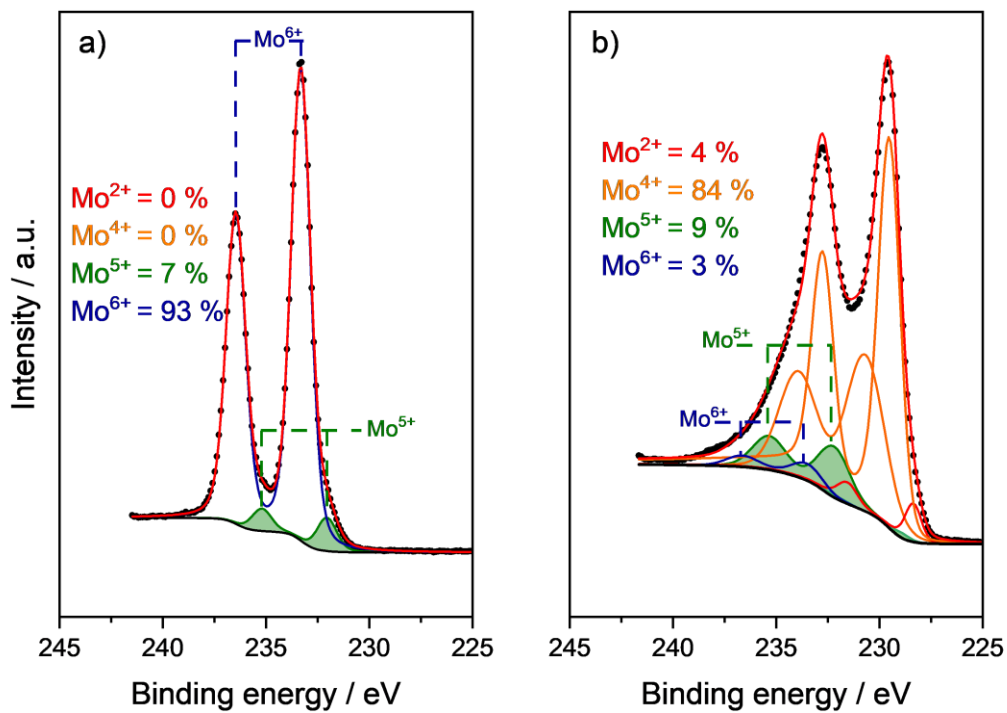
A-38: Ni 2p XP spectra of a) fresh Ni(5)MoO₃ b) spent Ni(5)MoO₃ after 17 h TOS at 325 °C for the gas-phase HDO.



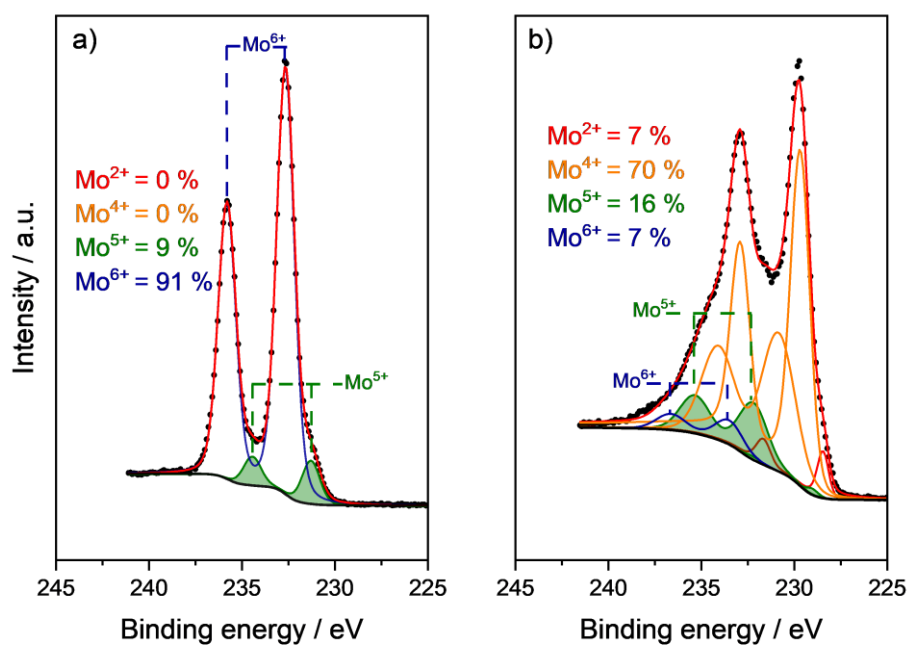
A-39: Ni 2p XP spectra of a) fresh NiMoO₄ b) spent NiMoO₄ after 17 h TOS at 325 °C for the gas-phase HDO.



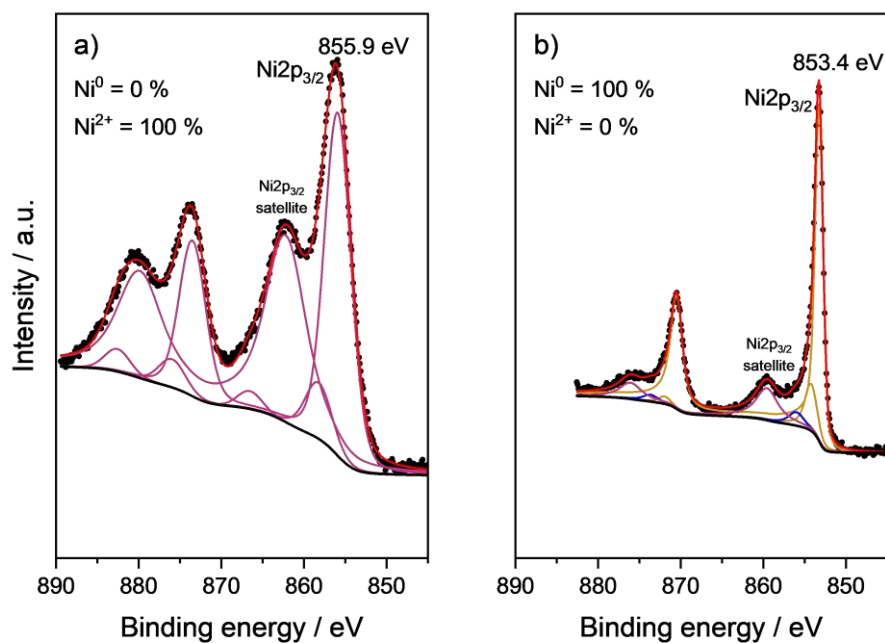
A-40: Mo3d Pseudo in-situ XP spectra. a) fresh NiMoO₄ b) NiMoO₄ after reduction in 100 % H₂ for 2 h at 325 °C.



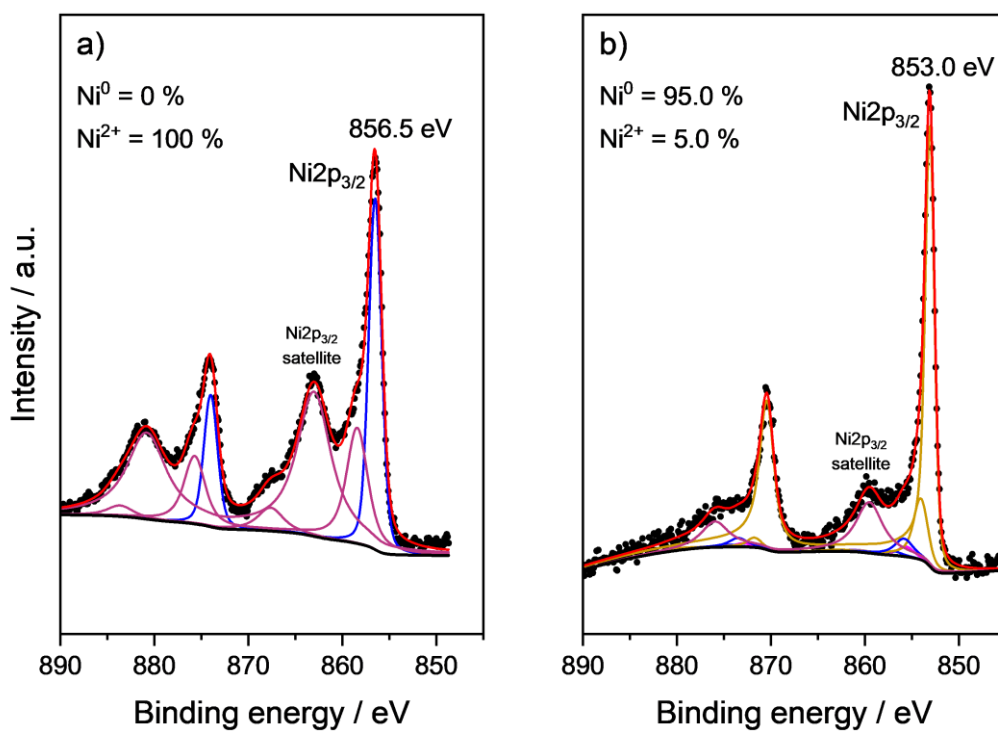
A-41: Mo3d Pseudo in-situ XP spectra. a) fresh Ni(5)MoO₃ b) Ni(5)MoO₃ after reduction in 100 % H₂ for 2 h at 325 °C.



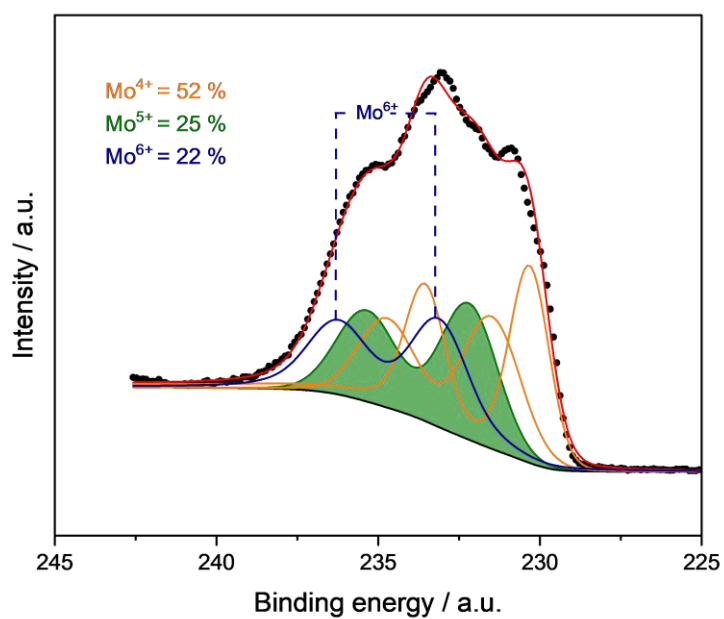
A-42: Mo_{3d} Pseudo in-situ XP spectra. a) fresh MoO₃ b) MoO₃ after reduction in 100 % H₂ for 2 h at 325 °C.



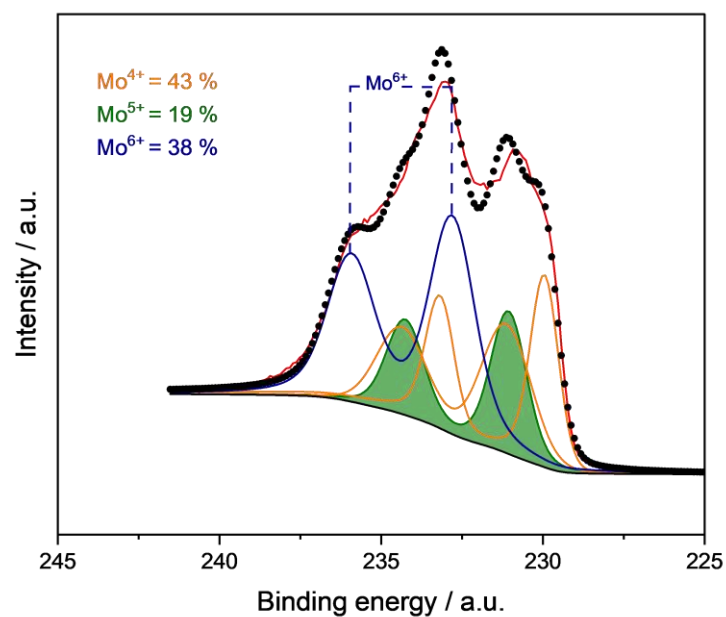
A-43: Ni_{2p} pseudo in-situ XP spectra. a) fresh NiMoO₄ b) NiMoO₄ after reduction in 100 % H₂ for 2 h at 325 °C.



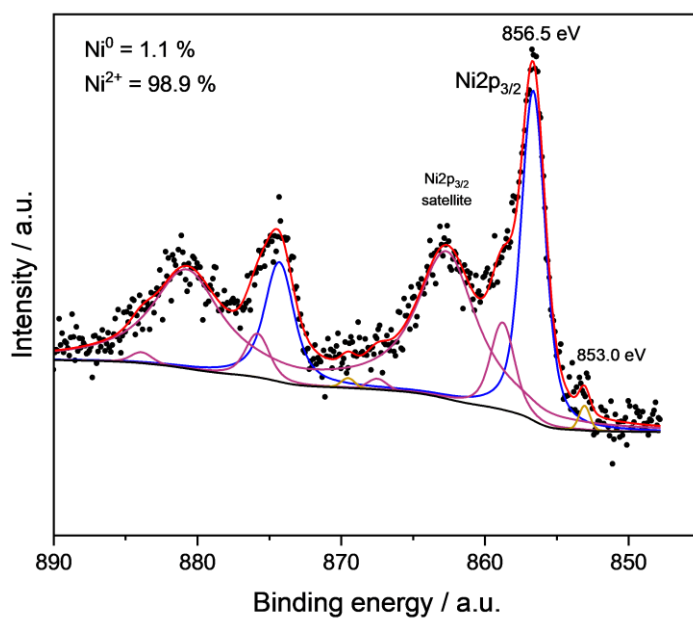
A-44: Ni2p pseudo in-situ XP spectra. a) fresh Ni(5)MoO₃ b) Ni(5)MoO₃ after reduction in 100 % H₂ for 2 h at 325 °C.



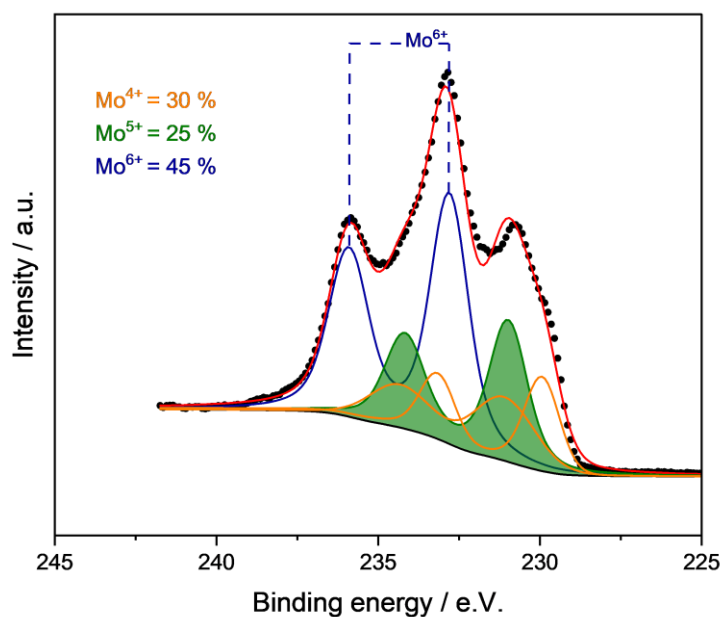
A-45: Mo3d spectra of spent MoO₃ after liquid-phase reaction at 350 °C and 50 bar H₂ with anisole.



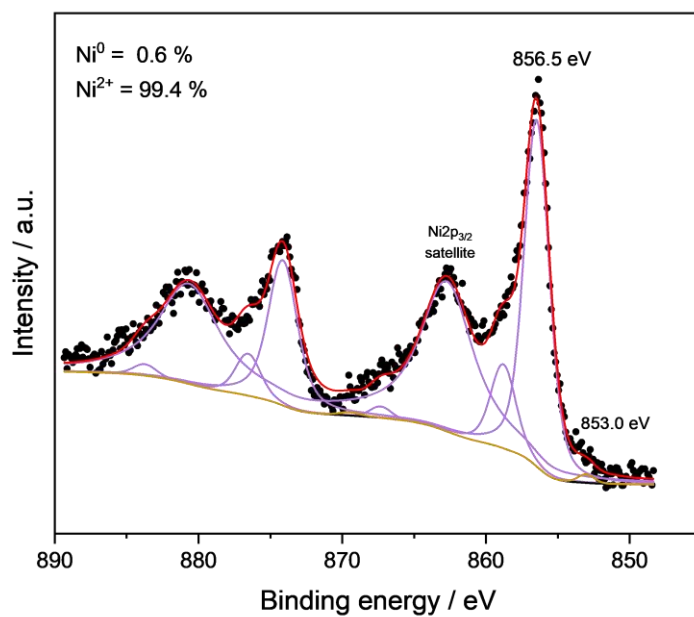
A-46: Mo3d spectra of spent Ni(1)MoO₃ after liquid-phase reaction at 350 °C, 50 bar H₂ pressure with anisole and 4 h reaction.



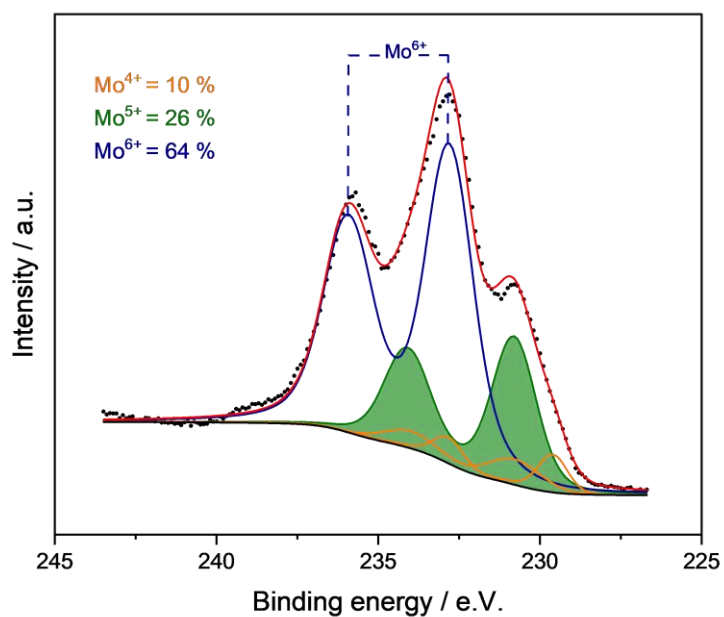
A-47: Ni2p spectra of spent Ni(1)MoO₃ after liquid-phase reaction at 350 °C, 50 bar H₂ pressure with anisole and 4 h reaction.



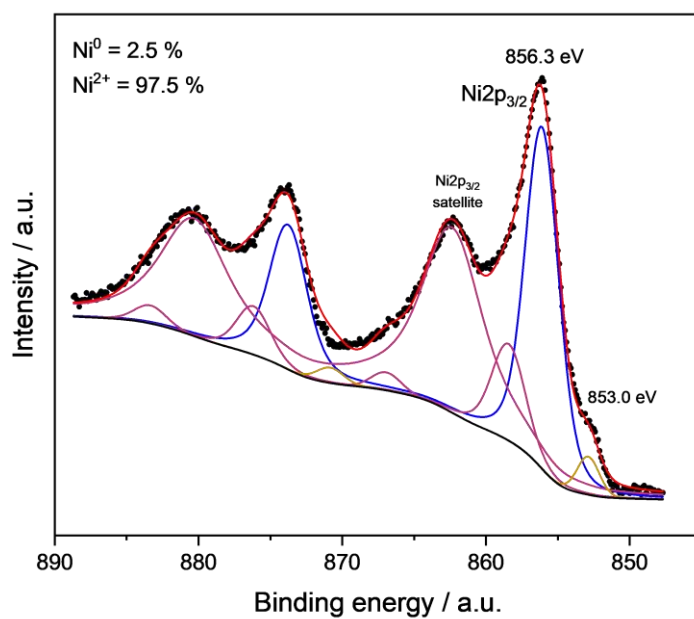
A-48: Mo3d spectra of spent Ni(5)MoO₃ after liquid-phase reaction at 350 °C, 50 bar H₂ pressure with anisole and 4 h reaction.



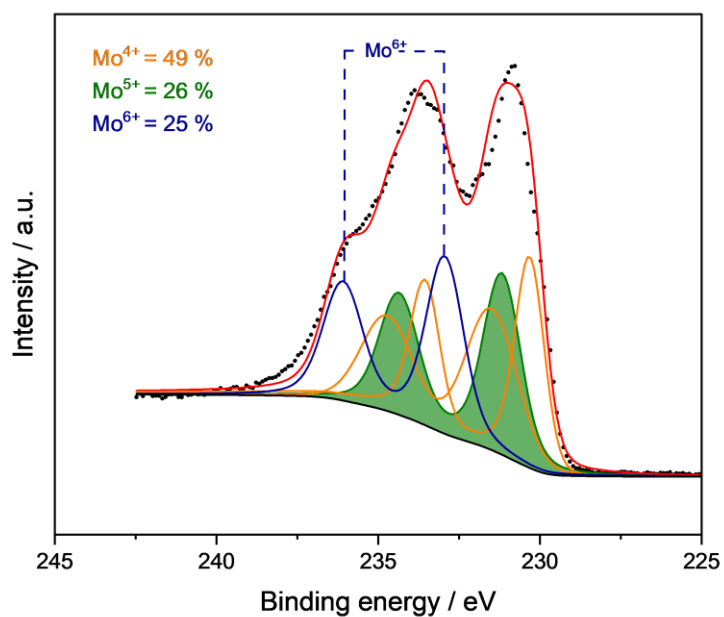
A-49: Ni2p spectra of spent Ni(5)MoO₃ after liquid-phase reaction at 350 °C, 50 bar H₂ pressure with anisole and 4 h reaction.



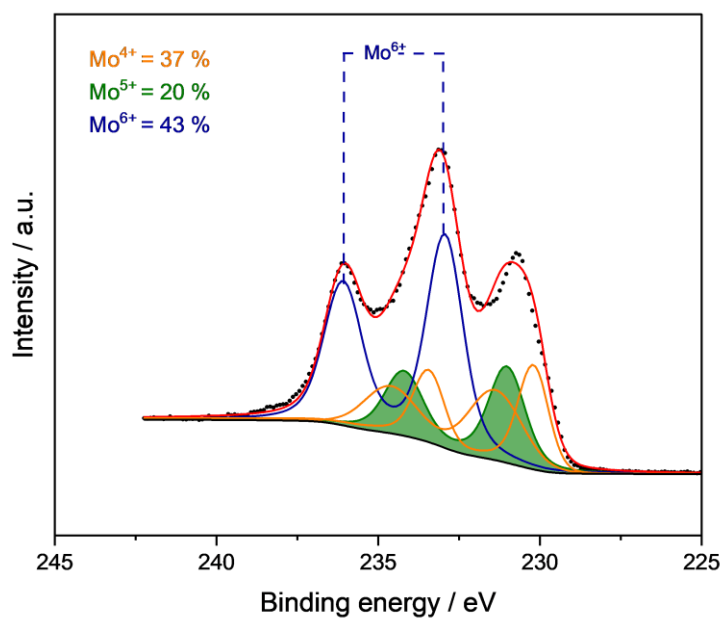
A-50: Mo3d spectra of spent NiMoO₄ after liquid-phase reaction at 350 °C, 50 bar H₂ pressure with anisole and 4 h reaction.



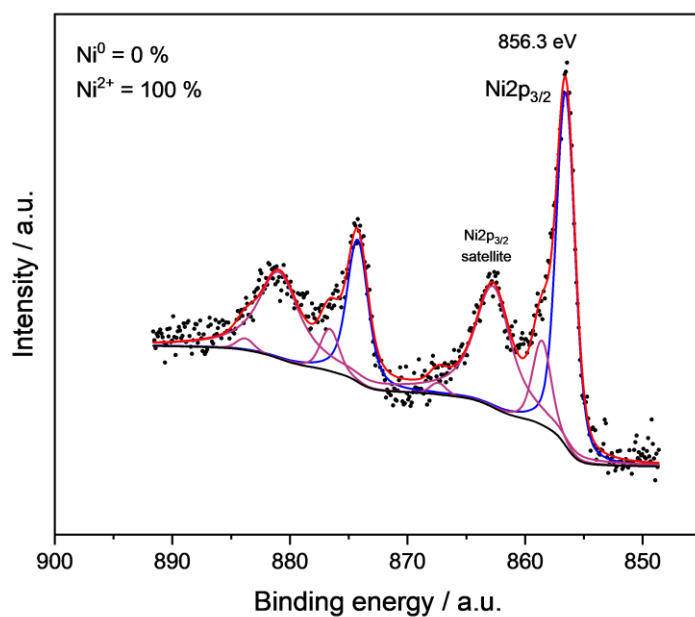
A-51: Ni2p spectra of spent NiMoO₄ after liquid-phase reaction at 350 °C, 50 bar H₂ pressure with anisole and 4 h reaction.



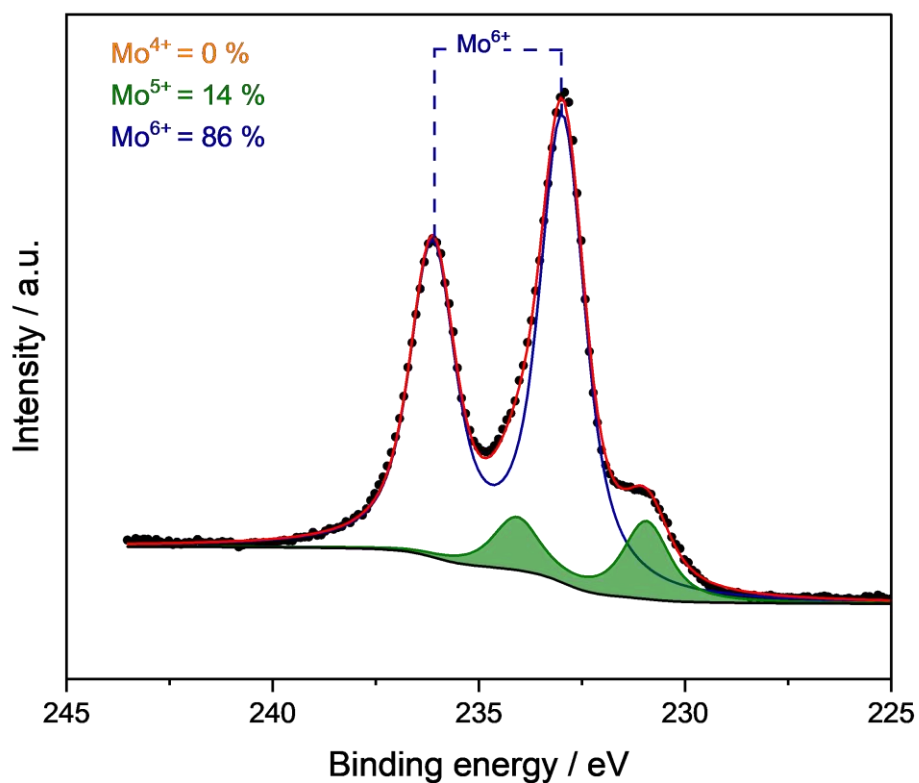
A-52: Mo3d spectra of spent MoO₃ after liquid-phase reaction at 350 °C, 50 bar H₂ pressure with guaiacol and 4 h reaction.



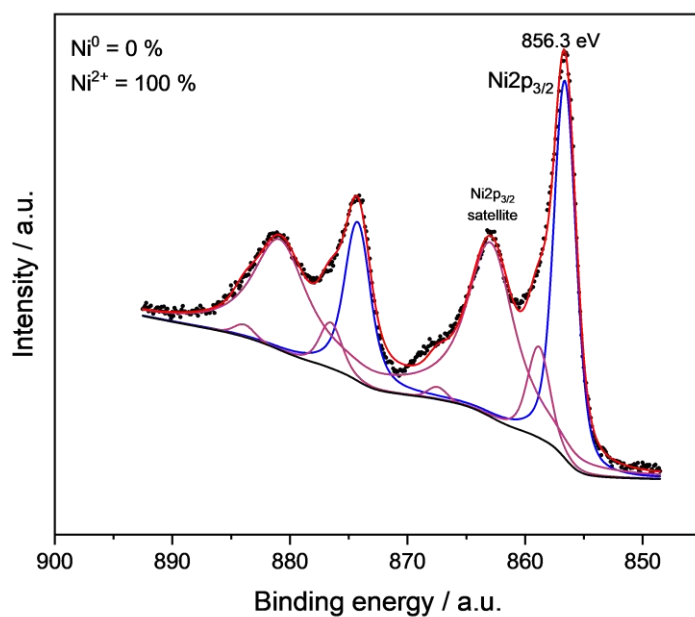
A-53: Mo3d spectra of spent Ni(5)MoO₃ after liquid-phase reaction at 350 °C, 50 bar H₂ pressure with guaiacol and 4 h reaction.



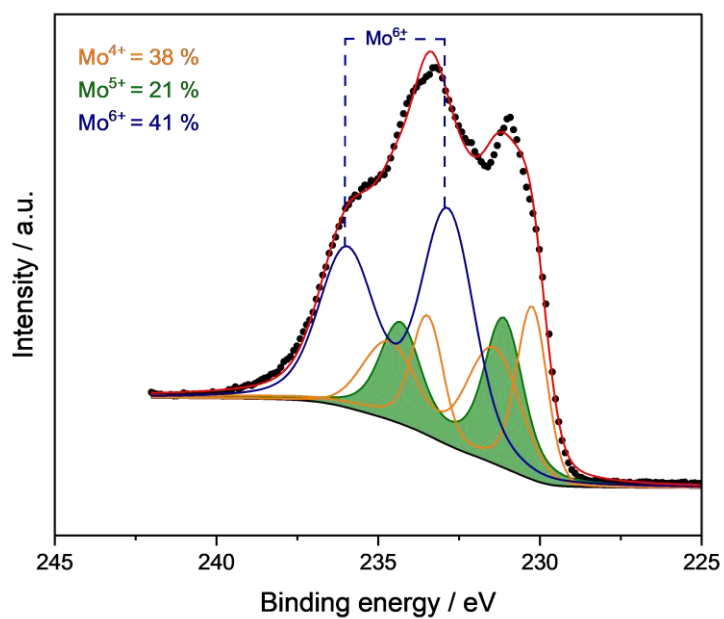
A-54: Ni2p spectra of spent Ni(5)MoO₃ after liquid-phase reaction at 350 °C, 50 bar H₂ pressure with guaiacol and 4 h reaction.



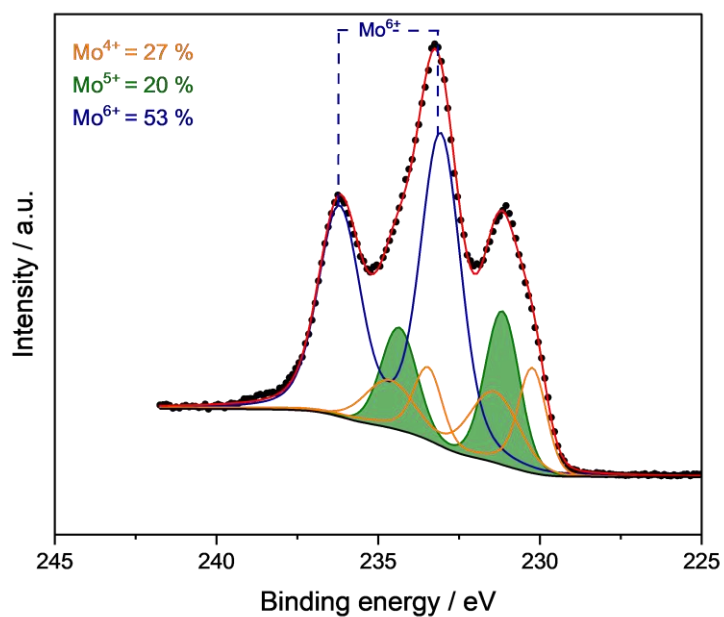
A-55: Mo3d spectra of spent NiMoO₄ after liquid-phase reaction at 350 °C, 50 bar H₂ pressure with guaiacol and 4 h reaction.



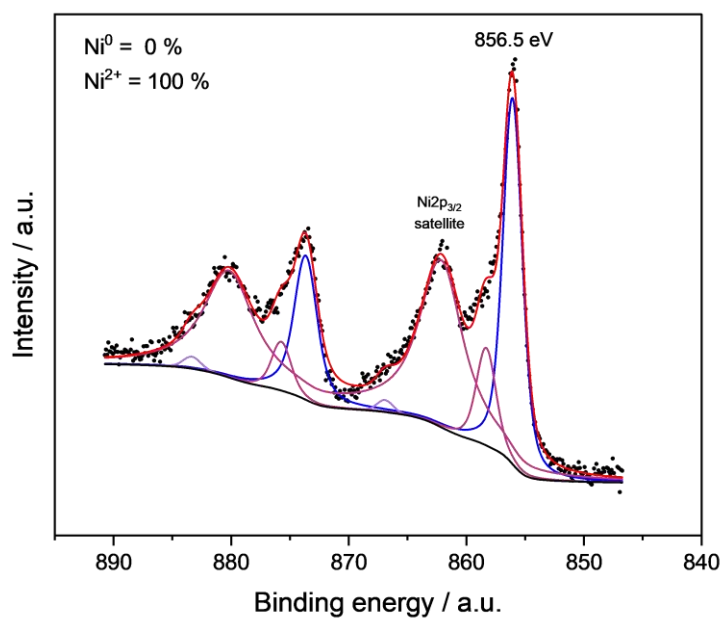
A-56: Ni2p spectra of spent NiMoO₄ after liquid-phase reaction at 350 °C, 50 bar H₂ pressure with guaiacol and 4 h reaction.



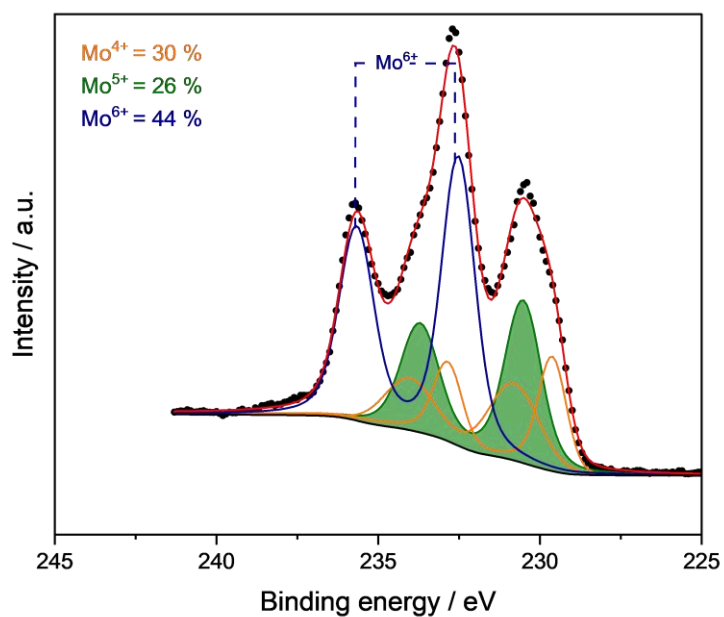
A-57: Mo3d spectra of spent MoO₃ after liquid-phase reaction at 350 °C, 50 bar H₂ pressure with phenol and 4 h reaction.



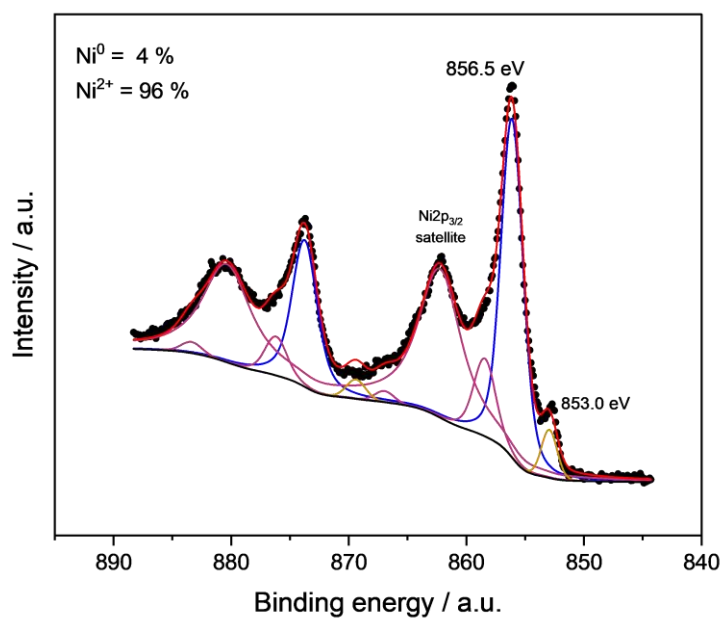
A-58: Mo3d spectra of spent Ni(5)MoO₃ after liquid-phase reaction at 350 °C, 50 bar H₂ pressure with phenol and 4 h reaction.



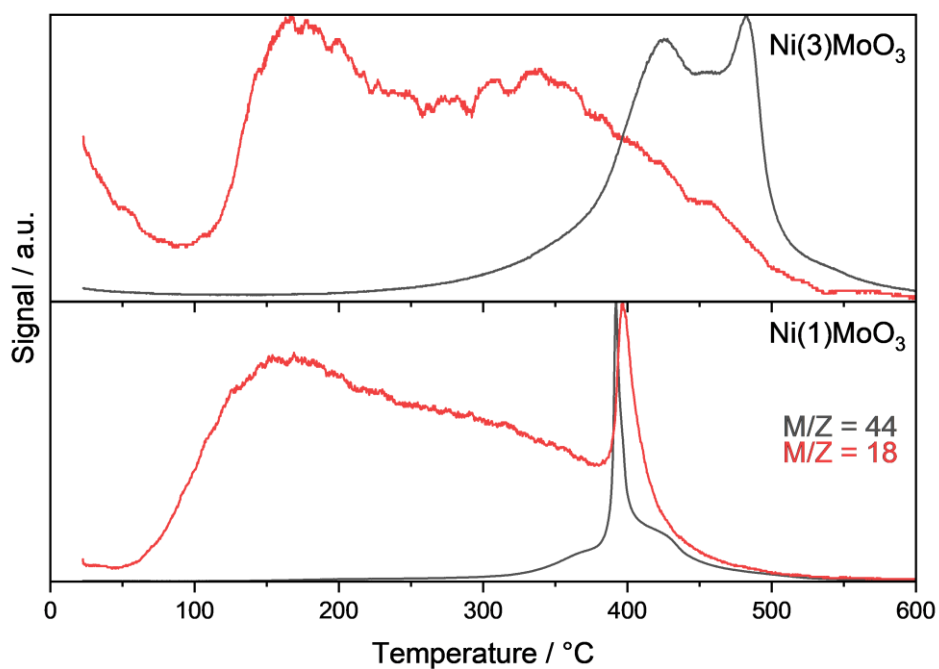
A-59: Ni2p spectra of spent Ni(5)MoO₃ after liquid-phase reaction at 350 °C, 50 bar H₂ pressure with phenol and 4 h reaction.



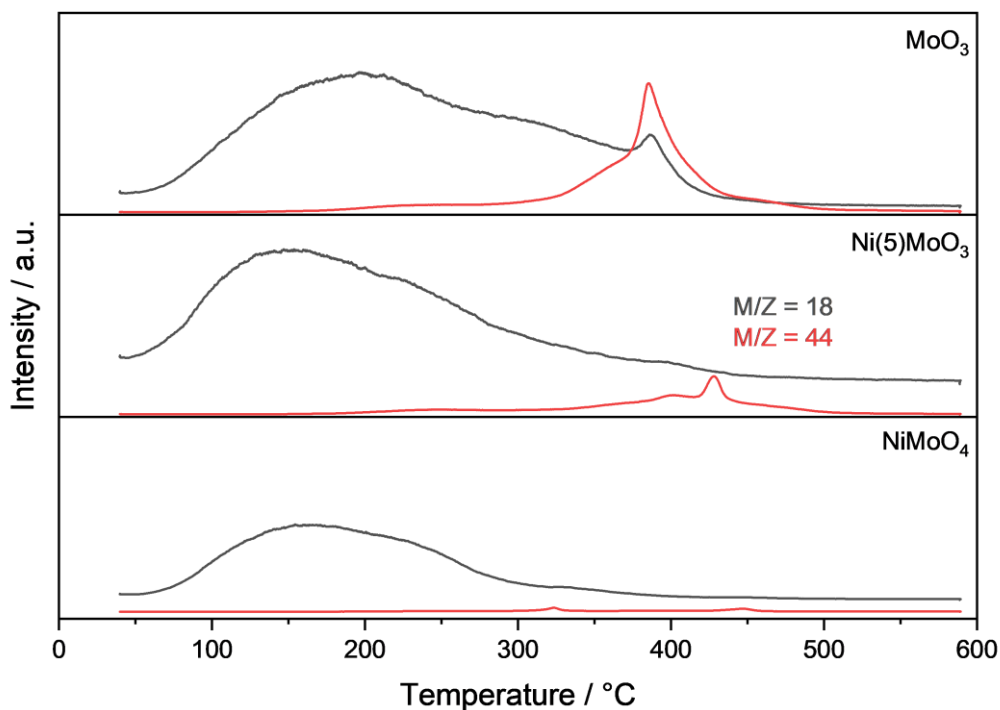
A-60: Mo3d spectra of spent NiMoO₄ after liquid-phase reaction at 350 °C, 50 bar H₂ pressure with phenol and 4 h reaction.



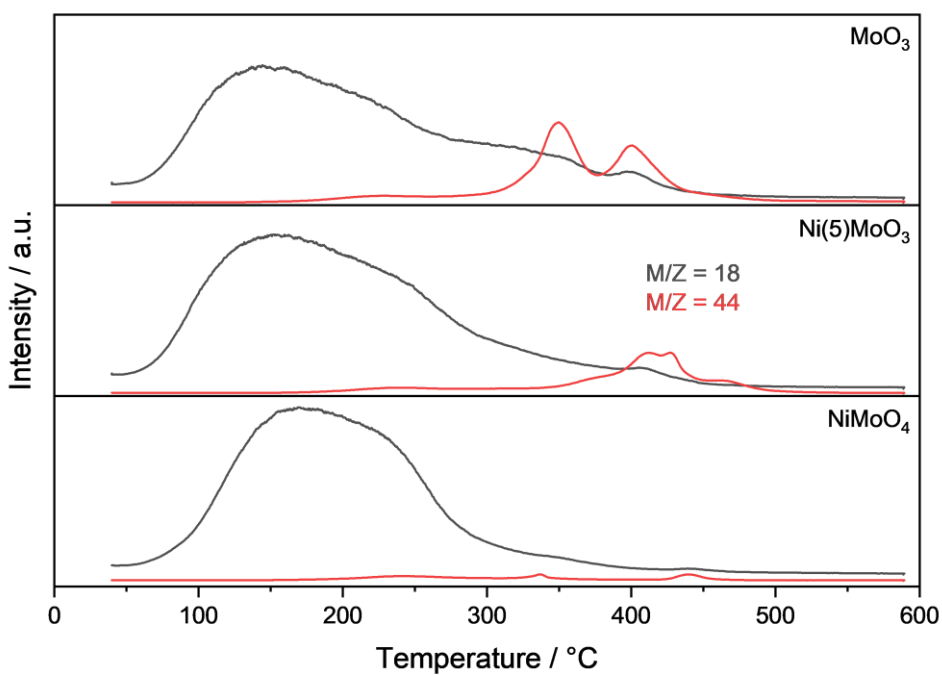
A-61: Ni2p spectra of spent NiMoO₄ after liquid-phase reaction at 350 °C, 50 bar H₂ pressure with phenol and 4 h reaction.



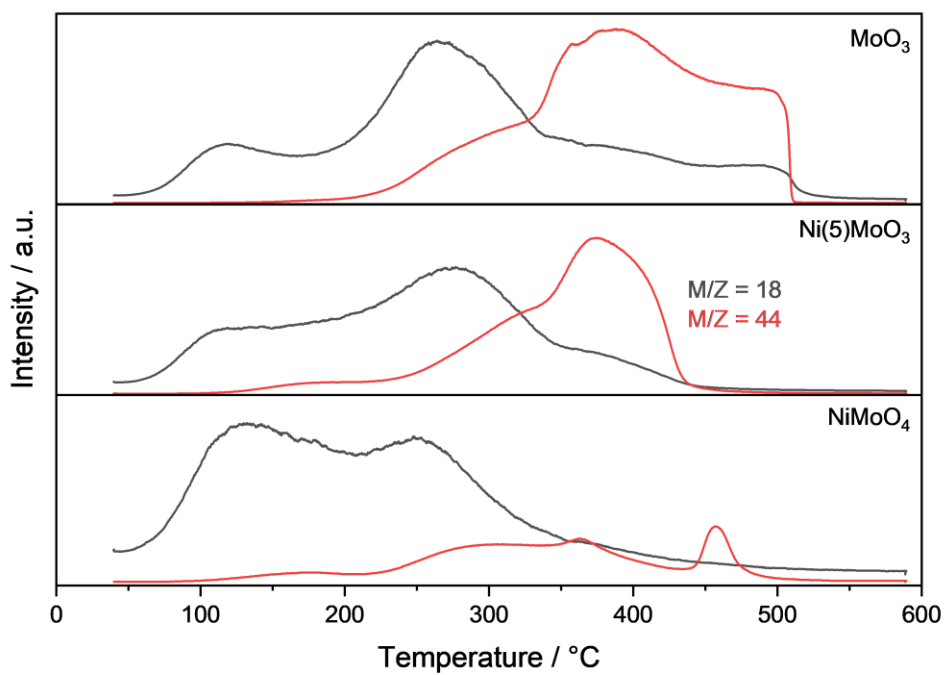
A-62: Normalized TG-MS profiles of spent catalysts after anisole HDO at 325 °C for 17 h treated in syn. air, 10 °C/min.



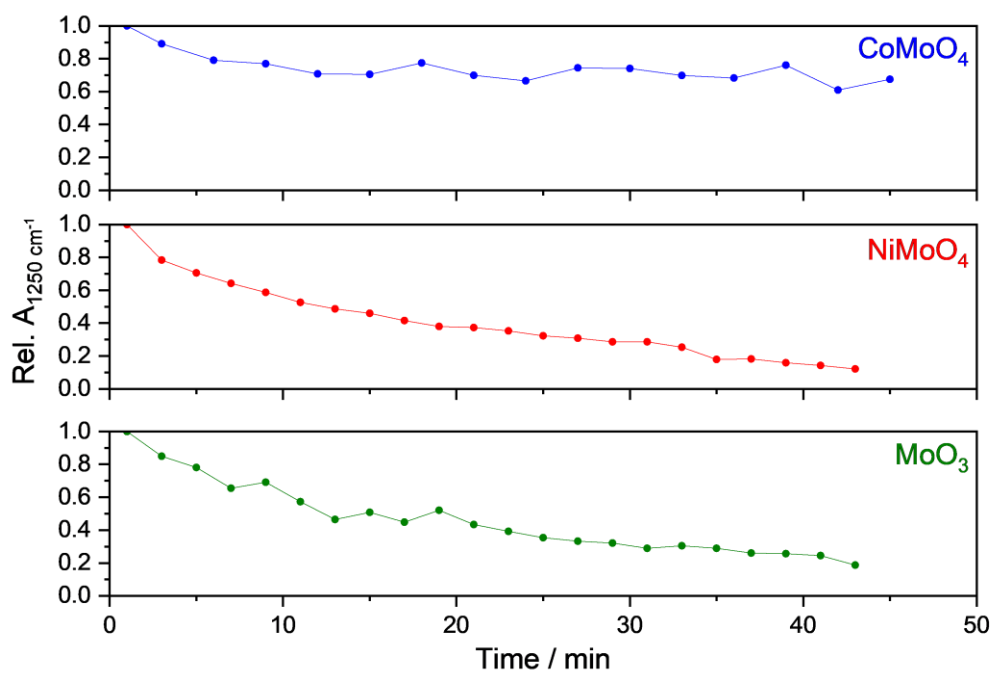
A-63: TG-MS profiles of spent catalysts after liquid-phase reaction at 350 °C and 50 bar H₂ pressure for 4 h with anisole in *n*-Dodecane.



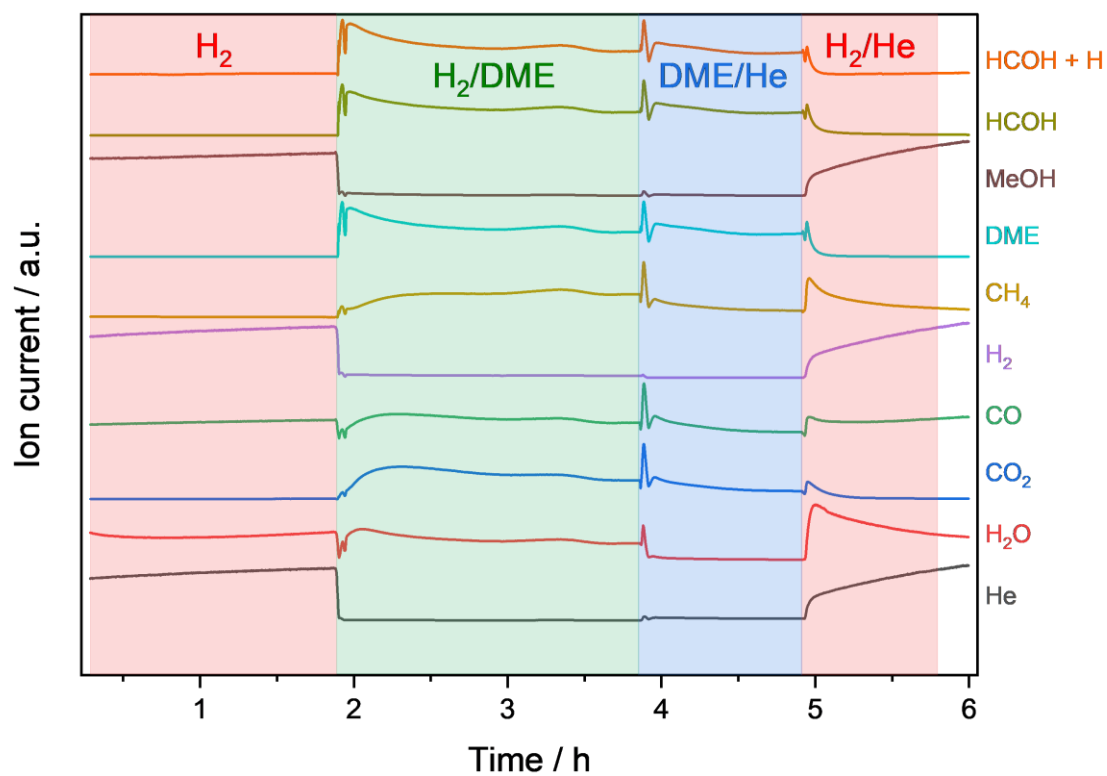
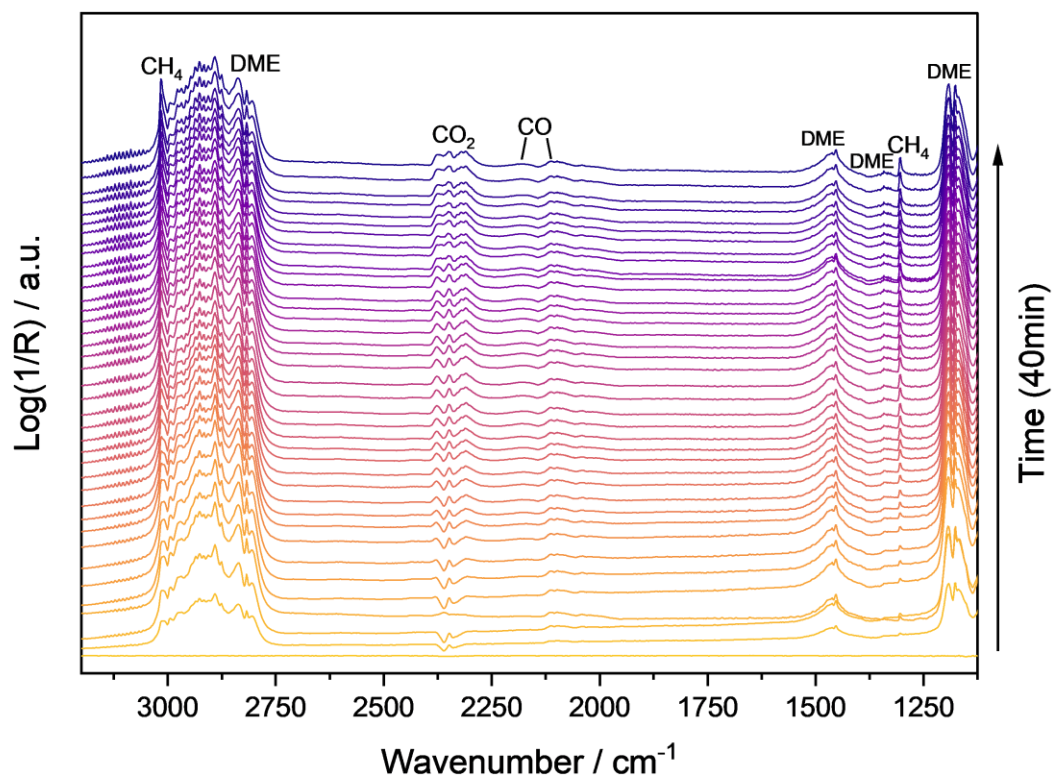
A-64: TG-MS profiles of spent catalysts after liquid-phase reaction at 350 °C and 50 bar H₂ pressure for 4 h with phenol in *n*-Dodecane.



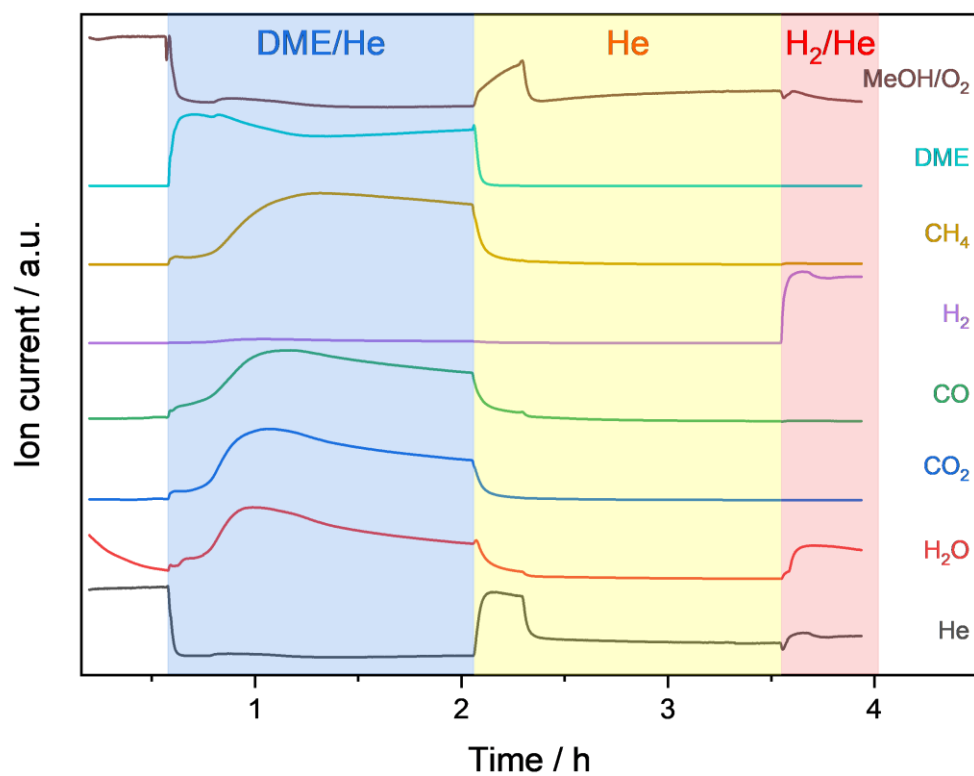
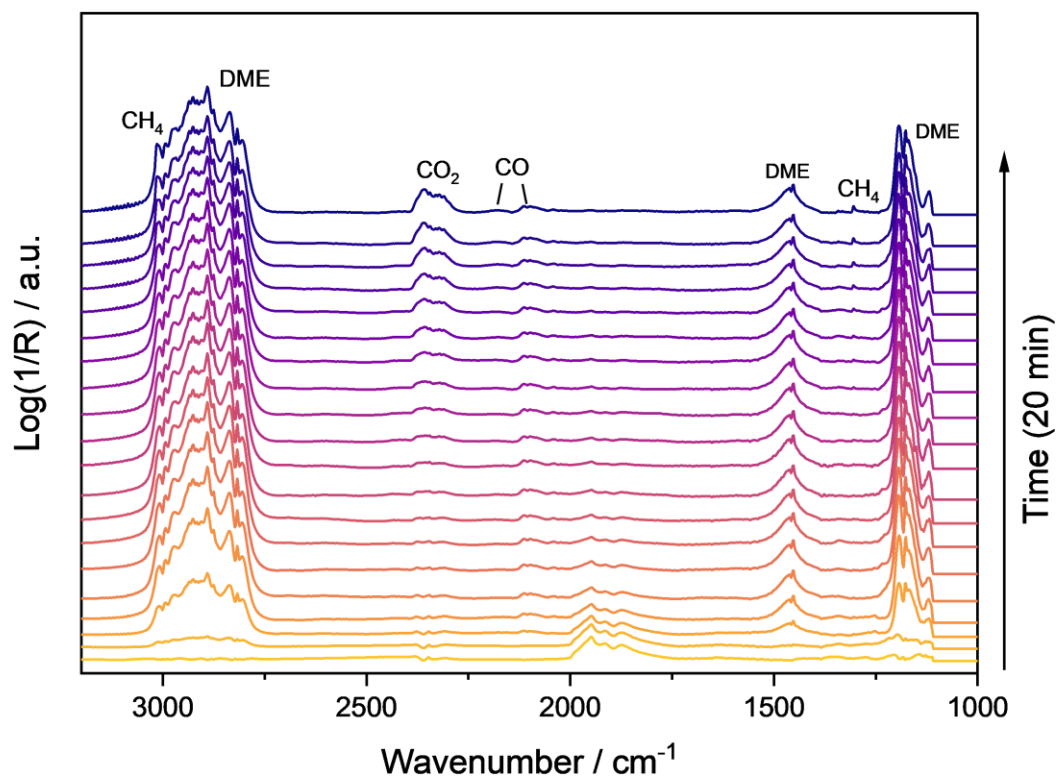
A-65: TG-MS profiles of spent catalysts after liquid-phase reaction at 350 °C and 50 bar H₂ pressure for 4 h with guaiacol in *n*-Dodecane.



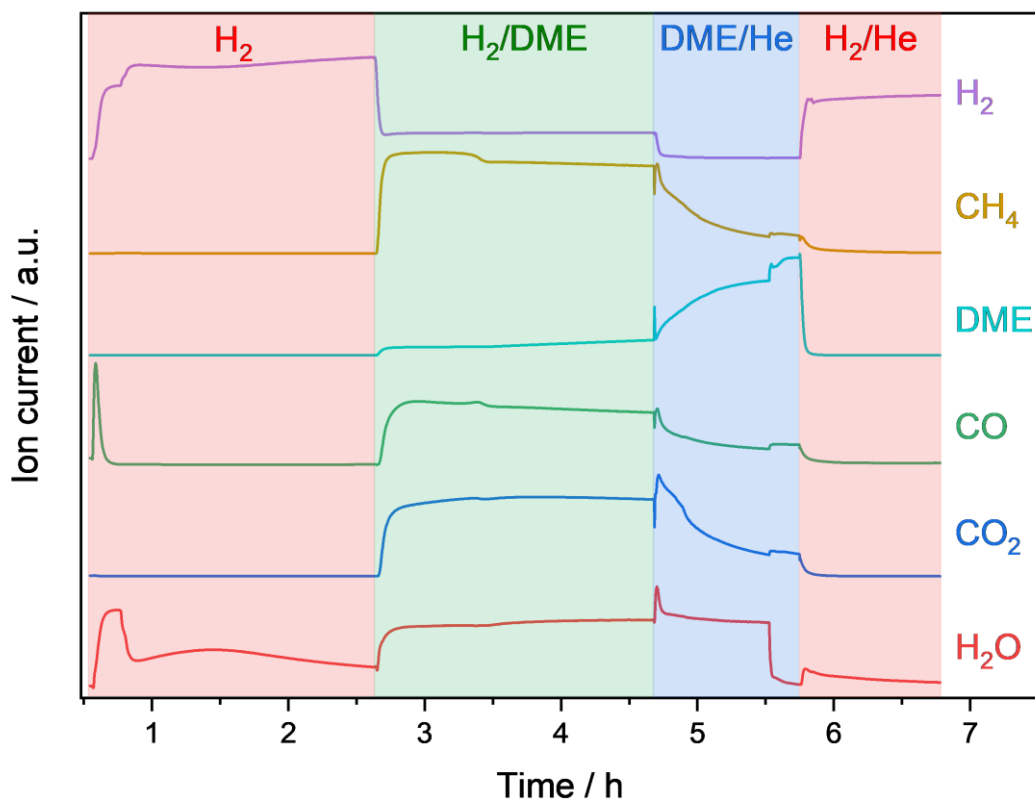
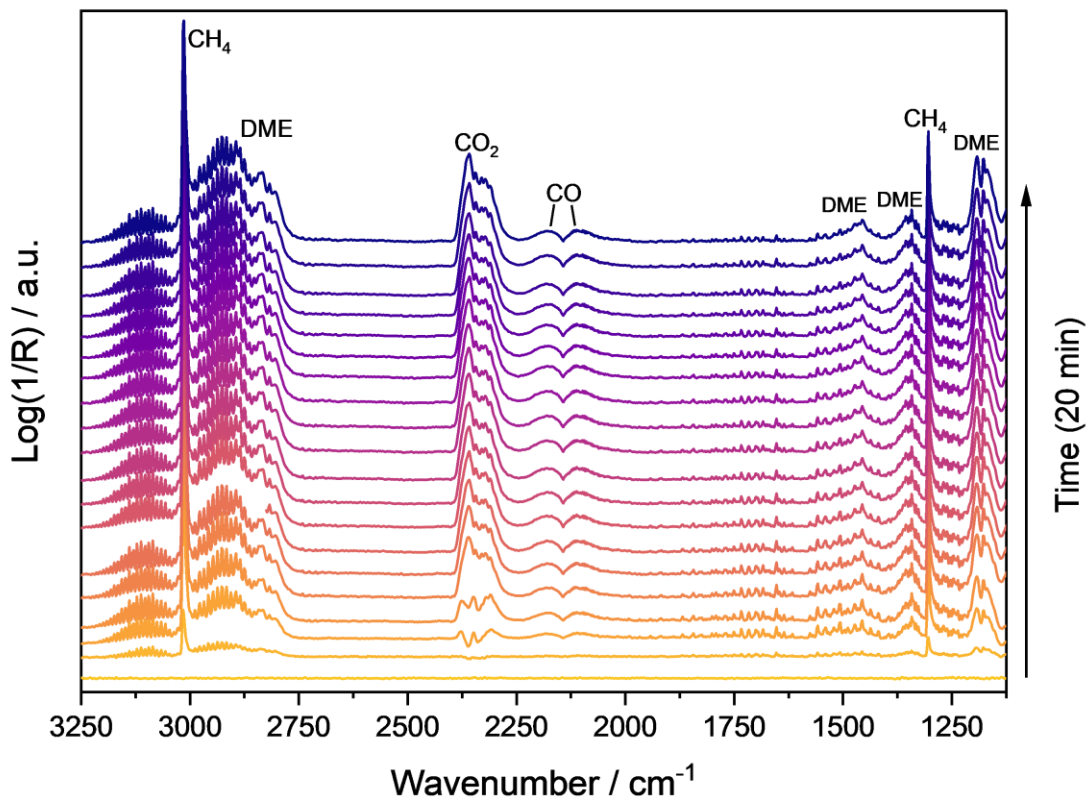
A-66: Relative integral values of absorption band at 1250 cm⁻¹ for the reaction of anisole at 325 °C in H₂ after adsorbing anisole at 325 °C in He.



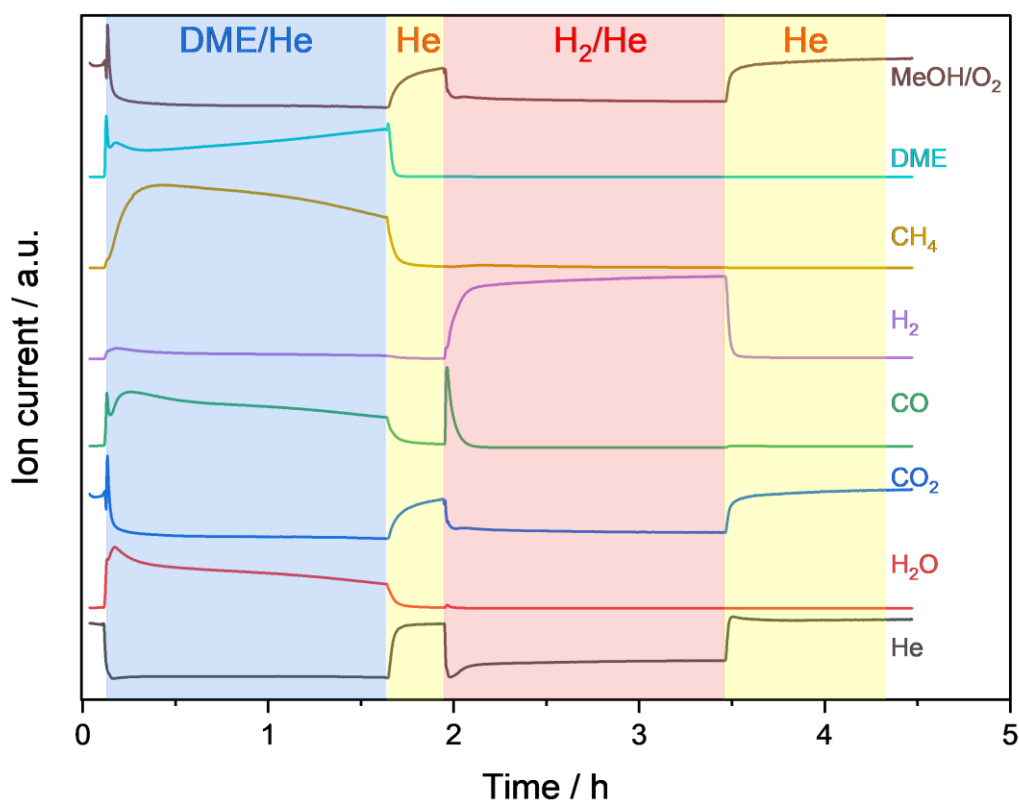
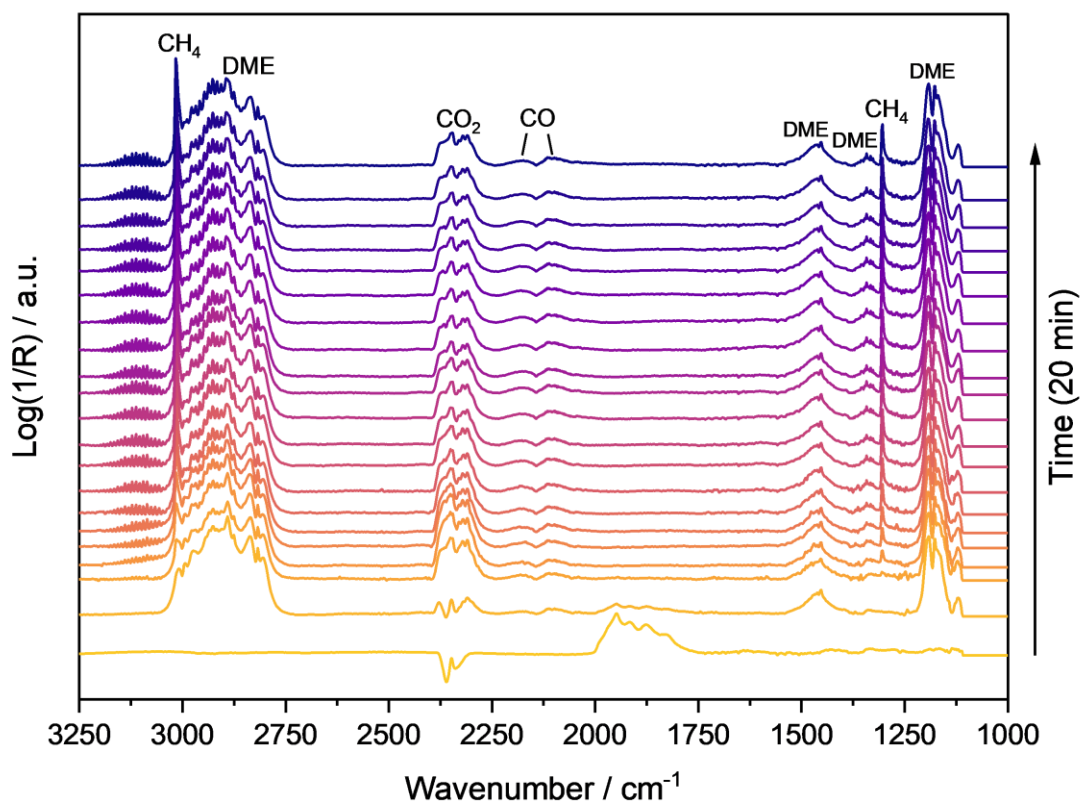
A-67: Operando DRIFTS experiment showing the hydrodeoxygenation of DME at 325 °C with MoO_3 . Sample is heated up in He to 325 °C and pre-reduction in 100 % H_2 for two hours. Afterwards, the feed was switched to a H_2/DME (9:1) mixture with a total flow of 25 mL/min.



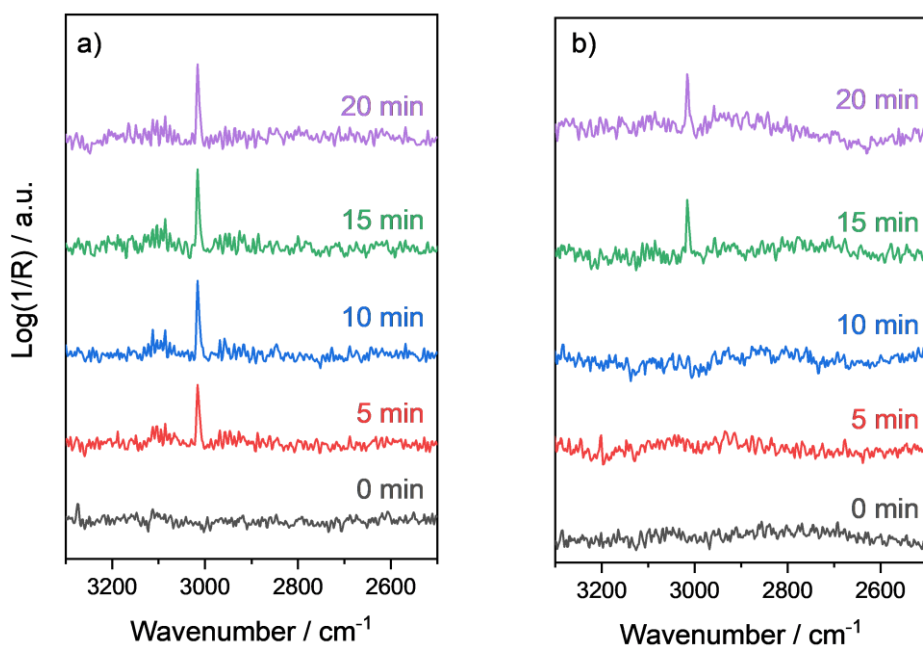
A-68: Operando DRIFTS experiment showing the hydrodeoxygenation of DME at 325 °C with MoO_3 . Sample is heated up in He to 325 °C. Afterwards, the feed was switched to a H_2/DME (9:1) mixture with a total flow of 25 mL/min.



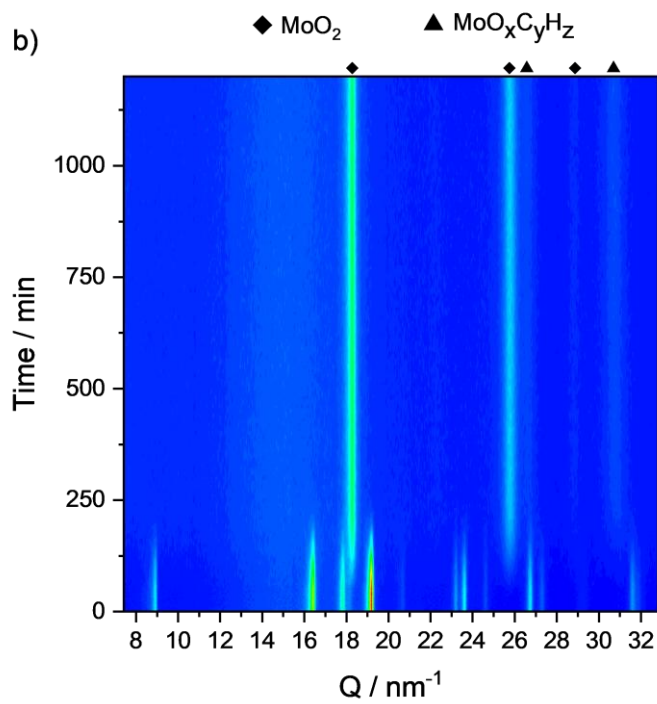
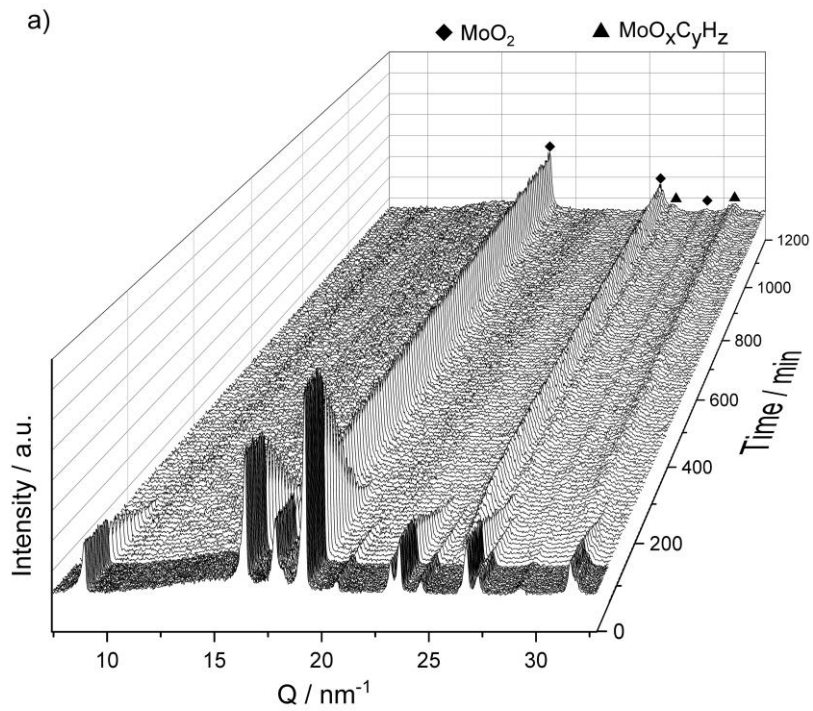
A-69: Operando DRIFTS experiment showing the hydrodeoxygenation of DME at 325 °C with Ni(5)MoO_3 and pre-reduction in 100 % H_2 for two hours. Sample is heated up in He to 325 °C and reduced in 100 % H_2 for two hours. Afterwards, the feed was switched to a H_2/DME (9:1) mixture with a total flow of 25 ml/min.



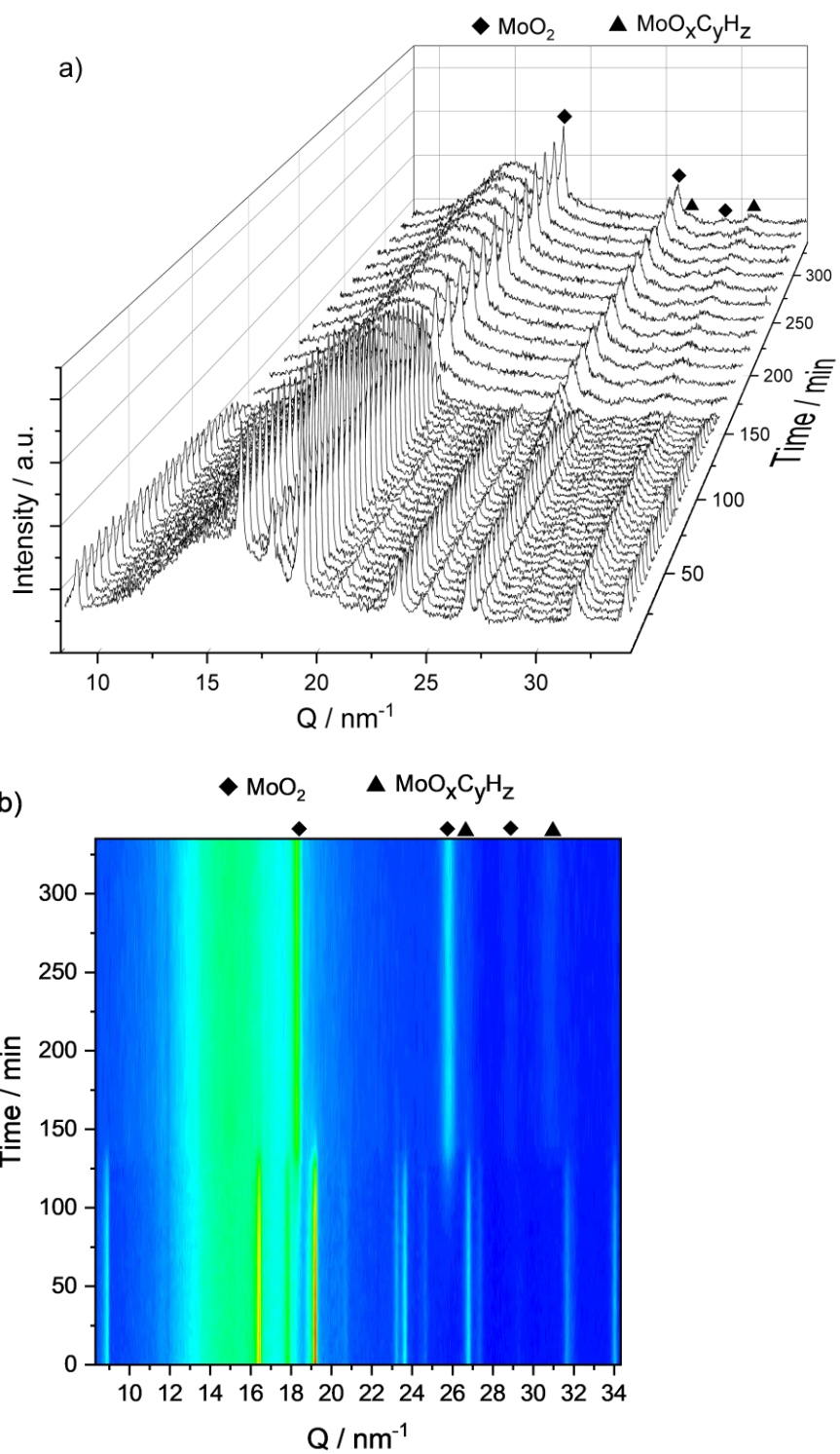
A-70: Operando DRIFTS experiment showing the hydrodeoxygenation of DME at 325 °C with $\text{Ni}(5)\text{MoO}_3$. Sample is heated up in He to 325 °C. Afterwards, the feed was switched to a H_2/DME (9:1) mixture with a total flow of 25 ml/min.



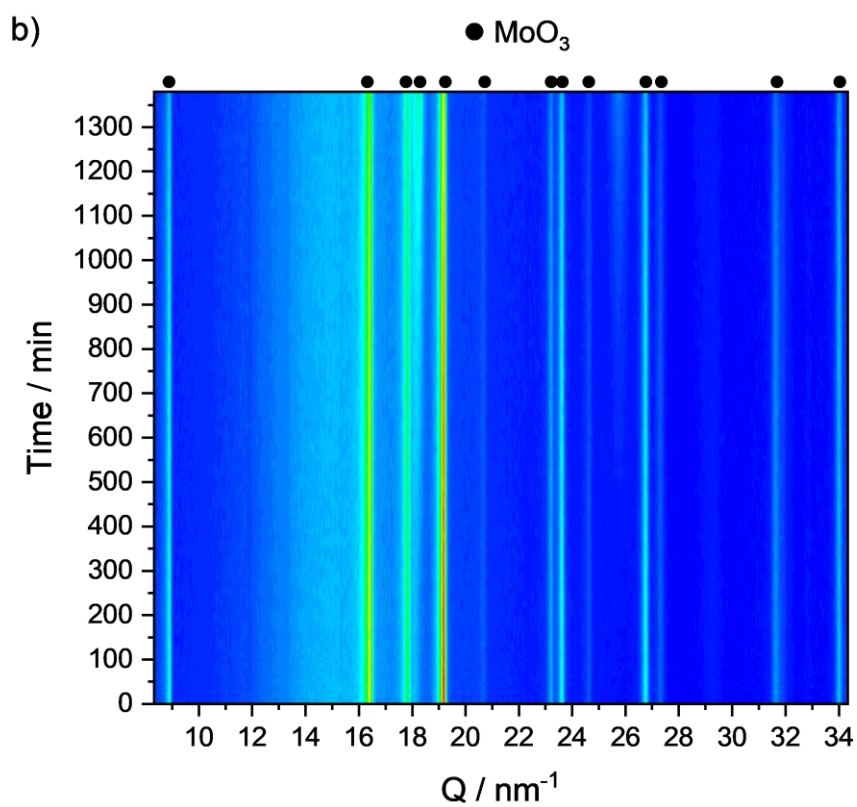
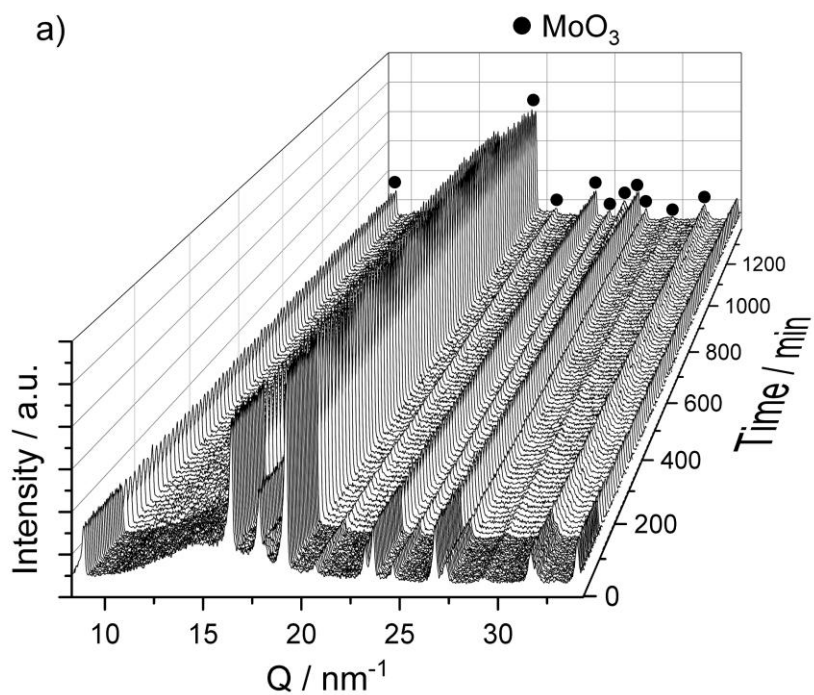
A-71: Comparison methane evolution after benzene adsorption in He and switch to H_2 at 325 °C and pre-reduction at 325 °C in 100 % H_2 for a) NiMoO_4 and b) CoMoO_4 .



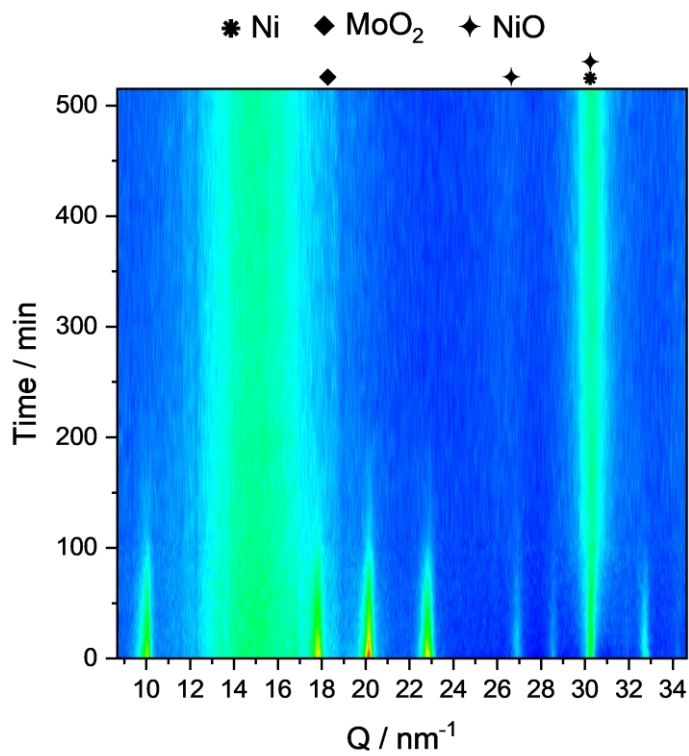
A-72: In-situ XRD of $\text{MoO}_x\text{C}_y\text{H}_z$ formation from MoO_3 in $\text{H}_2:\text{CH}_4$ (9:1) at 325 °C shown as a) waterfall plot and b) contour plot.



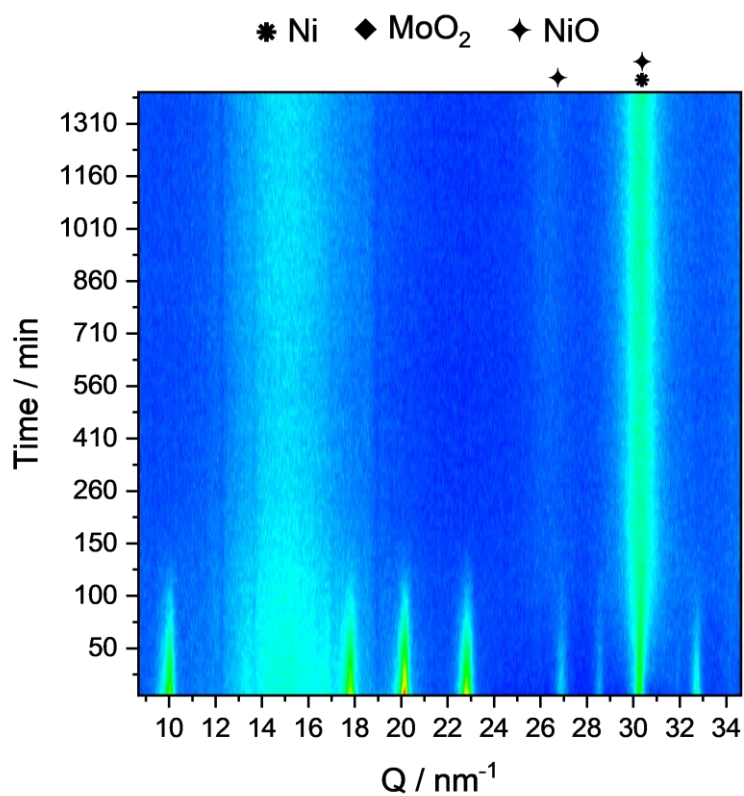
A-73: In-situ XRD of $\text{MoO}_x\text{C}_y\text{H}_z$ formation from MoO_3 in $\text{H}_2:\text{CH}_4$ (1:1) at 325°C shown as a) waterfall plot and b) contour plot.



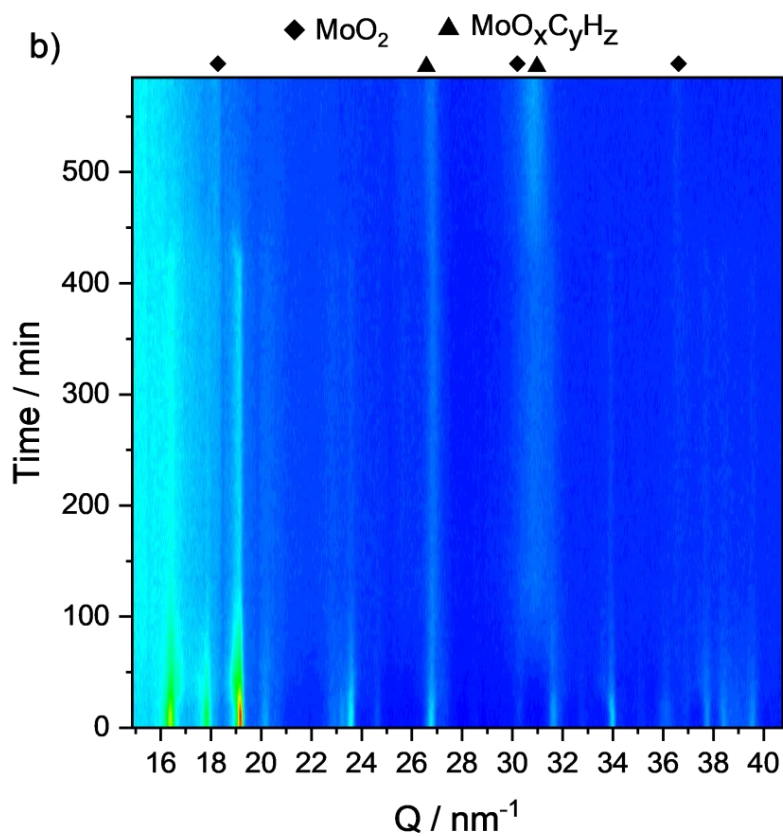
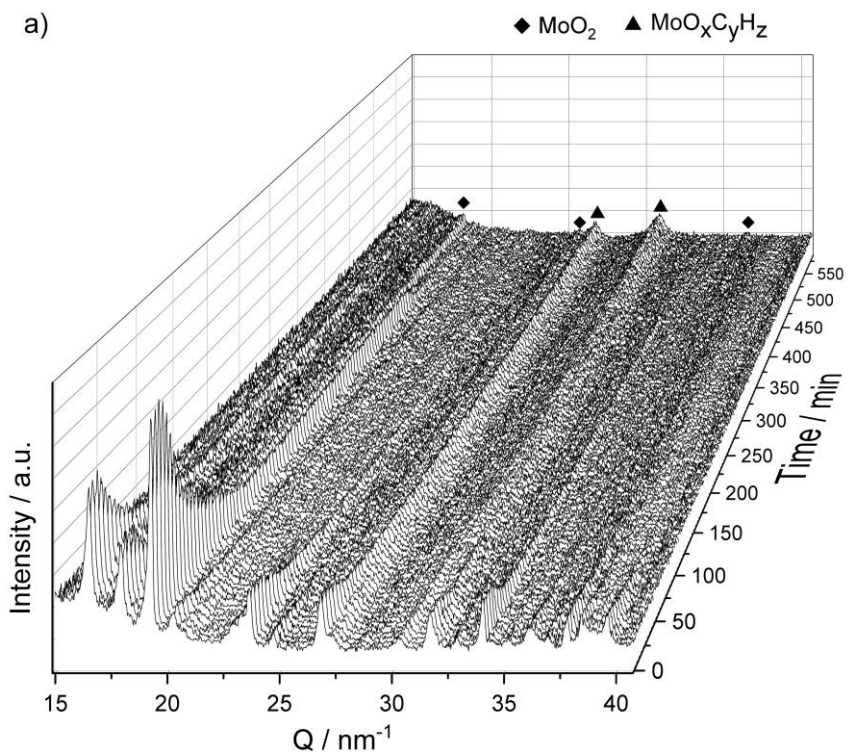
A-74: In-situ XRD of MoO_xC_yH_z formation from MoO₃ in H₂:CH₄ (1:9) at 325 °C shown as a) waterfall plot and b) contour plot.



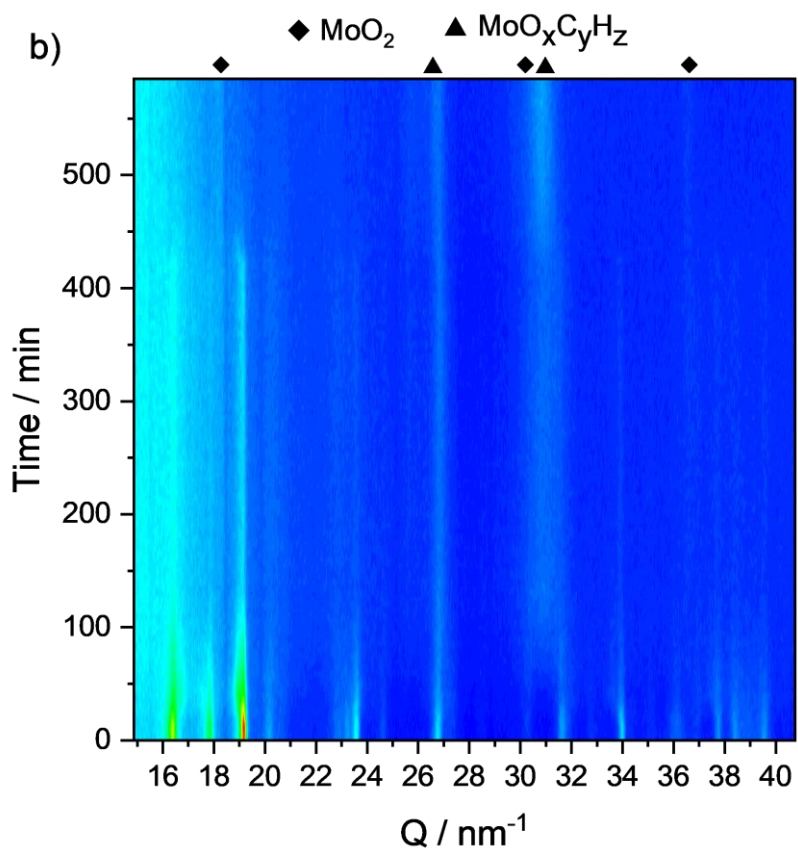
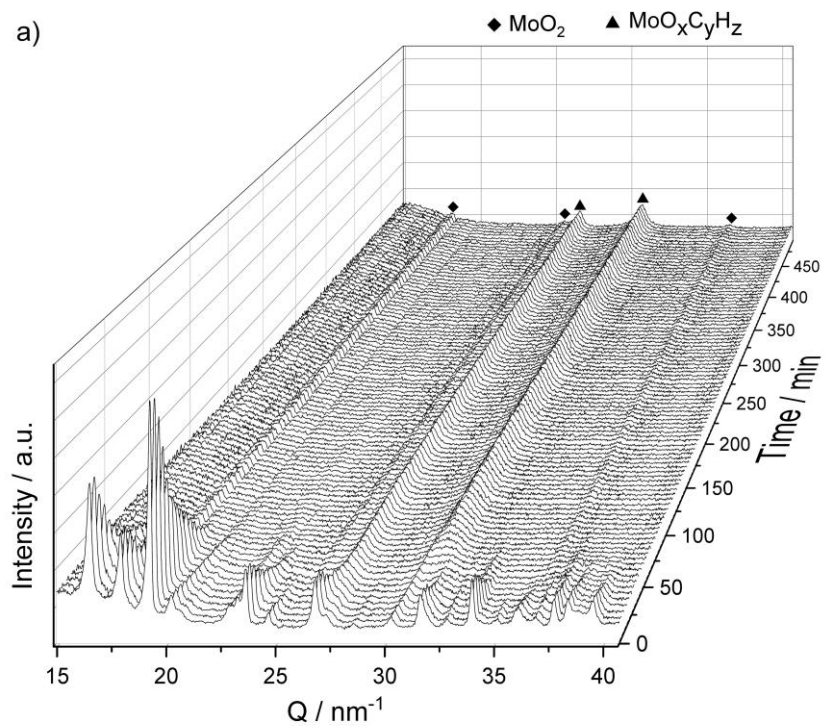
A-75: In-situ XRD reduction of NiMoO₄ in 100 % H₂ at 325 °C for 515 min.



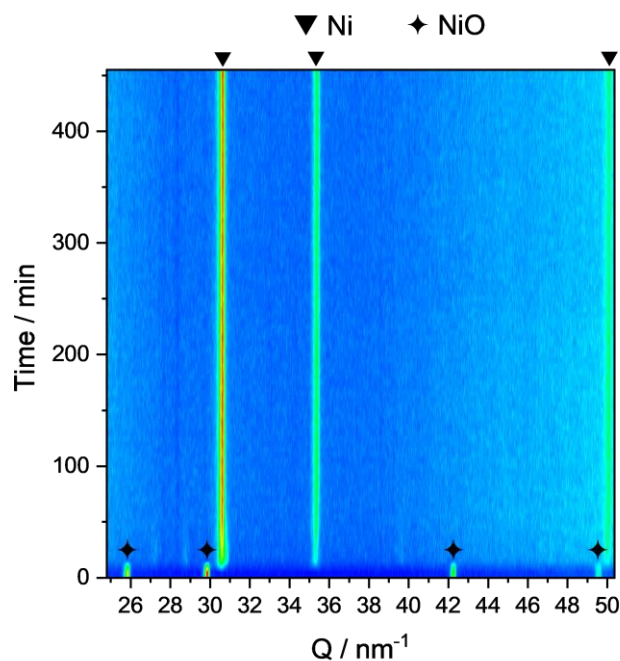
A-76: In-situ XRD of NiMoO₄ in H₂/CH₄ (9:1) at 325 °C for 1385 min.



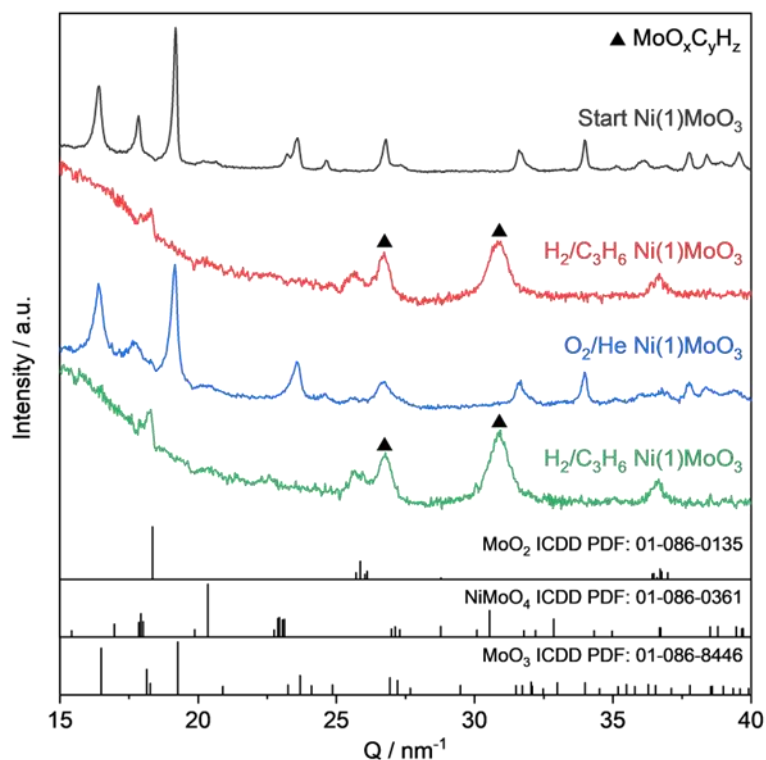
A-77: In-situ XRD measurement of Ni(5)MoO₃ heated up to 325 °C in He and switch to H₂ for 125 min followed by flushing with He and switch to CH₄ for 240 min. Afterwards, the sample was flushed again with He and treated for 160 min with H₂. Shown as a) waterfall plot and b) contour plot



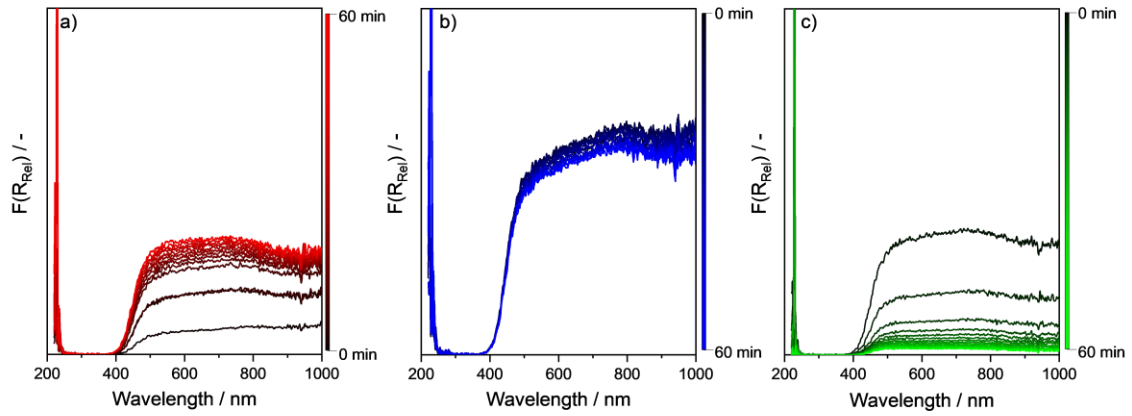
A-78: In-situ XRD measurement of Ni(5)MoO₃ in H₂/C₃H₆ (9:1) at 325 °C for 492 min shown as a) waterfall plot and b) contour plot.



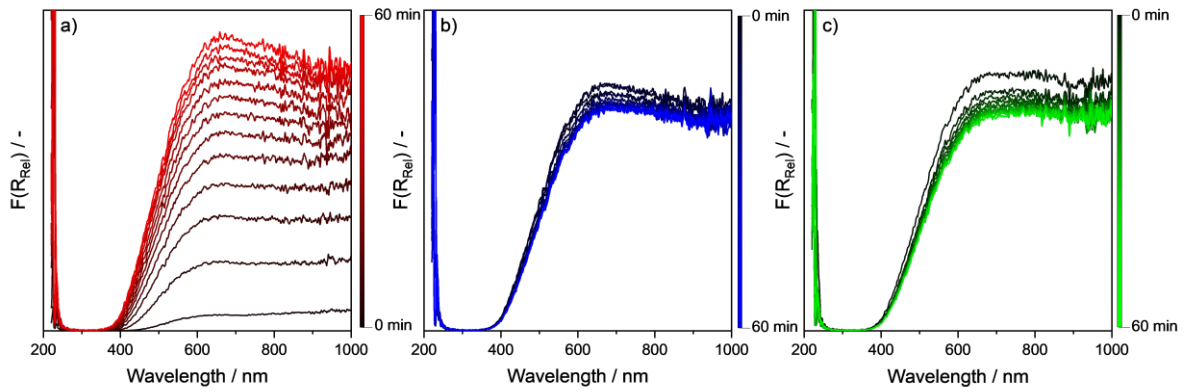
A-79: In-situ XRD measurement of NiO in $\text{H}_2/\text{C}_3\text{H}_6$ (9:1) at 325 °C for 492 min shown as contour plot.



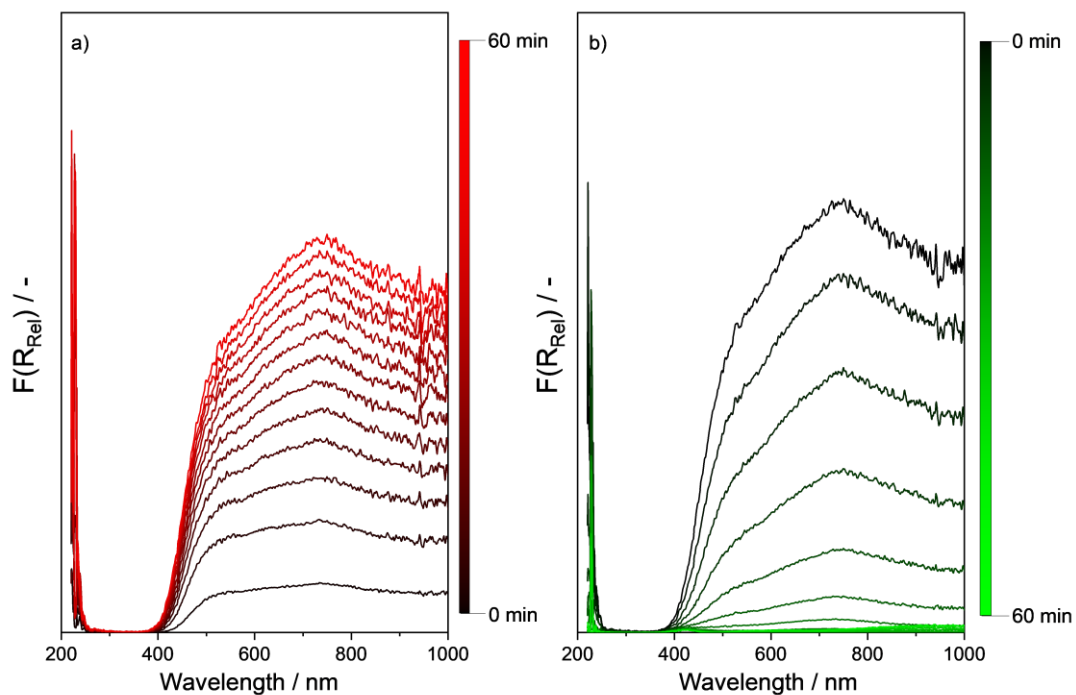
A-80: Normalized in-situ XRD-results from the monitoring of a stepwise active phase formation from $\text{Ni}(1)\text{MoO}_3$ with an intermittent reoxidation step at 325 °C for 4 h with 5 % O_2 in He and an $\text{H}_2/\text{C}_3\text{H}_6$ (9:1) mixture. Reproduced from Ref. with permission from the Royal Society of Chemistry.



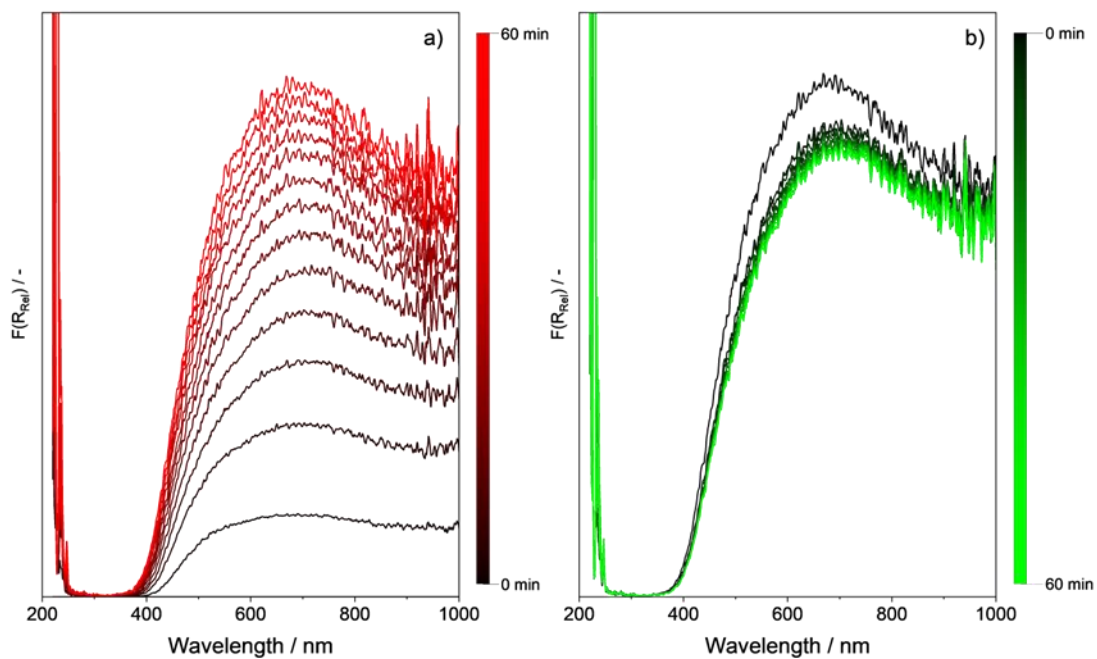
A-81: UV-Vis experiments on the a) reduction ($\text{H}_2/\text{C}_2\text{H}_6$ (9:1)), b) oxidation by H_2O (30 % in N_2) and c) oxidation by syn. air of MoO_3 at 325 °C for 1 h in a fixed-bed reactor (spectra in 5 min steps).



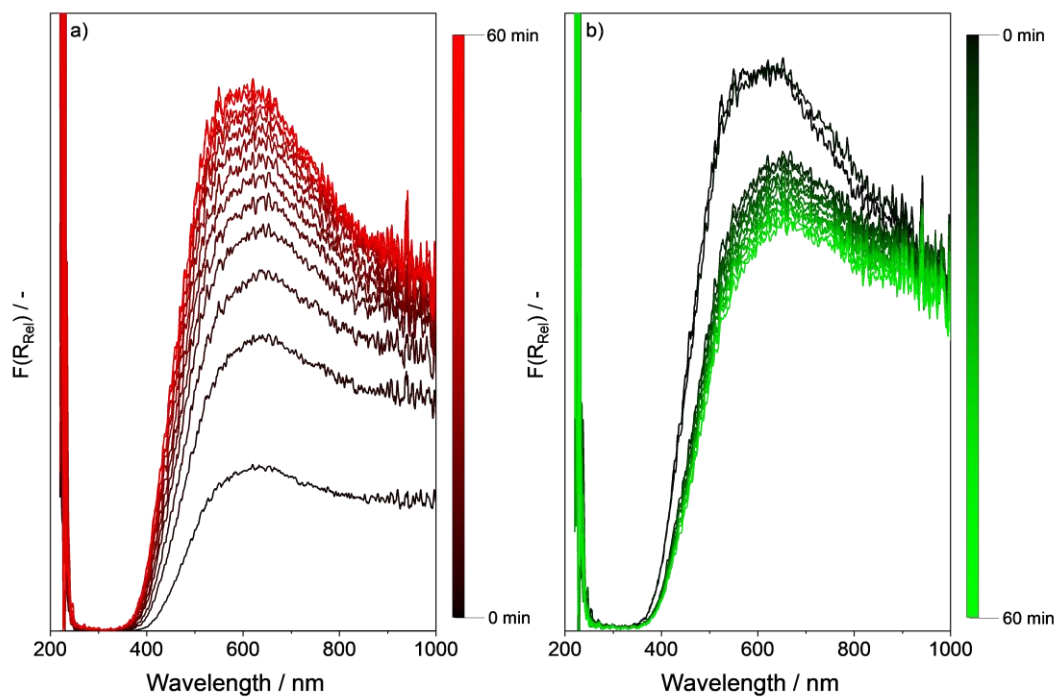
A-82: UV-Vis experiments on the a) reduction (100 % H_2), b) oxidation by H_2O (30 % in N_2) and c) oxidation by syn. air of Ni(5)MoO_3 at 325 °C for 1 h in a fixed-bed reactor (spectra in 5 min steps).



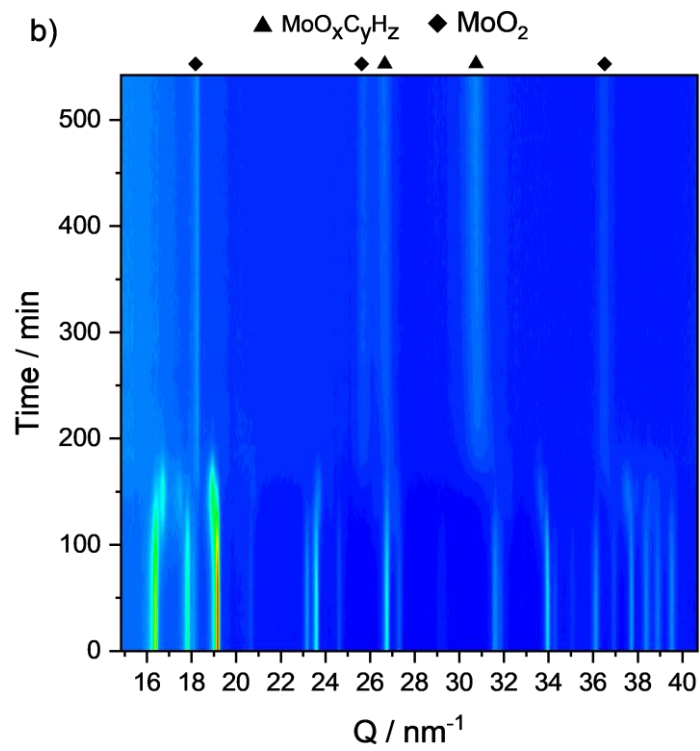
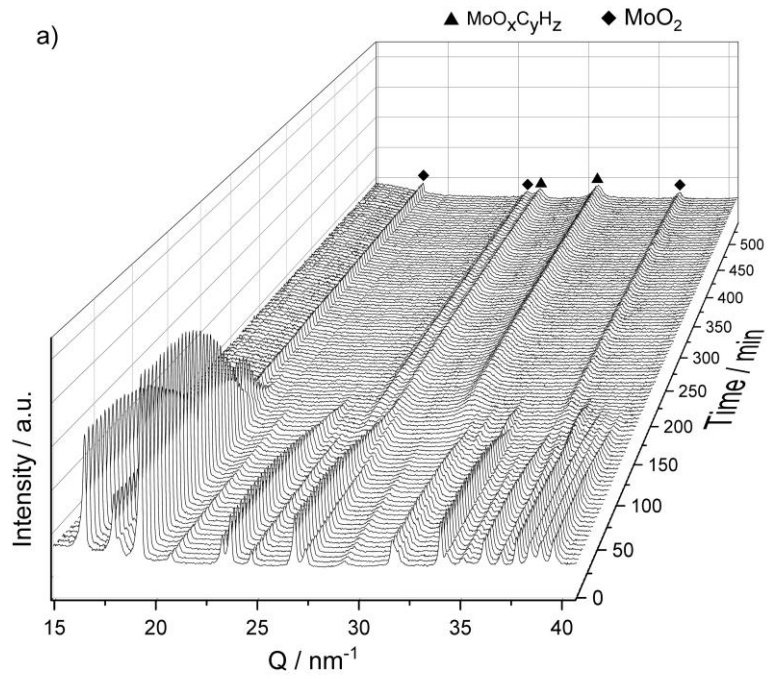
A-83: In-situ UV-Vis measurements for a) the MoO_3 reduction in $\text{H}_2/\text{C}_3\text{H}_6$ (9:1) at $325\text{ }^\circ\text{C}$ for 60 min (5 min steps) and b) for the oxidation at $400\text{ }^\circ\text{C}$ in 10 % O_2 in N_2 for 60 min (spectra in 5 min steps).



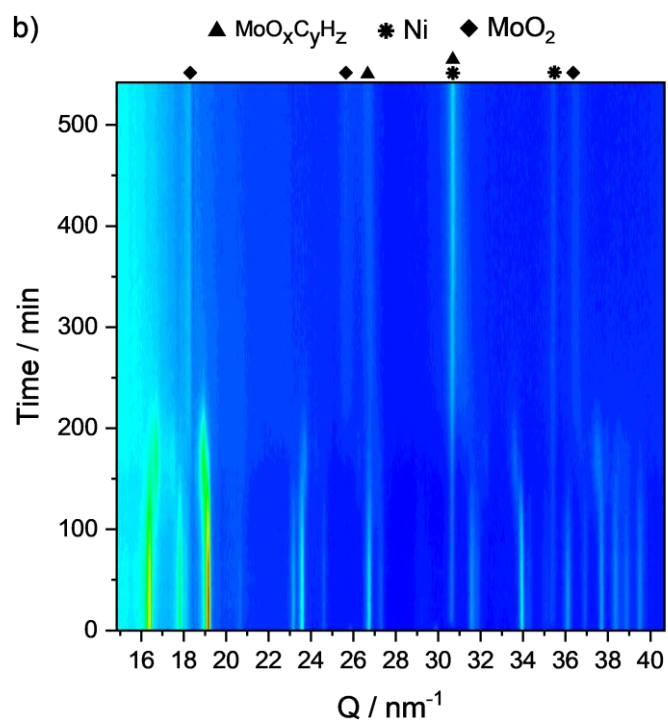
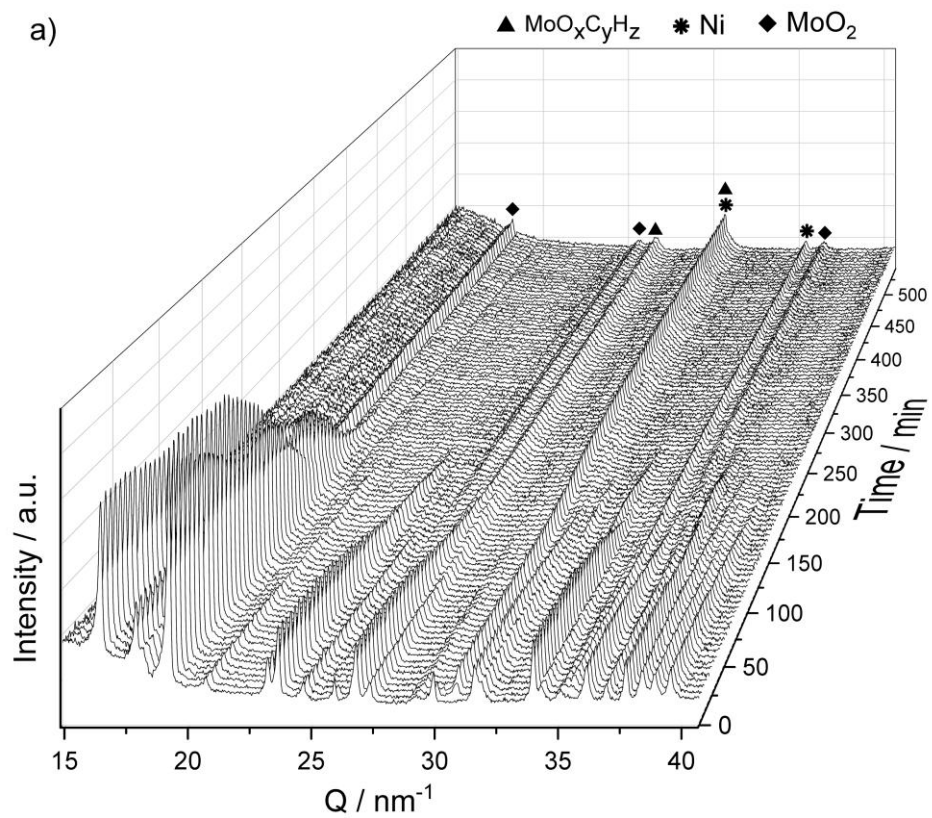
A-84: In-situ UV-Vis measurements for a) the $\text{Ni}(1)\text{MoO}_3$ reduction in $\text{H}_2/\text{C}_3\text{H}_6$ (9:1) at $325\text{ }^\circ\text{C}$ for 60 min (5 min steps) and b) for the oxidation at $400\text{ }^\circ\text{C}$ in 10 % O_2 in N_2 for 60 min (spectra in 5 min steps).



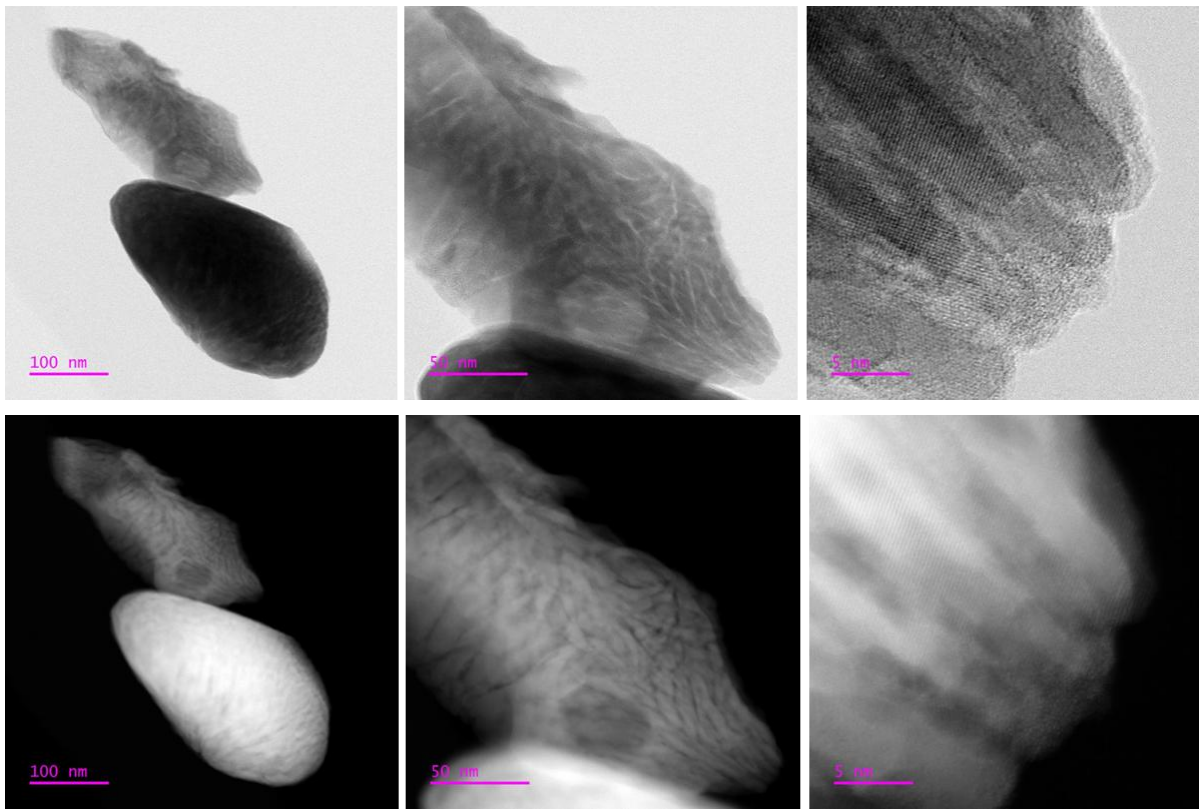
A-85: In-situ UV-Vis measurements for a) the Ni(5)MoO₃ reduction in H₂/C₃H₆ (9:1) at 325 °C for 60 min (5 min steps) and b) for the oxidation at 400 °C in 10 % O₂ in N₂ for 6 min (spectra in 5 min steps).



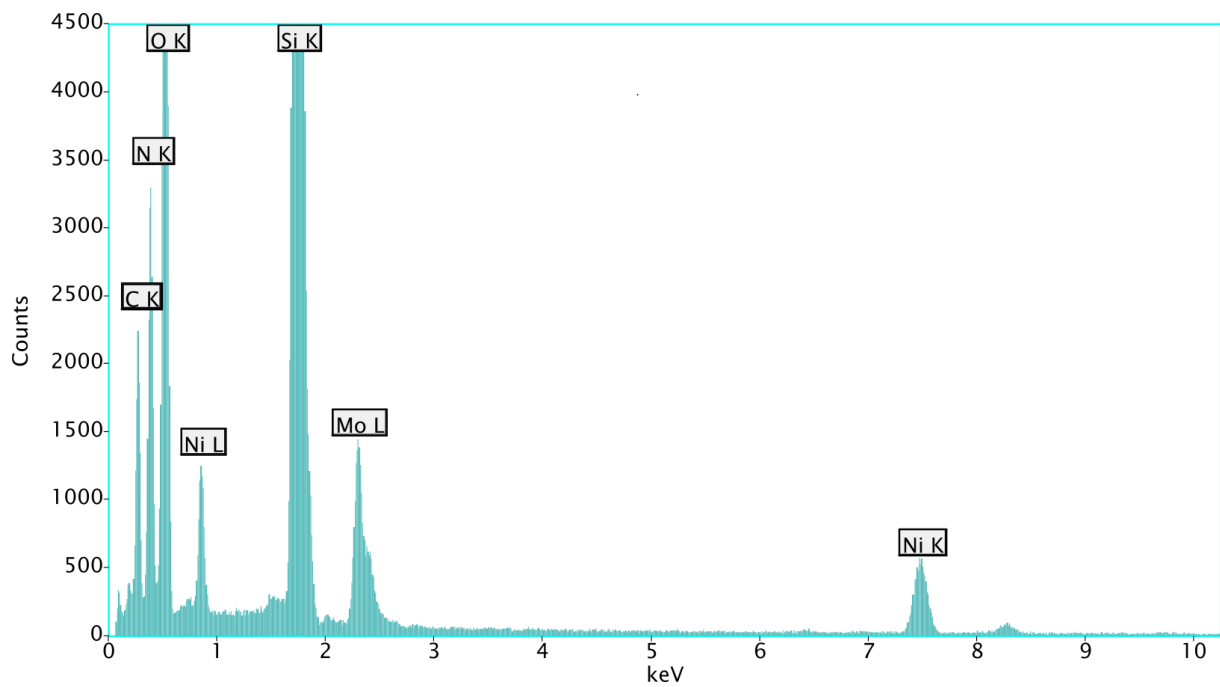
A-86: Two layered system with NiO and MoO_3 layer in $\text{H}_2/\text{C}_3\text{H}_6$ (9:1) at 325 °C for 542 min shown as a) waterfall plot and b) contour plot.



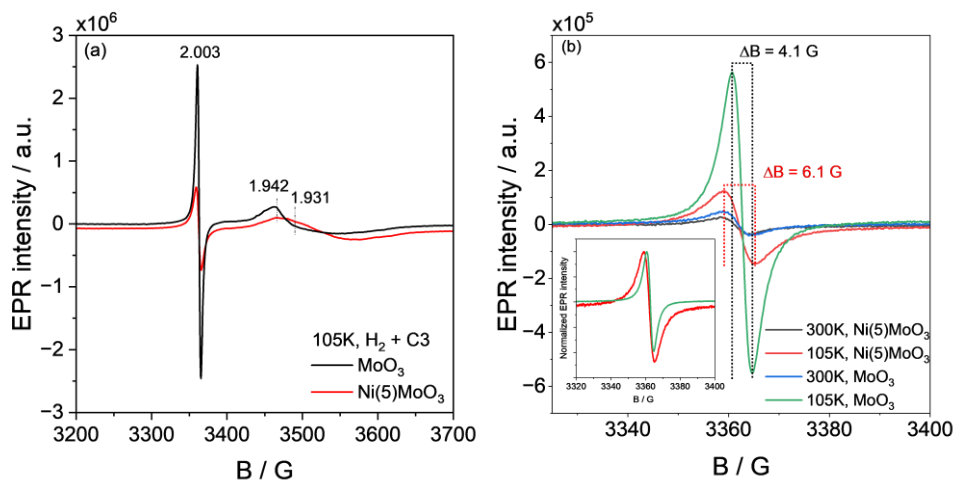
A-87: Physical mixture of NiO/MoO₃ in H₂:C₃H₆ (9:1) at 325 °C for 542 min shown as a) waterfall plot and b) contour plot.



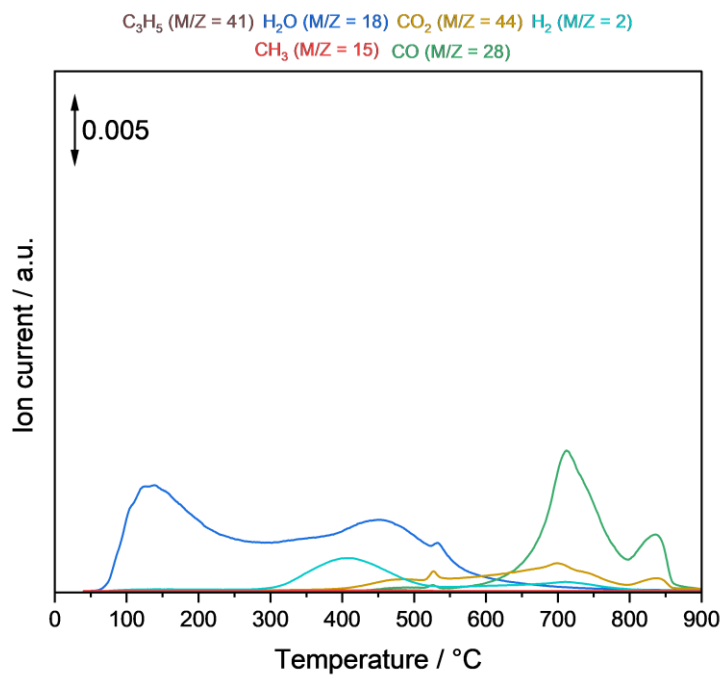
A-88: TEM pictures of MoO_3 treated in $\text{H}_2:\text{CH}_4$ (9:1) at 325°C for 8 h.



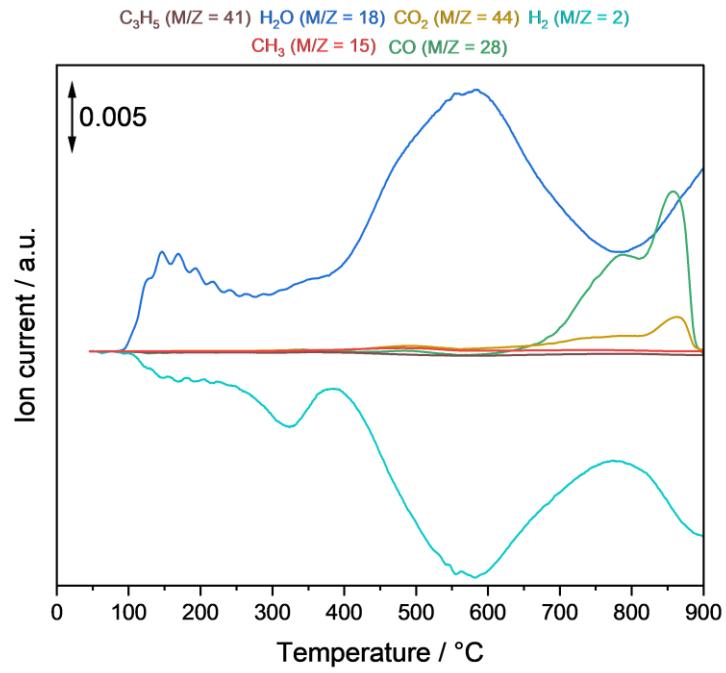
A-89: EDX spectrum of $\text{Ni}(5)\text{MoO}_3$ after in-situ TEM treatment in $\text{H}_2/\text{C}_3\text{H}_6$ at 325°C for 140 min.



A-90: In-situ EPR spectra of MoO₃ and Ni(5)MoO₃ recorded at -168 °C after reduction with a mixture of H₂/C₃H₆ for 120 min at 300 °C; b) the corresponding signal at g = 2.003 of both samples recorded at 25 °C and -168 °C with a modulation amplitude of 1.0G, after reduction with a mixture of H₂/C₃H₆ for 120 min at 300 °C.



A-91: TPD-MS in Ar with a heating rate of 10 °C/min of MoO₃ after 5 h treatment at 325 °C in H₂:C₃H₆ (9:1) for 5 h.



A-92: TPR-MS in H_2 with a heating rate of $10\text{ }^\circ\text{C}/\text{min}$ of MoO_3 after 5 h treatment at $325\text{ }^\circ\text{C}$ in $H_2:C_3H_6$ (9:1) for 5 h.